

Politecnico di Milano
Dipartimento di Chimica, Materiali e Ing. Chimica Giulio Natta
PhD program in Materials Engineering, XXXIII cycle



**Structure-property relationships of n-type doped
semiconducting polymers: a study based on
vibrational spectroscopy, electrochemical and
morphological investigation**

Supervisors:

Prof. Gianlorenzo Bussetti

Prof.ssa Chiara Castiglioni

Tutor:

prof.ssa Chiara Castiglioni

Coordinator: Prof. ssa Chiara Bertarelli

PhD Thesis of Ilaria Denti

To Orlando

Table of Contents

List of publications	8
Abstract	10
Introduction	12
1.1 An overview of organic semiconducting polymers	12
1.1.1 Doping mechanism in Conjugated Polymers	12
1.1.2 Doping methods	16
1.2 Characterization techniques	17
1.2.1 Vibrational spectroscopy techniques	18
1.2.2 Optical Absorption	20
1.3 Aim and outline of the work	21
Chapter 2: Polaron Structure and vibrational fingerprints of chemically doped P(NDI2OD-T2)	25
2.1 Introduction	25
2.2 Experimental methods	30
2.2.1 Polymer	30
2.2.2 Dopants	30
2.2.3 Sample preparation and doping procedure	31
2.2.4 Infrared and Raman Spectroscopy	31

2.2.5 Computational Details	32
2.3 Results and discussion	32
2.4 Conclusions	50
Chapter 3: Effects of annealing temperature on chemically doped P(NDI2OD-T2): morphological and spectroscopic investigation.....	53
3.1 Introduction	53
3.2 Experimental methods	56
3.2.1 Polymer	56
3.2.2 Dopants	56
3.2.3 Film deposition and infrared Measurements.....	56
3.2.3 GIWAXS sample preparation measurements.....	57
3.3 Results and discussion	58
3.3.1 Electrical properties	58
3.3.2 Infrared spectroscopy	60
3.3.3 GIWAXS measurements	73
3.4 Conclusions	82
Chapter 4: In-situ monitoring of electrochemical doping of P(NDI-gT2) through Raman spectroscopy: polaron and bipolaron formation	85
4.1 Introduction	85
4.2 Experimental methods	90
4.2.1 Materials and dopants.....	90

4.2.2 In-situ Raman setup	91
4.2.3 Electrochemical experiments	94
4.3 Results and discussion	98
4.3.1 Static cell	98
4.3.2 Flow cell.....	112
4.4 Conclusions and future developments.....	128
Chapter 5: A combined use of EC-AFM and Raman spectroscopy: HOPG modifications and porphyrin crystals dissolution in acid environment	132
5.1 Introduction	132
5.2 Experimental methods.....	136
5.2.1 Sample preparation	136
5.2.1 EC-AFM measurements	136
5.2.1 Raman measurements	138
5.3 Results and discussion.....	138
5.4 Conclusions and future developments.....	143
Conclusions	145
Bibliography.....	149

Attachment A	163
Attachment B	204
Attachment C	244
Attachment D	260
Attachment E	267

List of publications

Chapter 2

Denti, I.; Cimo', S.; Brambilla, L.; Milani, A.; Bertarelli, C.; Tommasini M.; Castiglioni C.; Polaron Confinement in n-Doped P(NDI2OD-T2) Unveiled by Vibrational Spectroscopy. *Chem. Mater.* **31**, 6726–6739 (2019)

Chapter 3

Cimo' , S. *et al.*, Room temperature activation of n-type doping of naphthalene diimide - bithiophene copolymer by 1H- benzimidazoles, manuscript in preparation, to be submitted to *Advanced Functional Materials*.

Chapter 5

Bussetti, G.; Yivlialin, R.; Ciccacci, F.; Duo', L.; Gibertini, E.; Accogli, A.; Denti, I.; Magagnin, L.; Micciulla, F.; Cataldo, A.; Bellucci, S.; Antonov, A.; Grigorieva, I.; Electrochemical scanning probe analysis used as a benchmark for carbon forms. *J. Phys. Condens. Matter* **33**, (2021).

Jagadeesh, M. S.; Calloni, A.; Denti, I.; Goletti, C.; Ciccacci, F.; Duo', L.; Bussetti, G.; The effect of cyclic voltammetry speed on anion intercalation in HOPG., *Surf. Sci.* **681**, 111-115 (2019).

Filoni, C.; Duo', L.; Ciccacci, F.; Li Bassi, A.; Bossi, A.; Campione, M.; Capitani G.; Denti, I.; Tommasini, M.; Castiglioni, C.; De Rosa, S.; Tortora, I.; Bussetti, G.; Reactive Dissolution of Organic Nanocrystals at Controlled pH. *ChemNanoMat* **6**, 567–575 (2020).

Abstract

Polymeric semiconductors represent a thrilling group of organic materials with outstanding properties that has proven, over the years, to be adaptable to many research fields. Their relatively low cost and intrinsic properties, such as easy processability and air stability made these materials particularly appealing for thermoelectric, energy storage and organic transistors, among many applications. These materials performances are heavily dependent on their electronic, molecular and super-molecular structure, which is affected by doping processes and doping mechanism. The constant search for new materials and better performances of existing devices needs to be supported by a deep understanding of the charge transport properties of both p-type and n-types polymers, pristine and doped. Among many techniques available to unveil the polymers properties and characteristics, this dissertation focuses on vibrational spectroscopies (Raman and infrared), which we used in searching structure-property relationships upon the formation of charge defects through doping of n-type organic materials (polarons and bipolarons). Moreover, fundamental aspects of doping kinetics and environmental factors will be unveiled in this work, focusing on both chemical and electrochemical doping. First, evidence of charge defect localization and hopping-type charge transport mechanism in chemically doped P(NDI2OD-T2), a pioneer n-type polymer, will be provided. Chemical doping kinetics will be further exploited regarding the effect of annealing time and temperature. To characterize these effects on a multiscale, the results of other complementary techniques will be presented, such as Grazing Incident Wide X-ray Scattering (GIWAXS), which probes the material morphology. Moreover, several aspects of the electrochemical doping will be analyzed, such as the influence of environmental oxygen on polaron and bipolaron formation, as well as the type of electrolyte; in addition, the reversibility of electrochemical doping is investigated. The study on electrochemically doped samples will be pursued through in-situ Raman spectroscopy coupled with an electrochemical characterization. Finally, the combination of Raman and Atomic Force Microscopy will be presented in the final part of this dissertation as a powerful toolset to characterize organic materials.

Introduction

1.1 An overview of organic semiconducting polymers

The search for organic semiconductors materials as promising alternative to their inorganic counterparts in applications, ranging from electronic to energy storage, as well as sensing, has been ongoing for more than 50 years. An interesting class of materials with outstanding properties are conjugated systems, whose most peculiar property is the delocalization of π -electrons. The overlap of nearby p orbitals results in a single bond/double bond configuration, showing more or less pronounced bond length alternation, which reflects the degree of delocalization of π -molecular orbitals. In the case of p-type and n-type conjugated polymers, the conjugated domain is commonly the polymer backbone. Their semiconducting properties are caused by the splitting of the π -band, resulting in an empty conduction band (π^* -band) and a filled valence band (π -band), whose electrons can be excited by an electromagnetic wave, while the bandgap value range from 1 to 4eV¹. Absorption phenomena take place when the energy of the incident light matches or exceeds the energy gap. This is the reason why, when illuminated by a source in the visible range, the polymer presents a specific color, which can change when its intrinsic properties are changed (for example, by doping).

1.1.1 Doping mechanism in Conjugated Polymers

Charge carriers density can be increased by injection (or withdrawal) of electrons in π^* (π orbitals) in different ways: the most common strategy is chemical/electrochemical doping of the polymer.

The conduction and valence bands structure for conjugated polymers presents analogies to the one existing for the inorganic materials. The Lowest Unoccupied Molecular Orbital (or LUMO) corresponds to the state at the bottom of the conduction band, and the Highest Occupied Molecular Orbital (HOMO) corresponds to that at top of the valence band.–However, the

conduction mechanism is usually very different, and is dominated – in the most cases – by intra-chain or inter-chain charge (hopping mechanisms) among different sites.

As for their inorganic counterparts, when talking about charge injection, or doping, of p- types polymers (transporting holes) and n-types polymers (transporting electrons), a distinction needs to be pointed out. In the case of p-type polymers, electrons are transferred from the HOMO of the polymer to the LUMO of the dopant (**Figure 1.1 -right side**). The two energy levels need to be aligned to promote the doping of the material. This condition is fulfilled when the electron affinity of the dopant is close to the ionization potential of the polymer². On the other hand, in the case of n-type polymers (**Figure 1.1 -left side**) the dopant is ionized and thus loses an electron, which is transferred to the LUMO of the polymer.

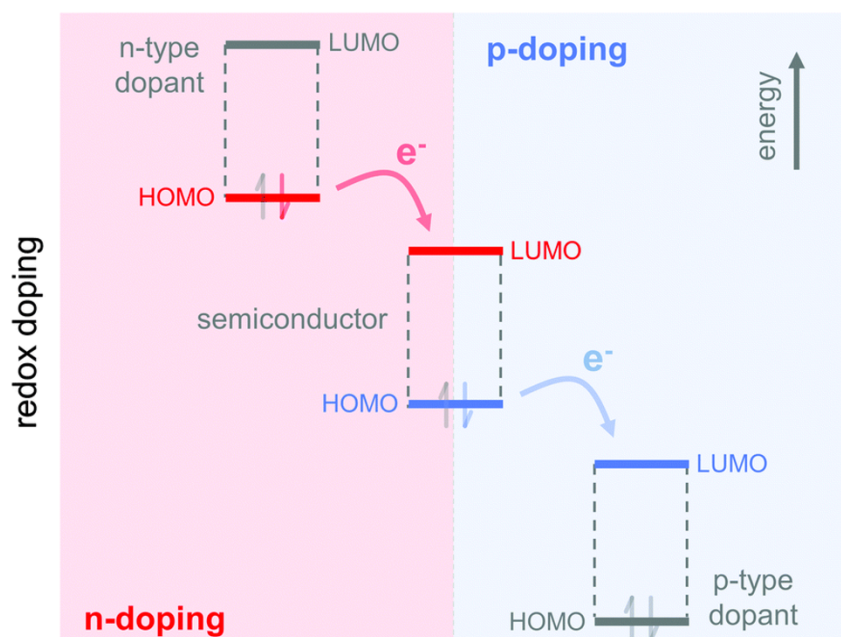


Figure 1.1: schematic of the doping principle for n and p-type semiconducting polymers. Adapted from²

When an electron or a hole is injected in the material, two possible charge transport mechanisms may occur. Overlapping between the π -orbitals occur either in the chain direction or between different chains. The charge can then either move along the polymer chain (intrachain) or between chains (interchain) (**Figure 1.2**).

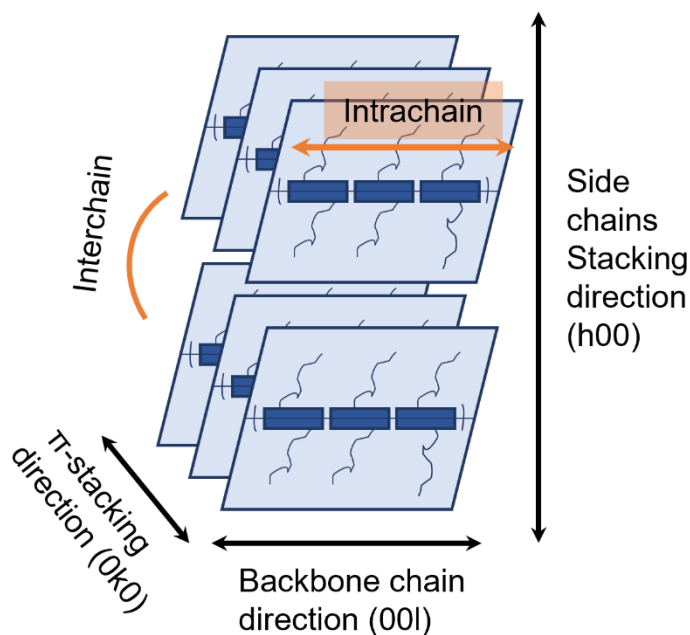


Figure 1.2: schematic representation of the interchain and intrachain charge transport mechanism for a generic polymer.

The charge defect (or charge carrier) formed upon doping is well-known as polaron. The polaron is defined as a quasi-particle, namely the electron or hole resulting from the doping, and the consequent distortion of the material (polymer) lattice. Similarly, a bipolaron is a quasi-particle describing the distortion of the material lattice upon injection of two charges (**Figure 1.3**).

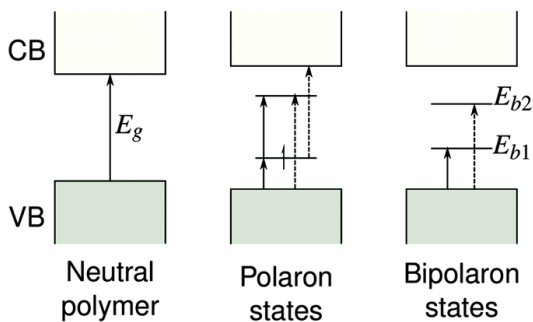


Figure 1.3: Band diagrams of pristine and doped (with polaron and bipolaron levels) semiconducting polymer, adapted from:³

Fully understanding and describing charge transport mechanism, polaronic and bipolaronic features is a hard task due to the intrinsic nature of polymer doping. Unlike the case of the inorganic materials, where doping consists in a defect obtained by the mere substitution of a single-atom, and high conductivity levels can be reached with low dopant quantities, for organic materials several factors need to be taken into account. First, the dopant is a molecule with a certain steric hindrance, that often needs to be mixed with the polymer in fairly large quantities for the doping to be effective. The dopant interacts with the polymer structure and morphology, drastically changing it. Both pristine and doped polymer morphology and structure is sensitive to many factors, like processing conditions⁴, temperature⁵ and depositions methods to cite some. In the case of doping, the structure is highly affected by the dopant position in the polymeric matrix⁶, as well as the effectiveness of the doping process (segregation effects of the dopant) or the doping methods⁷ and the degree of order of the deposited sample (higher disordered systems usually present lower conductivities)⁸.

Charge transport is strongly correlated with the polarons size and shape, as a more delocalized polaron along the chain is often symptom of an intrachain transport mechanism. A flatter structure of the polymer chain favors the delocalization of π electrons and thus of the charge defect, through the overlapping of π -orbitals.

While interchain transport mechanism could prevail when the torsional angle between the polymer units is pronounced, charge transport strongly depends on the coupling between

different polymer molecules, and the level of order in the polymeric film. An interesting case-study in this matter is the notorious P3HT, where the close interplay between the level of order in the film and the delocalization of the polaron was proved to be correlated with mobility⁹.

In this framework, another relevant issue is to achieve a good stability and reproducibility of the performances that are affected by several structural aspects: for this purpose, a deep understanding of the charge transport mechanisms, as well as providing strong structure property relationships is necessary.

1.1.2 Doping methods

Chemical and electrochemical doping, which will be used in this dissertation, are briefly presented in this section.

The most common way to achieve chemical doping is through a solution mixture of the dopant and the polymer in a suitable ratio. The mixture is then deposited on a substrate and annealed to favor the creation of the charge complex. Depending on the semiconductor type, the dopant can oxidize (n-types) or reduce the polymer (p-types). As previously mentioned, the presence of the dopant could affect the order of the film during deposition¹⁰ or, if present in large quantities, could segregate on the surface, causing the conductivity to plateau after reaching a threshold dopant concentration or even become lower¹¹. For this reason, a good miscibility of the dopant with the polymer would improve the overall quality of the film, without affecting the transport properties^{12,13}.

In the case of electrochemical doping, a redox reaction occurs when the polymer (redox active material), deposited on an electrode, is immersed in an electrolyte and a voltage difference is applied between two electrodes. The best way to build a setup is with 3 electrodes, a reference one, connected with the substrate, a counter and working electrodes. The potential difference is applied between the two latter. In this case, charge carriers (namely electrons or ions) are injected in the polymer backbone from the electrolyte, as oxidation (p-types) or reduction (n-types)

reactions take place¹⁴. A schematic of the charge migration upon electrochemical doping is showed in **Figure 1.4**.

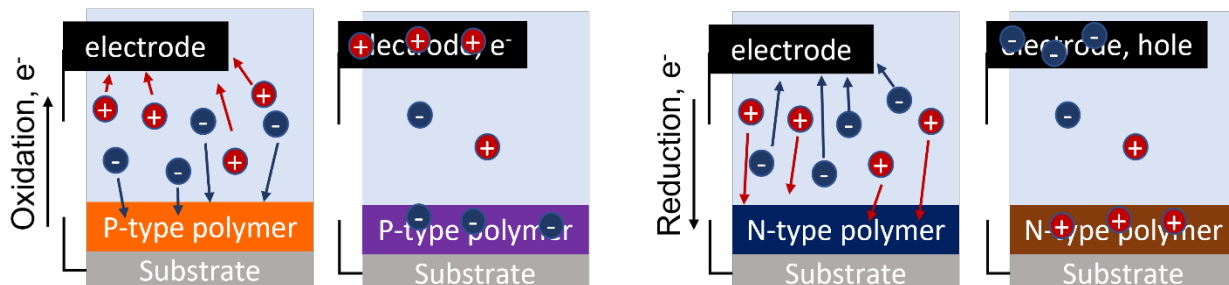


Figure 1.4: Schematic of the electrochemical doping for p-type (on the left) and n-type (on the right), highlighting the charge distribution and migration.

1.2 Characterization techniques

Establish structure-property relationships in semiconducting polymers is a challenge because of many factors. Their disordered nature, consisting of long entangled chains, the complexity of the doping processing conditions and of the kind of dopant cause figure of merit for applications to range on various scales¹⁵. A large variety of techniques, from molecular to the macroscale are often used to unveil structural characteristics and better understand these materials. Optical absorption and vibrational spectroscopy techniques proved to be among the most effective methods to study charge defects and doping mechanism. Despite this dissertation mainly focuses on vibrational spectroscopies, investigating other aspects such as crystallinity and morphology of the polymer is essential. The technique that is commonly used to achieve this goal is Grazing Incident Wide X-ray Scattering (GIWAXS), which provided great insights in the structural changes in the material due to environmental conditions on both pristine and doped polymers (e.g. temperature, annealing, water influence).^{5,16-19}

In the next session vibrational spectroscopy and optical techniques applied to the study of doped semiconducting polymers will be briefly presented.

1.2.1 Vibrational spectroscopy techniques

Vibrational spectroscopy (namely Raman and infrared spectroscopy) represents a non-disruptive group of techniques that can easily give insights on a sample at the molecular level thanks to the easy preparation of the samples and straightforward setup. They provide information about chemical composition and molecular structure and allow monitoring in-situ their alterations upon specific treatments (e.g., doping, or annealing) or weathering/degradation processes.

A turning point in the description of doped polymer spectra was reached in 1987 when Horovitz et al. developed the Amplitude Mode Theory (AMT), providing a description of the vibrational modes of *trans*-polyacetylene, showing a strong coupling with π -electrons²⁰. Amplitude modes, which modulate the Peierls gap, were previously described by the same authors to discuss Resonant Raman active vibrations in pristine $\text{trans}-(\text{CH})_x$ and $-(\text{CD})_x$ ²¹. Their groundbreaking theoretical work is accompanied with the experimental evidence coming from infrared spectra of doped polyacetylene, showing that the charge injected upon doping has a non-negligible impact on the activation of the Amplitude Modes in IR, giving rise to strong absorption bands, called IRAV, namely Infrared Activated Vibrations. IRAVs are ascribed as Raman modes of the pristine polymer that are activated in the infrared spectrum upon doping, due to the change in symmetry. A further development in the description of the charge carriers was conducted by Bredas group²²⁻²⁴, which described the charge distribution associated to geometry relaxation in the case of doped polyene chains.

An interpretation of the IRAV bands in doped polyacetylene was provided in 1988 by Castiglioni et al.²⁵ in the framework of the GF formalism²⁶ applied to the vibrational problem of polyacetylene. This theoretical model effectively reduced the number of parameters necessary to explain the relevant spectroscopic phenomena, introducing the Effective Conjugated Coordinate

(ECC); subsequently, this approach has been extended to a variety of polyconjugate organic materials²⁷⁻²⁹. These works demonstrated that IRAVs contain information about the charge carriers (i.e., charged solitons and polarons) in polyacetylene, polythiophenes and related polymers, providing polaron markers of doped semiconducting polymers. It is therefore possible to obtain a comprehensive description of the charge defect by means of vibrational spectroscopic techniques, characterizing the structure of the polaron at the molecular level.

IRAVs bands intensity is often much higher than the typical IR bands, as their dipole strengths is comparable with the electronic transitions, even for small doping percentage³⁰. By combining first-principle modelling with spectroscopic techniques, this behavior has been correlated to huge charge fluctuation associated to peculiar vibrational displacements of the atoms in the polaron region, i. e. to vibrations involving the ECC coordinate, which in turn is related to phonon assisted intrachain charge transport mechanism. This discover demonstrates that the study of the vibrational spectroscopic features gives a deep inside in the interchain vs intrachain charge transport mechanism and, in particular, about the possible existence of phonon-assisted intramolecular charge hopping processes.

Vibrational spectroscopy permitted a comprehensive description of charge defects in p-type doped semiconducting polymer, but a specular study for n-type polymers is still missing. The lack of vibrational studies on n-type polymers is partially explained because the first air-stable n-type polymer was synthesized for the first time in 2009 by Facchetti et al.³¹. In this work, an NDI-based donor-acceptor copolymer, poly{[N,N-bis(2-octyldodecyl)-naphthalene-1,4,5,8-bis(dicarboximide)-2,6-diyl]-alt-5,5-(2,2-bithiophene)} or P(NDI2OD-T2) was presented and it's nowadays one of the most studied in literature. In the effort to better characterized the structure of P(NDI2OD-T2), a theoretical and experimental work by Giussani et al. was presented in 2013³². Vibrational transitions were individuated in the IR spectrum, which intensity is sensitive to the polymer conformation and an estimate of the torsional angle between the NDI2OD unit and the T2 moiety was obtained. By comparing the C=O band intensity of the infrared spectra acquired in transmission and reflection-absorption IR spectroscopy (RAIRS) data the dihedral angle was estimated to be 38°, with the T2 units laying flat on the substrate and the NDI2OD units tilted,

when the polymer adopts the so-called face-on geometry. Through vibrational spectroscopy, charge transport properties of doped P(NDI2OD-T2) were also correlated with both the regioregularity of the backbone³³, as well as a remarkable supramolecular order of the polymer chains³⁴. Raman spectroscopy has proven to be an effective complementary tool to infrared techniques in exploiting polymeric material and the doping effects, showing vibrational features related to the formation of the charge defect^{35,36} or degradation due to water and oxygen exposure³⁷.

To further characterize in-situ semiconducting polymers, experimental techniques based on vibrational spectroscopy were developed or adapted.

Raman combined with custom-made electrochemical cells or Tip Enhanced Raman Spectroscopy setup perform comprehensive study of organic materials. When using these techniques applied to the description of doped organic semiconducting polymers, redox properties of different electrolytes can be exploited, from simple salt solutions¹⁶ to ionic gels³⁸.

1.2.2 Optical absorption

Optical absorption spectroscopies in UV-Vis range, are effective techniques in monitoring doping effects on semiconducting polymers^{39,40}, because of their intrinsic property to change color upon doping. In this short section I will concentrate on applications to n-type polymers, but a wide selection of studies is available in literature for p-types⁴¹.

A typical UV-Vis spectrum of pristine P(NDI2OD-T2) shows two bands: one, more intense, at higher-energy (approximately 390nm) is assigned to the π - π^* transition, the other, broader, at lower energy (750nm) presents more complex features. The peak visible at 705nm is ascribed to the Charge Transfer transitions between the NDI and the T2 moiety, the other at 800 nm to a transition involving intermolecular aggregates, namely interacting chains segments^{33,42}. When P(NDI2OD-T2) is doped and the polaron is formed, his absorption spectrum changes accordingly. The low-energy band (705nm) is quenched while the 390nm centered one undergoes a blue shift with the increment of doping level. Moreover, two absorption bands around 500 and 820nm arise, ascribed to the formation of charged species.⁴³

UV-vis-NIR spectroelectrochemistry is another way to visualize changes in the absorption spectra as the difference between a reference spectrum and that of a charged species. The spectral range is quite wide (200-2500nm), providing an insight on the excitations of the π - π^* transitions⁴¹. This interesting tool allows a direct monitoring of charge transfer states and their kinetics during doping and de-doping processes. A reference pristine spectrum is acquired at the beginning of the experiments and then subtracted to the charged spectra. Polaronic and bipolaronic features can be easily individuated upon doping, where the polaronic feature lays at higher energy (500 nm) and the bipolaronic features around 630 nm.^{44,45} Together with other experimental techniques, spectroelectrochemistry has proven to be a complementary tool in studying reaction reversibility⁴⁵, stability in the electrolyte⁴⁴ and polymeric design^{44,46}.

Finally, Charge Modulation Spectroscopy (CMS) is a sensitive technique that captures the changes in the spectrum of a material subjected to different voltages exploiting a field-effect transistor like set-up. This in-situ technique measures the light absorption by the polaron, involved in charge transport, in a device-like condition, at the dielectric semiconductor interface, when the proper voltage is selected. For this reason, the polaron size, coherence length and shape can be calculated, showing distinct features for intrachain and interchain absorption⁴⁷.

This technique was able to provide a direct measurement of both the intra and intermolecular charge interaction for p-types^{48,49} and Donor-Acceptor⁵⁰ polymers, where holes and electrons are distributed along the backbone in ordered aggregates.

1.3 Aim and outline of the work

In this dissertation I will mainly concentrate on the application of vibrational spectroscopy (infrared and Raman) to establish structure-property relationships for doped n-type semiconducting polymers. This PhD work aims at further confirming the role of vibrational spectroscopy in the characterization of the charge defect created upon doping, and the effect on charge transport property. Moreover, various aspects of polymeric doping will be studied, as the effect of annealing temperature, doping techniques and pH of the electrolyte solution on the formation of polaron and bipolaron. The experimental findings will be supported by DFT

calculations, as well as GIWAXS experiments to further characterize the polymeric structure and crystallinity.

Moreover, the opportunities that the combination of Raman spectroscopy and other experimental techniques offer in characterizing organic compounds will be exploited, concentrating on electrochemical characterization and Atomic Force Microscopy.

In **Chapter 2** Raman and transmission infrared experiments were conducted on pristine and chemically doped P(NDI2OD-T2). New vibrational bands ascribed to the polaron were individuated, both for infrared and Raman spectra. The radical anion is localized on the NDI2OD unit, whereas the T2 moiety doesn't seem to contribute to charge defect. This behavior is confirmed by Resonant Raman experiments, which can selectively highlight features of the T2 by tuning the excitation wavelength. Because of the torsional angle between the two polymer building blocks and the localization of the charge defect on the NDI2OD unit, the charge transport mechanism is most likely to be inter-chain. DFT calculations were also conducted to support the spectra analysis. Despite giving an experimental toolset to understand properties of the charge defect, many aspects of doping mechanism still need to be unveiled.

The temperature and the kinetics of doping effect on conductivity and the structure of chemically doped P(NDI2OD-T2) is presented in **Chapter 3**, where infrared spectroscopy, temperature-dependent, in situ measurements were conducted together with a GIWAXS characterization of samples annealed with different temperatures and time, conductivity measurements and DFT calculations. The conductivity of the doped film remarkably enhances of more than 3 orders of magnitude before annealing takes place, and the structure of the sample is already shifted from face-on (typical of pristine P(NDI2OD-T2)) to edge-on, showing that the dopant is already active at room temperature. Moreover, further rearrangements of the morphology can be correlated with the doping conditions and the subsequent evolution of the crystalline phase, upon annealing.

Chapter 4 highlights the study of electrochemical doping on modified P(NDI2OD-T2), characterized by glycol chains which make it water compatible. The effect of oxygen and pH of the electrolyte are studied using a custom-designed in-situ electrochemical cell, to monitor differences of the spectra in-real time with the applied potential. Electrochemical experiments

were also conducted to further monitor the stability of the electrochemical reaction. Remarkably, not only the polaron vibrational bands and onset voltages are individuated, but also bipolaronic Raman features are reported. The reaction reversibility and effectiveness can be successfully monitored through this technique.

Finally, **Chapter 5** focuses on the combination of Raman spectroscopy, electrochemical characterization techniques and Atomic Force microscopy to characterize organic samples surfaces on a multiscale, providing an example of their potential. This exciting relatively new combination of different in-situ techniques presents is a very promising tool for a comprehensive analysis of surfaces.

Published and draft papers reporting my results described in **Chapters 2,3,5**, are attached at the end of the specific chapter.

Chapter 2: Polaron Structure and vibrational fingerprints of chemically doped P(NDI2OD-T2)

In this chapter I report the use of vibrational spectroscopy (infrared and Raman) to unveil the formation of the polaron in P(NDI2OD-T2) doped with N-alkyl based benzimidazole molecules. The experimental findings are supported by DFT calculations. The analysis of vibrational spectra proves that the charge defect formed upon doping is mainly localized on the NDI unit. This finding supports the hypothesis that the mechanism responsible for charge transport in these systems is inter-chain (hopping between units).

2.1 Introduction

Conjugated polymers doped with organic molecules have been extensively studied in the recent years, due to their easy processability, tunable properties and high conductivity, which can be used in many fields, from biosensing to transistors. One of the main goals for these materials is learning how the charge transport process upon polaron (i.e., charge defect) formation takes place. Polaron formation in p-conjugated polymers is favored by the strong electron-phonon coupling of these material^{23,27,28,30,51}, resulting in charge carriers characterized by a localized distortion of the nuclei. There are two main charge transport mechanisms possible for doped semiconducting polymers: interchain (hopping between chains) and intrachain. The latter dominates in p-type polymers, which were widely studied in the past due to their high conductivity values (up to $\sigma = 4380$ S/cm for poly(3,4-ethylene-dioxythiophene):polystyrenesulfonate (PEDOT:PSS) with H₂SO₄)⁵² as well as easy processability when exposed to air. In this case, the charge transport is associated to the formation of a rather delocalized polaron (or charge defect) and can be investigated through vibrational spectroscopy. Beside the presence of a strong polaronic electronic transition, sometimes occurring in the NIR

range, new vibrational bands appear in the MIR range, namely the infrared activated vibrational bands or IRAVs (Infrared Active Vibrations) or intense vibrational modes (IVMs)^{20,27,28,51}, with absorption intensities comparable to those of the electronic transitions. These vibrational features consist in strong Raman bands activated in the infrared upon doping, when in the positive charge delocalized along the backbone, with intensities higher than normal infrared bands, even when a small percentage of dopant is used. These high intensities are associated by a coupling of the charge defects formed upon doping with a large electron charges flux.

While p-types polymers have been extensively studied for a few decades, the charge transport mechanism for their n-type counterpart has not been unveiled yet. In fact, experimental data for n-types are non-trivial to acquire, due to the air instability of both the polymers and the dopants. The real turnover for these material started in 2009, when Facchetti^{31,53} synthesized a n-type polymer highly stable in air, the Poly[[N,N'-bis(2-octyldodecyl)-naphthalene-1,4,5,8-bis(dicarboximide)-2,6-diyl]-alt-5,5'-(2,2'-bithiophene)] or P(NDI2OD-T2) Polyera ActivInk N2200, with a high electron mobility of 0.85 cm²/(Vs), **Figure 2.1**.

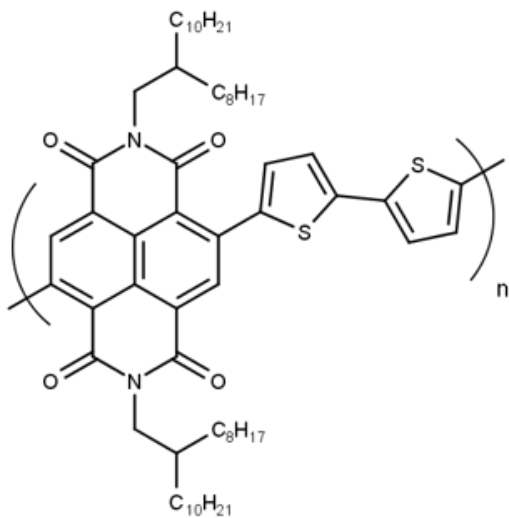


Figure 2.1: P(NDI2OD-T2) chemical structure.

Another setback in the research for n-type polymers was finding an air stable, solution processable dopant. The work by Bao et al. of 2010 overcame this issue⁵⁴, as it showed how the use of 1H-benzimidazole based molecules successfully doped PCBM. This breakthrough allowed the synthesis of the compound DMBI as a dopant P(NDI2OD-T2)⁵⁵.

The doping mechanism for the 1H-benzimidazole molecules/ P(NDI2OD-T2) compound was proposed to be a hydride transfer, followed by an electron exchange, as shown in **Figure 2.2**.^{56,57}

One of the main issues to overcome when doping polymers is phase segregation of the dopant, especially with high concentrations of dopant. This phenomenon has been extensively reported in literature, and directly observed through Atomic Force Microscopy (AFM)⁵⁸.



Figure 2.2: Hypothesized mechanism for n-type doping, composed of 2 steps, a hydrogen transfer followed by an electron transfer.⁵⁹

After these pioneering results, several works aimed at functionalizing these molecules to increase the conductivity of the polymeric doped films.

An interesting way to increment the doping ratio avoiding phase segregation is to functionalize the dopant with alkyl chains, as Saglio et al demonstrated in 2011.¹¹

This work focuses on tailoring the alkyl chains, focusing on branched and linear chains, as shown in **Figure 2.3**.

The molecules with linear chains should have a better miscibility with the polymer, without change in the electron transfer process. The increase of electron conductivity is probably due to intermolecular interaction between the dopants and the polymer.

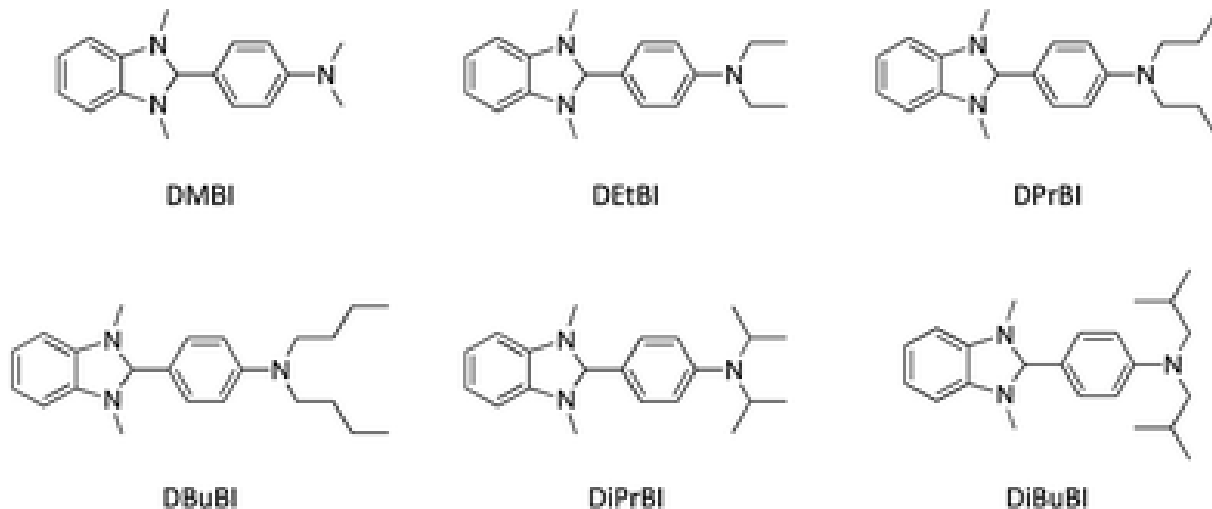


Figure 2.3: N-DMBI based dopants with tailored side chains, to increment conductivity. Both linear and branched side chains were used in this work (courtesy of ¹¹).

In the work of Saglio⁵⁹, the electrical conductivity of P(NDI2OD-T2) doped with different concentrations of the N-alkyl benzimidazole molecules was characterized. In particular, the following findings were highlighted:

1. The highest conductivity values (up to $4.1 \times 10^{-3} \text{ S/cm}^{-3}$) for the samples with the linear alky side chains was reached with DBuBI, the one with the longest linear side chains. Moreover, the conductivity starts to decrease at higher dopant concentration with respect to DMBI⁵⁸, confirming the better miscibility with the polymer with the increase of the side chains (**Figure 2.4**).

2. The maximum value of conductivity for this series of dopants was reached with DiPrBi, the one with the shortest branched alkyl chains (**Figure 2.4**).
3. Dopant segregation was confirmed for high levels of doping through AFM measurements
4. Differential Scanning Calorimetry measurements confirmed that a blend between the polymer and the dopant is formed (melting temperatures shifts toward lower values). Moreover, for long alkyl chains (both branch and linear) the transition peak disappears, indicating a lower degree of crystallinity in the blend. These changes were characterized by GIWAXS measurements.

To further extend Saglio's study, I conducted vibrational spectroscopy measurements, namely Raman and infrared spectroscopy.

In this chapter will show how Raman and infrared measurements, coupled with DFT calculations, can give an insight on the polaron formation when the charge transfer is created upon doping. In fact, it is possible to individuate polaronic features in the Raman and infrared spectra of the doped samples.

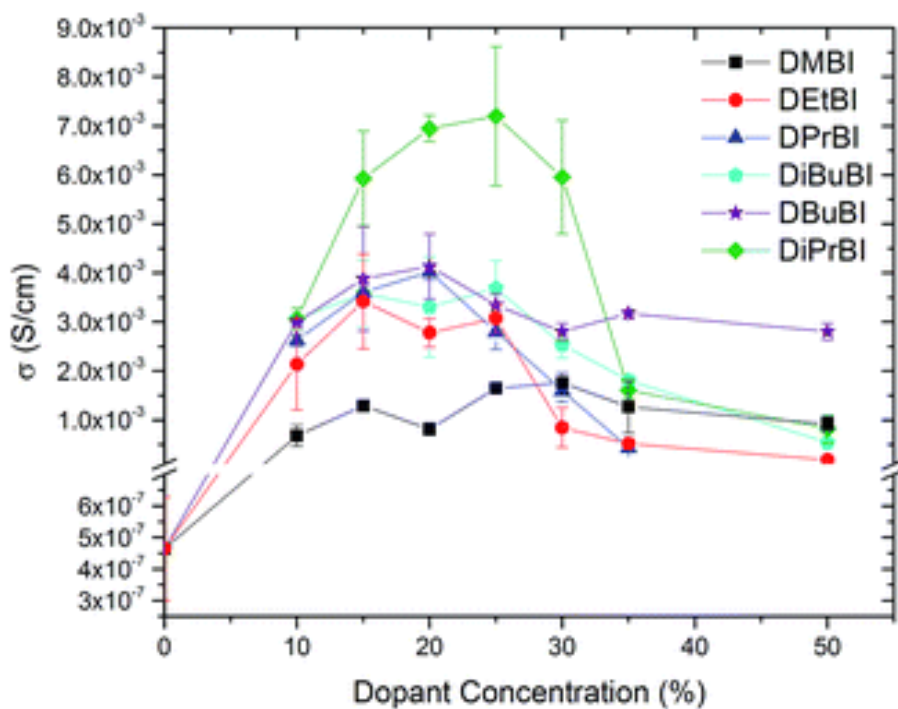


Figure 2.4: Conductivity dependence on concentration for the N2200/DMBI based dopants in Saglio's study. DiPrBI (green line) was the dopant reaching the highest conductivity values, at a concentration of 20%. The conductivity drops significantly after 35% dopant/polymer concentration for all samples, indicating possible segregation of the dopant itself (courtesy of ¹¹).

2.2. Experimental methods

2.2.1 Polymer

Poly{[N,N'-bis(2-octyldodecyl)naphthalene-1,4,5,8-bis(dicarboximide)-2,6-diyl]-alt-5,5'-(2,2'-bithiophene)} (P(NDI2OD-T2)) was purchased from Ossila Lim. (Polyera ActivInk N2200). The polydispersity index (PDI) is ~2-3, the average polymer molecular weight 150 kDa.

2.2.2 Dopants

The chemicals for the synthesis of the dopants were purchased by Sigma Aldrich. N,Ndiisopropyl-

4-(1,3-dimethyl-2,3-dihydro-1H-1,3-benzodiazol-2-yl)-aniline (**DiPrBI**), N,N-diphenyl-4-(1,3-dimethyl-2,3-dihydro-1H-1,3-benzodiazol-2-yl)aniline (**DPhBi**), and N,N-dibutyl-4-(1,3-dimethyl-2,3-dihydro-1H-1,3-benzodiazol-2-yl)aniline (**DBuBI**). Details of the chemical synthesis of the dopants can be found in the Supporting Information of ref.⁶⁰

2.2.3 Sample preparation and doping procedure

P(NDI2OD-T2) was dissolved in Chloroform (CHCl₃) with a concentration of 10 mg/ml, then stirred for 1h at 60 °C. The solution was then filtered using a 0.45 µm pore size polytetrafluoroethylene (PTFE) filter. The dopants were also dissolved in chloroform, using the same concentration. Different aliquots of the dopants were added to a vial with 200 µl of the pristine polymer, to reach different doping concentrations. Molar ratio (MR) between the number of dopant molecules and the number of monomeric polymer units of 0, 0.14, 0.43, and 1.00 were studied in this chapter. The MR were chosen accordingly to ref¹¹ to monitor the effect of doping on conductivity. The solution was then drop casted on Thallium bromo-iodide (KRS5) and zinc selenide (ZnSe) substrates and annealed in a Schlenk tube in argon atmosphere at 150 °C for 6h, to avoid air contamination.

2.2.4 Infrared and Raman Spectroscopy

FT-IR spectra of all the samples (pristine, doped annealed and not annealed) were acquired at room temperature, in air. Transmission spectra were acquired using a Nicolet Nexus spectrometer, with resolution of 2 cm⁻¹. 256 scans were acquired to enhance the noise to signal ratio. Raman spectra were acquired using a Jobin Yvon Labram HR800 Raman spectrometer equipped with an Olympus BX41 microscope and an edge filter system. Different excitation wavelengths were used ($\lambda_{exc} = 457.9$ nm and $\lambda_{exc} = 514$ nm (Ar+ laser)). An excitation wavelength of 633 nm was also used for the experiments. The laser power was set at 0,2 mWatt to prevent sample degradation and a Si wafer was used as calibration sample (spectral line 520.7 cm⁻¹). A backscattering geometry was used with a 50× objective to acquire spectra in the range 200–3200 cm⁻¹ in the Stokes region. The spectra at 1064 nm were acquired using a Nicolet NXR 9650

spectrometer equipped with a MicroStage (resolution 4 cm^{-1} , 1024 scans, laser power 200 mW). Infrared and Raman spectra were analyzed using OMNIC software.

2.2.5 Computational details

Periodic DFT calculations were carried out on the 1D infinite polymer. Pristine and doped state were both simulated using CRYSTAL14 software with hybrid B3LYP functional combined with 6-31G(d,p) basis set. A full geometry optimization of the atom coordinates and the cell parameters was done before the simulations of the vibrational spectra. Postprocessing programs developed at Politecnico di Milano were used to analyze the vibrational normal modes obtained from the DFT calculations and plot the theoretical spectra.

In addition, we carried out gas-phase DFT calculations on selected molecular fragments of P(NDI2OD-T2) the same functional and basis set of the periodic boundary calculations, using the Gaussian suite ⁶¹

2.3 Results and discussion

Three dopants of the family of the N-alkyl benzimidazole were chosen for this study, with different steric hindrances. Molecular Ratios (MR) of 0, 0.14, 0.43 and 1 were exploited, corresponding to Saglio's dopant concentrations of 5, 20 and 35%¹¹. In particular, the MR of 0.43 (20% dopant concentration) is the value for which the highest conductivity for the dopants is reported, while the other values allow a comparison with samples with a low and a high dopant concentration. All the samples, regardless of the type of dopant used, report the same polaronic behavior. Only small changes in the spectra are reported for the different dopants at the same concentration, which allow to distinguish the dopant species, whereas polaronic signature bands are almost independent of the dopant and show similar position, shape and intensities in all the spectra (see **Attachment A**).

The first interesting result was found before the annealing process: infrared spectra of the not annealed samples are the exact superposition of the dopant and the polymer pristine spectra, weighted on the MR of the dopant. The 1120 cm^{-1} band of the dopants was used as a weight for

the subtraction, because it is situated in an area of the spectra free of the polymer bands, indicated with a black arrow in **Figure 2.5**.

The spectra in **Figures 2.5** are the results of the weighted subtraction of the dopant spectra to the dopant/polymer compound one for samples doped with DPhBI. It is worth noting the presence of a residual dopant band at 1490 cm^{-1} in the subtraction, corresponding to the most intense band of the dopant spectra. The band is most possibly due to an intermolecular rearrangement of the dopant when mixed to the polymer, rather than an indication of charge transfer, as doping induced marker band as easily individuated after annealing. These results are an indication that, for bulk sample prepared and analyzed in air, the annealing procedure seems a fundamental process to create the charge transfer complex.

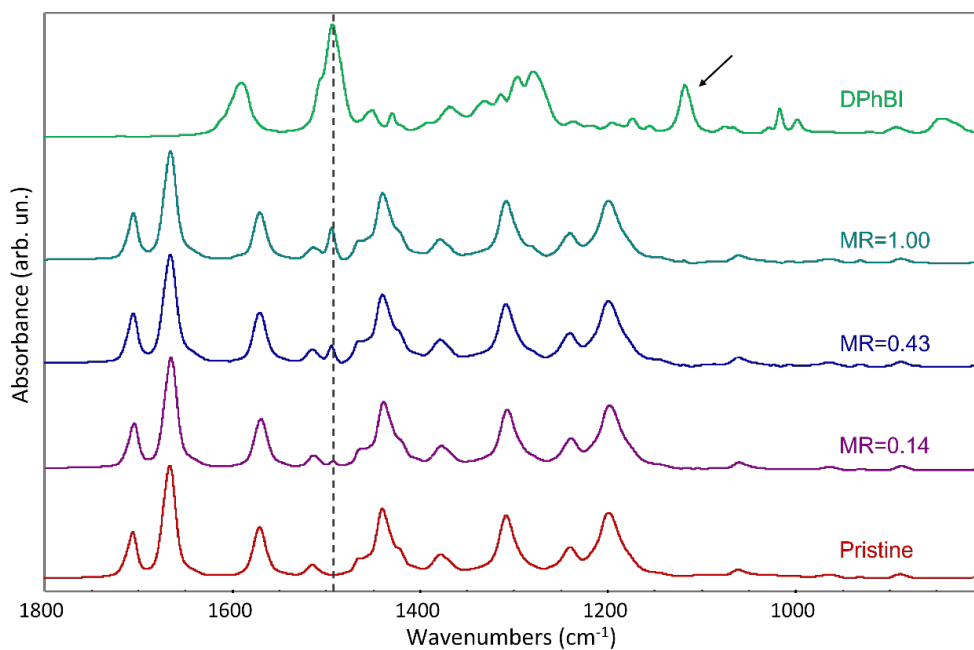


Figure 2.5: comparison between the pristine P(NDI2OD-T2) spectrum (red bottom line), the dopant spectrum (DPhBI, green line) and the weighted subtraction of the dopant spectra to the dopant/polymer compounds with MR of 0.14, 0.43 and 1.00.

Spectra of samples of P(NDI2OD-T2):DBuBI and P(NDI2OD-T2):DPrBI with different concentrations, before annealing, are reported in **Figures 2.6** and **2.7**, respectively. The 1120 cm^{-1}

¹ dopant band is visible in the polymer/dopant samples, with intensity proportional to the degree of doping (i.e. quantity of dopant in the mixture). The behavior is similar to that observed for samples doped with DPhBI, so we can conclude that in the films just deposited the charge transfer process has not yet occurred.

After the annealing in an inert atmosphere is completed, the spectra change drastically (**Figures 2.8, 2.9, 2.10**).

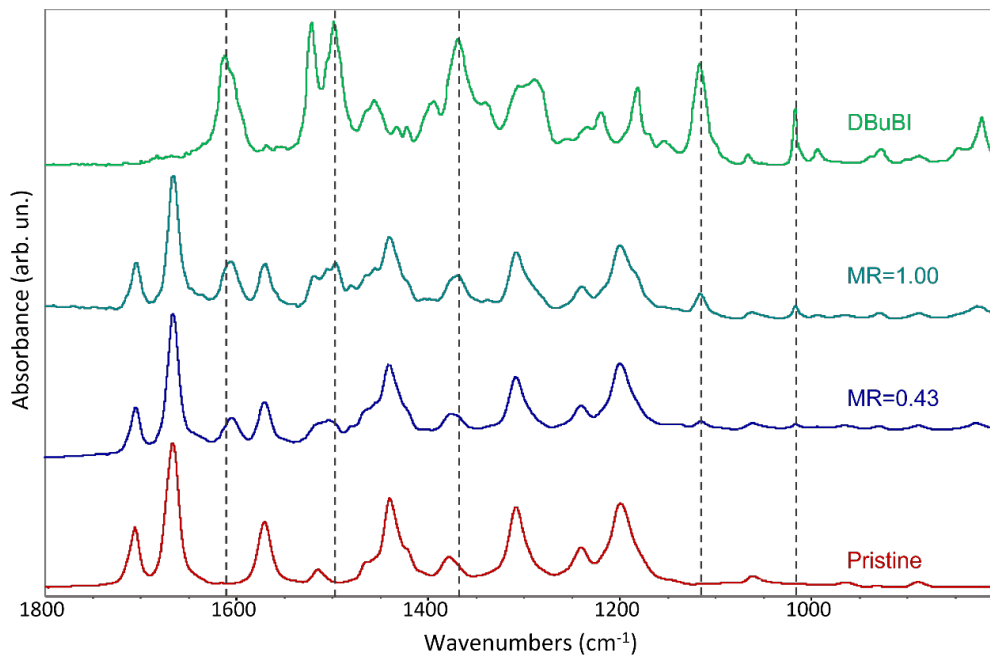


Figure 2.6: comparison between the pristine P(NDI2OD-T2) spectrum (red bottom line), the dopant spectrum (DBuBI, green line).

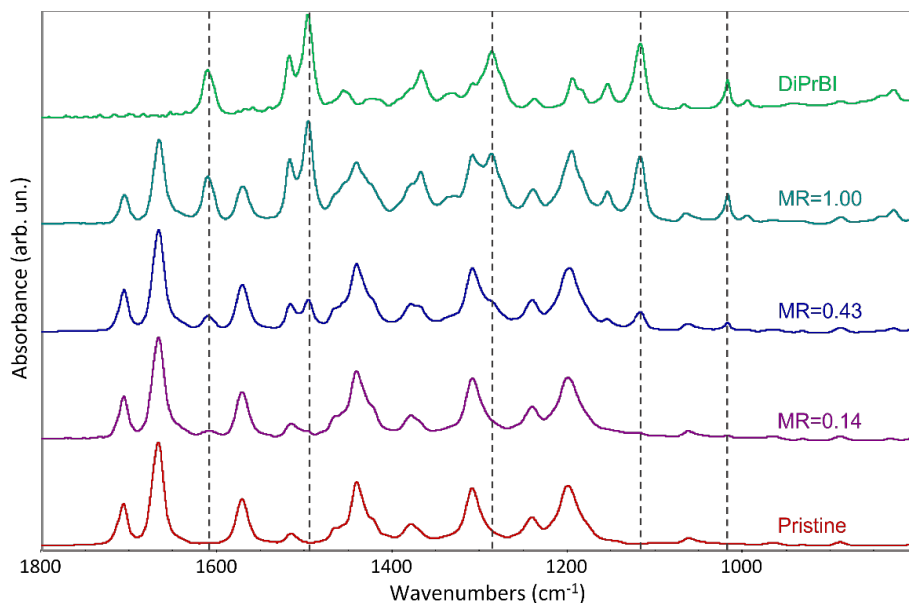


Figure 2.7: comparison between the pristine P(NDI2OD-T2) spectrum (red bottom line), the dopant spectrum (DPrBI, green line).

New bands, labeled with asterisks in **Figure 2.8**, arise, which are not ascribed to the pristine nor the dopant spectra. In particular, in the region characteristic of C=O and the CC stretching bands of the NDI2OD unit we observe a drastic change of the spectral pattern. New bands (1638 cm^{-1} , 1160 and 1100 cm^{-1} , as well as 1513 and 1468 cm^{-1}), which are not in correspondence with any pristine dopant or pristine polymer spectroscopic fingerprints, increase intensity with the dopant concentration. The bands marked with an asterisk are an indication of the formation of the polaron. Bands in correspondence with one of the dopants (labeled with a triangle, 1597 cm^{-1} , 1490 cm^{-1} , the broad vibrational band at 1300 cm^{-1}) and of the pristine spectra (labeled with a circle) can be individuated and are not affected by doping, independently from the dopant concentration. As a reference for the pristine polymer and for the dopant two peaks are highlighted with dashed lines, respectively the red line corresponds to the symmetric CO of the pristine polymer and the green line to the 1490 cm^{-1} peak of the dopant.

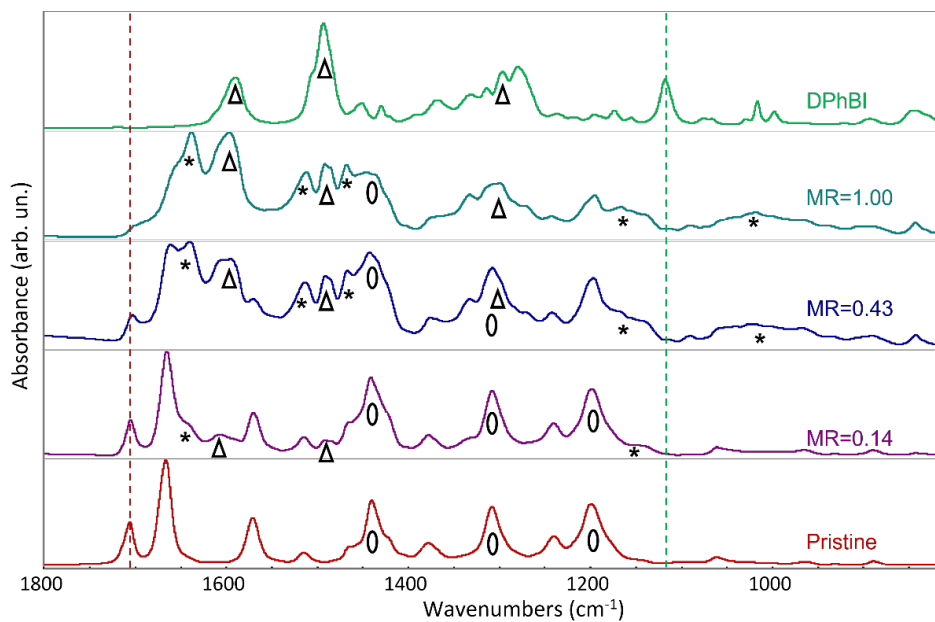


Figure 2.8: from bottom to top, pristine spectra of P(NDI2OD-T2) (red), doped annealed spectra (purple with MR=0.14, blue with MR=0.43 and dark green MR=1.00), dopant spectra (DPhBI, light green)

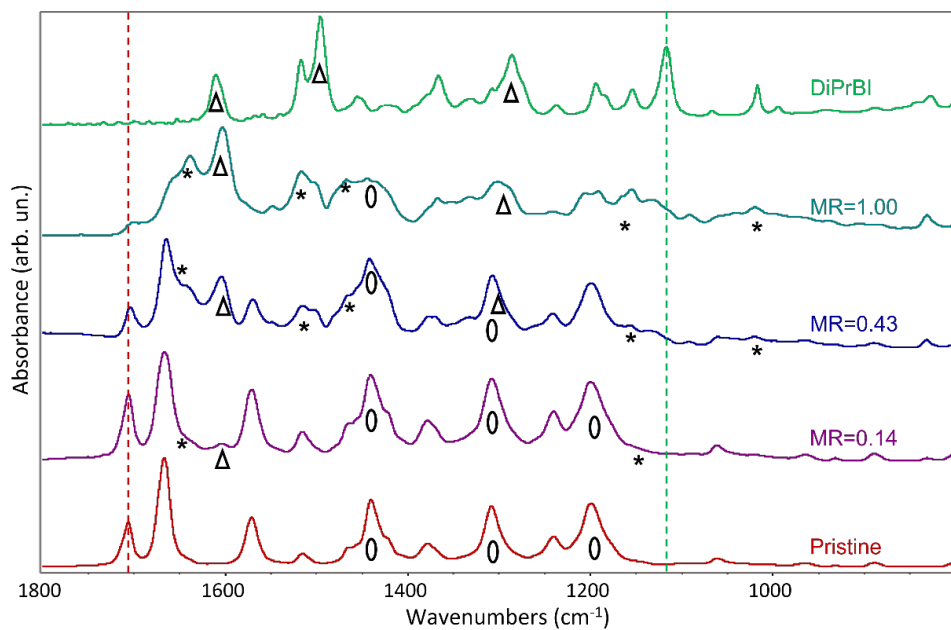


Figure 2.9: from bottom to top, pristine spectra of P(NDI2OD-T2) (red), doped annealed spectra (purple with MR=0.14, blue with MR=0.43 and dark green MR=1.00), dopant spectra (DiPrBI, light green)

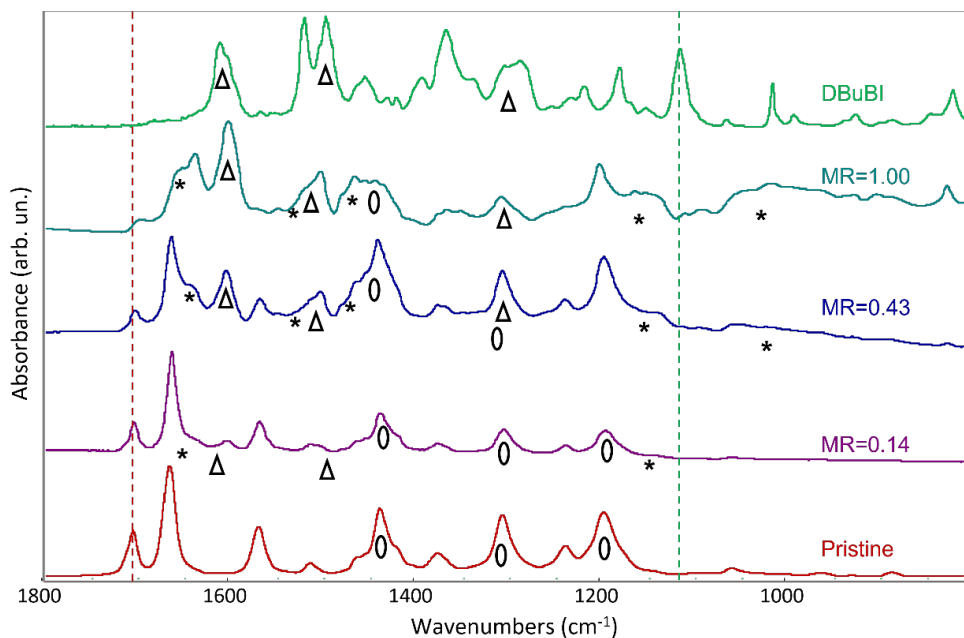


Figure 2.10: from bottom to top, pristine spectra of P(NDI2OD-T2) (red), doped annealed spectra (purple with MR=0.14, blue with MR=0.43 and dark green MR=1.00), dopant spectra (DBuBI, light green)

The position of the doping induced bands described in this chapter do not change varying the dopant functionalization (see **Figure 2.11** for a comparison of the spectra doped with different dopant molecules at MR=1.00). This behavior suggests that the charge defect created upon doping is almost independent of the dopant type. This hypothesis will be further explored in **Chapter 4**, dealing with electrochemical doping.

These experimental observations lead to the conclusion that the charge defect (involving structural relaxation of the polymer) is formed upon doping, after annealing the samples. A comparison of the IR features of doped P(NDI2OD-T2) with p-type polymers data shows a remarkably different behavior: for p-type polymers (i.e., polyacetylene or P3HT) the polaron formation is associated to very strong IR features (IRAVs), which are related to a highly delocalized charge defect. These bands present high intensities, comparable to the one of pristine bands, even with very small doping percentages. In the case of the doped P(NDI2OD-T2), IRAVs (i. e. the

bands labelled with *) present similar intensities to pristine bands, at very high dopant concentrations in the film (molar ratio of the order of 1).

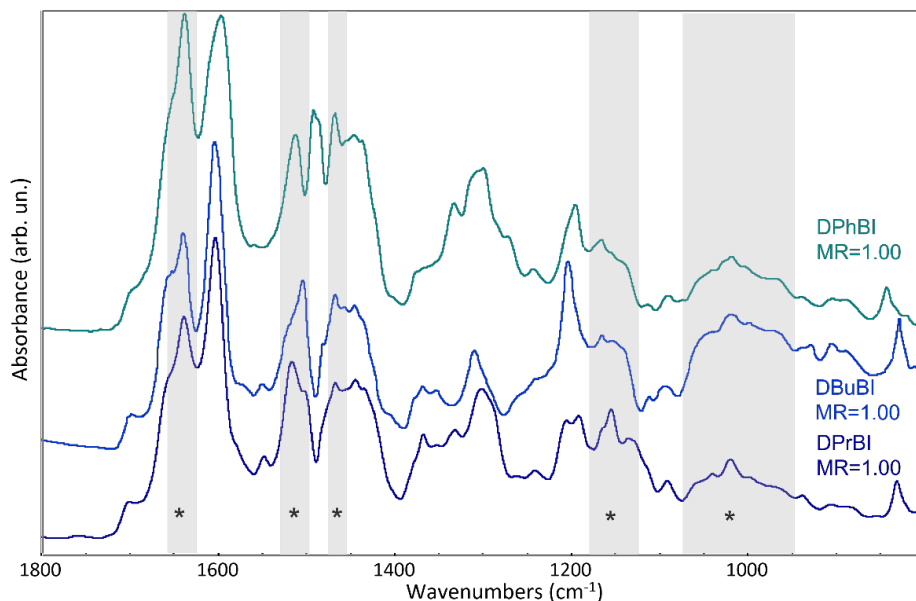


Figure 2.11: comparison of the spectra doped with different molecules at MR=1. The main polaronic features are highlighted with an asterisk and a vertical grey rectangle. These features are independent of the dopant chosen. Other differences in the spectral displacements are due to different fingerprint of the dopant used.

Due to the sensitivity of n-type polymers and dopant to air and to rule out any possible degradation effect, we prepared one sample in the glovebox and analyze it in air a few minutes after air exposure (**Figure 2.12**). The vibrational band of the doped samples prepared in air and in nitrogen atmosphere are compatible, thus demonstrating that the vibrational spectrum is mostly unaffected by air exposure.

A comprehensive Raman study with excitation at different wavelengths was conducted on the pristine and the doped samples. The wavelengths used in this study (458, 514, 632 and 1064 nm) are indicated in the UV-Vis spectra of **Figure 2.13**.

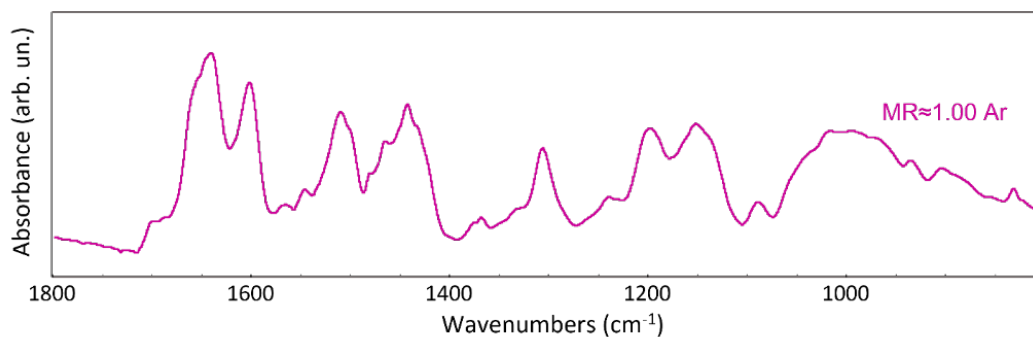


Figure 2.12: spectrum of P(NDI2OD-T2) doped with DiPrBI at MR=1.00, prepared and annealed in inert atmosphere.

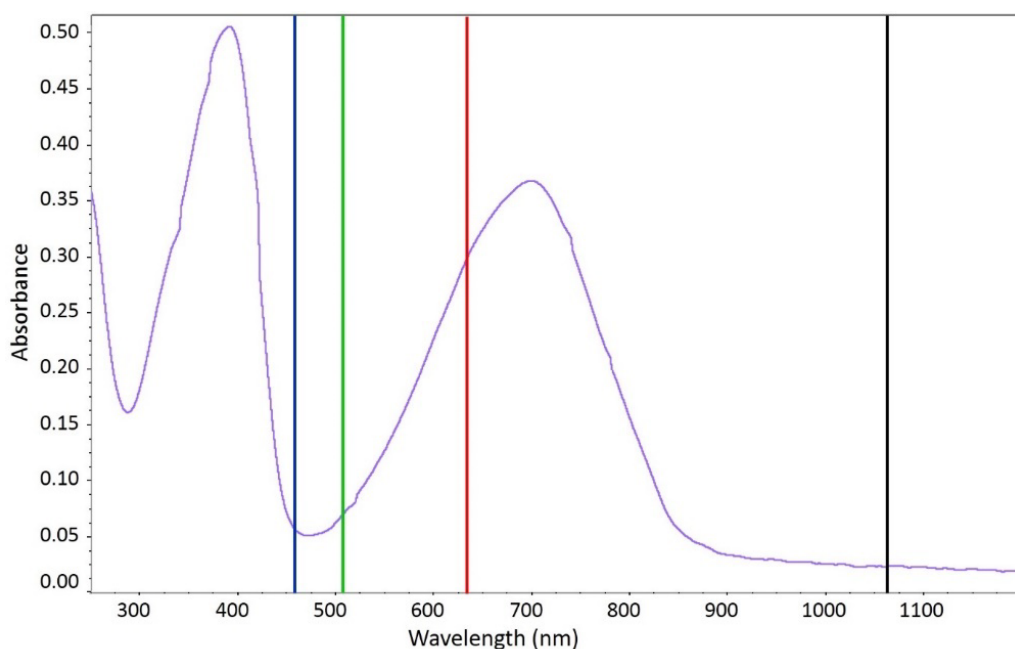


Figure 2.13: UV-Vis spectra of P(NDI2OD-T2) on quartz slide, with vertical lines indicating the excitations wavelength used in the Raman experiments.

Raman experiments on the pristine polymer acquired at different wavelengths show how the Raman spectra of the P(NDI2OD-T2) varies with the excitation energy (**Figure 2.14**). In particular, the bands intensities change with the chosen wavelengths, allowing to focus on different “blocks”

of the polymer structure. It is of remarkable interest the triplet at 1464, 1434 and 1406 cm^{-1} , whose assignments can be found in ref³².

The 1464 cm^{-1} peak is a marker band for the T2 unit, associated to a collective CC stretching mode which can be described as the oscillation between a more quinoidal and a more aromatic ring. The peaks at 1434 and 1406 cm^{-1} are vibrational collective displacements involving the CC stretching of NDI2OD and modes of the T2.

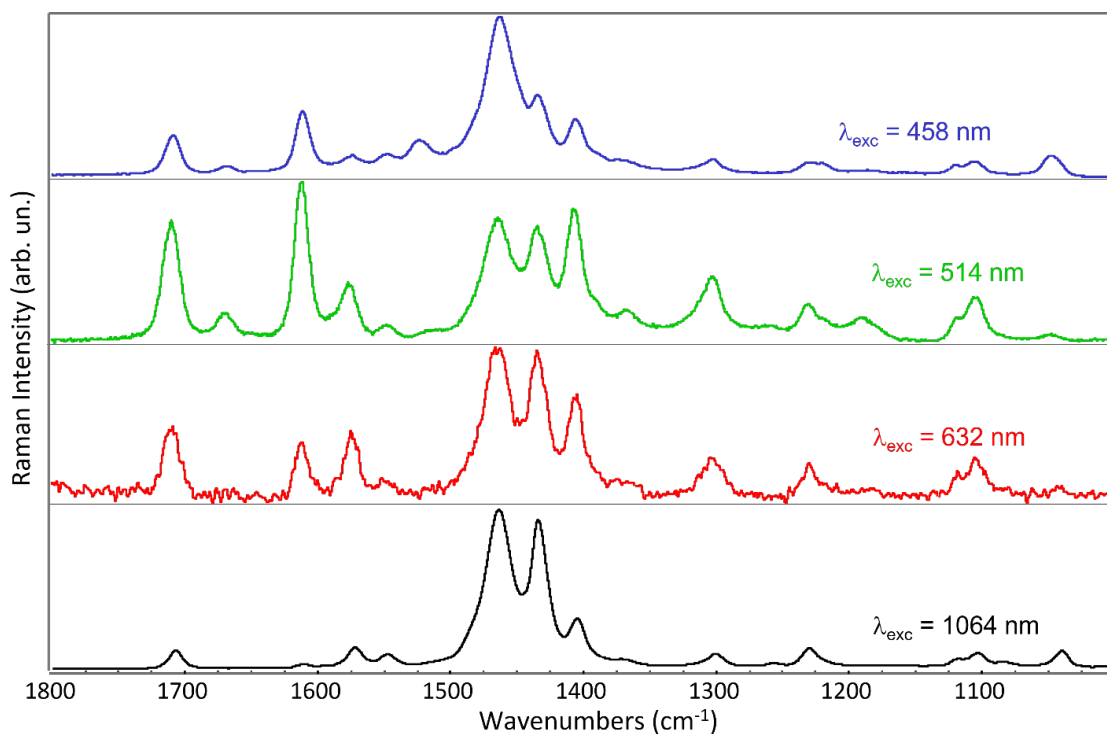


Figure 2.14: Raman spectra of pristine P(NDI2OD-T2) drop casted films acquired at different excitations wavelengths: 458 nm (blue line), 514 nm (green line), 632 nm (red line), 1064 nm (black line).

An interesting consideration can be done for the Raman peaks acquired with the 1064 nm wavelength (in the NIR region). Vibrational modes associated with the T2 present a higher intensity than the bands corresponding primarily to modes localized on NDI2OD. In fact, π - π^*

transitions (low in energy) typical of electronic excitations from the HOMO localized on the T2 undergoes a pre-resonance phenomenon. When the laser energy is increased, Raman bands assigned to NDI2OD modes start to gain intensity, as shown in **Figure 2.14**. In particular, Raman bands assigned to C=O and CC stretching (1708 cm^{-1} , 1610 and 1572 cm^{-1}) arise using 632 and 514 nm excitation wavelengths, while in the 458 nm Raman spectra features ascribed to T2 are still dominating. Also in the case of the doped polymer, we can focus on different building blocks selecting the wavelength.

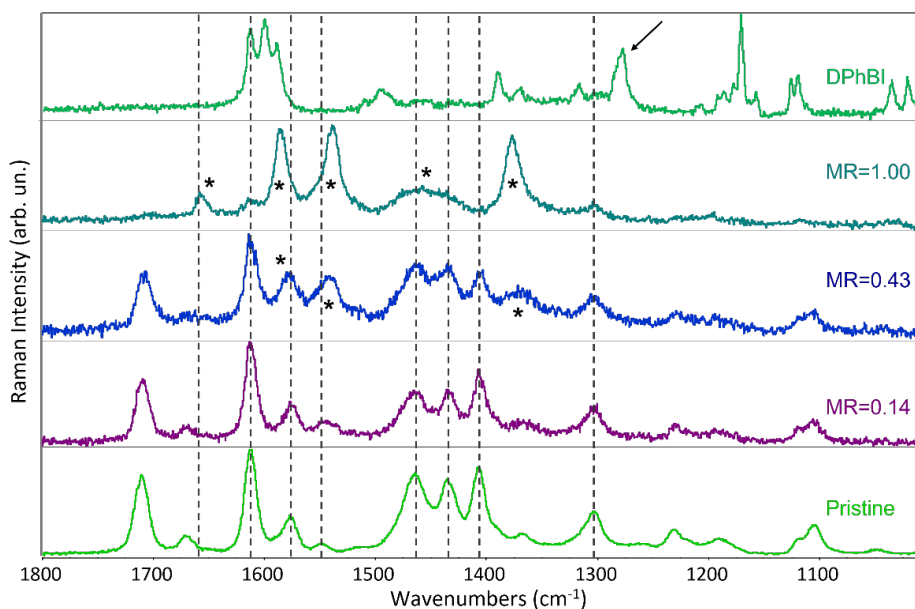


Figure 2.15: Raman spectra of P(NDI2OD-T2) doped with DPhBI with different MR (0.1 purple spectrum, 0.43 blue spectrum, 1.00 dark green spectrum), acquired at 514nm . The bottom and top spectra are of the pristine polymer and dopant, respectively. Vertical dashed lines indicate band of the pristine polymer. An arrow indicates the band of the dopant that disappears in the doped samples, indicating that the Raman bands possibly due to residual pristine dopant are intrinsically very weak and/or that the doping process was effective. Asterisks indicates new bands, which can be ascribed to the formation of the polaron.

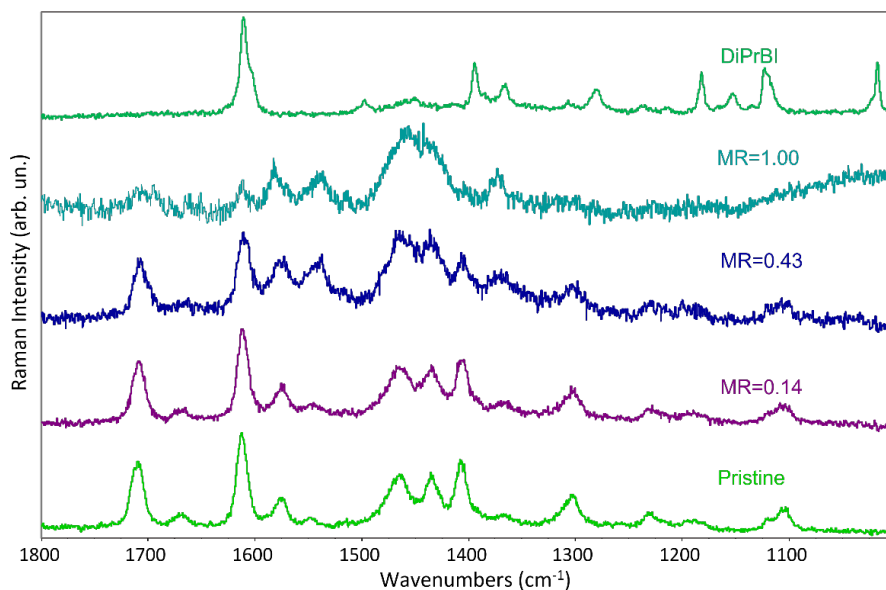


Figure 2.16: Raman spectra of P(NDI2OD-T2) doped with DiPrBI with different MR (0.1 purple spectrum, 0.43 blue spectrum, 1.00 dark green spectrum), acquired at 514nm. The bottom and top spectra are of the pristine polymer and dopant, respectively.

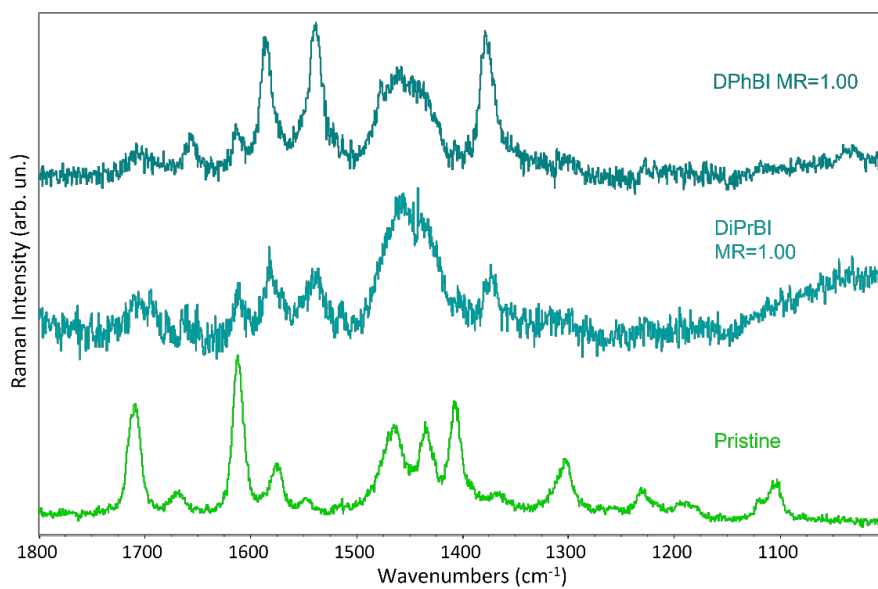


Figure 2.17: Comparison of the Raman spectra of P(NDI2OD-T2) doped with DiPrBI and DPhBI with MR=1.00, acquired at 514 nm with the pristine P(NDI2OD-T2).

The Raman spectra acquired at 514 nm show quite a few drastic changes. The triplet at 1464, 1434, and 1406 cm^{-1} weakens and broadens and a few other bands, namely 1658, 1586, 1540, 1378 cm^{-1} , labeled as asterisks in **Figure 2.15** arise. These bands, as in the case of the infrared spectra, can be ascribed to the polaron formation upon charge complex creation. **Figure 2.16** show the same data acquired with DiPrBI instead of DBuBI. A comparison of the spectra of the blends P(NDI2OD-T2):DiPrBI and P(NDI2OD-T2):DBuBI at MR=1.00 with the pristine polymer is shown in **Figure 2.17**. Despite the high noise to signal ratio of the doped samples, it is possible to notice that the new polaronic peaks that arise upon doping are the same in the doped samples, further corroborating the thesis that the polaronic peaks do not change with the dopant.

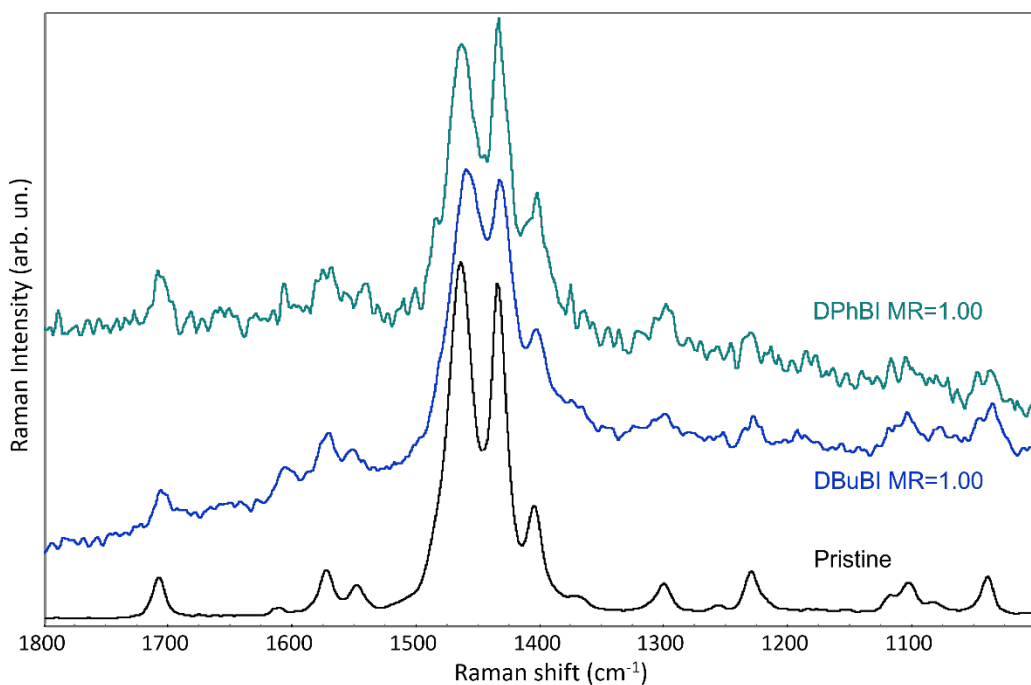


Figure 2.18: Comparison of the Raman spectra of P(NDI2OD-T2) doped with DiPrBI and DPhBI with MR=1.00, acquired at 1064 nm with the pristine P(NDI2OD-T2).

On the other hand, the spectra acquired at 1064 nm (**Figure 2.18**) do not exhibit significant changes in the vibrational bands, other than a higher noise to signal ratio. The selected

wavelength for this series enhances normal modes of the T2 unit. This observation leads to the conclusion that the thiophene moiety is almost unaffected by the dopant.

Raman spectra acquired with the 458 nm excitation wavelength exhibit a very pronounced band at 1464 cm^{-1} only when the highest dopant ratio (MR=1.00) is reached (**Figure 2.19**). Its shape seems a convolution of the two lines observed for the pristine polymer, thus suggesting that we are observing a phenomenon similar to that already described for the spectra with excitation in the green. At lower dopant percentages (**Figure 2.20, 2.21**) the vibrational bands remain unmodified after doping.

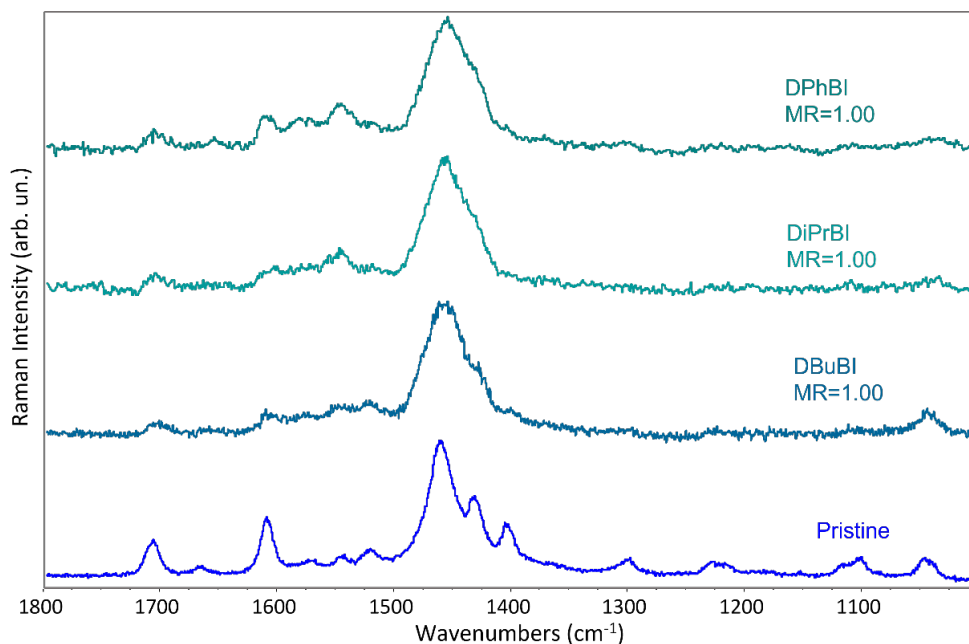


Figure 2.19: Comparison of the Raman spectra of P(NDI2OD-T2) doped with DiPrBI, DBuBI and DPhBI with MR=1.00, acquired at 458 nm with the pristine P(NDI2OD-T2).

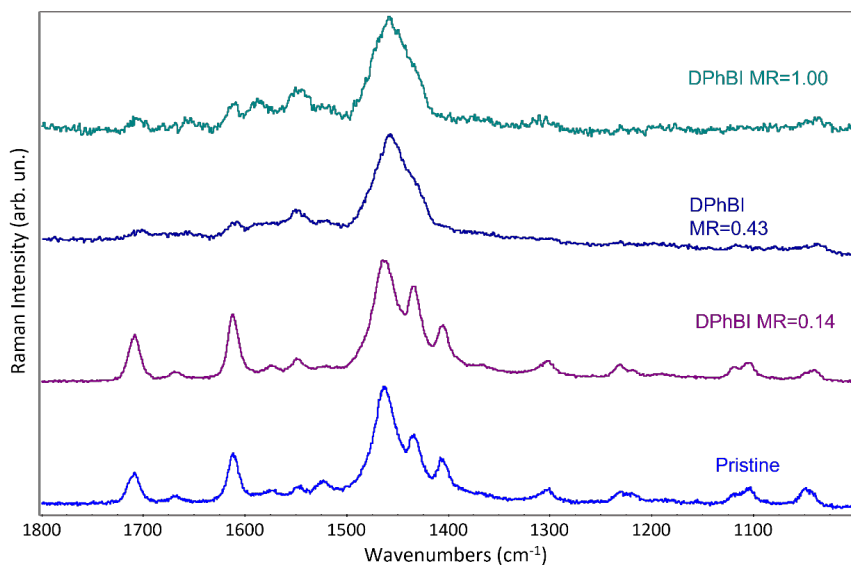


Figure 2.20: Raman spectra of P(NDI2OD-T2) doped with DPhBI with different MR (0.1 purple spectrum, 0.43 blue spectrum, 1.00 dark green spectrum), acquired at 458 nm. The bottom and top spectra is of the pristine polymer.

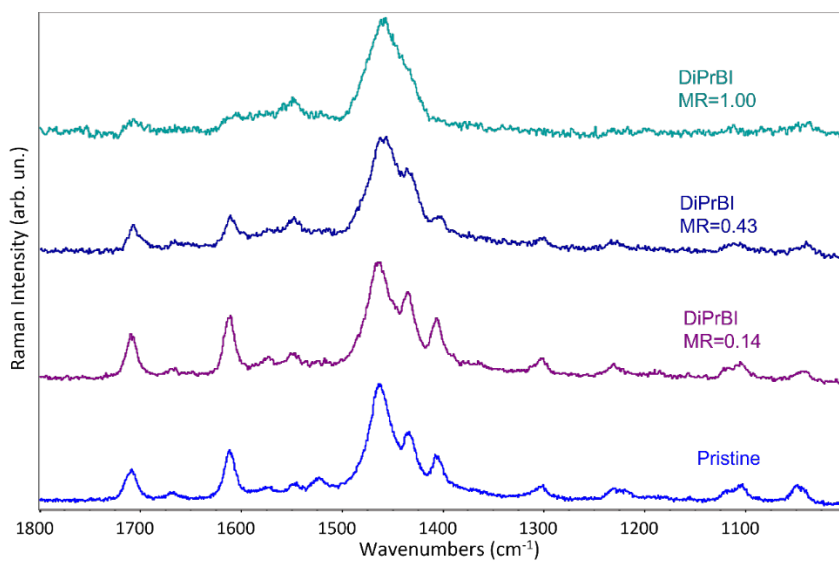


Figure 2.21: Raman spectra of P(NDI2OD-T2) doped with DiPrBI with different MR (0.1 purple spectrum, 0.43 blue spectrum, 1.00 dark green spectrum), acquired at 458 nm. The bottom and top spectra is of the pristine polymer.

Interestingly, Raman experiments show that the polaronic induced features are clearly visible only with the 514 nm excitation wavelength.

DFT calculations were performed by Alberto Milani and Matteo Tommasini. Two models were adopted for this study:

1. 1-D crystal with the translational unit coincident with the polymer chemical unit (NDI2OD-T2) was used to explore effects of the long-range interactions both in the pristine polymer and in the anion.

A molecular fragment T2-NDI2OD-T2 and its radical anion has been adopted for a thorough modelling including the study of the effect on the vibrational spectra of changes in the conformational degrees of freedom, by varying the torsional angles θ around the CC link between NDI2O2 and T2 units and τ around the CC bond linking the two thiophene rings.

Despite to its simplicity the computed spectra of T2-NDI2OD-T2 model show a very good correspondence to the spectra obtained for 1-D crystals, thus showing that long-range intramolecular interactions between polymer structural units are small. Moreover, the computed infrared spectrum vibrational bands of T2-NDI2OD-T2 is in good agreement with the experimental one of the pristine polymer (**Figure 2.22 a**). This shows that the T2-NDIO2-T2 model, despite lacking boundary conditions, is a good model to probe the overall spectrum. Indeed, the agreement can be associated to a limited delocalization of the electrons. The higher ratio of intensity of the bands between 1400 cm^{-1} and 1500 cm^{-1} can be ascribed to the highest ratio of T2 in the model, being these bands mainly assigned to T2 related vibrational modes. Other differences in the intensity pattern or frequency can be related to the conformation effects or scaling factors.

Raman computed spectra (**Figure 2.22 b**), on the other hand, present quite a few differences with respect to the experimental ones. This is due to very prominent Raman resonance effects. The closer spectra to calculations would be the one recorded at 1064 nm, although disagreements remain visible. These discordances could be explained by pre-resonance effects or the chosen basis set (6-31G(d,p)) limitations.

For these reasons, the infrared spectra were chosen to further investigate the changes in the vibrational normal modes upon doping. A radical anion fragment (T2-NDI2OD-T2) was used to calculate the doping induced spectra.

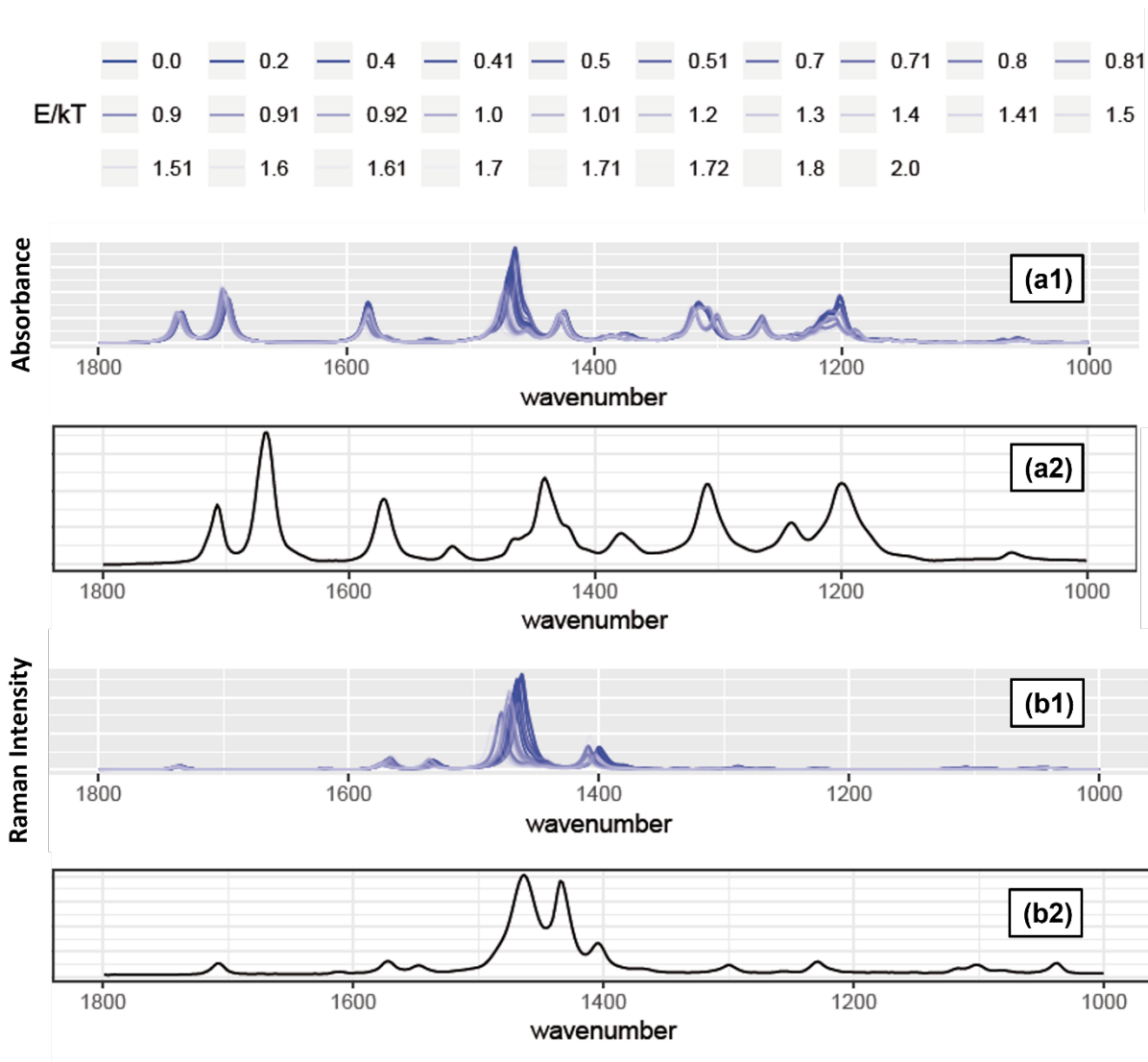


Figure 2.22: DFT computed spectra (a1) infrared and (b1) Raman of the T2-NDI2OD-T2 conformers (corresponding to a pair of selected theta and tau) obtained with an energy variation of the range $(E-E_0)/kT \leq 2$, where E_0 is the energy of the lower energy conformer. The spectra (a2) and (b2) are the infrared and Raman experimental spectra of pristine P(NDI2OD-T2).

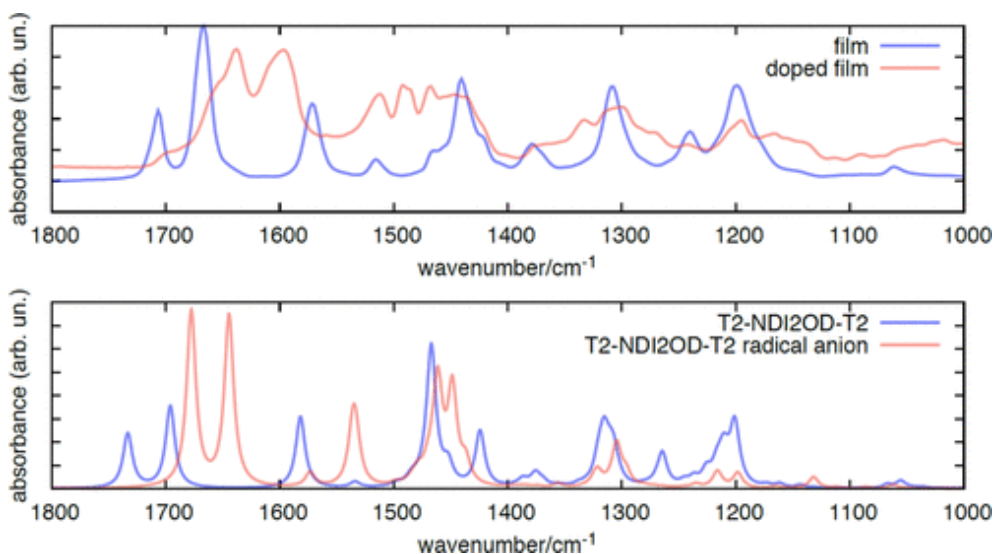


Figure 2.23: DFT infrared computed spectra are shown in the bottom panel, whereas the experimental ones are reported in the top panel. In both panels, the blue line is the pristine P(NDI2OD-T2) and the red line is the doped one.

As shown in **Figure 2.23**, the calculated bands are very similar to the experimental spectra. In particular the spectra are able to predict the experimental features at 1638, 1595 cm^{-1} at scaled frequency values 1677 and 1644 cm^{-1} , the ones at 1513 and 1468 cm^{-1} (the doublets predicted at 1533–1536 and 1461–1448 cm^{-1}). The intensity values predicted for these features is similar to the those of the pristine model. This is a further confirmation that the doping process does not give raise of strong IRAVs. Moreover, the fact that a small molecule allows such a nice prediction of the doped vibrational features is a further confirmation of the localization of the polaron. To have an even better insight of the structural changes occurring upon doping, the bond distance change ΔR was calculated subtracting the pristine from the doped distance on the molecule with the alkyl chains. **Figure 2.24** reports a schematic of it, showing that the changes are mainly localized on the NDI unit.

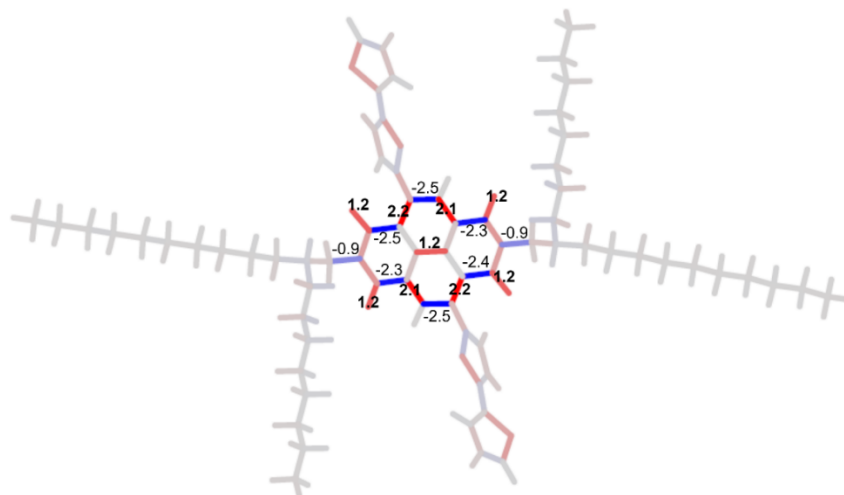


Figure 2.24: Bond distances changes (ΔR , 10^{-3} nm = pm) occurring upon charging T2-NDI2O2-T2. Gray color indicates that bond lengths are not modified; red and blue color scales are adopted to describe stretching and shrinking of the bonds, respectively. Only values $|\Delta R| \geq 0.9$ pm are reported in the figure.

Tables reporting the DFT optimized bond lengths of the pristine and doped T2-NDI2OD-T2 model and the difference of the neutral minus the charge specie (right column) is reported in **Table S.1** of the Supporting Information in **Attachment A**. The measurement unit is Å. The bond labels are also identified in Sketch S.1 of the Supporting Information in **Attachment A**.

2.4 Conclusions

Vibrational spectroscopy is proved to be a powerful tool to monitor the polaron formation in doped polymers.

First, I showed through infrared spectra that for drop casted samples, prepared and measured in air, the thermal annealing is a mandatory step to create the charge transfer complex. Infrared

spectra were also used in this chapter to individuate distinct polaronic features in doped samples, different from the dopants or the polymer fingerprints. At molar ratio MR=1, these new vibrational transitions are of the same intensity (dipole strength) of the pristine bands and can be nicely modeled by a radical anion localized on the NDI unit. Resonant Raman spectra add more information, showing how, by changing probing wavelength, we can tune the response of the polymer and highlight different building blocks. The spectra acquired at 1064 nm, which allow focusing on the T2 unit, were unaffected by the doping even at high concentrations of dopant. Spectra acquired at 514 nm (and 632 nm) showed major changes and new polaronic features. Calculations agreed with the data, further confirming that the T2 is not playing an active role in the formation of the charge defect. The extreme localization of the polaron on the NDI unit and the torsional angle between the NDI unit and the thiophene³² are responsible of the interchain nature of the charge transport mechanism in n-type polymers.

Evidences from vibrational spectra are also inconsistent with the hypothesis of a hydride transfer as doping mechanism for the 1H-benzimidazole based molecules used to dope P(NDI2OD-T2), but with an electron transfer between an electron donor and acceptor.

Chapter 3: Effects of annealing temperature on chemically doped P(NDI2OD-T2): morphological and spectroscopic investigation

In this chapter I present temperature-dependent measurements on P(NDI2OD-T2) doped with a N-alkyl based benzimidazole molecule (DIPrBI). I studied the effect of temperature on the doped samples during the annealing process through in-situ infrared spectroscopy and GIWAXS measurements. The assumptions of these chapter are supported by conductivity measurements, which I will show briefly, and Molecular Dynamics calculations, not reported in this work. In conclusion, the experimental findings indicate that the doping process for this system does not require thermal activation, but the thermal history plays a fundamental role in changes in conductivity and morphology.

3.1 Introduction

Thermoelectric generators, which allow to convert heat into electricity, represent the new frontier in the renewable energy field. An efficient device is built through a thermoelectric module, consisting of a p-type and an n-type material thermocouples, thermally connected in parallel and electronically in series^{11,59}. The most notable figure of merit that provides information on the efficiency of the thermoelectrical devices is expressed as follows (**eq. 3.1**):

$$zT = \frac{S^2\sigma}{k}T \quad \text{eq. 3.1}$$

Where T is the absolute temperature, k is the thermal conductivity, σ the electrical conductivity and S the Seebeck coefficient. The Seebeck coefficient is a measure of the thermoelectrically induced voltage in a material when heated. The change voltage is due to a redistribution of the charges inside the material, as the free carriers tend to move on the hot side. Because of the interconnection between all the parameters, it is tricky to enhance zT. Semiconducting polymers

qualify as class of organic materials with good thermoelectrical properties, providing both p and n-type choices. Through chemical doping it is possible to increase the charge carrier concentration, which gives room of improvement for the figure of merit discussed above. On the other hand, material morphology is expected to influence the charge carrier mobility, both in the pristine and in the doped state.

To fabricate an all-organic thermoelectric generator, a greater effort needs to be directed in understanding how thermal treatments affect n-types polymers and their charge transport properties, to achieve better performances as for their p-types counterparts.

An interesting study for understanding how annealing temperatures affect the crystalline structure of pristine films of P(NDI2OD-T2) was conducted by Rivnay et al.⁵

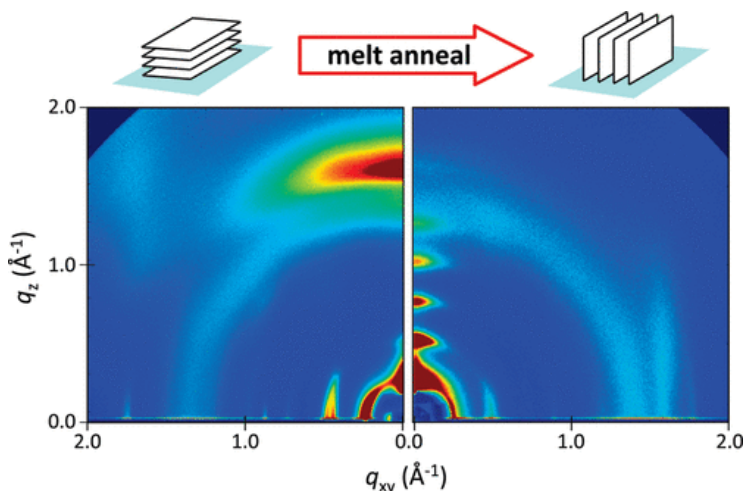


Figure 3.1: GIXS 2D pattern for a pristine room temperature P(NDI2OD-T2) sample (left) and melt annealed sample (right)⁵

A very interesting finding of this study is the change in the lamellar orientation upon melt annealing (from face-on to edge-on, **Figure 3.1**). The in-situ GIXS measurements were able to quantify the percentage of lamellar planes changing direction, as well as give an estimate of the increasing disorder of the film when melt annealing takes place. The face-on orientation of the spin coated pristine films is correlated with a kinetic trapping of the high weight molecular chains

when the film is deposited, whereas upon melt-annealing, a thermodynamic equilibrium state (edge-on) is reached. The characterization of the morphology was also conducted through AFM and polarized microscopy, showing the disappearance of the spherulites, typical structures of the organic spin-coated polymer, upon melt annealing. To conclude their study, the researchers⁵ perform electron-only and bottom-gate TFT measurements to monitor charge transport, understanding that the temperature of annealing affect crucially the performances.

According to the above observations on the pristine material, the enhancement of the conductivity of about 3 orders of magnitude observed upon doping P(NDI2OD-T2) can be correlated with the doping induced change of morphology giving rise to an improvement of charge transport related to the edge-on configuration. However, the leading mechanism should be the increase of the density of charge carriers, because of the formation of polarons.

The crystalline structure of the polymer changes upon doping, as widely reported in literature, becoming edge-on from the pristine face-on lamellar stacking^{11,62-65}. A systematic study on how annealing temperature affects charge transport properties was recently proposed by Kluge in 2020⁶³, aimed at understanding the thermoelectric generators discrepancies in performance by understanding the doping process. These differences are correlated with the in-plane or cross-plane charge transport. To perform this study, they chose N-DMBI as dopant, as it is widely known in literature to be an excellent dopant for these systems. The introduction of the dopant not only increases the conductivity, but also the power factor. UV-Vis is used to confirm the doping level and doping effectiveness in the film^{40,43}. The assumption made in this paper states that the doping process takes place because of an acid-base reaction, causing a hydride transfer, where the passage of the π -stacking from out-of-plane to in-plane is favored by the doping process. The hydride formation as explanation for the doping process was ruled out by other works⁶⁶, and different hypothesis were proposed. An intriguing one explains the charge transfer with the formation of an intermediate level, the SOMO, followed by a direct electron transfer from the SOMO to the LUMO of the polymer, which agrees with the thermal activation of the N-DMBI molecules^{67,68}.

The standard chemical doping for P(NDI2OD-T2) establishes to mix a solution of the polymer and the dopant in an organic solvent, generally CHCl_3 or DCB, then deposit the samples and anneal

them at a temperature above 100°C, for a time that varies between a few minutes to a few hours. The annealing process is often carried in an inert environment, to prevent oxygen to hinder the charge transfer. How the annealing temperature and time affect the film conductivity, as well as what is the charge transfer mechanisms, are the questions we try to answer in this chapter. In our approach, we use GIWAXS coupled to infrared spectroscopy to further make light on the doping mechanism and charge transfer kinetics and properties upon doping. As reported in the previous chapter, vibrational spectroscopy techniques can be a powerful tool to give an insight into the polarons formation upon doping. DFT calculations, not reported in this thesis, were also performed to further corroborate our hypothesis concerning the mechanism and the energetic of the charge transfer between dopant and polymer.

3.2 Experimental methods

3.2.1 Polymer

Poly{[N,N'-bis(2-octyldodecyl)naphthalene-1,4,5,8-bis(dicarboximide)-2,6-diyl]-alt-5,5'-(2,2'-bithiophene)} (P(NDI2OD-T2)) was purchased from Ossila Lim. (Polyera ActivInk N2200). The polydispersity index (PDI) is ~2–3, the average polymer molecular weight 150 kDa.

3.2.2. Dopants

Ndiisopropyl-4-(1,3-dimethyl-2,3-dihydro-1H-1,3-benzodiazol-2-yl)-aniline (**DiPrBI**) was used for this study. Details of the chemical synthesis of the dopants can be found in the Supporting Information of ref.⁶⁹. All the chemicals for the synthesis of the dopants were purchased by Sigma Aldrich.

3.2.3 Film deposition and infrared measurements

P(NDI2OD-T2) was dissolved in 1,2-dichlorobenzene (DCB, 10mg/mL). The solution was then stirred at 80°C for 1h and loaded into a syringe to be filtered with a 0.45 µm pore size polytetrafluoroethylene filter. Aliquots of 50µL of such solution were added to vials with 0.153

mg of DiPrBI, to reach a doping level of 100% (1 dopant molecule for each polymer unit). The concentration is expressed in Molar Ratio (MR), meaning dopant moles divided by P(NDI2OD-T2) repeating unit moles. A Zinc Selenide window for the temperature cell was cleaned with optic paper with isopropyl alcohol. Doped P(NDI2OD-T2) films were drop casted in air, then the cell was sealed, and the solvent was left to evaporate in a nitrogen environment. A temperature-controlled stage (Linkam heating cell, FT-IR 600) operating in a nitrogen atmosphere was used to perform infrared measurements. The cell was mounted on a Thermo Nicolet NEXUS FT-IR spectrometer (4 cm^{-1} resolution, 128 scans) equipped with a ThermoElectro Continuum FT-IR Microscope (4 cm^{-1} resolution, 128 scans). The spectra were recorded in transmission mode.

3.2.4 GIWAXS samples preparation and measurements

Native oxide p+ silicon substrates (area 2 cm^2) were cleaned with acetone, isopropyl alcohol, and ethanol. The film preparation was performed in a N₂ glovebox (<1 ppm of O₂). The film solution was prepared and doped as described above. The first sample was measured without thermal treatment, the others were annealed for 5, 30 and 90 minutes at 110°C and 70°C. To prevent the thermal annealing to proceed further after removing the samples from the hop plate, each sample was quenched on a metal cold support.

Grazing incidence wide-angle X-ray scattering (GIWAXS) measurements were performed at the Stanford Synchrotron Radiation Lightsource, SLAC National Accelerator Laboratory, Beamline 11-3. An area detector (Rayonix MAR-225) was used to collect the data, with an incident energy of 12.73 keV. The samples were placed in a helium sealed chamber during the measurements. This trick minimizes both beam damage to the sample and air scattering. The sample to detector distance (321 mm) was calibrated with a LaB₆ polycrystalline standard. The incident angle was chosen at 0.1°. Data analysis, including correction for geometric distortions introduced by a flat area detector, was performed with the Igor Pro software packages NIKA 1D SAXS29 and WAXStools^{70,71}. The data were normalized by incident beam flux and sample thickness.

3.3. Results and discussion

3.3.1 Electrical Properties

To evaluate the effects of temperature on the kinetics of the annealing, conductivity measurements were performed on samples deposited as the one used in GIWAXS study of this chapter. These measurements were performed at the Italian Institute of Technology in Milano by Simone Cimo'. Annealing temperatures of 70, 110 and 150°C were selected considering the literatures annealing temperatures^{40,56,63,69,72-74} and were conducted *in-situ*. **Figure 3.2(A)** shows the measurements at different temperatures on the pristine polymer. As expected, the conductivity does not vary for all the samples ($4.0 \times 10^{-7} \text{ S cm}^{-1}$), independently from the temperature and time of the annealing. Doping ratio of 76%_(mol/mol) and 100%_(mol/mol) were studied, as in the GIWAXS and infrared series.

It is worth noting that the conductivity of the not-annealed samples is already more than three order of magnitude higher than the pristine (10^{-3} Scm^{-1} , +5000 times the initial value), independent from the dopant concentration. This demonstrates that the dopant molecule is already active at room temperature, and the doping mechanism does not need a thermal activation.

Figure 3.2(B) represents the data at 100% doping ratio, showing a decrease in conductivity with time, indicating a possible segregation of the dopant.

76% DiPrBI:P(NDI2OD-T2) molar ratio results are shown in **Figure 3.2(C)**, in comparison with the 100% doped samples. At 70°C and 110°C temperatures the 76% doped sample show higher conductivity, further validating the previous hypothesis of dopant segregation with higher dopant level^{11,58}. Moreover, the samples annealed at 70°C presents lower conductivity values, which decrease further during the annealing process. This behavior implies that there are many concurrent mechanisms responsible for the conductivity changes, which are ruled by the annealing temperature. In **Figure 3.2(D)** we focused on 76% doped samples annealed at 110°C and 150°C, monitored for up to 5h. The data show that the conductivity increases for the first 30 minutes, reaching then a plateau.

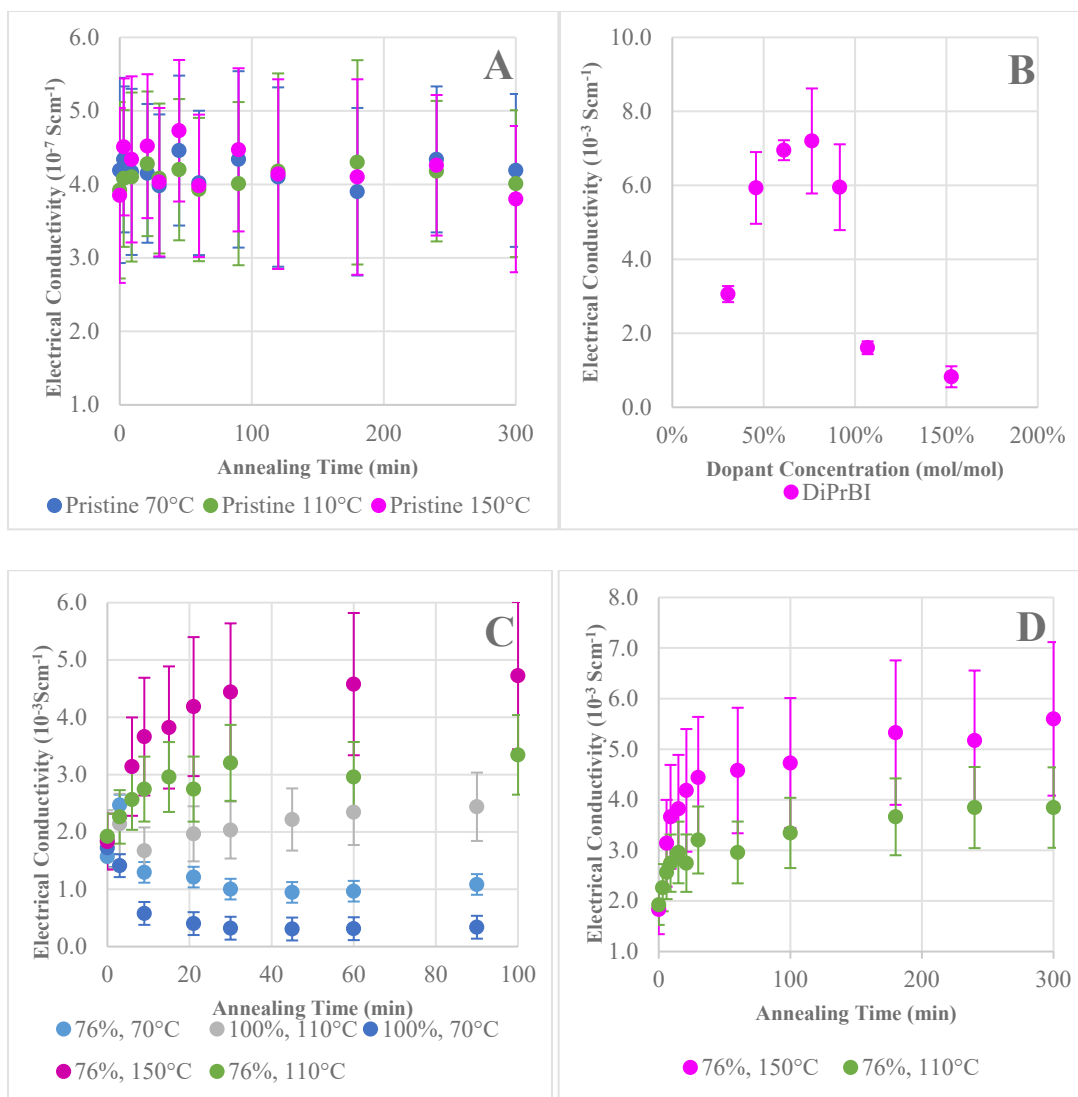


Figure 3.2: (A) P(NDI2OD-T2) pristine films' electrical conductivity (annealing temperature 110°C and 70°C). (B) P(NDI2OD-T2) doped films' electrical conductivity (76% and 100% concentration of DiPrBI, annealing temperature 150°C, samples monitored for 5h). (C) Comparison of the conductivity of doped P(NDI2OD-T2) spin coated films annealed at different temperatures. Dark blue and light blue dots refer to films of P(NDI2OD-T2) 100% and 76% doped with DiPrBI annealed at 70°C, respectively. Grey and green dots refer to doped samples at 100% and 76%, annealed at 110°C. The pink series refers to 76% doped samples annealed at 150°C. (D) P(NDI2OD-T2) 76% doped samples conductivity annealed at 150°C and 110°C, measured for up to 5h.

The annealing and doping process can thus be synthesized in 3 parts:

- 1) At room temperature, after deposition, we observe an initial remarkable increase of conductivity (more than 3 order of magnitude)
- 2) during the first 15-30 minutes of annealing, the conductivity increases of 50/100%
- 3) After 4-5 hours of the annealing, the conductivity increases of another 20/30%

3.3.2 Infrared Spectroscopy

All the infrared measurements presented in this chapter are performed on a drop-casted sample, whereas thin spin coated films were used for conductivity measurements and X-rays determinations. This choice is due to the difficulty in the acquisition of spectra with a good signal-to-noise ratio on thin films. It is then reasonable to expect that the temporal scale for the evolution of doping processes would be faster in thin films and some influence of a different initial morphology of the film is expected.

Infrared measurements were conducted in-situ to monitor the effects of annealing on the formation of the charge transfer complex, namely of the polaron, by exploiting the ideas and the method discussed in **Chapter 2**. To achieve this goal, a dedicated cell for in-situ measurements, which allows to control temperature, was used (**Figure 3.3**). The cell operates in a nitrogen environment. Spectra were recorded for 2h and 30 minutes, with a ramp of 50°C.

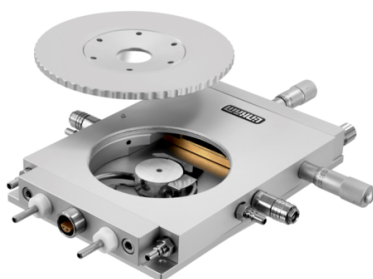


Figure 3.3: Representation of the temperature-controlled cell, connected to nitrogen, for the in-situ measurements.

Before conducting the in-situ heating we recorded the infrared spectra of a not annealed sample, doped at MR=1.0. The latter was drop casted on the Zinc Selenide window, then sealed in the temperature-controlled cell, in a nitrogen environment. Spectra were acquired for 120 minutes, with no exposition to oxygen. The infrared measurements show that, when the sample is not exposed to oxygen, the polaronic bands are already present at room temperature. In fact, it is possible to observe the rising of the polaronic band at 1638 cm^{-1} , while the CO symmetric stretching of the pristine polymer at 1706 cm^{-1} decreases in intensity (**Figure 3.4, panel (b)**). The feature at 1638 cm^{-1} was already reported in **Chapter 2** for doped annealed samples and described as a vibrational marker band associated to the polaron defect (**Figure 3.4, panel (a)**). The relative intensity of the polaronic features growth with time, thus indicating that the doping process is kinetically limited but spontaneously evolves at room temperature. Moreover, even at long times (2 hours after deposition) the polaronic band is still weaker than in the case of the annealed samples (see below).

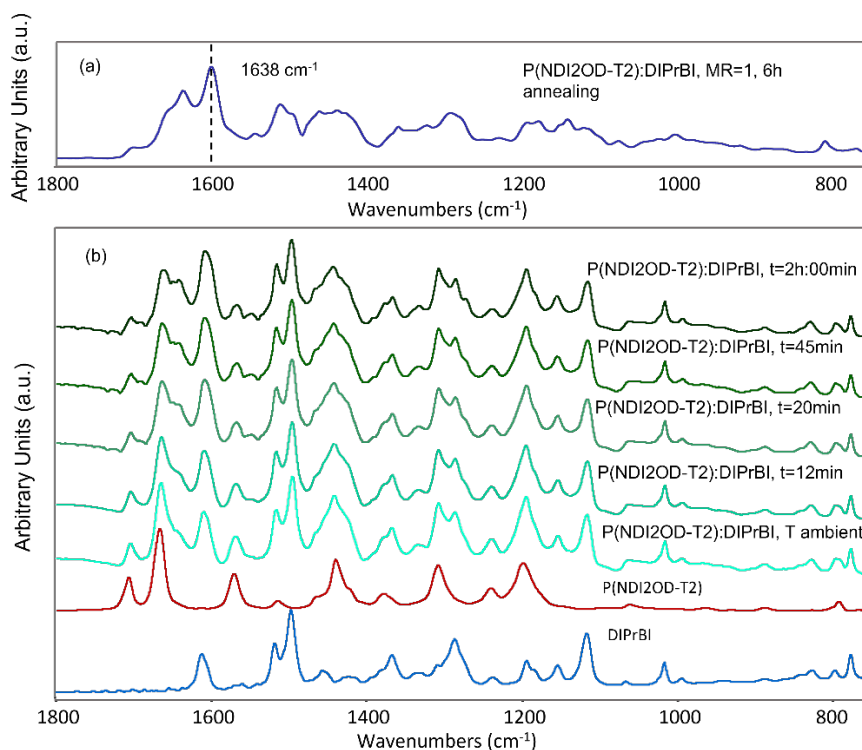


Figure 3.4: (a) P(NDI2ODT2):DiPrBI, MR=1, annealed at 110°C for 6 hours. A dashed line reports the polaronic vibrational feature at 1638 cm⁻¹; (b) Evolution of the not annealed sample in time. The spectra of the dopant molecule and of the pristine N2200 correspond to the bottom blue line and to the red line, respectively. The spectra were monitored for 120 minutes to show the time-dependent effects of doping without annealing on vibrational spectra.

Recalling that for thin films the time evolution of the process could be quicker, we can conclude that the appearance of the novel – doping induced - infrared features already at room temperature confirm the conductivity measurements data on the not annealed sample, in nitrogen environment. In this scenario, the conductivity increases of about three orders of magnitude before annealing, at room temperature, corroborating the hypothesis that the dopant is already active.

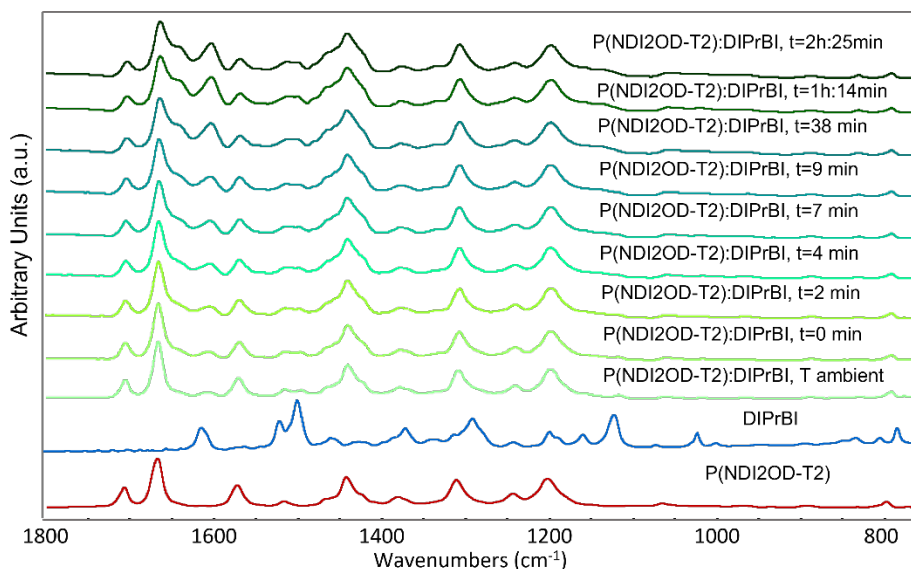


Figure 3.5: Evolution of the 70°C annealed sample in time. Spectra of the dopant molecule and the pristine N2200, correspond to the bottom blue and red line respectively. The spectra were monitored for more than 120 minutes to show the time-dependent effects of doping without annealing on vibrational spectra.

Further samples were then analyzed using a fast-heating ramp (50°C/min) to reach the desired temperature. The first annealing temperature studied was 70°C, shown in **Figure 3.5**. This experimental series indicates that 70°C is not a sufficiently high temperature to reach the maximum concentration of charge-defects. As in the case of the non-annealed sample, after 2 hours of annealing at 70° the polaronic features are not as pronounced as with higher annealing temperatures. To better highlight the changes in the vibrational spectra, a subtraction between the spectra obtained at adjacent time steps ($I_{t+1} - I_t$) is shown in **Figure 3.6**. It is worth noting that when the annealing process begins (up to 40 minutes), doping induced bands arise (positive features), but as time passes, the doping process starts to become less effective. After 2:30 hours the CO bands of the pristine growth newly, thus suggesting that some de-doping phenomenon could take place.

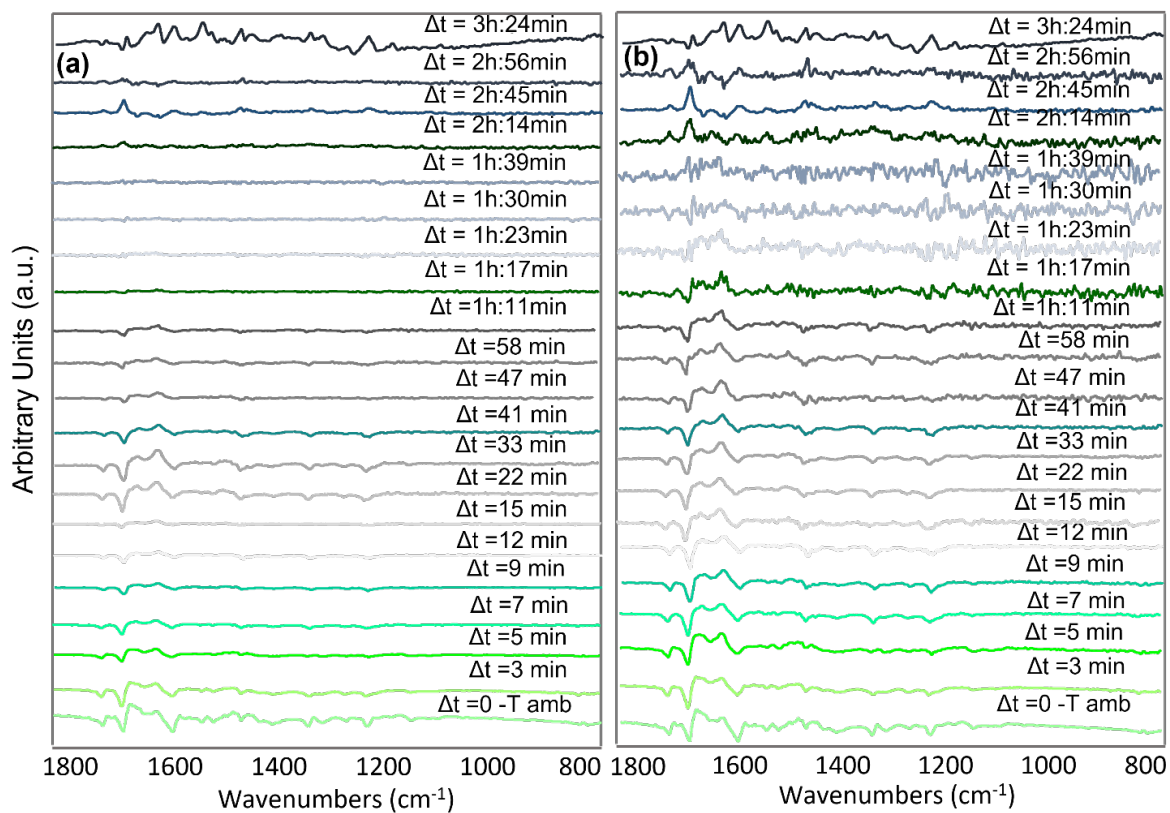


Figure 3.6: Spectral differences between the adjacent temperature spectra ($I_{t+1} - I_t$) for the 70°C series. Panel (a) shows as-acquired spectra subtractions. To further highlight the possible differences, the spectra were normalized on the most intense peak in panel (b).

The evolution of the spectra is completely different when the annealing temperature is raised of 20°C. In the 90°C series, shown in **Figure 3.7 and 3.8**, the doping process and polaron formation is much faster than in the previous case, and it is already well established in the first few minutes. However, as noted from the top purple spectrum, there are still hints of the undoped polymer, as CO stretching symmetric and antisymmetric bands of the pristine polymer are still visible after 1h and 20 minutes, suggesting that also this sample is not fully doped at the longer times of observation.

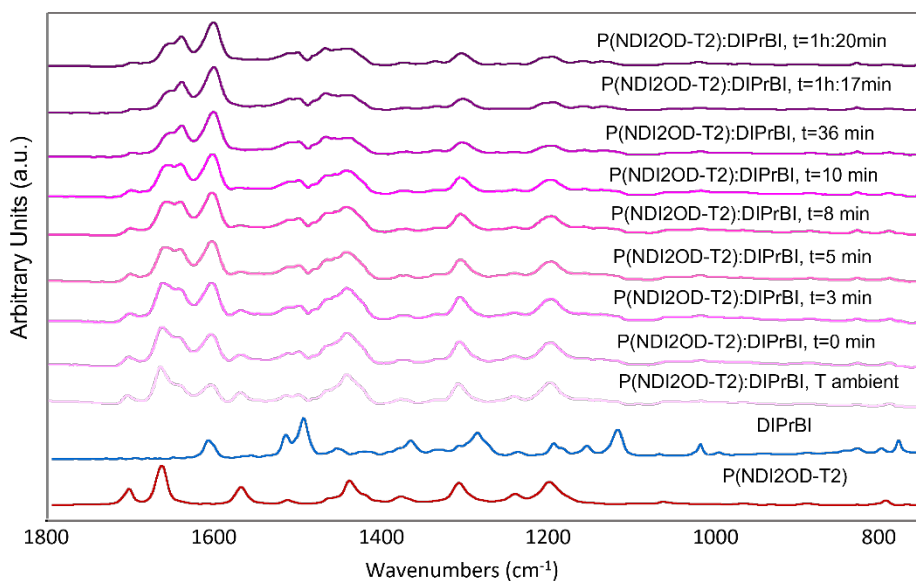


Figure 3.7: Evolution of the 90°C annealed sample in time. Spectra of the dopant molecule and the pristine N2200, correspond to the bottom blue and red line respectively. The spectra were monitored for more than 120 minutes to show the time-dependent effects of doping without annealing on vibrational spectra.

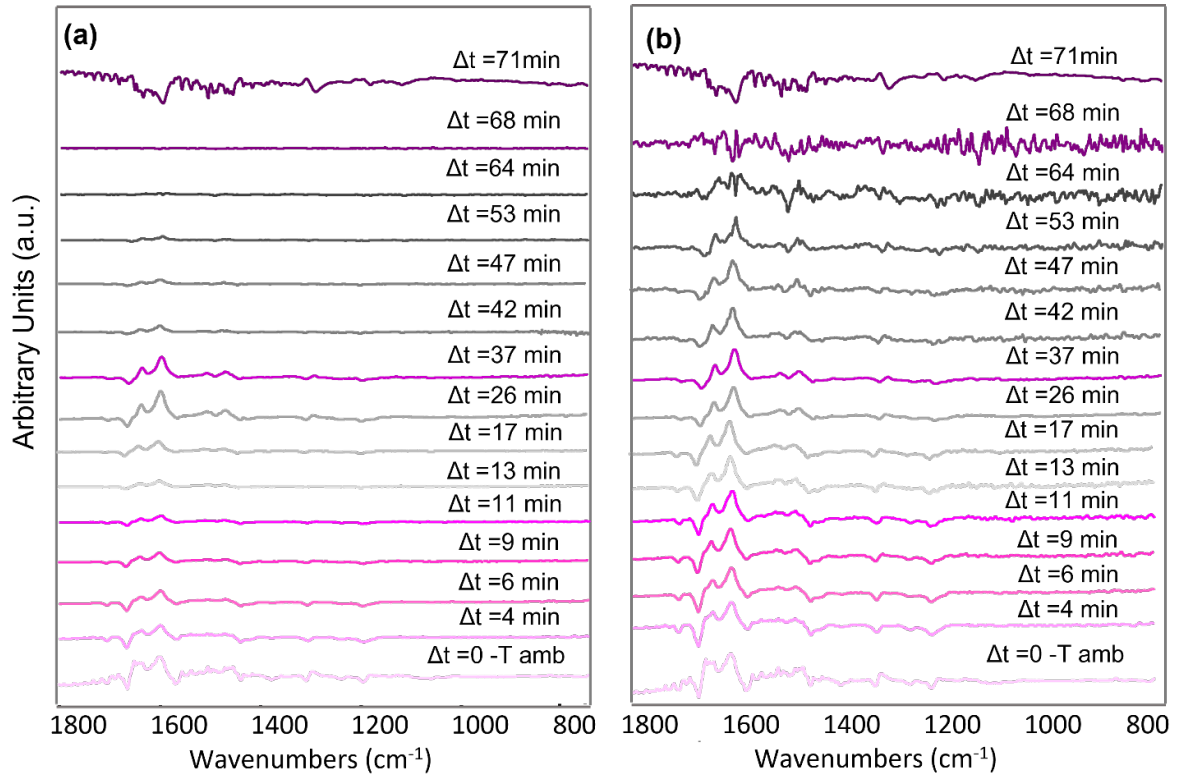


Figure 3.8: Spectral differences between the adjacent temperature spectra ($I_{t+1}-I_t$) for the 90°C series. Panel (a) shows as-acquired spectra subtractions. To further highlight the possible differences, the spectra were normalized on the most intense peak in panel (b).

A similar trend is observed for the 110°C and 150°C data (**Figure 3.9, 3.10, 3.11 and 3.12**), regarding the rate of doping. Doping induced vibrational features reach their maximum intensity after 10/15 minutes. Interestingly, peaks ascribed to the pristine polymers newly arise after 30 minutes of annealing time. This behavior is very similar to the one described for the annealing at 70°C, and it could be related to an oxygen leakage in the cell, as n-type polymer doping is extremely sensitive to oxygen.

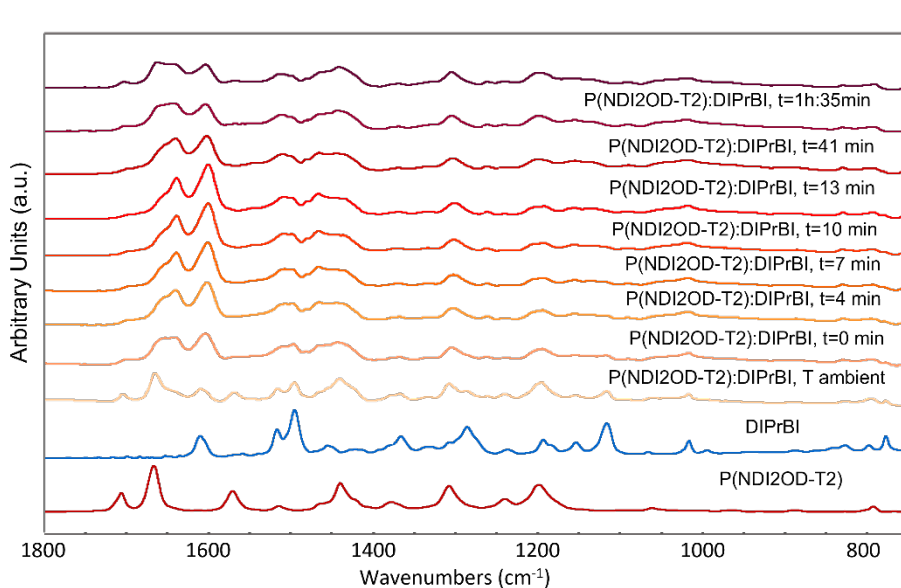


Figure 3.9: Evolution of the 110°C annealed sample in time. Spectra of the dopant molecule and the pristine N2200, correspond to the bottom blue and red line respectively. The spectra were monitored for more than 120 minutes to show the time-dependent effects of doping without annealing on vibrational spectra.

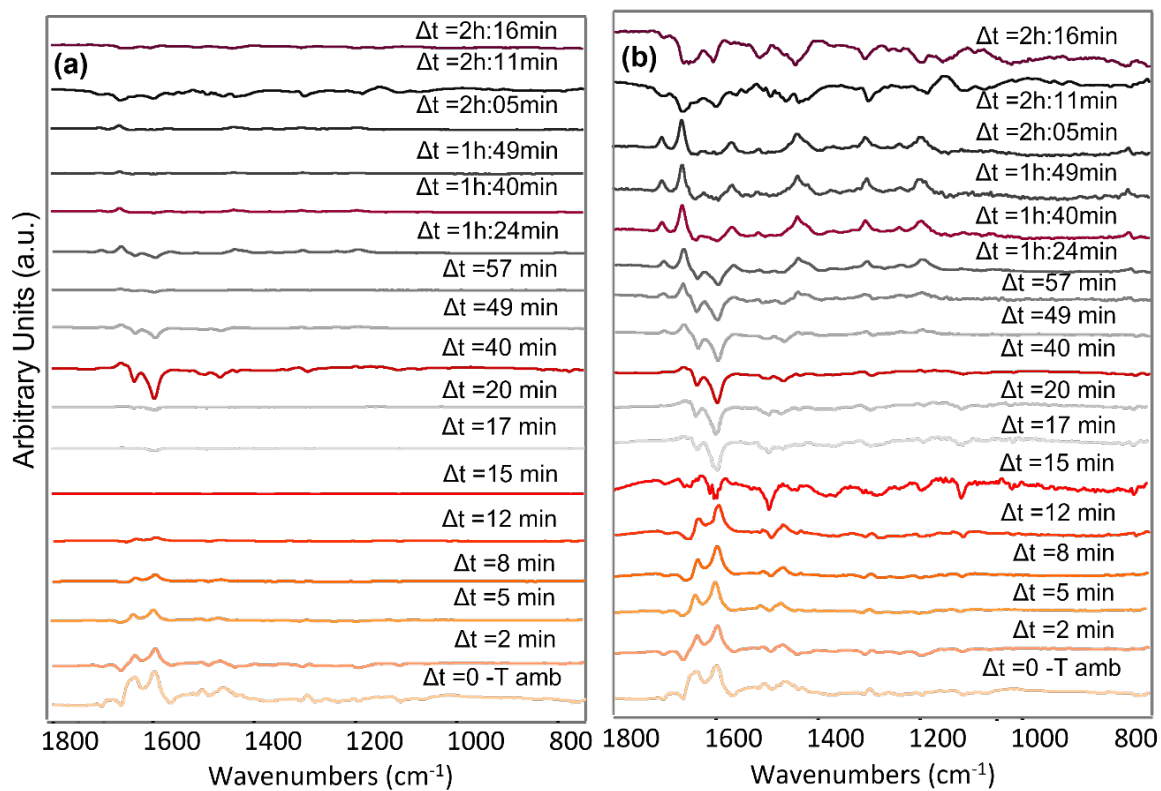


Figure 3.10: Spectral differences between the adjacent temperature spectra ($I_{t+1}-I_t$) for the 110°C series. Panel (a) shows as-acquired spectra subtractions. To further highlight the possible differences, the spectra were normalized on the most intense peak in panel (b).

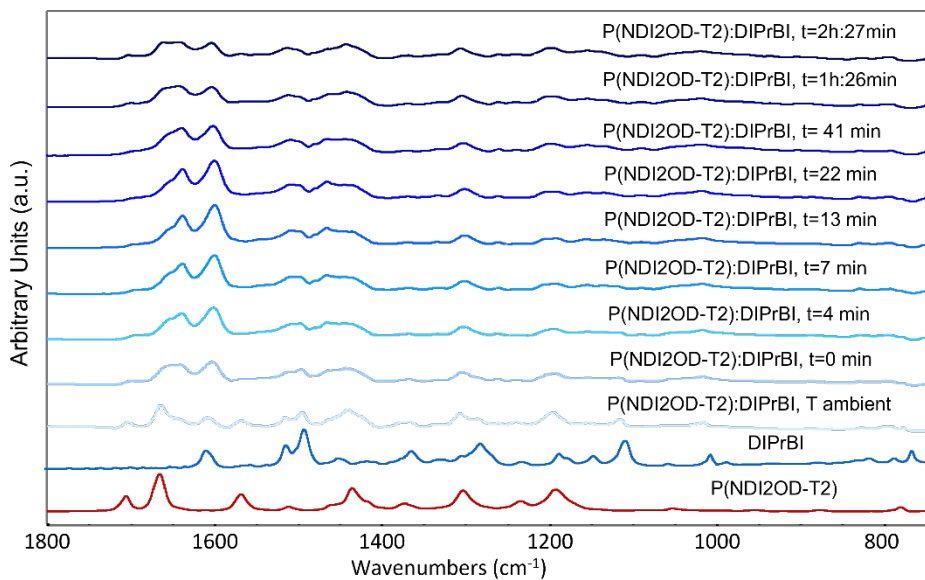


Figure 3.11: Evolution of the 150°C annealed sample in time. The bottom blue spectra and red spectra represents the dopant molecule and the pristine N2200, respectively. The spectra were monitored for more than 120 minutes to show the time-dependent effects of doping without annealing on vibrational spectra.

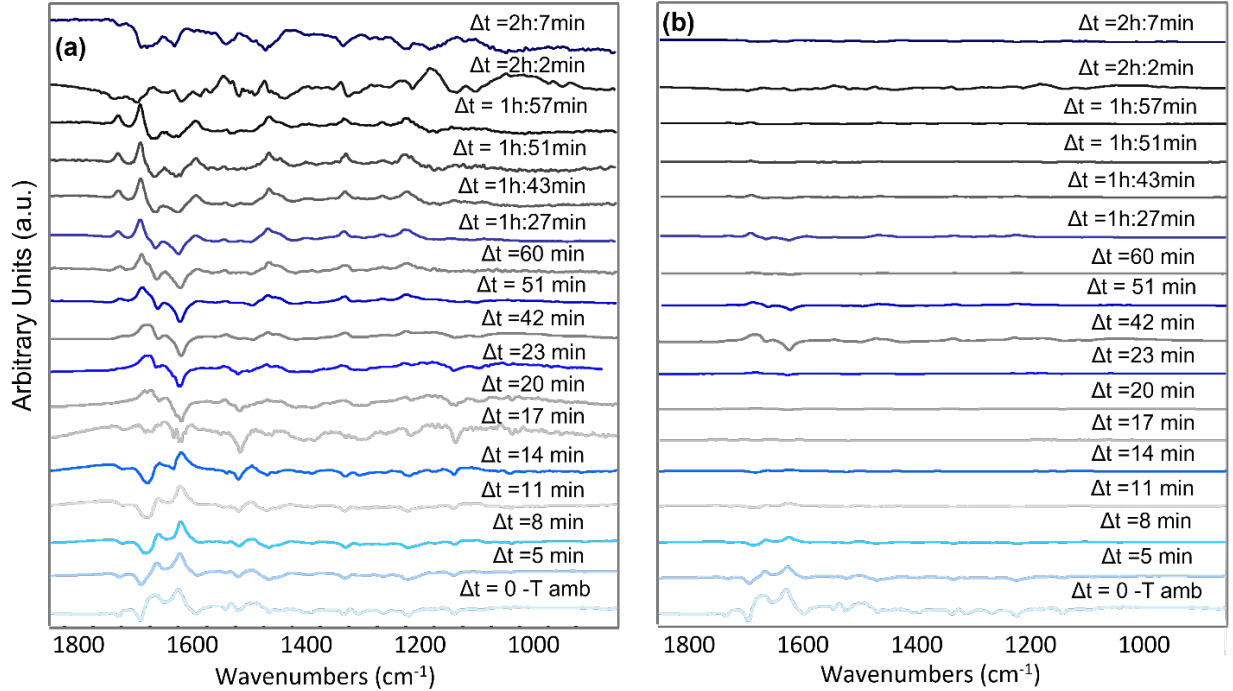


Figure 3.12: Spectral differences between the adjacent temperature spectra ($I_{t+1}-I_t$) for the 150°C series. Panel (a) shows as-acquired spectra subtractions. To further highlight the possible differences, the spectra were normalized on the most intense peak in panel (b).

Beside the observation that de-doping process can occur overtime, possibly due to a small leakage of the cell or the presence of oxygen, this experimental set of data proves temperatures lower than 110°C are not enough to allow completing the doping process in few hours, as the spectra confronted in **Figure 3.13** shows. Panel (a) shows how spectra evolve after about 4 minutes of annealing, highlighting that the polaronic bands are only starting to rise in the 70°C series, whereas the polaronic features are already very clear in 90°C series, but the maximum polarons concentration is not completely reached. If we look at the data at 110°C and 150°C, we can still see a hint of the pristine features. After 10 to 15 minutes (**Figure 3.13**, panel (b)), we can see an evolution of the spectral pattern according to the different annealing temperature towards a more doped system: at this short time, the samples for the two higher annealing temperatures

reach the maximum doping (maximum intensity of the polaronic bands) for. It is interesting to point out the result for the not annealed sample, which was monitored in the same cell, under nitrogen flux. The sample shows some polaronic features, compatible with those observed for the sample annealed at 70°C, but also many peaks that could be ascribed to the dopant, as a direct comparison with the dopant spectra shows. The dopant features disappear in all the annealed series. This behavior could indicate that, despite doping takes place even in the not annealed state, responsible for the conductivity spike, at least for thick samples, the annealing process is a mandatory step to accelerate the effective the formation of charge transfer complexes between the dopant and the polymer.

Finally, the situation seems stabilized around 30 to 40 minutes, as shown in **Figure 3.13**, panel (c), with small changes in all the spectra. The 110 and 150°C spectra show the same polaronic features of a fully doped sample after 30 minutes of annealing.

This section highlights the role of the annealing process in accelerating the formation of charge transfer defect, as well as how the temperature of annealing plays a fundamental role on this topic.

Temperatures higher than 110°C should be enough to fully dope the samples, after a rather short time waiting (approximately 30 minutes).

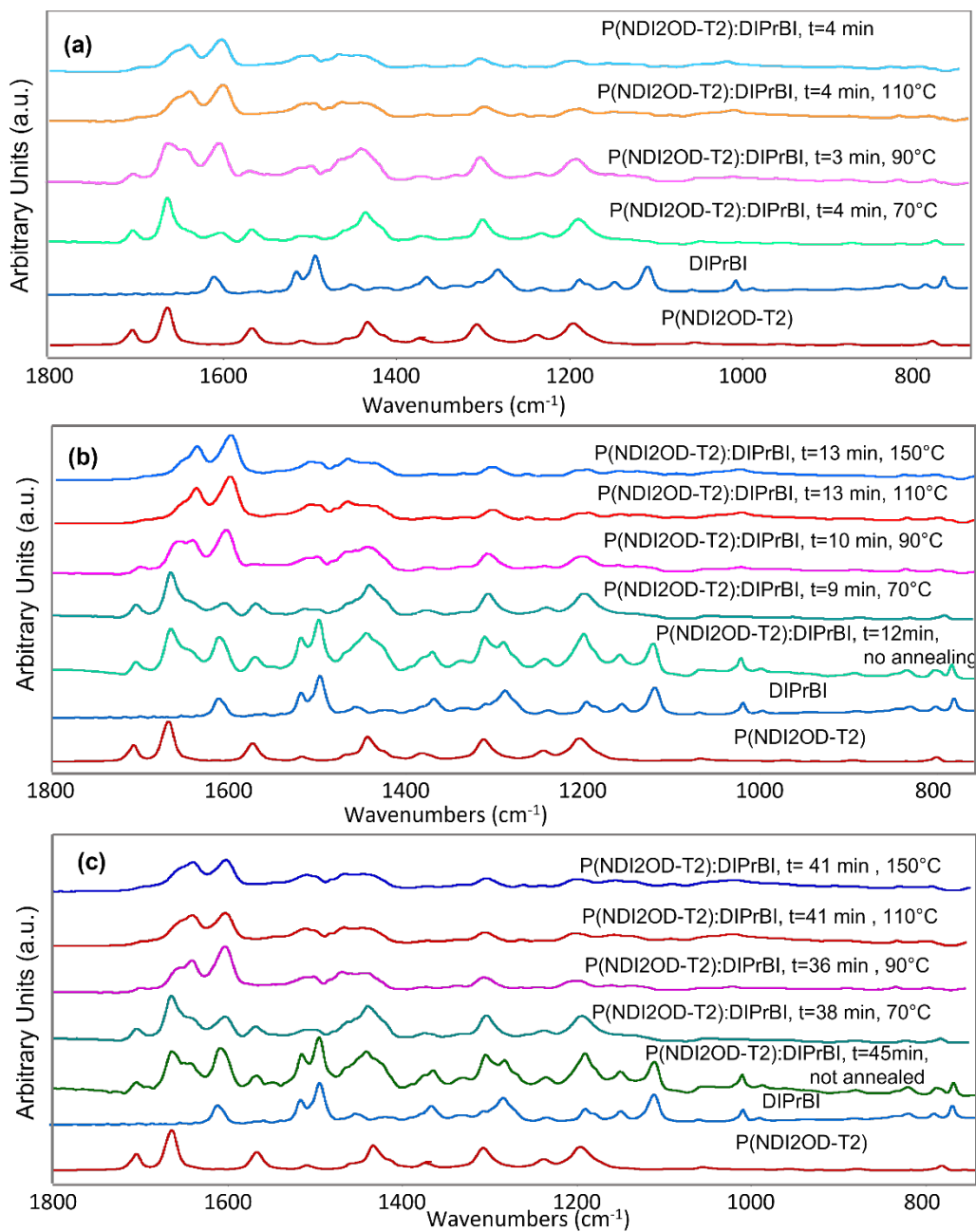


Figure 3.13: Comparison of the spectra at different annealing times and temperatures for all the temperatures used in this study (70°,90°,110°,150°C) and the doped, not annealed sample. Panel (a) shows the comparison after 3 to 4 minutes of annealing, panel (b) after 10 to 15 minutes and panel (c) after 35 to 40 minutes.

3.3.3 GIWAXS measurements

A fundamental aspect to understand how the annealing process works and how it affects polaron formation and structure refinement is the study of the morphology and crystallinity of the samples, through GIWAXS experiments. Spin-coated samples doped with MR=0.76, as the one used for the conductivity measurements, were prepared, and annealed at different temperature, for different amounts of time. A pristine and doped-not annealed samples were also studied. The GIWAXS patterns for all samples are shown in **Figure 3.15**. From this figure it is immediately possible to point out that the doped sample crystals present the typical edge-on configuration, no matter the annealing temperature and time, whereas pristine samplinfrarees crystallites exhibit the face-one configuration^[40, 45]. This behavior is switched on by the mere presence of the dopant, without the need to anneal the samples.

To better understand finer changes in morphology, the reduced 1D lines were taken along both the horizontal (in plane, q_{xy}) and approximately vertical (out of plane, $\sim q_z$) scattering directions (**Figure 3.16, 3.17, 3.18, 3.19**). The scattering peaks in both directions are each associated with a specific stacking direction of the polymer units, synthesized by the following bullet point:

- (h00) peaks correspond to the lamellar stacking peaks
- (010) peaks correspond to the backbone direction
- (00l) peaks correspond to the π -stacking direction (charge transport direction)

There are several (h00) and (00l) scattering peaks along the q_{xy} direction, up to four orders of lamellar stacking and up to two orders of backbone repeat unit scattering (**Figure 3.16, 3.18**). This is an indication of the exceptional in-plane crystalline order of P(NDI2OD-T2), already well documented in literature^{5,75}. The $\sim q_z$ direction presents a remarkable peak at $q \sim 1.6 \text{ \AA}^{-1}$, attributed planes along the π -stacking direction (**Figure 3.17, 3.19-panel b**).

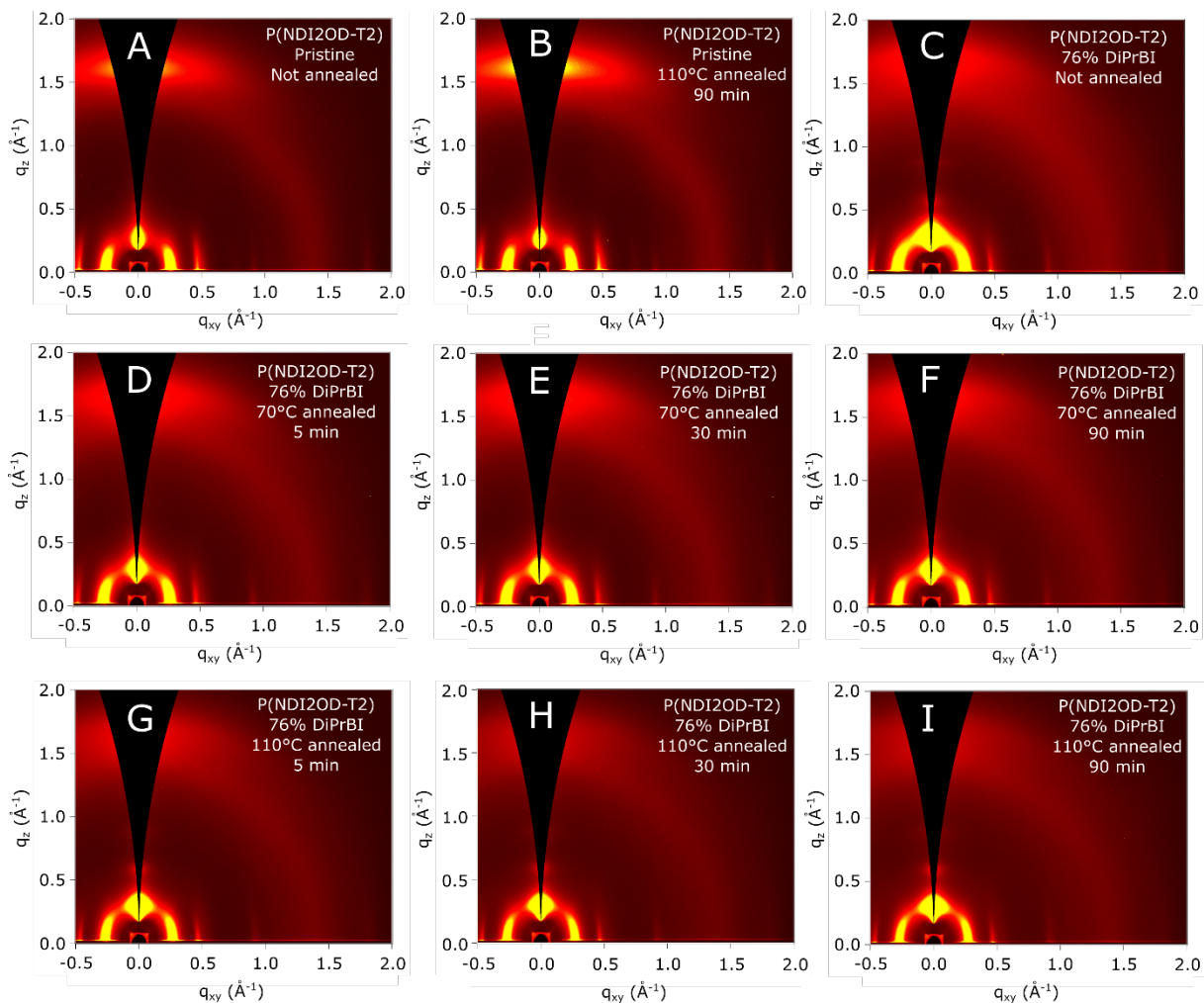


Figure 3.15: GIWAXS diffraction patterns for pristine P(NDI2OD-T2): (A) not annealed; (B) pristine P(NDI2OD-T2), annealed at 110°C for 90 min; and for DiPrBI doped P(NDI2OD-T2), MR=0.76 (C) not annealed; annealed at 70°C for 5 (D), 30 (E) and 90 (F) min; annealed at 110°C for 5 (G), 30 (H) and 90 (I) min.

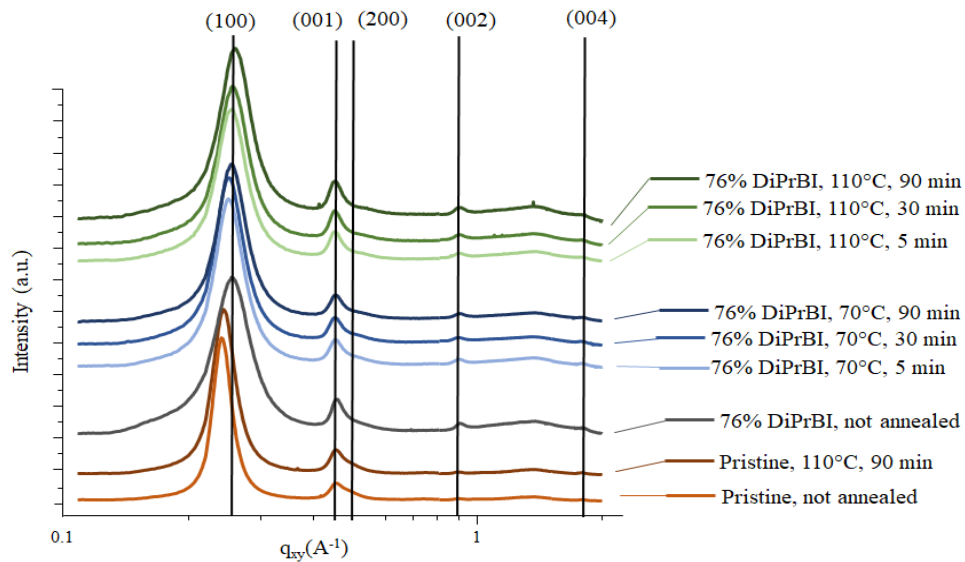


Figure 3.16: Vertical line-cuts (in plane direction) of the 2D GIWAXS diffraction pattern for P(NDI2OD-T2) doped with DiPrBi, MR=0.76. The various represented samples are, from bottom to top: pristine samples not annealed and annealed at 110°C for 90 minutes (brown lines); doped not annealed sample (grey line); doped samples annealed at 70°C for 5, 30 and 90 minutes (blue line); doped samples annealed at 110°C for 5, 30 and 90 minutes (green line).

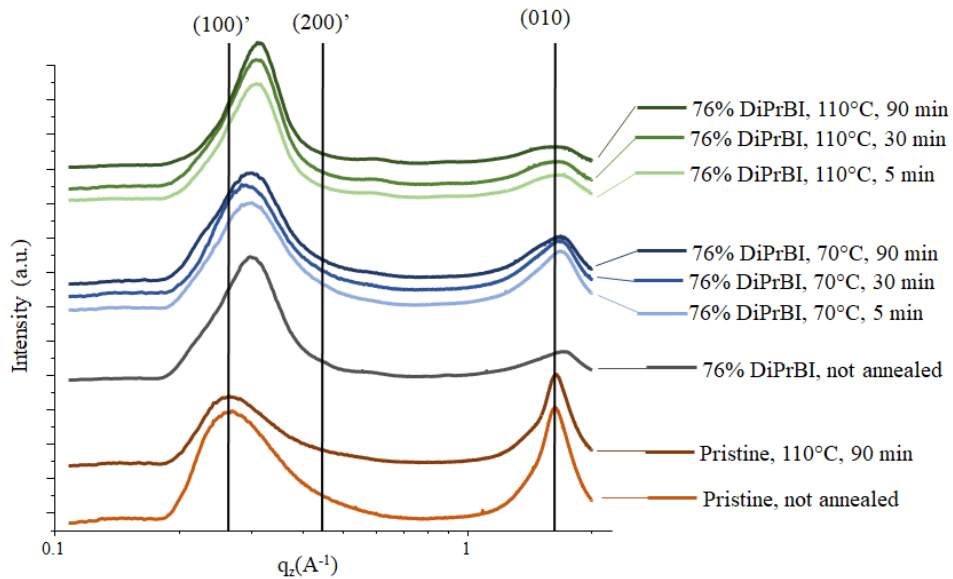


Figure 3.17: Horizontal line-cuts (out of plane direction) of the 2D GIWAXS diffraction pattern for P(NDI2OD-T2) doped with DiPrBi, MR=0.76. The various represented samples are, from bottom to top: pristine samples not annealed and annealed at 110°C for 90 minutes (brown lines); doped not annealed sample (grey line); doped samples annealed at 70°C for 5, 30 and 90 minutes (blue line); doped samples annealed at 110°C for 5, 30 and 90 minutes (green line).

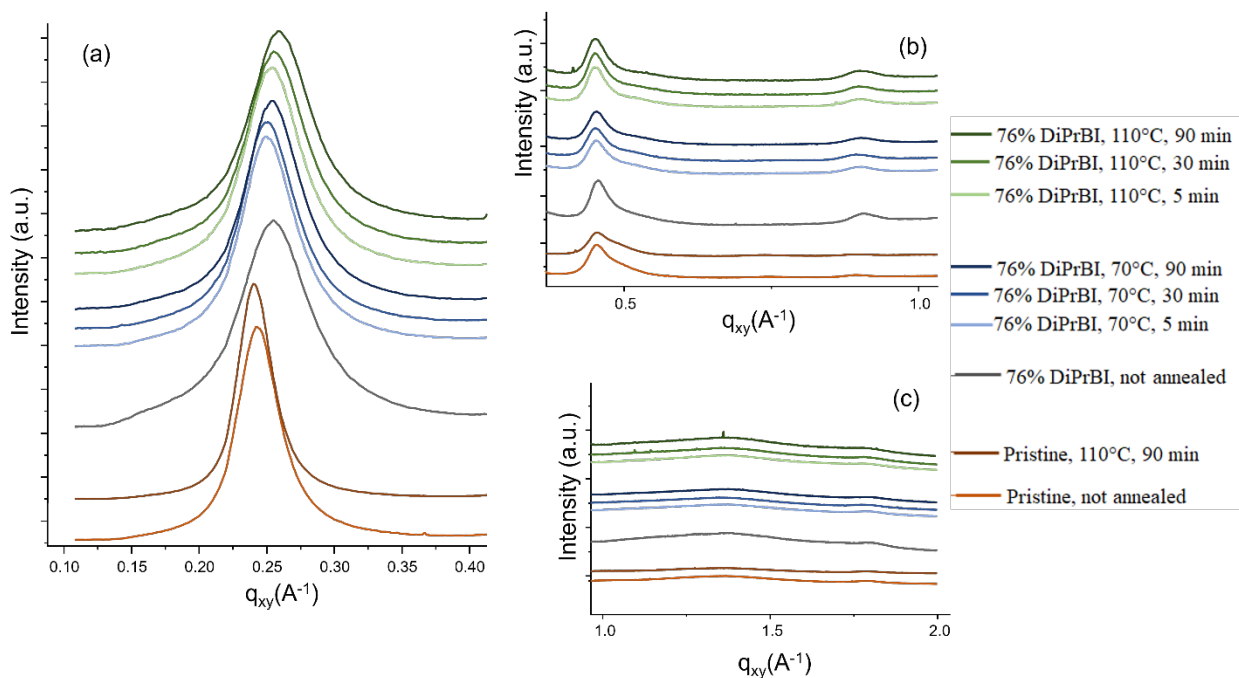


Figure 3.18: Zoom for the vertical line-cuts (in plane direction) of the 2D GIWAXS diffraction pattern for P(NDI2OD-T2) doped with DiPrBi, MR=0.76. Panel (a) represents the (100) peaks, corresponding to the lamellar direction, panel (b) the (001), (200) and (002), respectively associated with the backbone first order, lamellar second order, and backbone second order diffraction scattering peaks, panel (c) represents the (004) associated with the backbone fourth order diffraction scattering peak.

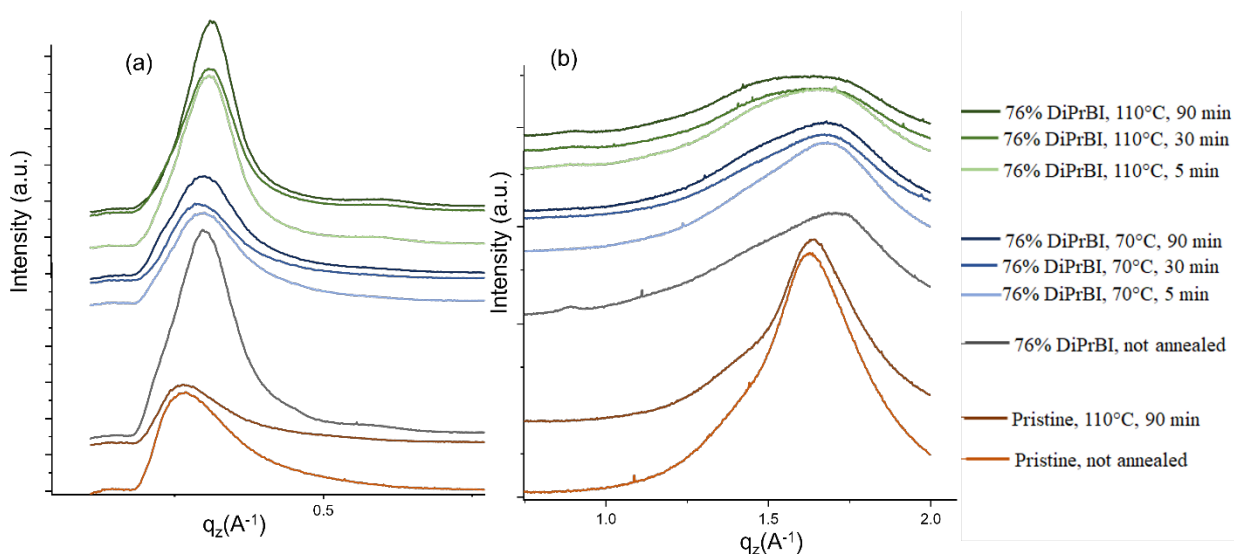


Figure 3.19: Zoom for the horizontal line-cuts (out of plane direction) of the 2D GIWAXS diffraction pattern for P(NDI2OD-T2) doped with DiPrBi, MR=0.76. Panel (a) represents the (100)' and (200)' diffraction peaks, associated with the backbone direction, panel (b) the (010) diffraction peak, associated with the π -stacking direction.

The pristine samples, as-spun and annealed (110°C, 90 minutes), were measured as reference. The face-on orientation of the as-spun sample remains unchanged in the annealed sample. This behavior is typical when annealing temperatures do not reach the melting point. The annealing does not effectively alter the crystallite structure, as confirmed by the conductivity data. The only effect of annealing on the morphology is a minor reduction of the intensity of q_z (010) peak with respect to the q_{xy} (100) and the q_z (100)' peak. A possible explanation of this phenomenon is the beginning of the transition from face-on to edge-on, but it could be as likely be a structural relaxation. The introduction of the dopant in the system changes completely the morphology, both when annealed and not annealed. While the backbone-related peaks are undisturbed by the presence of the dopant, the π -stacking $q_z \sim 1.6 \text{ \AA}^{-1}$ peak is disrupted, as its intensity decreases, and the peak broadens. The π -stacking changes will be further discussed later in this chapter. The (100) in-plane lamellar peak ($q_{xy} \sim 0.3 \text{ \AA}^{-1}$) shifts toward higher values as the temperature and time

of annealing increase. The values of the peaks are reported in **Table 3.1** and **Table 3.2** for the 70°C and 110°C series, respectively.

Sample	In plane (Å)		Out Of Plane (Å)	
	(100)	(001)	(100)'	(010)
Pristine @110°C	26.07	13.84	25.44	3.88
Pristine not annealed	24.84	13.78	22.68	3.75
5 min @70°C	25.17	13.75	21.16	3.9
30 min @70°C	25.06	13.78	21.59	3.9
90 min @70°C	24.75	13.78	21.16	3.9

Table 3.1. Scattering peaks position from the 1D reduced lines for both the pristine series and the annealed at 70°C series samples. Both the in-plane (q_{xy}) and out-of-plane ($\sim q_z$) direction are reported.

By comparing the in-plane (100) peaks positions at 70 and 110°C, it is possible to note that the 70°C, 90 minutes annealed sample has the same q_{xy} value of the sample annealed at 110°C for 5 minutes.

An interesting parameter to look at is the coherence length. The coherence length in GIXS experiments correlates the broadening of a peak in a diffraction pattern with the size of a crystallite in the material. It is calculated from the Scherrer equation as follows (**eq. 3.2**):

$$D = \frac{\kappa\lambda}{\beta \cos\theta} \quad \text{eq. 3.2}$$

Where D is the coherence length, indicating the average crystallite size, k is the Scherrer constant, varying between 0.68 to 2.08 (0.93 in this case), λ is the X-ray wavelength, β is the line broadening at the FWHM, expressed in radiant, and θ is the Bragg angle in degrees. For a polymeric system, the coherence length can be expressed as in **eq. 3.3**:

$$D = \frac{0.93 \cdot 2\pi}{\Delta q} \quad \text{eq. 3.3}$$

where Δq is the diffraction peak position.

Sample	In plane (Å)		Out Of Plane (Å)	
	(100)	(001)	(100)'	(010)
Pristine @110°C	26.07	13.84	25.44	3.88
Pristine not annealed	24.84	13.78	22.68	3.75
5 min @110°C	24.74	13.81	22.28	3.86
30 min @110°C	24.54	13.9	21.44	3.95
90 min @110°C	24.35	13.87	21.44	3.96

Table 3.2. Scattering peaks position from the 1D reduced lines for both the pristine series and the annealed at 110°C series samples. Both the in-plane (q_{xy}) and out-of-plane ($\sim q_z$) direction are reported.

Table 3.3 and 3.4 express the coherence length values for these experiments.

As the temperature of annealing increases, the q_z (010) peak loses coherence and intensity with respect to the (100)' lamellar peak. This behavior is exacerbated for the 110°C dataset, where contemporaneously a new shoulder at 1.6 \AA^{-1} is visible, as well as in the 70°C, 90 minutes annealed sample. This perturbation of the π -stacking was already reported in literature for P(NDI2OD-T2)

doped with DMBI molecules. A hypothesis that could explain such perturbation on the π -stacking planes, characterized by short-range order, is the intercalation of the dopant between NDI units.

Another confirmation of the intercalation of the dopant in between the polymer backbones is the gain in intensity of the (200)' peak with temperature and time of annealing, as highlighted in **Figure 3.19(b)**, as Saglio et al.¹¹ discussed in their work.

Another interesting observation is related to the comparison between the doped samples not annealed, 70°C and 110°C π -stacking direction (OPLA (010), **Figure 3.19, panel b**). The intensity of the not annealed (010) with respect to the (100)' is lower than the 70°C sample, which show a more prominent face-on, and more similar to the 110°C. This result might seem a little odd, but it actually relates with the decrease in conductivity shown for the 70°C samples. This behavior seems to suggest that for low annealing temperatures a face-on morphological rearrangement is favored, while for higher annealing temperature a more edge-on configuration is to be expected, leading to a better performance conductivity.

Sample	In plane (Å)		Out Of Plane (Å)	
	(100)	(001)	(100)'	(010)
Pristine @70°C	209.06	210.65	48.33	17.07
Pristine not annealed	107.38	315.35	53.29	7.37
5 min @70°C	132.95	227.90	45.86	10.41
30 min @70°C	133.84	200.80	49.13	10.39
90 min @70°C	131.31	204.38	48.26	9.51

Table 3.3. Coherence length calculated through the Scherrer equation for the pristine and doped annealed at 70°C samples.

Sample	In plane (Å)		Out Of Plane (Å)	
	(100)	(001)	(100)'	(010)
Pristine @110°C	209.06	210.65	48.33	17.07
Pristine not annealed	107.38	315.35	53.29	7.37
5 min @110°C	128.94	279.85	59.07	8.34
30 min @110°C	125.39	259.59	59.46	8.27
90 min @110°C	120.71	284.49	67.16	7.38

Table 3.4. Coherence length calculated through the Scherrer equation for the pristine and doped annealed at 110°C samples.

3.4 Conclusion

The most interesting finding of this chapter is the fact that 1H-benzimidazoles dopants of P(NDI2OD-T2) are already active at room temperature, showing an increase in conductivity 3 orders of magnitude. The finding parallels by GIWAXS and infrared in-situ measurement, indicating that the charge defect is already formed at room temperature, contrarily to what is so far believed in literature⁷³. The annealing has a further effect on the conductivity, doubling the conductivity value in conjunction with a morphology refinement.

The infrared data collected for thick samples show how a higher annealing temperature favors the doping process, affecting its kinetics. As the temperature of annealing increases, the polaron formation seems to proceed faster, then reaching a plateau. The important conclusion of this study is that the charge transfer/polaron formation process takes place spontaneously but has a rather slow kinetic in thick films at ambient temperature. This explains why the IR experiments on doped films as deposited - reported in **Chapter 2** - showed absorption features well described

by the mere weighted sum of the spectra of the pristine polymer and dopant. Interestingly, we showed here that in absence of oxygen, which can give rise to competitive reactions, an incipient doping is observed also immediately after the casting of the film from the polymer/dopant solution.

The GIWAXS data, obtained for thin spin coated films, summarized in this paragraph show that the crystalline structure changes upon doping from face-on to edge-on, as well as giving intercalation sites for the dopant, in between the polymer backbones. A more accurate analysis of the GIWAXS measurements conducted on samples at different temperatures show that the edge-on phase is highly predominant in the 110°C annealed samples, whereas when the annealing is conducted at lower temperatures (70°C) the face-on phase slightly increases, explaining why the conductivity for these samples presents lower values.

In order to explain the energetic of the dopant-polymer charge transfer, in **Attachment B** a novel doping mechanism is proposed, based on theoretical modelling, that implies the quasi-planarization of the dopant, which is a process that could be expected during intercalation. In the flat conformation of the dopant, the HOMO of the dopant rises significantly, reducing the distance from the LUMO of the polymer, thus eliminating the barrier for electron injection.

Chapter 4: In-situ monitoring of electrochemical doping of P(NDI-gT2) through Raman spectroscopy: polaron and bipolaron formation

In this chapter I present the Raman spectra of the electrochemically doped random copolymers P(NDI-gT2). The Raman data were acquired in-situ through a custom-designed electrochemical cells. Electrolytes of various pH and composition were tested to highlight possible changes in the formation of the charge defect through various experimental conditions, as well as studying the effect of side reactions happening in the electrolyte. The data show that the polaron and the bipolaron are formed under certain experimental conditions, and that the presence of oxygen hinders the bipolaron formation.

4.1 Introduction

Organic Mixed Ionic Electric Semiconductors (OMIECS) are a wide class of polymers used in many application fields, in particular bioelectronics, thanks to some of their outstanding property, as chemical redox activity, ionic and electronic transport, easy processability and functionalization. OMIECs are formed by a conjugated backbone responsible for electronic conduction, with side chains that allow ionic intercalation and facilitate their solubility in solvents. Their peculiarity to transport both ions and electrons represents a fundamental and unique aspect: for this reason, studying the coupling between ionic and electron transport, as well as transport mechanisms is the state-of art research. Organic Electrochemical Transistors (OECTs), first invented by Wrighton⁷⁶ are the benchmark for electrochemical field transistors. Similarly to their predecessor, they work as a 3-electrode system: when a gate voltage is applied across the electrolyte, ions are injected into the active layer, inducing a volumetric change. The active layer conductivity changes as the mixed conductor oxidation level is altered, resulting in a difference in the drain current^{77,78}. A schematic of an OECT is reported in **Figure 4.1**.

The two main qualities that make a good OECT are its transistor-like capacity to amplify signal, as well as working as a good sensor for the ions in the active layer⁷⁹. The extent of applications for OECTs is particularly wide, and some of the most interesting ones are related to healthcare and sensing. To give an idea of the impact in everyday life that OECTs could play, a group led by Guo⁸⁰ was able to produce OECT-based disposable sensing device able identify rapidly the spike proteins of COVID-19, SARS-CoV-2 and MERS-CoV, as well as providing a quantification of the viral load. The sensor uses a glycolated polymer, p(gOT2-g6T2), as well as disposable protein-based electrodes.

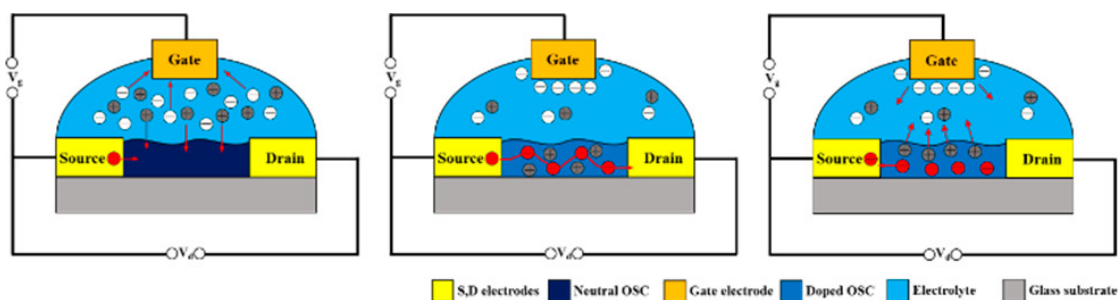


Figure 4.1: Working principles steps of a n-type accumulation mode OECT (1) upon application of a positive gate voltage, electrons move from the source and cations are injected into the film, electrochemically doping it. (2) electrons are transported from source to drain through the doped n-type semiconductor. (3) When the gate potential is reversed, electrons migrate in the source and cations outside of the n-polymer⁸¹.

The new exciting biomedical applications of OMIECs are strictly linked to synthetic design strategies to modify or create new materials with glycolated chains or soluble in water, maintaining the same properties of mixed conduction, possibly addressing and improving stability, mobility and swelling of the materials. One of the simplest, yet effective, approach to reach these goals is the modification of the polymer side chains. In this chapter we will focus on

Naphtalenediimide (NDI) based random copolymers, originated by progressively substituting the alkyl chains of the well-known P(NDI2OD-T2) with glycol chains, or P(NDI-gT2) (**Figure 4.2**).

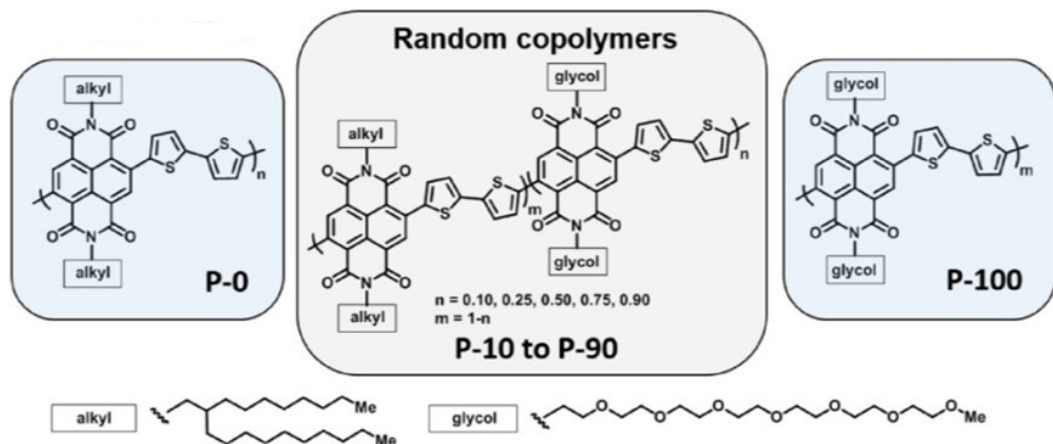


Figure 4.2: Schematic representation of the P0-P100 random copolymer series from¹⁷.

When side chains are progressively substituted, the electrochemical and optical response of the materials change accordingly. First, the reduction potential in aqueous solutions decreases as the glycol chains ratio increase. Moreover, a higher percentage of glycol chains drastically affects the reversibility of the electrochemical reaction, improving it for copolymers with a minimum of 50% glycol chains. However, the electron mobility decreases of at least 2 orders of magnitude with respect to pristine P(NDI2OD-T2), pointing out the constant need of improving the synthetic strategies for these materials¹⁷.

Despite there is room for further development of their conductive properties, P(NDI-gT2) are perfect candidates for spectroscopic studies aiming at establishing better structure-property relationship and advance the understanding of the role of side reactions and interaction with oxygen during electrochemical doping.

In this chapter, I will concentrate on presenting a few works where optical techniques and vibrational spectroscopies are applied at electrochemically doped polymers.

In a very interesting study of Silva's group⁸², charge transfer intermediates in conjugated polymers without long-range order are unveiled using in-situ ultrafast Raman spectroscopy, during electrochemical doping. In their work the mechanism of electrochemical doping in an oligoether-functionalized 3,4-propylenedioxythiophene (ProDOT) copolymer is investigated by means of transient absorption and resonant Raman in-situ spectroscopy, considering the external environment and intrinsic polymeric structure.

In 2019, Moia et al.⁴⁴ reported the study of a novel redox-active NDI-based polymer with a random combination of polar and zwitterion side chains, that could be used in electrochemical energy storage. The charge and discharge of the polymer's electrode was monitored through spectroelectrochemistry in the UV-Vis region. These experiments provided evidence that the electrochemically doped NDI polymer could take up to 2 charges per repeat unit (forming a bipolaron), and that the process is completely reversible.

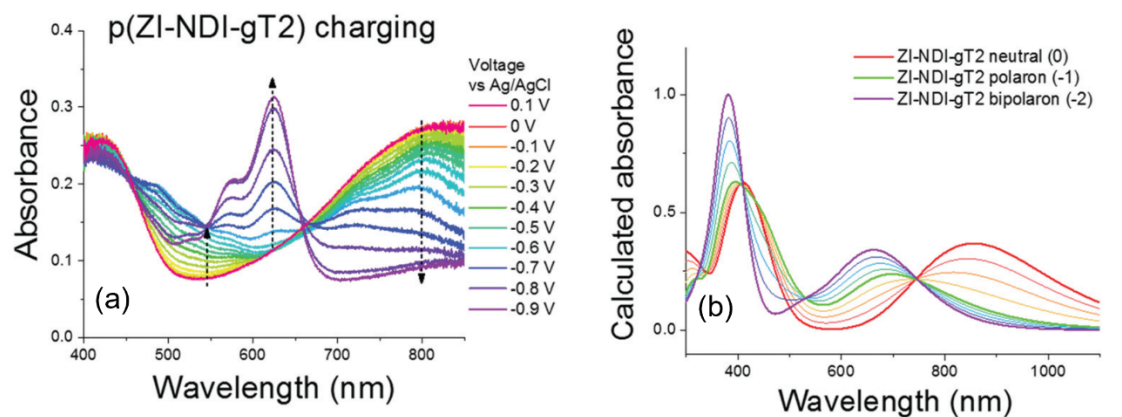


Figure 4.3: (a) Spectroelectrochemical experiment conducted on an NDI-based polymer. The voltage swept goes from 0.1V to 0.9V. The bipolaronic features and isosbestic point are highlighted by arrows. (b) DFT calculations of the spectroelectrochemical experiments (image modified from⁴⁴).

The negative polaron formation takes place at -0.4V, whereas the bipolaron features are assigned at voltages from -0.5V to -0.75V (**Figure 4.3(a)**). The change from polaron to bipolaron state is further confirmed by the presence of two isosbestic points in the spectrum. The bipolaron peak is centered between 600 and 650nm, and the spectral features are further confirmed by DFT calculations (**Figure 4.3(b)**). Interestingly, the authors use spectroelectrochemistry to exploit the effects of side reactions using degassed electrolytes. This technique is often used to monitor the formation of oxygen and hydrogen peroxide and highlight the charge retention issues of n-type OSCs.

When working with organic polymeric transistors in liquid environment, both the ion-electron coupling in the electrochemical doping process and the influence of water and oxygen on the performances of OECTs needs to be addressed. Many studies were conducted on p-type polymers regarding both matters. Cendra et al. report that, upon electrochemical doping of p(g2T-TT), ions modify permanently the lattice space, intercalating in the polymer, while the residual water is responsible for the film swelling⁸³. The effect of swelling on the performances of the devices was reported by Savva et al¹⁶. By varying electrolyte ion concentration and solution pH, they were able to quantify the amount of water incorporated in the polymeric film, resulting in an irreversible change in the polymer structure. The latter has a direct impact on reversibility, efficiency and speed of the doping process. Their work highlights the fact that, despite swelling and water intake are necessary for ion-electron transduction, they also negatively affect the performances of the material.

On the other hand, the impact of oxygen and humidity on n-type semiconducting polymers, due to their shallow LUMO, is well known. Oxygen and water can act as electron traps⁸⁴, being detrimental to charge transport performances, as well as affecting the chemical stability of the polymers⁸⁵.

A comprehensive explanation on how oxygen and water particularly affect n-type polymers is reported by Griggs et al.¹⁹.

An interesting study on how oxygen and water affect the performances of P(NDI2OD-T2) was presented by Di Pietro et al.³⁷ in 2012. Their approach involves the use of different spectroscopic techniques in the effort to separate the effect of molecular oxygen present in air and in water solution. They proved that the oxygen present in air acts as trap for the electrons, whereas for experiments in water environment, two reactions take place. One is reversible, and involves the electron transfer due to the shallow LUMO energy level (electrochemical oxidation process). The second is irreversible and leads to polymer degradation; it involves chemical reactions with water, highlighted by Raman spectroscopy.

Stability issues for presence of water or oxygen could be overcome by either working in inert conditions or designing polymers with a deeper LUMO.

Despite side reactions could obstruct the performances of transistor, their products (namely hydrogen peroxide resulting from oxygen reduction)^{44,86} are essential in other fields, as electrocatalysis. The search of green methods for the production of hydrogen peroxide finds a match in the electrochemical synthesis through side reaction for polymers chemical doping⁸⁷. This finding, first discovered in 2013 for the well-studied PEDOT, has opened the path for a new, exciting research field⁸⁶.

4.2 Experimental methods

4.2.1 Materials and dopants

The NDI random copolymer P(gNDI-T2) was synthesized at Oxford University. P(gNDI-T2) consists in a modification of P(NDI2OD-T2), where units with alkyl chains (C_8H_{17} , $C_{10}H_{21}$) are randomly combined with units with 7-unit glycol side chains¹⁷. The polymer thus created is therefore able to work in aqueous solutions. The random copolymers are then labelled according to the percentage of glycol chains, namely P100, P90, P75 up to P0, respectively from 100% glycol chains to 0% (**Figure 4.2**).

P100, P90 and P75 were used in the study presented in this chapter. Only the data for the P100 and P75 series will be showed.

Aliquots of the polymer were dissolved in Chloroform (CHCl_3) following the typical 10 mg/ml polymer/solvent ratio. The solution was stirred overnight on a 60°C hotplate, then either drop casted (7 μm , for the static cell, see next section) or spin coated (70 μm , 800rpm for 60s for the flow cell, see next section) on an ITO slide. The samples were then annealed at 110°C for 1h.

Different electrolytes were chosen to monitor the formation of polaron and bipolaron features, exploiting different pHs and experimental conditions. In the following, cells equipped for in-situ spectroscopic measurements are identified as “in-situ” cells. A list with the electrolytes, experimental conditions and properties is here provided:

1. NaCl, 0.1M, pH=7, used in the static in-situ cell
2. Glucose (0.1M in PBS) with Glucose Oxidase (Gox, 20.4 mg/ml in PBS), used in the static in-situ cell
3. Glucose (0.1M in PBS) with H₂O₂, 0.1M, used in the static in-situ cell
4. PBS, 0.1M, used in the static in-situ cell
5. KOH, 0.1M, pH=13, used in the flow in-situ cell
6. KCl, 0.1M, pH=7, used in the flow in-situ cell

The solution of glucose and glucose oxidase were prepared according to literature⁸⁸. For the experiments with glucose addition, glucose solutions were added to glucose oxidase and H₂O₂ (30 μl added to 180 μl of solution) and the measurements were performed after 20 minutes, in order to allow the electrolyte to reach the equilibrium.

4.2.2 In-situ Raman setup

Two different setups were used to perform the in-situ measurements. First, a static electrochemical cell was implemented to understand the feasibility of the Raman experiments. The setup consists of a glass (2.5x2.5cm²) substrate patterned with two ITO parallel stripes. The

sample is drop casted on the ITO, as shown in **Figure 4.4**. A custom-made polydimethylsiloxane (PDMS) wall is attached to the substrate, leaving a little portion of the ITO on the edge of the substrate outside of the PDMS wall, to be used to contact the Working electrode (K2200 probe). The electrolyte is inserted in the PDMS wall, without the possibility to be bubbled before the experiments. This is not ideal for the measurements, as the electrolyte contains oxygen, and this issue will be discussed in the next section. The Ag/AgCl reference electrode (BaSi) and the Platinum mesh (counter electrode) are then immersed in the electrolyte, without touching the ITO stripes.

Despite it would be possible to saturate the electrolyte with an inert gas before the measurements and then transfer it in the static cell, the setup would still present issues, as the electrolyte would not be protected from the oxygen in atmosphere, and the solution would still become oxygen saturated over time.

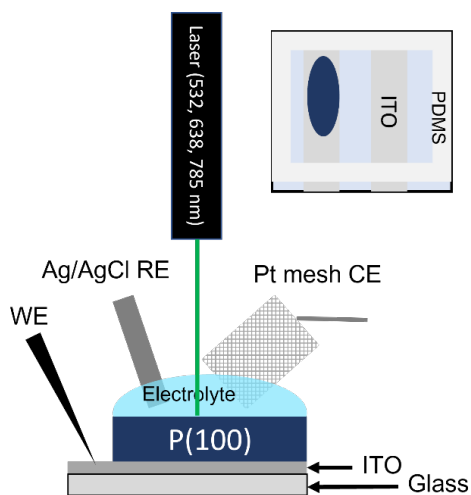


Figure 4.4: schematic of the static 3-electrodes electrochemical cell used for the in-situ Raman measurements.

To completely avoid the presence of oxygen in the cell, I partnered with Allen Liang, a PhD candidate from the Chueh laboratory at Stanford university, who developed a new set-up. **Figure**

4.5 shows pictures and a schematic of the cell used for the measurements. The first difference is that the new setup consists of a flow cell, therefore the bubbled electrolyte flows in the cell where the sample is situated through small diameter tubes and is collected in a vial, being able to control the experimental conditions of the electrolyte throughout the whole experiment duration. We connected the electrolyte container to an argon or oxygen tank, in order to conduct the experiments in a nitrogen and oxygen saturated environment, respectively. In this way, we were able to exploit the effect of oxygen on the formation of the bipolaron. Moreover, two electrolytes with different pHs (neutral and acidic) were used with this setup, to highlight possible differences in the spectral behavior by changing experimental conditions. The RE electrode consists in a Mini Leakless electrode (eDaq), while the CE is a platinum foil (0.025mm).

A fully covered ITO slide with half area coated by the polymer by means of the spin coating procedure is inserted in the cell and the data are collected through a sapphire window (6.35mm diameter, 0.5mm thickness). The cell is sealed through vitium o-ring, to avoid leakage of the electrolyte during measurements. The fact that the cell is completely sealed has two positive effects: it protects the sample and electrolyte from the external environment (air/humidity) and protects the optical objective for Raman measurements from the electrolyte itself, making this cell better and safer than the previous one. Despite the sapphire window is a fundamental part of the setup, it makes the focus on the sample more difficult, as the visibility is scarce, both before and after introducing the electrolyte. For this reason, the polymer surface was scratched with a q-tip before conducting any measurement.

The laser for the Raman experiments is situated above the cell, in a typical backscattering geometry. 532 and 638 nm laser wavelengths were used for the experiments, with a 10x objective (Olympus). A Horiba Xplora Raman was used for the spectra acquisition. The laser power was kept around 1mW for all the wavelengths when the electrolyte was inserted, to still have a good noise to signal ratio. 10/20s spectra, 2 repetitions were acquired during the in-situ voltage swept, to avoid stressing the material by applying voltage for too long. A reference spectrum was acquired before each in-situ characterization, through a longer acquisition (30s, 4 repetitions, 0.1mW laser power to avoid degradation).

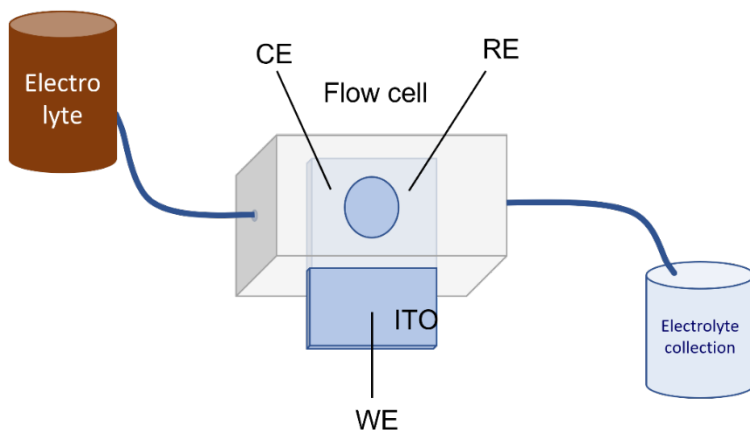


Figure 4.5: Top (from left to right): images of the flow 3-electrodes electrochemical Raman cell used for the in-situ experiments, before measurements and during measurements. Bottom: schematic of the electrochemical cell used for the in-situ Raman measurements. The electrolyte is bubbled with nitrogen.

4.2.3 Electrochemical experiments

Before and after the Raman measurements, both for the static and flow cell, cyclic voltammetry (CV) measurements were performed to better understand the nature of the reaction, as well as the presence and modification of the reduction peaks with and without oxygen. The CV measurements provide a voltammogram which indicates the current flowing through the working electrode in function of the applied potential. A scan rate of 50 mV/s was used in this study. When the electroactive species are exhausted near the electrode surface, a faradaic reaction occurs, and the slope of the curve changes, creating a peak. The number of anodic peaks indicate

the number of oxidation reactions, while the cathodic peaks are related to the reduction reactions. The analysis of the peaks position and shape of the CV curve gives a lot of information on the reactions taking place on the samples. A electrochemical process is considered reversible if the potential for both the peaks is similar and is a fast process. On the other hand an electrochemical process is considered slow if there is a non-negligible distance between anodic and cathodic peak or one of the peaks is not present (asymmetrical shape of the CV). A representative voltammogram of P-75 is shown in **Figure 4.6**, without and with oxygen in the electrolyte, acquired through the flow cell. Before starting the CV measurement the open circuit potential (OCV) was monitored until reaching a constant value of a few mV.

In the voltammogram acquired with the nitrogen-saturated electrolyte (left) the reduction onset is around -0.25V, while it shifts slightly in the oxygen saturated CV (around -0.3V, on the right). This shift is most likely explained by the difference in ion penetration in the bulk during the redox reaction, as the polymer is the same for both experiments (thus there are not structural differences in the backbone).

The reduction peak around -0.85V is clearly visible for the nitrogen saturated electrolyte. A second peak visible at lower voltages was observed for P75, P90 and P100, and it is an indication of the water intake in the material upon voltage swept, indicating that the material is swelling upon ion intercalation in the bulk of the polymer¹⁷. The positive and the negative area of the voltammogram are similar, indicating that the reaction is reversible and that no side reactions are happening in the material. On the contrary, the voltammogram acquired with an oxygen saturated solution is quite different: the peak ascribed to swelling is still present, but there is not a clear second peak visible, and the voltammogram is quite asymmetric. This is the main indicator that the process is irreversible as side reactions are happening, likely the formation of Hydrogen Peroxyde, which could hinder the development of the bipolaron on the material.

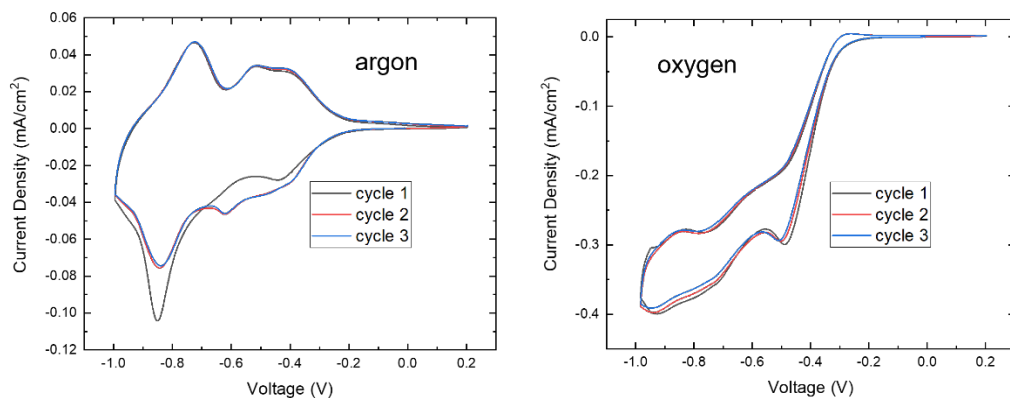


Figure 4.6: typical cyclic voltammograms of P(gNDI-T2) in an nitrogen saturated electrolyte (left) and an oxygen saturated electrolyte (right). These experiments were conducted in the flow cell.

The typical voltage swept used for the experiments are showed in **Figure 4.7**. On the left a up-down voltage swept was chosen to allow the material to dope and dedope at each cycle. On the right a ladder approach was selected, where the material was kept at negative potential for longer time and then slowly reversed to positive potential. Both approaches are valid and were tested to prove if the materials would respond differently to the external stimuli. Because the voltages swept gave similar results with the static cell, only the latter was used for the measurements with the flow cell. Each voltage was applied for 30 or 60s, depending on the experiment conducted.

The *in-situ* Raman experiments allow observing the doped species during electrochemical cycles, at different voltages, as well as the reversibility of electrochemical doping processes.

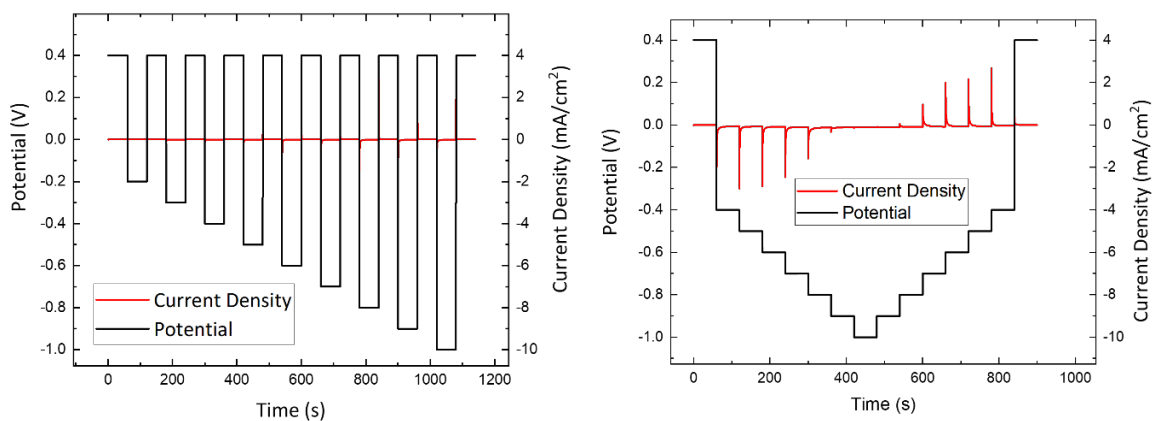


Figure 4.7: examples of the typical potential swept used for the in-situ experiments.

Table 4.1 synthesizes the experiments presented in this chapter.

	Static Cell $\lambda_{exc} = 532\text{nm}, 638\text{ nm}$	Flow Cell $\lambda_{exc} = 532\text{nm}$ $\lambda_{exc} = 638\text{ nm}$ for KOH only
Oxygen	<ul style="list-style-type: none"> • NaCl, 0.1M, pH=7 • Glucose (0.1M in PBS) with Glucose Oxidase (Gox, 20.4 mg/ml in PBS) • Glucose (0.1M in PBS) with H₂O₂ • 0.1M, PBS, 0.1M 	<ul style="list-style-type: none"> • KOH, 0.1M, pH=13 • KCl, 0.1M, pH=7
Nitrogen		<ul style="list-style-type: none"> • KOH, 0.1M, pH=13 • KCl, 0.1M, pH=7

Table 4.1: overview of the *in-situ* Raman experiments presented in this chapter.

4.3 Results and discussion

4.3.1 Static cell

The results of the experiments for the static cell, aimed at proving the feasibility of the experiments, are showed in this section. Both excitations at 532 nm and 638 nm were exploited for the study. Pristine Raman spectra of P-75, P-100 and their precursor P(NDI2OD-T2) show the same spectral features, as they share the same backbone and only the percentage between the ratio of glycol and alkyl chains changes. A comparison of the pristine spectra of P-75 and P-100 with N2200 is showed in **Figure 4.8**.

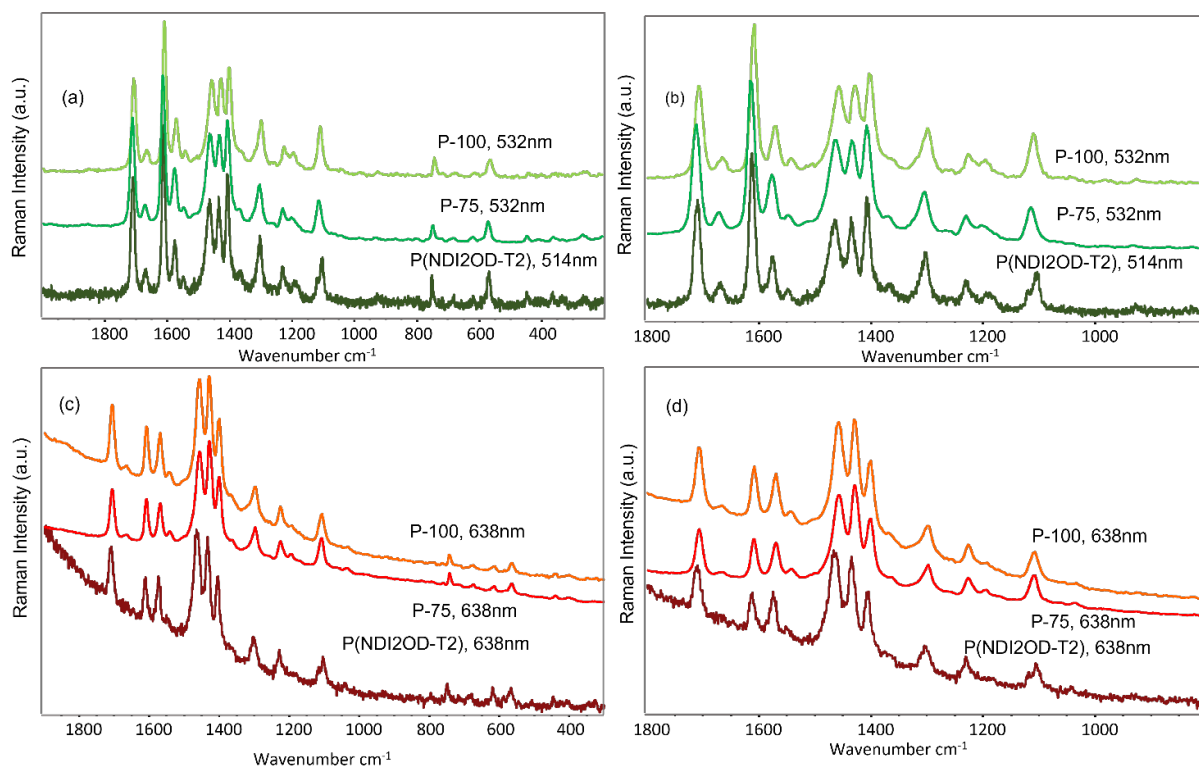


Figure 4.8: Comparison of pristine P(NDI2OD-T2), P-75 and P-100 (a) with excitation wavelength 514nm (for P(NDI2OD-T2)) and 532nm and a zoom (b), with excitation wavelength 638nm (c) and zoom (d).

The results presented in **Figure 4.9** show results for P-75 with NaCl 0.1M as electrolyte, using up-down potential swipe.

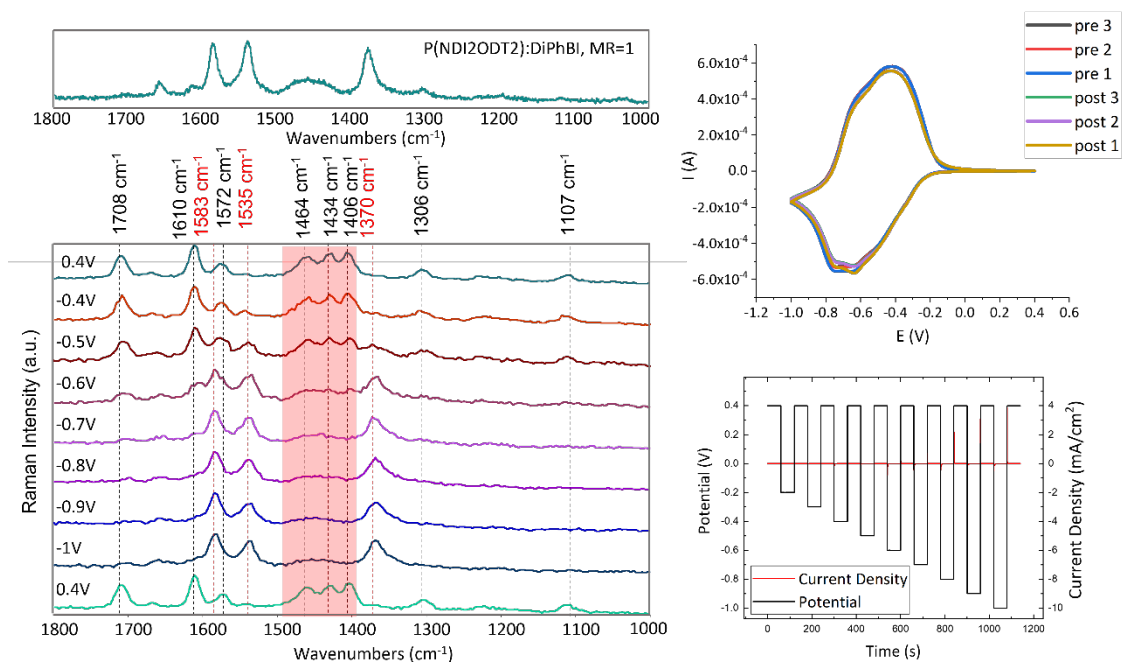


Figure 4.9: On the left, top panel: P(NDI2OD-T2):DIPhBI, MR=1, annealed for 6h at 110°C, acquired with the 514nm excitation wavelength; bottom panel: P-75 doped with NaCl, in the static cell setup, acquired with the 532nm excitation wavelength. On the right: CV and voltage swept are reported. Cyclic Voltammetry was performed up to -0.5V. Raman bands of the pristine polymer, assigned in³², are highlighted by black dotted lines. Polaronic features are highlighted in red.

Cyclic Voltammeteries were performed before and after Raman measurements, up to -1V. No significant changes are observed, meaning that the sample is stable, and the measurement is repeatable. The upper and lower area of the CV is comparable, and the anodic and cathodic peak shift is visible but not significant, indicating that the process is quasi-reversible.

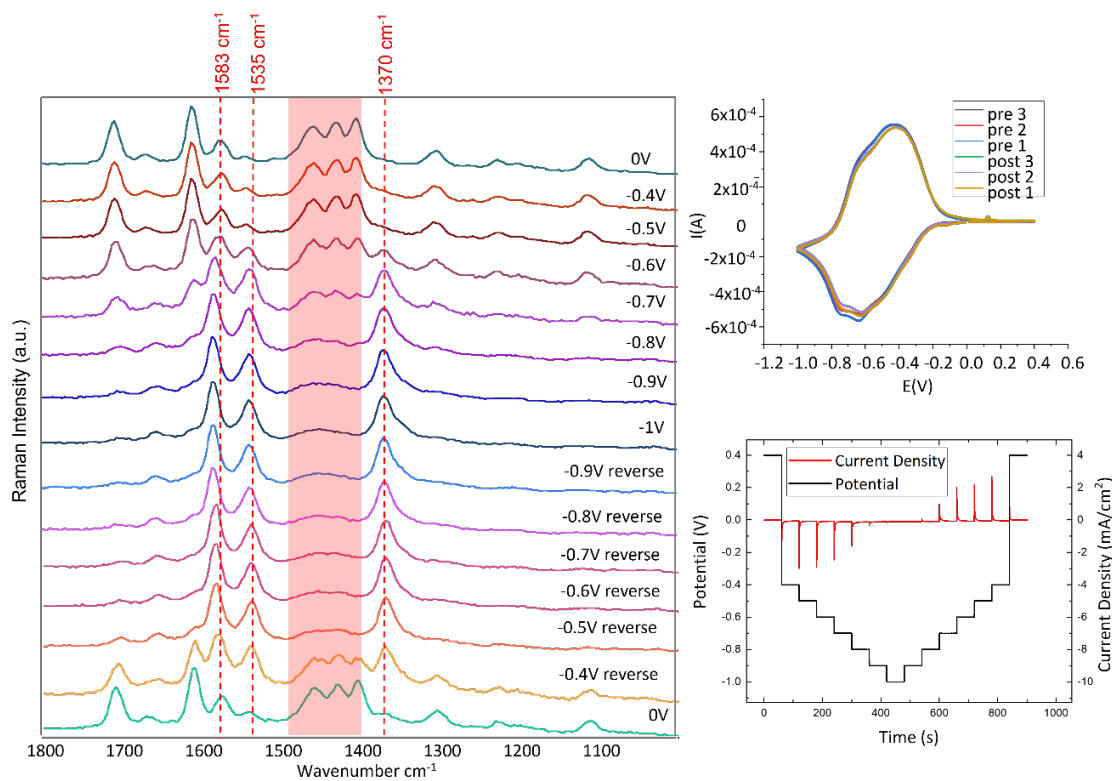
The Raman spectra series is reported on the left, showing only the initial and final 0V spectra. The intermediate measurements at 0V were omitted in the figure, as the spectral features were stackable with the initial and final 0V measurement.

At lower voltages ($<-0.4\text{V}$), no differences in the spectral features can be highlighted with respect to the 0V spectrum. However, when the voltage reaches -0.5V , two new bands arise at 1360 and 1610 cm^{-1} . By incrementing the negative voltage, polaronic signature bands, already described in **Chapter 2 (Figure 4.9, top left panel)**, arise, as:

1. the broadening and shift of the triplet bands of the pristine polymer at $1406, 1434$ and 1464 cm^{-1}
2. formation of new bands at 1360 cm^{-1} , 1535 cm^{-1} and 1583 cm^{-1}
3. decrease in intensity/ disappearance of the bands of the pristine polymer at 1610 and 1708 cm^{-1}
4. disappearance of 1306 and 1107 cm^{-1} Raman bands

When using a ladder potential, the same vibrational characteristics are highlighted during the potential sweeping down (from 0V to -1V) (**Figure 4.10**, spectra from top to -1V dark blue one). The ladder potential allows studying the reversibility of the doping when the negative potential is applied for a considerable amount of time (a few minutes), as the potential is also reversed (range $[-1, 0]\text{ V}$) (**Figure 4.10**, from dark blue middle spectrum at -1V blue to the bottom one). The doping is mostly reversible with one-to-one potential correspondence (same spectral differences between a voltage and same potential “reversed”). Slight changes in the potential -0.6V and reverse, as well as -0.7V and reverse can be individuated. By comparing the two latter (-0.7V and reverse), it is evident that the spectrum at -0.7V still shows the presence of the triplet band 1464 cm^{-1} , whereas in the -0.7 reverse data the spectral features correspond to a fully polaron doped sample (broadening of the triplet etc.). Moreover, -0.6V reverse is still showing all the polaronic bands, with negligibly weak bands of the pristine polymer, which start to emerge at -0.5V reverse. The overall doping is completely reversible, but the potential does not completely coincide. This behavior could be explained by the swelling and speed of response of the material to the applied voltage, as the negative potential is kept for a long time, allowing the water intake in the polymer

to be greater than the case analyzed in **Figure 4.8**. The overall performance of P-75 during electrochemical doping is outstanding, completely reversible, and a good doping level is reached.



Figures 4.10: P-75 doped with NaCl, in the static cell setup, acquired with the 532nm excitation wavelength. The CV and voltage swept are also reported on the right. Cyclic Voltammetry was performed up to -0.5V. The spectra were acquired from top to bottom. Polaronic features are highlighted in red.

A direct comparison with the spectra of N200 chemically doped with DiPrBI, presented in **Chapter 2**, showed in **Figures 4.11 and 4.12**, further highlights the similarities in the spectra obtained by different doping methods.

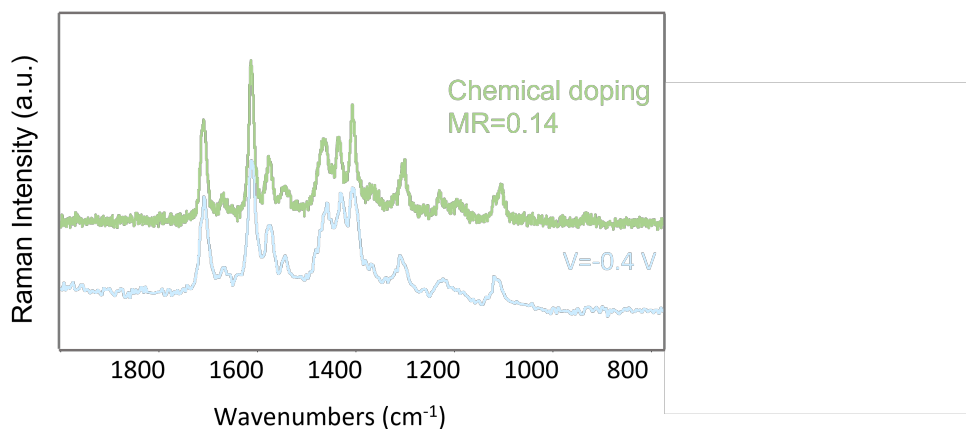


Figure 4.11: comparison between chemical doping at MR=0.14 (top, green spectrum) and electrochemical doping at -0.4V voltage (bottom, light blue spectrum), acquired with the 532nm excitation wavelength.

Both P-100 and P-75 samples can be compared with chemically doped spectra of P(NDI2OD-T2), with the only change of the onset voltage for polaron formation, as reported below in **Table 4.2**. Spectral features of N2200 samples, chemically doped with different percentages as showed in **Chapter 2**, are directly compared to the ones of electrochemically doped P-75 and P-100. We report in **Table 4.2** the voltage range corresponding to Raman spectra with features closely resembling (bands intensity pattern) to the chemical features, observed at the selected doping percentages, e.g. to different molar ratios (MR).

		Electrochemical Doping=	
		P-75	P-100
Chemical doping	MR=0.14	-0.4V	[-0.4V, -0.6V]
	MR=0.42	[-0.5V, -0.6V]	-0.7V
	MR=1.00	[-0.7V, -1V]	[-0.8V, -1V]

Table 4.2.: comparison of Raman features of chemical and electrochemical doping onset voltages.

The differences in the on-set voltage might be due to the swelling and stability of the polymer, as P-100 is less stable than P-75 and tend to swell more, thus degrading faster, affecting ion intercalation in the polymer. It is worth noting that the spectra of the chemically and electrochemically doped polymer show the same spectral changes upon polaron formation, indicating that the assumption made in **Chapter 2** on polaron localization on the NDI unit are also valid in this scenario. Moreover, it further demonstrates that these spectral changes are not related to the polymer-dopant coupling, but to the charge defect created on the polymeric chain, as they are independent from the doping method.

More electrolytes were exploited in this preliminary study, as glucose with either Glucose Oxidase and hydrogen peroxide. The study of these electrolytes on n-type OSCs, working in water environment is a fundamental step toward biological sensing, while many p-type materials are already explored, as reported in the introduction of this chapter.

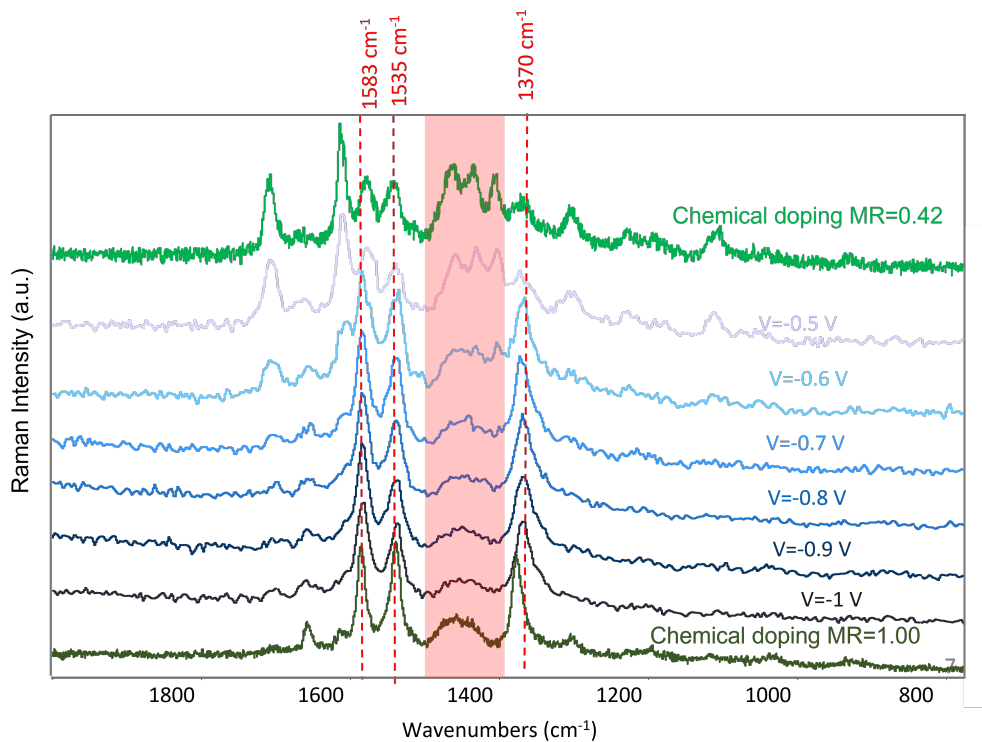


Figure 4.12: comparison between chemical doping at MR=0.43, 1.00 (top and bottom, green spectrum) and electrochemical doping at [-0.5, -1] V voltage (bottom, light blue spectrum), acquired with the 532nm excitation wavelength. Polaronic features are highlighted in red.

The results, described in this section, were acquired using P-100. **Figure 4.13** shows the spectra for P-100 doped with glucose and Gox. As described above, the solution of Gox was added inside the cell and monitored for a couple of minutes, then glucose was added, as showed in the lower right panel of **Figure 4.13**, which represents the monitoring of OCV when glucose is added. A step is visible when the solution is inserted in the cell; then, if the potential remains stable and reaches a plateau, the voltages swept can start. Raman spectra and the spectral difference between the 0V and each voltage are also highlighted. The change of electrolyte does not affect the polaron structure (the spectral features of the polaron are the same as those already observed) but the onset voltages, corresponding to a polaron spectrum with no pristine features, is formed at -0.9V.

The analysis of the CV (upper right panel, acquired up to -0.5V), shows a drop in current intensity before and after the electrochemical doping (change in the areas and shift of the cathodic/anodic peak) meaning that the doping process is irreversible, probably due to degradation and swelling of the polymer upon ion intake. A further confirmation of the degradation of the sample after the cycle of measurements is the detachment of the polymer from the surface, visible by eye after drying the sample. Despite the Raman features remain reversible during one electrochemical cycle, the quality of the film and the CV indicate that this material, under these experimental conditions, cannot uptake many electrochemical cycles.

Evidence of a similar behavior are shown in **Figure 4.14**, for a P-100 sample doped with the blend of glucose and H₂O₂. In this case, the polaronic formation is further delayed, at -1V. The cyclic voltammetry area decreases upon doping, similarly to the previous case. Both glucose electrolytes tend to hinder the formation of the charge defect, slowing the response of NDI-based polymers to the applied voltage.

A less reactive electrolyte, PBS, was also exploited. The spectra and cyclic voltammetry are showed in **Figure 4.15**. As expected, the spectra do not present features of the doping as pronounced as the other experiments. At high voltages applied (-0.9V, -1V), the bands at 1535 and 1360 cm⁻¹ start to arise, but no other polaronic signatures (broadening of the triplet etc.) can be individuated, as expected.

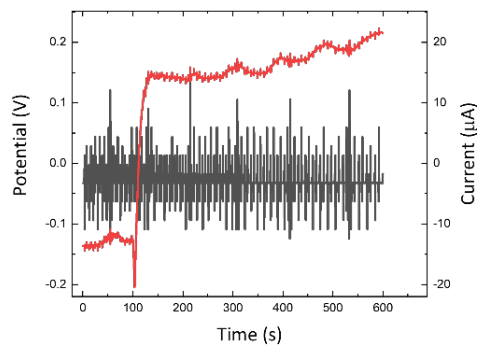
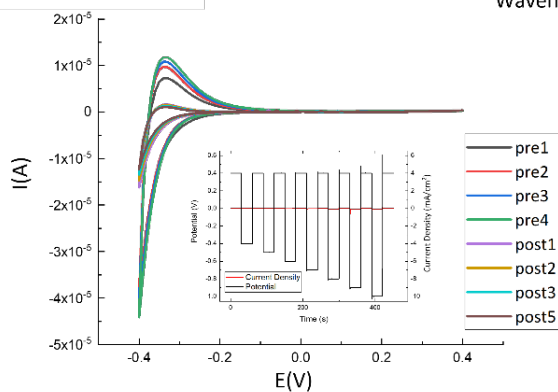
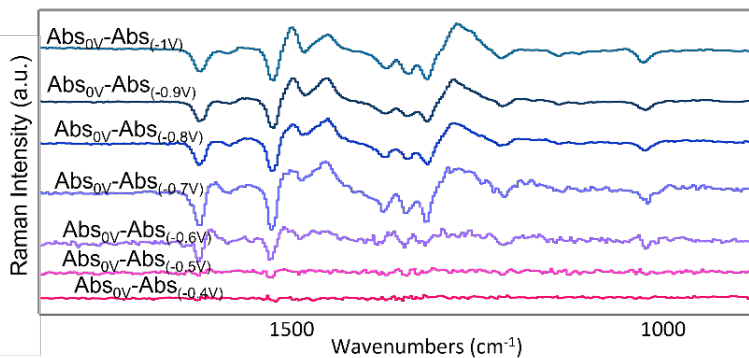
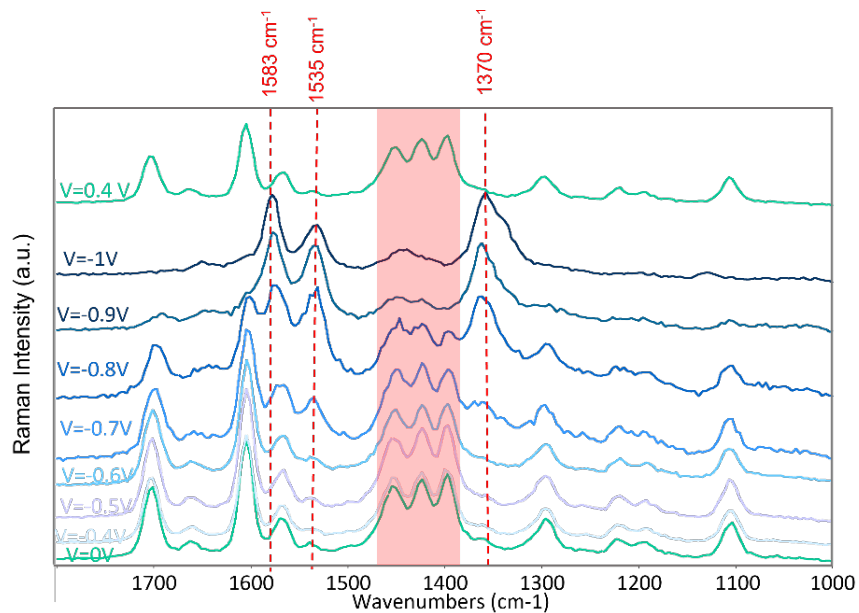


Figure 4.13: P-100 doped with Gox and glucose, in the static cell setup, acquired with the 532nm excitation wavelength. The CV and voltage swept are also reported at the bottom right. Cyclic Voltammetry was performed up to -0.5V. The spectra were acquired from top to bottom;

difference spectra between spectra recorded at different voltages and the spectrum at $V=0$ is also reported. OCV was monitored upon insertion of glucose in the Gox electrolyte and is reported in the bottom left.

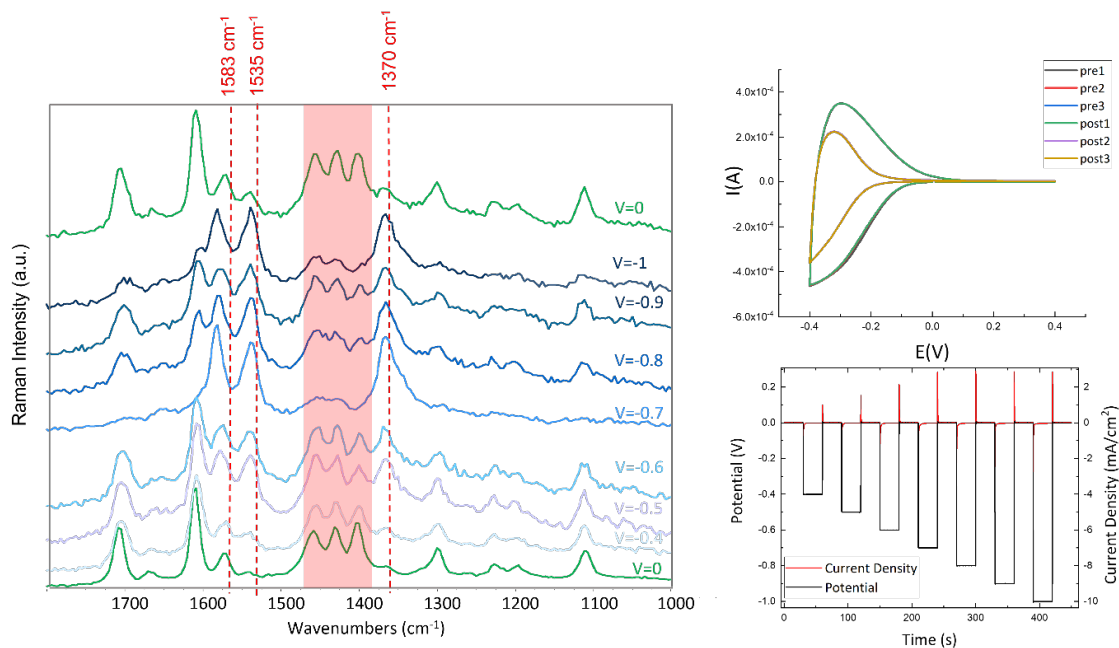


Figure 4.14: P-100 doped with Gox and H_2O_2 , in the static cell setup, acquired with the 532nm excitation wavelength. The CV and voltage swept are also reported on the right. Cyclic Voltammetry was performed up to $-0.5V$. The spectra were acquired from top to bottom. Polaronic features are highlighted in red.

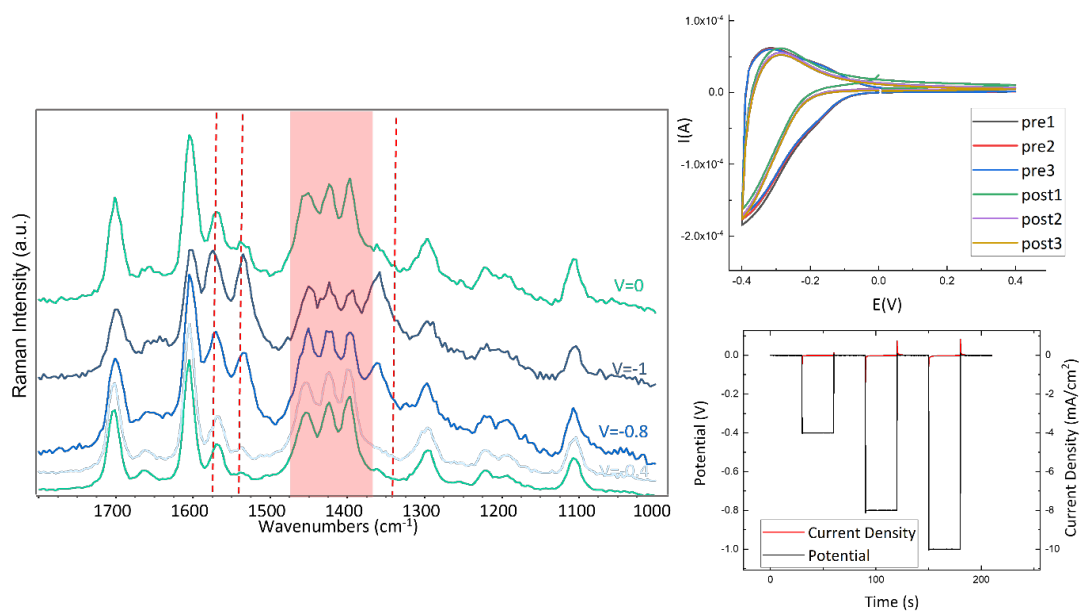


Figure 4.15: P-100 doped with PBS, in the static cell setup, acquired with the 532nm excitation wavelength. The CV and voltage swept are also reported on the right. Cyclic Voltammetry was performed up to -0.5V. The spectra were acquired from top to bottom. Polaronic features are highlighted in red.

The results for 638 nm excitation wavelength are reported in **Figures 4.16, 4.17, 4.18** for NaCl, glucose with Gox and glucose with H_2O_2 . Both Raman and CV data are compatible with the measurements performed at 532nm Raman excitation. The main difference in the Raman data is the absence of the band at 1535 cm^{-1} , which is only present at 532 nm excitation wavelength. This behavior could be explained by resonance effects, which favors the polaron transitions when the 532nm excitation wavelength is applied and the bipolaronic ones with the 638nm. Polaronic and bipolaronic (not visible in this case) band intensities are subjects to variation, modulated by the change of wavelength. From the experimental evidences presented, it seems that the 638nm excitation wavelength is not suitable to show all the polaronic marker bands.

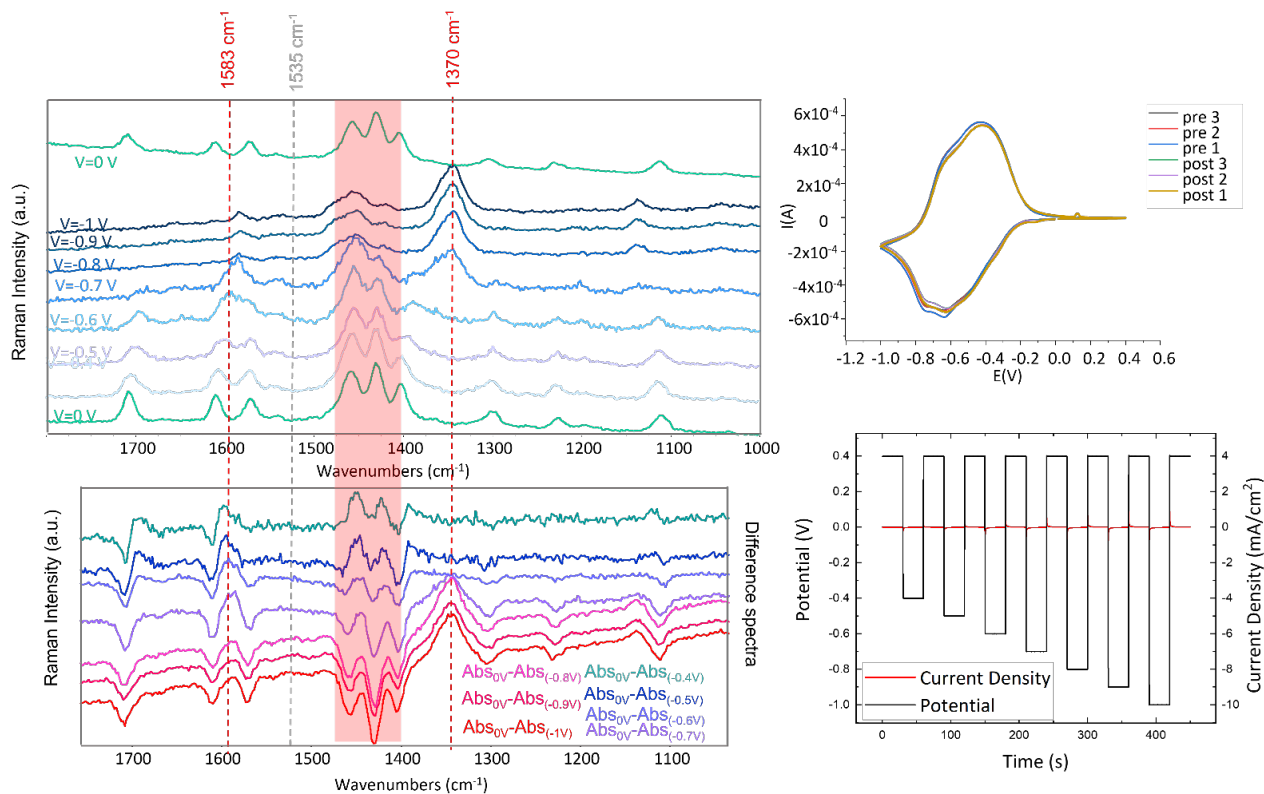


Figure 4.16: P-100 doped with NaCl, in the static cell setup, acquired with the 638nm excitation wavelength. The CV and voltage swept are also reported on the top right. Cyclic Voltammetry was performed up to -0.5V. The spectra were acquired from top to bottom, difference between spectra different voltages and the spectrum at V=0 are also reported. Polaronic features are highlighted in red. The 1535 cm^{-1} polaronic vibrational band, not visible with the 638nm excitation wavelength, is highlighted in grey.

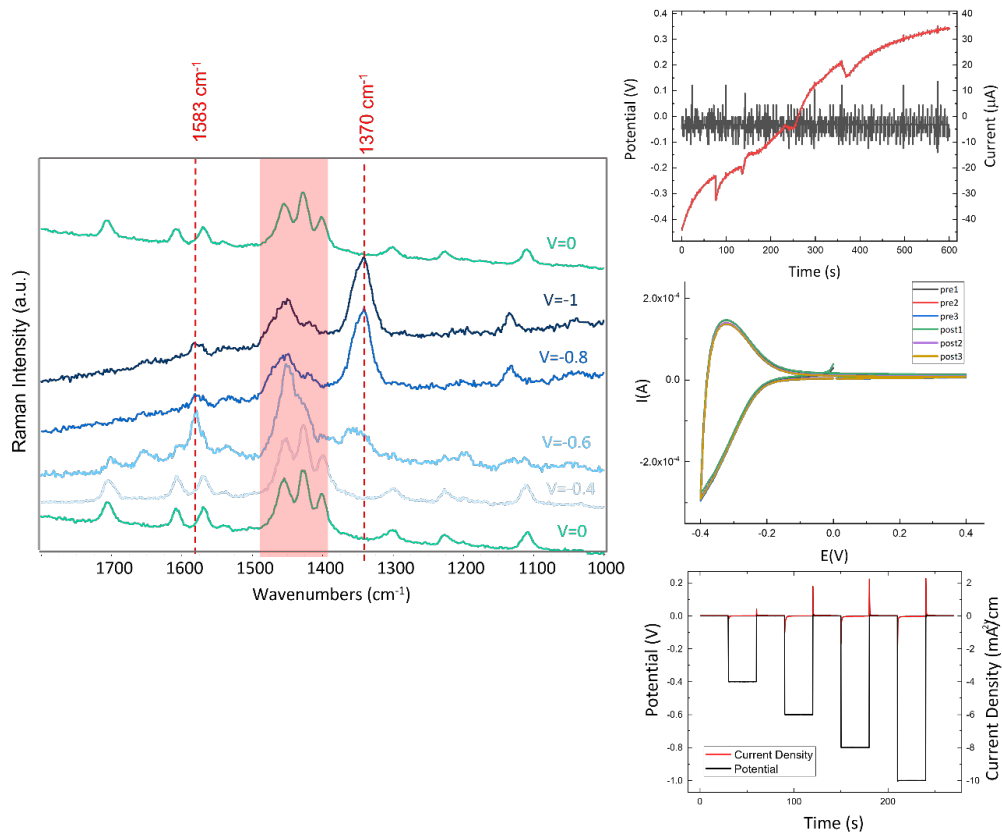


Figure 4.17: P-100 doped with Gox and glucose, in the static cell setup, acquired with the 638nm excitation wavelength. The CV and voltage swept are also reported on the right. Cyclic Voltammetry was performed up to -0.5V. OCV was monitored upon insertion of glucose in the Gox electrolyte and reported in the top right. Polaronic features are highlighted in red.

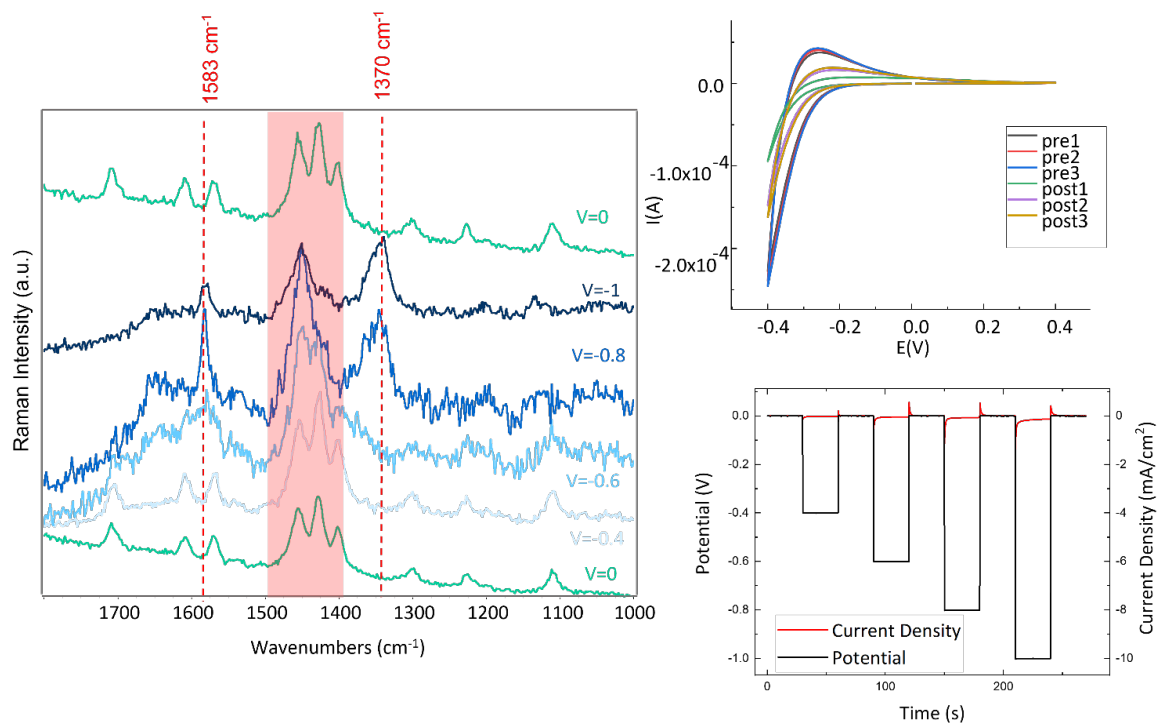


Figure 4.18: P-100 doped with H₂O₂ and glucose, in the static cell setup, acquired with the 638nm excitation wavelength. The CV and voltage swept are also reported on the right. Cyclic Voltammetry was performed up to -0.5V. Polaronic features are highlighted in red

As stated before, the presence of oxygen in the electrolyte hinders the formation of the bipolaron, although polaronic features are still observed. To observe bipolaronic features in the Raman experiments, data acquired with the flow cell are now analyzed.

4.3.2 Flow cell

Two electrolytes with different pH were chosen, namely KCl and KOH (neutral and acidic electrolyte), to exploit possible differences in the behavior of the polaronic and bipolaronic bands of p(gNDI-T2). Nitrogen and oxygen saturated electrolytes were used for the experiments, to study both cases in a controlled environment, and will be showed in this section. At the end of the section, I will provide additional data with a finer voltage swept, to reach a better knowledge of the onset voltages for the polaronic and bipolaronic features.

Figure 4.19 show the Raman series of P-75 immersed in KCl, saturated with nitrogen, acquired with the 532 nm excitation wavelength. The polaronic features can be individuated when a voltage of -0.7V is applied (red dashed lines). When the voltage reaches -1V new changes of the spectrum can be detected in the spectrum, highlighted with green dashed lines, which do not correspond to either the charged polaron vibrational features nor to those of the pristine polymer. In particular, the following changes, which we assign to the bipolaron spectrum should be noted:

- A new band arises at 1446 cm^{-1} , in the middle of the broad feature coming by the triplet of the pristine polymer
- A shoulder can be individuated at 1419 cm^{-1}
- A new band arises at 1344 cm^{-1} , close to the polaronic band at 1370 cm^{-1}
- A new band arises at 1137 cm^{-1}
- Decrease in intensity/disruption of the polaron bands at 1583 and 1535 cm^{-1} is observed

At the bottom of **Figure 4.19**, the voltage swept and images of the surface of the sample were acquired with the Raman optical microscope. The images at -1V does not show an evident degradation of the surface of the sample.

A finer swept of the potential ($\Delta V=0.1V$), **Figure 4.20**, allows understanding the onset potential for polaronic and bipolaronic features. Initial changes in the spectra are visible at -0.4V, which is

a lower voltage than the corresponding onset for the static cell. This behavior could be again ascribed to the presence of oxygen in the latter experiments, partially making the formation of the bipolaron slower. The polaron is completely formed between -0.6V and -0.7V. At -0.7V the bipolaronic features start to be visible, and the bipolaron is completely formed for voltages higher than -0.8V.

UV-Vis spectroelectrochemical data, not showed in this dissertation, acquired by PhD candidate Ana La Fuente Durand (Stanford university, Chueh group), further confirm these data regarding the onset voltages for polaron and bipolaron formation. The spectroelectrochemical features present a peak around 500 nm ascribed to the polaron formation and a secondary peak that arises when the bipolaron is formed around 650 nm.

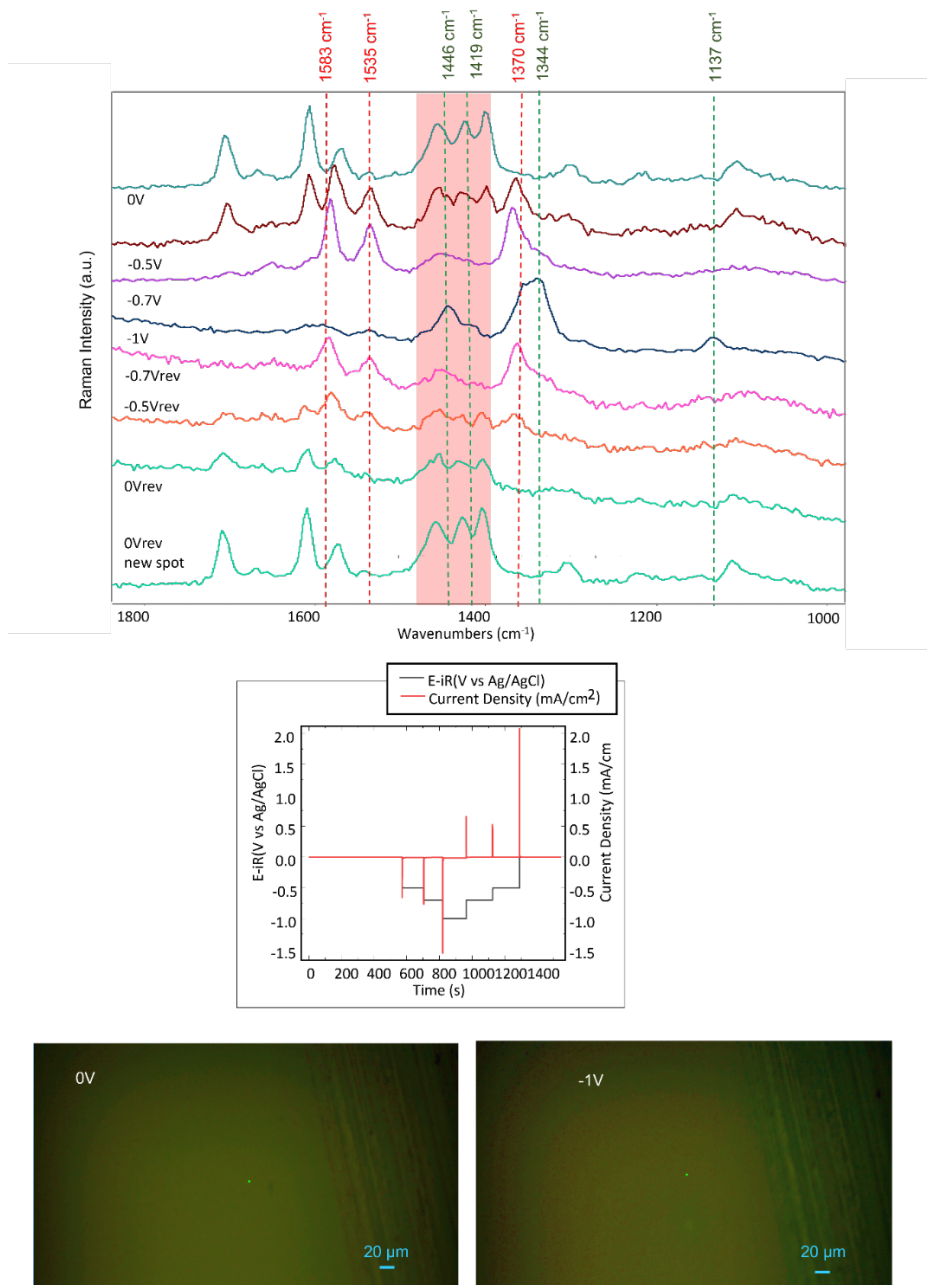


Figure 4.19: P-75 doped with KCl saturated with nitrogen, in the flow cell setup, acquired with the 532nm excitation wavelength. In the middle of the image, the voltage swept and at the bottom images of the sample surface, acquired with the Raman optical microscope at 0V and -1V (bottom

left and right, respectively) are shown. Polaronic features are highlighted in red and bipolaronic features are highlighted in green.

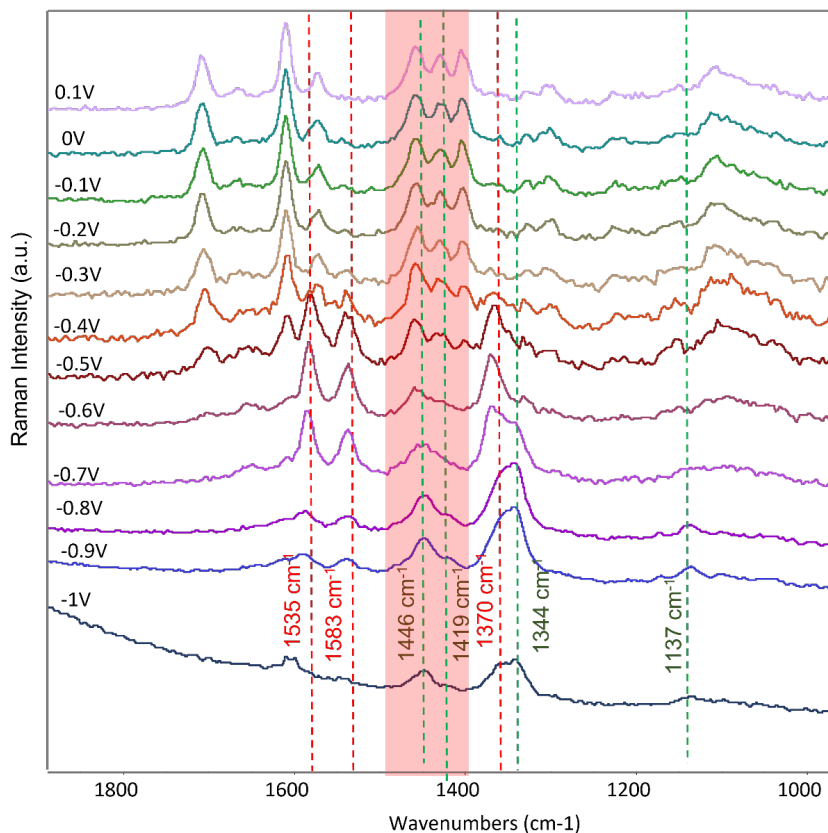


Figure 4.20: P-75 doped with KCl saturated with nitrogen, in the flow cell setup, acquired with the 532nm excitation wavelength. The voltage step between measurements is set at -0.1V. Polaronic features are highlighted in red and bipolaronic features are highlighted in green.

It is interesting to point out the trend of the band of the pristine polymer at 1706 cm^{-1} when the voltage is increased. The band is present until the maximum concentration of polarons is reached, then is not visible anymore. This could mean that the majority of the polymer units contain one (polaron) or 2 (bipolaron) charges, namely that the pristine units ratio to the doped ones is negligible. Moreover, resonance effects with polaron and bipolaron, occurring at 532nm and

638nm excitation wavelengths respectively, could enhance charge defect related features with respect to the pristine ones.

Similar experiments conducted with oxygen saturated KCl are reported in **Figure 4.21**, with 532nm excitation wavelength. Not many changes in the spectral features can be emphasized, except a little modification in intensity ratio for the triplets' bands around 1450 cm^{-1} , as well as a hint of the formation of the signature polaronic band at 1583 and 1360 cm^{-1} at -1V . This indicates that, despite the presence of a considerable amount of oxygen in the electrolyte, the polaron is still forming. This result agrees with the data presented for the static cell and the UV-Vis data acquired in the same experimental conditions.

The CV reported in **Figure 4.21** is highly affected by the presence of oxygen both before and after the voltage swept. The shape of the cyclic voltammetry, highly asymmetrical, indicates that the reaction is irreversible. When compared to data acquired with the static cell, in a neutral electrolyte (namely NaCl), the area of the CV is quite smaller, indicating that the solution contains higher oxygen quantities. This explanation could also be valid for the higher voltage onset with respect to the static cell case and the "incomplete" polaronic spectral features showed in the flow cell experiments, as if the polaron formation and the oxygen presence were inversely correlated.

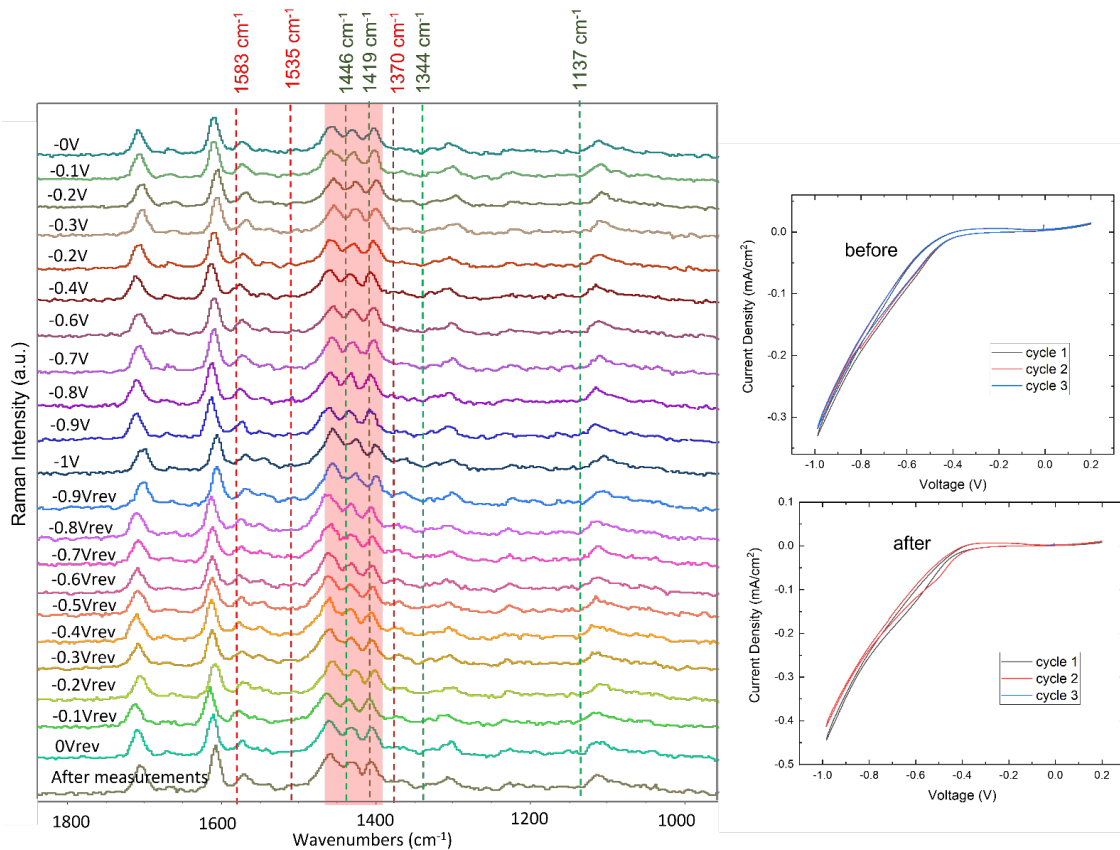


Figure 4.21: P-75 doped with KCl saturated with oxygen, in the flow cell setup, acquired with the 532nm excitation wavelength. The voltage step between measurements is set at -0.1V. The sets of cyclic voltammetry acquired before and after the electrochemical doping are reported on the right. Polaronic features are highlighted in red and bipolaronic features are highlighted in green.

The same series of experiments was conducted using KOH as electrolyte. **Figure 4.22** shows the results for a P-75 sample electrochemically doped up to -1V, acquired at 532 nm excitation wavelength. The polaron and bipolaron vibrational features correspond to the ones of P-75 doped with KCl, and the doping and dedoping process is reversible (CV features). The voltammogram before the measurements was taken up to -0.5V, whereas the one after the voltage swept up to -1V, to have a broader characterization of the cyclic voltammetry and the two reduction peaks.

The cyclic voltammetry indicates that the reaction is overall reversible, despite a little asymmetry in the CV features, that could be a sign of degradation due to the more acidic nature of the electrolyte, with respect to more neutral counterparts (KCl/NaCl, see CV in **Figure 4.22**) Images acquired with the Raman optical microscope are also reported, at 0V and -1V. The image at -1V presents many bubbles, which were not visible in the NaCl images, a further confirmation that KOH affects the quality of the film.

Figure 4.23 reports the data acquired in a KOH oxygen saturated electrolyte. The data are compatible with the KCl ones, as minor changes occur in the spectral features and the 1583 and 1360 cm^{-1} polaronic features are only present when higher voltages are reached (namely -1V).

In conclusion, when oxygen is present, polaronic features usually appeared at higher voltages than in nitrogen saturated experiments; moreover, bipolaronic features are not observed.

A finer voltage swept (**Figure 4.24**), with steps of $\Delta V = -0.1\text{V}$, was carried out to understand the voltages onsets for polaron and bipolaron for KOH saturated with Nitrogen. At voltages -0.4V and -0.5V, 1535 and 1360 cm^{-1} vibrational bands start to arise, and the spectral features are in a hybrid situation between polaronic and pristine regime. At -0.6 and -0.7V, the polaron is completely formed, and all its vibrational characteristics are present, whereas bipolaronic features are noted for higher voltages (red arrows). The onset voltage for charge transfer is similar to the KCl case, confirmed by UV-Vis data. The material is very stable and reversible, as confirmed by both the cyclic voltammetries acquired before and after the voltage swept (**Figure 4.24**, upper right corner) and the reversed voltages data conducted in the same experiment.

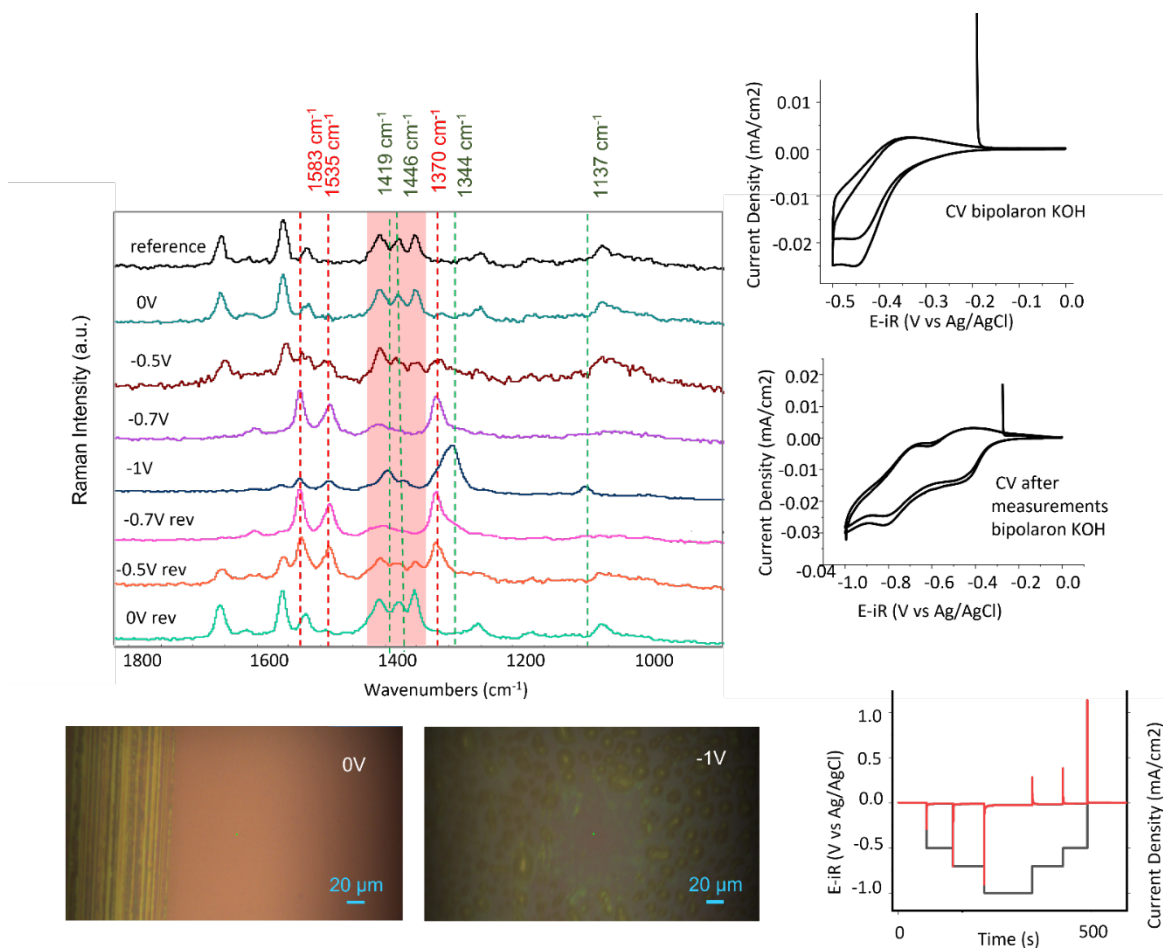


Figure 4.22: P-75 doped with KOH saturated with nitrogen, in the flow cell setup, acquired with the 532nm excitation wavelength. The cyclic voltammetry acquired before and after the voltage swept is reported on the right of the image. At the bottom images of the sample surface, acquired with the Raman optical microscope at 0V and -1V (bottom left and right, respectively) are shown. Polaronic features are highlighted in red and bipolaronic features are highlighted in green.

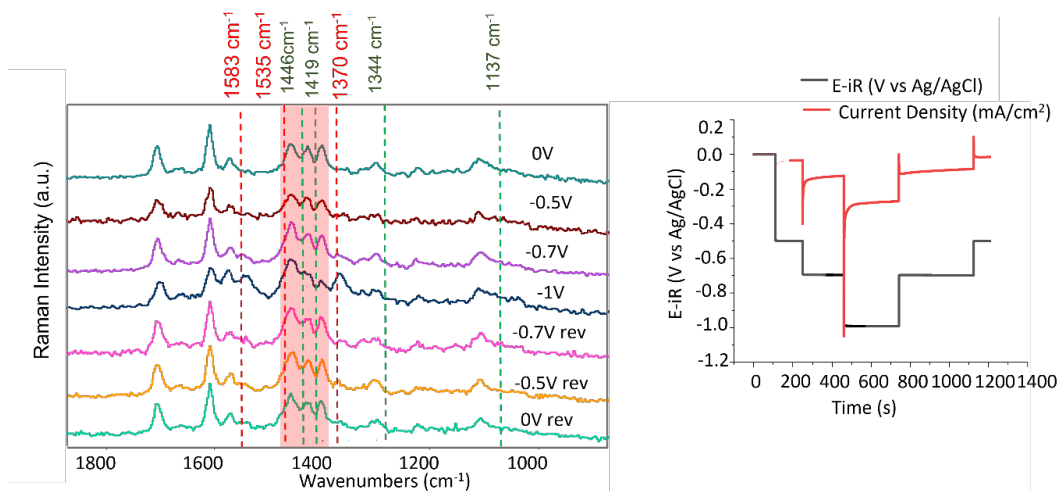


Figure 4.23: P-75 doped with KOH saturated with oxygen, in the flow cell setup, acquired with the 532nm excitation wavelength. The voltage swept is reported on the right. Polaronic features are highlighted in red and bipolaronic features are highlighted in green.

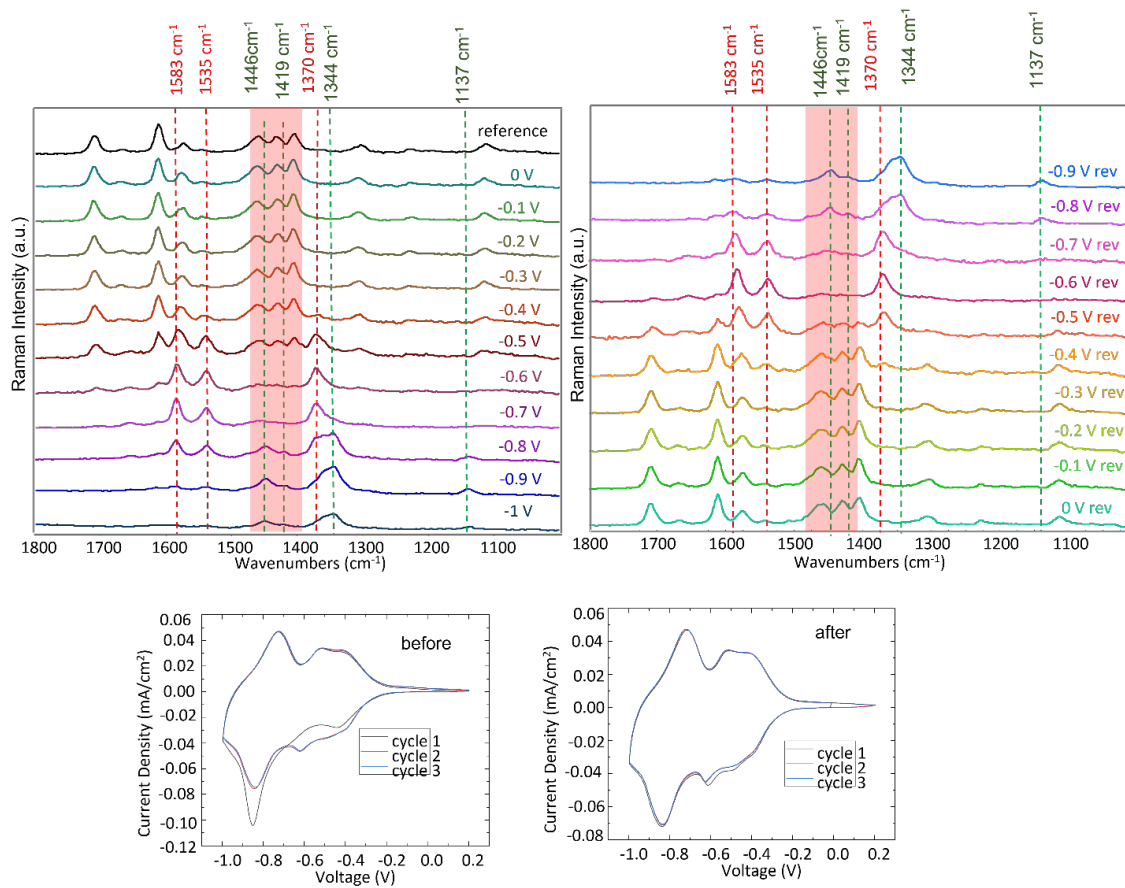


Figure 4.24: P-75 doped with KOH saturated with nitrogen, in the flow cell setup, acquired with the 532nm excitation wavelength. Spectra corresponding to voltage swept from 0V to -1V are reported on the left, the ones corresponding to -1V to back to 0V (reverse cycle) on the right. Polaronic features are highlighted in red and bipolaronic features are highlighted in green. The voltage swept is reported at the bottom of the figure, before and after the electrochemical experiments.

Resonant Raman experiments were conducted for experiments with KOH, to highlight possible changes in the bipolaronic features, as the 638 nm excitation wavelength is in resonance with the bipolaron electronic transition. The results for 638 nm are showed in **Figure 4.25**. The spectra of electrochemically doped samples with KOH saturated with nitrogen are reported in panel a. The first notable difference from experiments recorded with 532nm excitation is steep change of the background line, possibly ascribed to some fluorescence, due to the resonance with the bipolaron transition.

The main vibrational bipolaronic features observed at 638 nm excitation are the same observed in the experiments at 532 nm, namely:

1. A shoulder at 1448 cm^{-1} , and new bands at 1420 cm^{-1} , 1343 cm^{-1} and 1139 cm^{-1} are observed.
2. The polaron bands at 1582 and 1535 cm^{-1} loose intensity
3. The triplet characteristic of the pristine polymer further broadens, shifting its “center” of about 10 cm^{-1} toward higher wavenumbers.

In panel b the oxygen saturated measurement is reported, where no changes in the vibrational spectra can be highlighted.

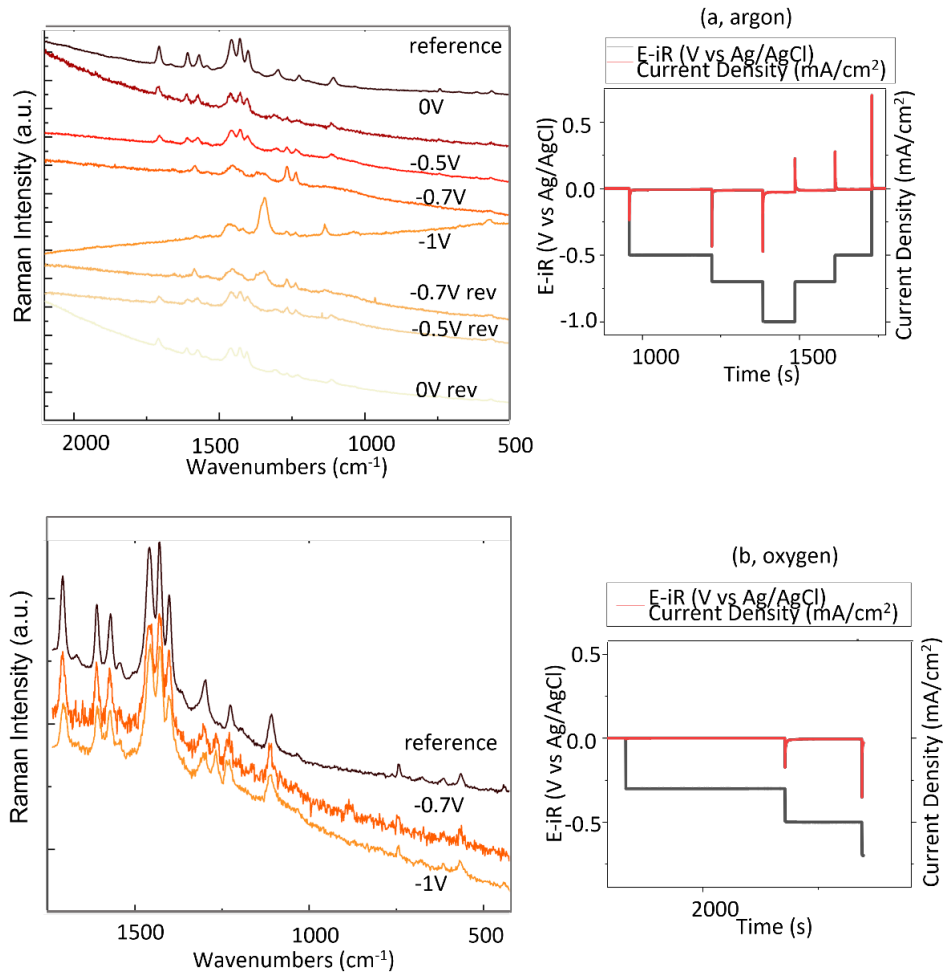


Figure 4.25: (a) P-75 doped with KOH saturated with nitrogen, in the flow cell setup, acquired with the 638nm excitation wavelength. On the right the voltage swept is reported, (b) P-75 doped with KOH saturated with oxygen, in the flow cell setup, acquired with the 638nm excitation wavelength. On the right the voltage swept is reported.

Finally, **Figure 4.26** directly compares the bipolaronic spectra, acquired at -1V in KOH, for 532 (resonant with the polaron absorbance) and 638 nm (resonant with the bipolaron absorbance) excitation wavelength.

The spectra are normalized on the band peaking at 1370 cm^{-1} which intensity is due both to the polaronic vibrational feature and to a contribution by bipolaron (shoulder at 1344 cm^{-1}). A few differences between the spectra can be individuated. The polaronic vibrational modes at 1583 and 1535 cm^{-1} give strong Raman lines in the spectrum acquired at 532 nm and weaken in the spectrum recorded at 638 nm excitation. This is a confirmation that the 638 nm is no more in resonance with the polaron electronic absorption, but with a bipolaron transition. Because of the normalization adopted, the polaronic 1370 and the 1344 cm^{-1} bipolaronic bands seem to be unaffected by the different excitation energy, but changes can be individuated in the shape broadened triplet; moreover the 1137 cm^{-1} transition, assigned to the bipolaron defects is more pronounced in the spectrum recorded with excitation in the red. Two new features assigned to the bipolaron, namely the bands at 1419 and 1446 cm^{-1} are present in both spectra, as described above, with some differences. The 1446 cm^{-1} transition is more clearly detectable for the spectrum with excitation wavelength of 532 nm, probably because of the different shape of the broadened triplet in this region in the two spectra.

For a better comparison of the spectral features and highlighting the effect of the experimental conditions on polaron and bipolaron formation, spectra at 0V, -0.5V, -0.7V and -1V are compared in **Figures 4.27** and **4.28**. Experiments with nitrogen and oxygen saturated electrolyte are showed, acquired with 532 and 638 nm excitation wavelength.

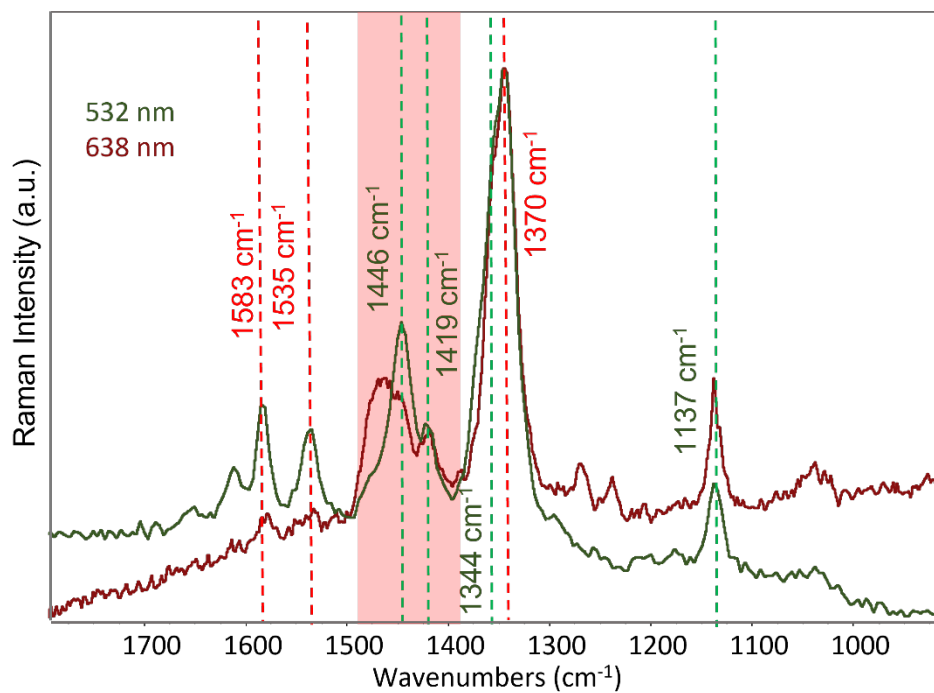


Figure 4.26: comparison of the P-75 electrochemically doped spectra acquired at -1V, with nitrogen saturated KOH, using 532 and 638 nm excitation wavelength. The figure provides a direct comparison of the polaronic and bipolaronic features in different resonance conditions.

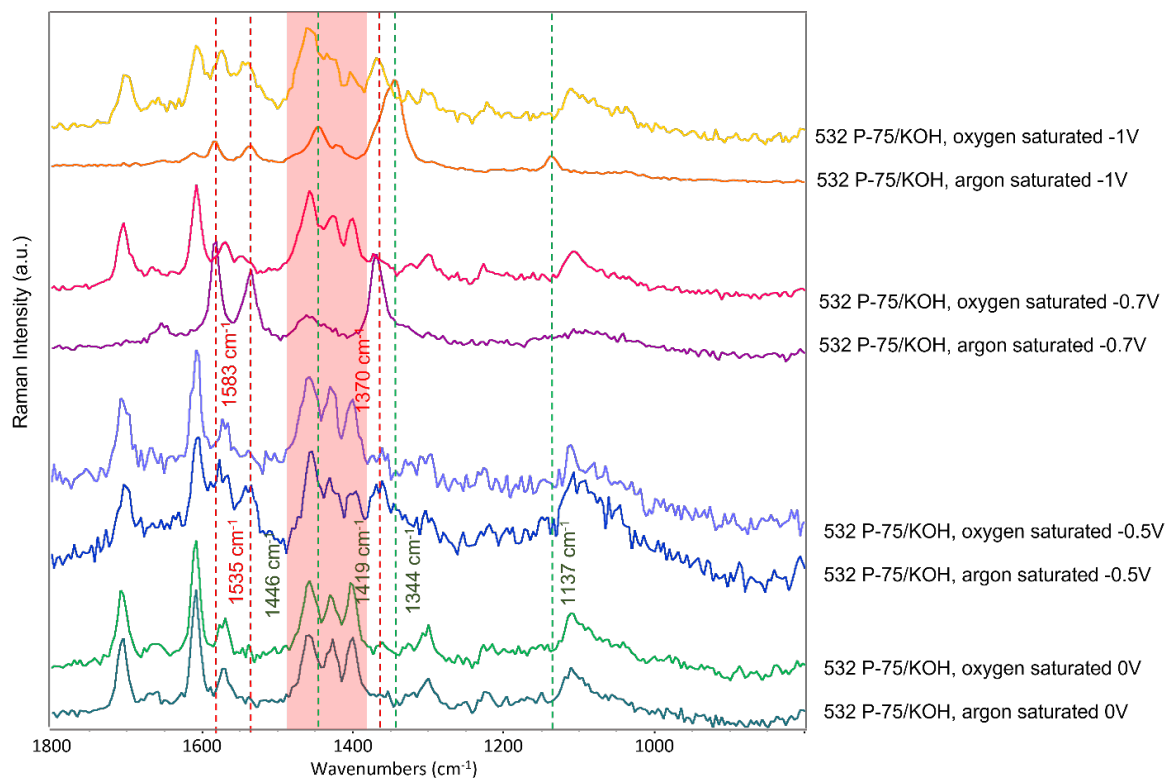


Figure 4.27: comparison of the P-75 electrochemically doped spectra acquired, from bottom to top, at 0, -0.5, -0.7 and -1V, with nitrogen and oxygen saturated KOH, using the 532 nm excitation wavelength. Polaronic and bipolaronic features are highlighted in red and green, respectively.

It is worth noting that the spectra acquired at 532nm, -1V in the oxygen saturated environment present similar spectral features to the one acquired at -0.5V, in the nitrogen saturated electrolyte. Polaronic features are present, together with pristine polymer features, showing that the polarons are forming, but the voltage or the experimental conditions do not allow reaching the maximum concentration. Moreover, in the set of spectra recorded with 638nm excitation in presence of oxygen, the polaronic features are not present even at -1V. This difference could be within the normal fluctuation of voltage for polaron formation, further confirming the results of the 532nm series. On the other hand, this behavior could be ascribed to the resonance for the

polaron features at 532nm, which is not effective when 638nm excitation wavelength is adopted, thus explaining the weakening of the polaronic marker bands.

Moreover, the hydrogen peroxide strong peak at 880 cm^{-1} is not visible in any of the electrochemically doped Raman series, whereas hydrogen peroxide formation is confirmed by CV data. From the experimental evidence collected so far, it seems that hydrogen peroxide degrades the polymer and hinders charge defects formation, although it does not directly adsorbate on the polymer surface nor intercalates. Although these findings are an interesting starting point, more studies are needed to confirm these hypotheses.

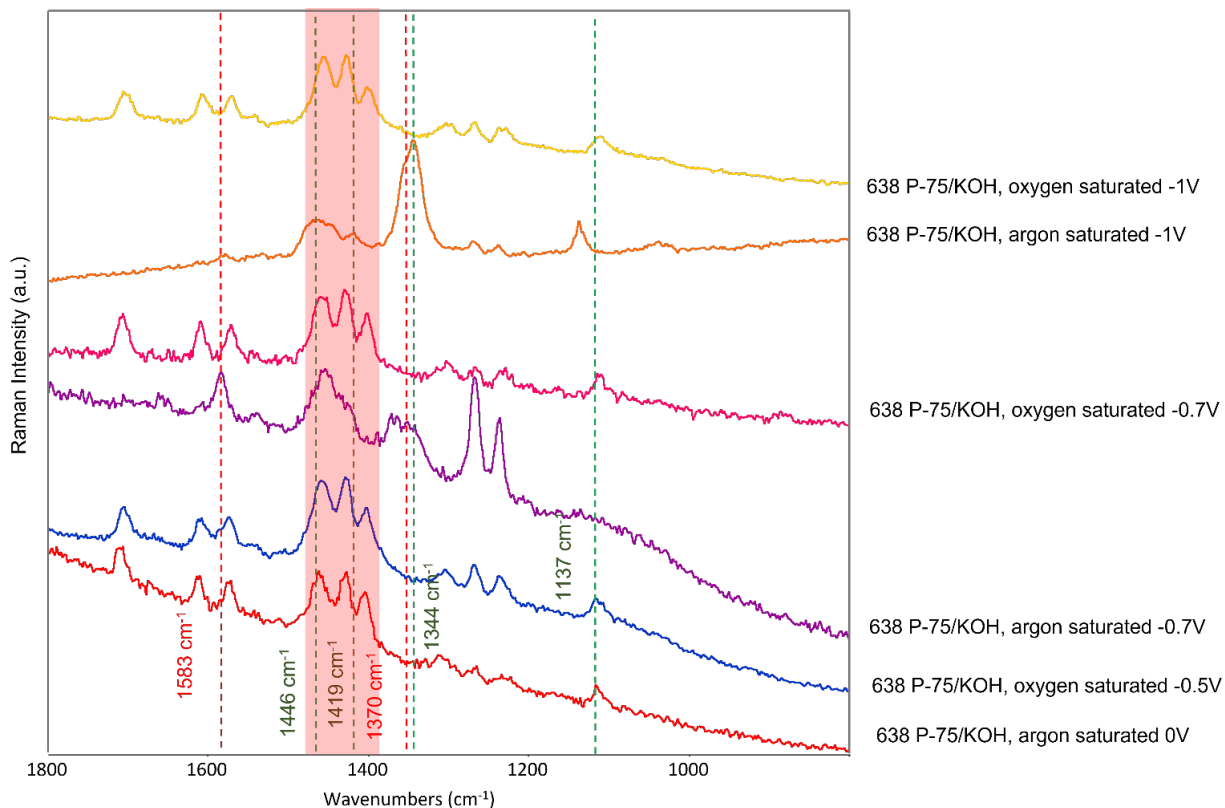


Figure 4.28: comparison of the P-75 electrochemically doped spectra acquired, from bottom to top, at 0, -0.5, -0.7 and -1V, with nitrogen and oxygen saturated KOH, using the 532 nm excitation wavelength. Polaronic and bipolaronic features are highlighted in red and green, respectively.

4.4 Conclusions and future developments

In this chapter, signature Raman bands ascribed to the polaron and bipolaron are individuated through in situ measurements. The measurements were performed under different experimental conditions, using different electrolytes. Regardless of the electrolyte composition and acidity, similar vibrational features are individuated, with slight changes in the voltage onset. The main differences are highlighted by saturating the electrolyte with an inert gas or oxygen. The Raman data show that oxygen hinders the formation of the bipolaron even at high voltages applied. This is probably due to side reaction happening in the electrolyte, such as the formation of hydrogen peroxide. A direct comparison with the chemically doped N2200 spectra, showed in **Chapter 2**, confirms that the bipolaron formation does not take place in this case. In the last case, this could be due to several factors, such as the segregation of the dopant at high doping levels in the chemically doped samples. Differently, electrochemical doping can give rise to bipolarons formation and Raman measurements in resonance with the bipolaron absorption, show changes in the vibrational bipolaronic features.

So far, the analysis of the Raman features ascribed to polarons and bipolarons has been done by means of empirical correlations of the spectroscopic data collected, while Quantum Chemical modelling is required for a detailed vibrational assignment of the polaronic/bipolaronic Raman peaks and for the rationalization of their modulation with the excitation wavelength. It is worth noting that the polaronic Raman bands are independent from the doping method, namely the marker bands are the same for chemical and electrochemical doping and they do not depend on the chemical dopant species nor on the ions involved in the electrochemical process. For the above reasons, we can confidently correlate doping induced Raman bands the formation of charged defects on the polymer chain, characterized by their peculiar vibrational features. Moreover, P-75 and P-90, both considered at the beginning of this study, report similar polaronic features, whereas the main difference in their behavior can be imputed to the swelling of the materials during electrochemical doping.

Further progress on the study of electrochemically doped n-type polymers includes a better understanding of their stability, swelling, ion transportation and other properties, but also an

additional development of the design of the flow in-situ Raman cell. As showed in **Figure 4.29**, we encountered some issues in the nitrogen saturated measurements, due to the presence of oxygen bubbles in the cell. The Cyclic voltammetry in the bottom left of the figure, as well as the absence of polaronic Raman features at high voltages (Raman data on the left side), clearly show the presence of oxygen inside the cell. After the bubble was cleared, we performed the swipe back of the voltage. Both the Raman measurements and the CV performed at the end of the experiments confirmed that the environment was oxygen free.

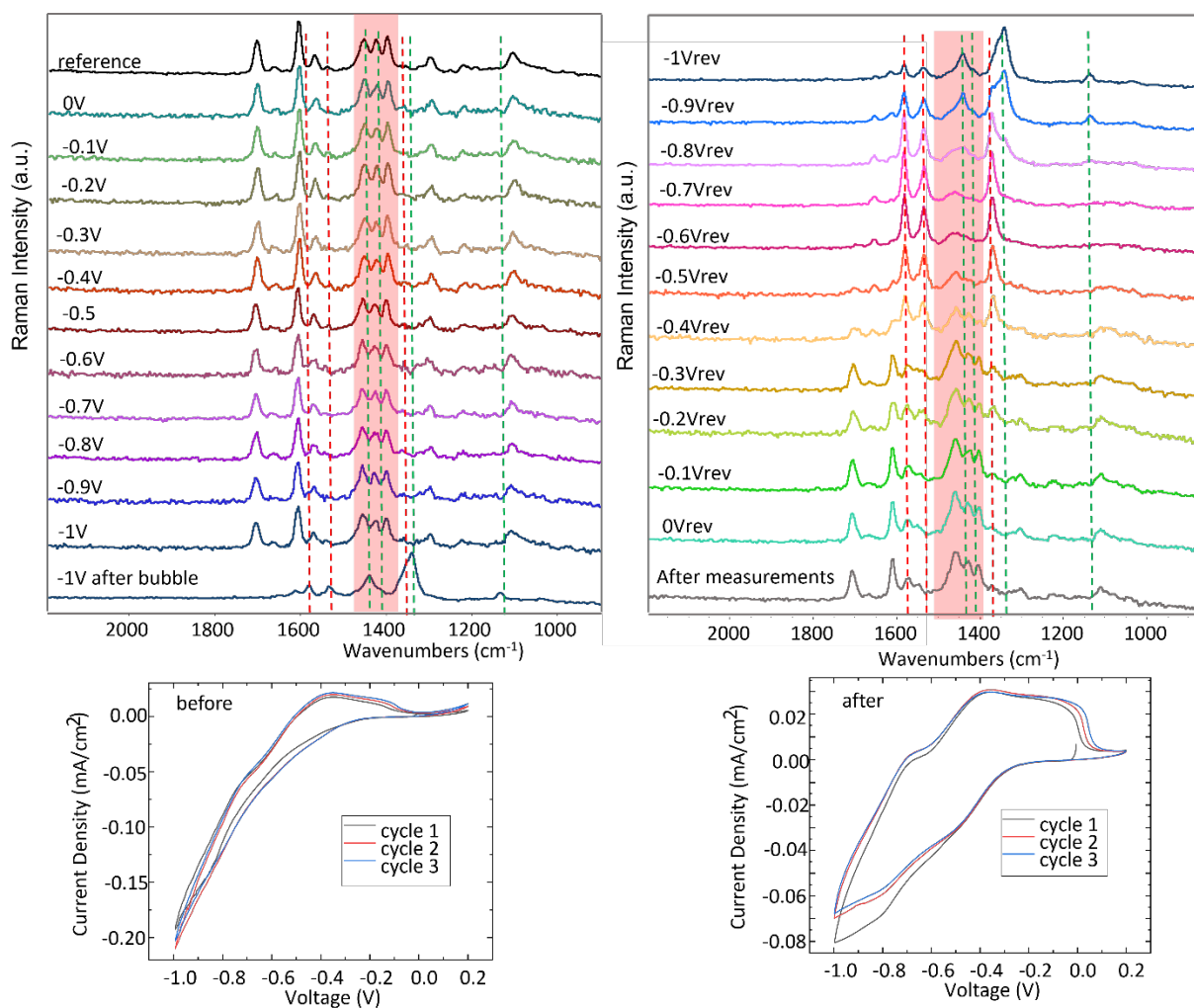


Figure 4.29 P-75 doped with KOH saturated with nitrogen, in the flow cell setup, acquired with the 532nm excitation wavelength, when an oxygen bubble was present in the setup. On the left

spectra on when the voltage swept is applied are presented, on the right the spectra when the voltage was reversed. At the bottom CV during and after the presence of the oxygen bubble are reported.

Chapter 5: A combined use of EC-AFM and Raman spectroscopy: HOPG modifications and porphyrin crystals dissolution in acid environment

In this chapter I present an innovative combination of techniques to perform in-situ characterization of materials. The combination of electrochemical scanning probe microscopy and Raman spectroscopy allows performing a comprehensive study of organic compounds, taking into consideration the morphological as well as molecular changes during electrochemical processes. An explanation of the techniques, proof of concept measurements and future development is presented in this chapter.

5.1 Introduction

The study of the redox reactions affecting a material when subjected to electrochemical cycles is used for a wide range of technologies, from batteries to the food industry, fuel cells, electrochemical reactors and so on⁸⁹⁻⁹³. An essential aspect of these reactions is their property to be reversible under certain experimental conditions, constituting an asset in recycling processes, especially when organic materials are involved. A comprehensive in-situ study of these reactions is essential in understanding their kinetics and propose structure-property relationships for the materials undergoing these treatments. A very powerful technique to understand how the electrochemical reactions affect the morphology of the surface of the studied samples is Electrochemical Atomic Force Microscopy (EC-AFM)⁹⁴⁻⁹⁷. Many surfaces can be studied while undergoing an electrochemical treatment and high-resolution images of the surface changing can be acquired, at the nanometer length scale. The invention of Atomic Force Microscopy (AFM) by Binnig, Quate and Gerber in 1986⁹⁸ has allowed the investigation of both conductive and

insulating samples. Depending on the type of substrate, resolution and desired information, many parameters can be changed to acquire images, as the tip type and material or the scanning mode. Images can easily be acquired in air, vacuum, and liquid. In this dissertation, I will focus on the Electrochemical AFM, working in liquid environment, aiming at studying the liquid-solid interface of samples during spontaneous or electrochemical reactions.

Farrington's group was the first to perform AFM measurements inside an electrochemical cell in 1993 studying the morphological evolution of graphite and copper used as working electrodes in a chloride-based electrolyte, during electrochemical dissolution and deposition of copper⁹⁷.

One very interesting system to study with EC-AFM is the detriment of carbon electrodes in acidic environment⁹⁹. Carbon electrodes, as graphite, pyrolytic graphite, highly oriented pyrolytic graphite (HOPG), glassy carbon, carbon foam, graphene, buckypaper, play a major role in energy storage and conversion research^{95,100}, as well as numerous other fields thanks to their outstanding properties^{97,101,102}, as their easy tunability and functionalization, mechanical properties and more.

At SoLINano laboratory, situated at Politecnico di Milano, we recently used EC-AFM to test the quality of many electrodes as well as their properties when working in contact with an acid electrolyte. The results of this study were compared to the performance of HOPG, as one of the most studied and used form of carbon in electrochemistry for EC-SPM¹⁰³ (see **Attachment C**). Polycrystalline HOPG consists of a polycrystalline material composed of graphite monocrystals. The latter consist of graphite grains of different sizes, with different orientation. The degree of orientation among crystals, and consequently the HOPG quality, is controlled through the mosaic spread parameter. Its layered structure results in an easy exfoliation of the material in the direction perpendicular to the basal planes. Because it is easy to peel the surface and obtain a clean, atomic-flat surface, HOPG represents an excellent candidate for AFM imaging. However, the HOPG stratified structure causes ions from the electrolytes to intercalate between the graphite layers. The presence of water inside the graphite layers leads to the formation of gasses (CO, CO₂ and O₂), which are responsible to the swelling of the HOPG surface (blister formation)¹⁰⁴. Murray et al.¹⁰⁵ proposed the first model to explain blisters formation in the HOPG layers, composed of 3 steps. This model explains the main mechanism to form blisters, which were

considered an indication of anion intercalation, but it leaves a few questions open, as the kinetics and conditions of blister formation. A work by Bussetti et al.¹⁰⁶ revealed how the Cyclic Voltammetry speed can hinder blisters formation, despite leaving the characteristic features of intercalation in the Cyclic Voltammetry intact. This result led to a follow up work attempting to understand if the CV speed could suppress the intercalation itself¹⁰⁷, in which X-ray photoemission spectroscopy (XPS) analysis was performed on the samples to further analyze the composition of the HOPG surface after the immersion in acidic electrolytes and subjected to CV. We performed experiments using both a standard CV speed (25mV/s), where we observed blister formation as expected, and a higher one (600 mV/s), where no blisters were observed. Samples undergoing the same electrochemical treatments show no changes in the XPS patterns. The XPS experimental evidences, together with the CV results, proved that anion intercalation still occurs varying the electrochemical scanning parameters, as velocity and pH of the acid solution, and it is not directly related to morphological changes on the samples (blister formation). This result is not only interesting to understand the kinetics of blister formation, but also to point out the degradation effects on exposed electrode surface (see **Attachment D**).

Despite EC-AFM being a remarkable asset in surface characterization, it does not provide information on what happens at the molecular scale. As proven in the previous chapter, Raman spectroscopy allows to characterize the composition and structural changes of a material, following the evolution of the vibrational spectrum at the liquid-solid interface. This non-invasive technique can be coupled with EC-AFM to study the behavior of organic materials in various electrolytes, from acid solutions to water, making it suitable for a large variety of samples, including biological tissue¹⁰⁸.

In 2016, Castiglioni et. al¹⁰⁹ presented a comprehensive study of the effect of phosphoric acid solution on HOPG comparing EC-AFM data with ex-situ Raman spectra acquired at different excitation wavelengths. This preliminary work highlighted the presence of a surface layer of highly disordered graphitic phase after electrochemical experiments.

Another interesting work by Duo' et al¹¹⁰ combines EC-AFM with in-situ Raman to observe an intermediate phase in HOPG undergoing acidic EC treatments, described as incipient

intercalation, below the potential at which graphite intercalation occurs. This result is described as the creation of a charge transfer complexes between anions and HOPG layers.

Prevention of graphite oxidation during electrochemical processes in acid electrolytes is a fundamental step to prevent electrodes damage. One way to achieve this goal is through deposition, on top of the electrode itself, of an organic molecule layer, which should be both water and acid resistant. A suitable species for this role is the porphyrin molecule, thanks to the tunability of its chemical properties by changing its functionalization¹¹¹.

Through the combination of ex-situ Raman, EC-AFM and other techniques we studied the mechanism of crystal dissolution in porphyrins. In particular, we analyzed the phenomenon of the spontaneous dissolution of porphyrin crystals in acid solutions: this study does not exploit the application of CV cycles but make use of the EC-AFM cell to perform AFM analysis in liquid. The porphyrins crystals are deposited on HOPG: when an acid is added on the substrate, crystal dissolution could occur, depending upon the functionalization and concentration of the porphyrin. The dissolution mechanism as a function of pH and solvent has already been extensively studied and modeled in literature on a multi-scale¹¹²⁻¹¹⁴, through various techniques.¹¹⁵⁻¹²³ According to these models, dissolution of crystals happens near a terrace or a crystal defect, forming etch-pits, when certain experimental conditions occurs (i.e. solvent undersaturation). The so-called etch-pits are depressions caused by preferential etching in small areas, whose shape and sizes could be related to the intrinsic properties of the crystal¹²⁴. By extensively studying the behavior of H2TPP deposited on HOPG in a diluted acidic solution, we tried to understand the dissolution phenomenon at the nanoscale, giving an insight into the formation of crystal pits. For this work, we opted to perform the Raman experiments ex-situ, as the in-situ apparatus was not available yet in the laboratory. To combine the techniques, a reference Raman “pristine” spectrum of the film and the porphyrin powder were acquired. EC-AFM experiments were performed in-situ, then dried samples after the electrochemical and AFM scanning were analyzed at the Raman spectrometer. The main rationale for these experiments was to validate the interest in combining the techniques to study these samples.

5.2 Experimental methods

5.2.1 Sample preparation

Porphyrins layers were deposited on a z-grade Highly Oriented Pyrolytic Graphite (HOPG) purchased by Optigraph (0.2cm²). The substrate surface was exfoliated before each measurements using an adhesive tape. Sulfuric acid (H₂SO₄, 1M, de-aerated in argon) was used as solution. H₂TPP films are grown by physical vapor deposition (PVD, layer-plus-island growth mode) with a growth rate of 0.4–0.5 Å/s. The thickness of the film is calculated from the time-integrated molecular flux, and it is calculated to be approximately 20 nominal layers.

5.2.2 EC-AFM measurements

The apparatus used for the measurements consists of an Atomic Force Microscope (AFM) integrated with a 3-electrode cell, represented in **Figure 5.1**.

The material used to build the cell needs to be resistant to acid environment, without any affect to the mechanical stability of the cell, and preferably being low-cost. For these reasons, polytetrafluoroethylene (PTFE) is generally the preferred choice. The sample acts the working electrode (WE) in this setup, the reference electrode (RE) is usually made of AgCl or Platinum and the counter auxiliary electrode (CE) of platinum. The electrolyte is inserted on the sample from the top of the setup, inside the electrochemical cell. The AFM works as passive elements in this setup, as it is not biased but simply monitors the changes occurring on the surface.

The bias is directly applied to the sample by a potentiostat, which is able to perform cyclic (CV) or pulse voltammetry (NVP). These electrochemical techniques, in particular the CV, are discussed in **Chapter 4**. The electrolyte needs to be chosen carefully, as it need to be optically transparent allowing the laser to reach the AFM tip and register its deflection, without affecting the reading on the photodiode. The right opacity is usually reached using diluted solutions.

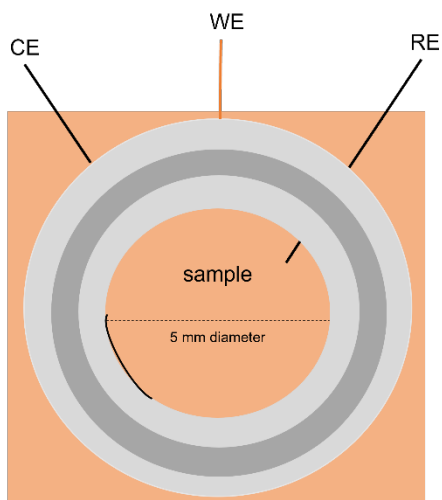


Figure 5.1: Schematic representation of the three-electrode electrochemical cell used to acquire in-situ AFM images. The sample is positioned under the cell and acts as WE.

The EC-AFM apparatus is a Keysight 5500, with a reference and counter electrodes both made of a 0.25 mm Platinum wire. A Viton O-ring is placed between the cell and the sample, to avoid any leakage of the electrolyte. The cell nominal capacity is about 1 ml.

The sample mounted on the electrochemical cell is then clipped onto the main sample holder of the apparatus, as shown in **Figure 5.2**.

A very important precaution in choosing the right (diluted) acid solution needs to be addressed to the AFM scanner and cantilever, which might be ruined by acid solutions. For this reason, the scanner needs to be protected.

The images were collected using the non-contact acquisition mode with specific tips for tapping measurements (NanoandMore, Poinprobe plus, silicon tip coated with Al on detector side). The resonance frequency of the tip was recorded at 130kHz in liquid. The largest scan area for these measurements was of $(6 \times 6) \mu\text{m}^2$ and images were acquired with a frequency of about 1 mHz, as the low scan rate to avoid damaging of the porphyrin crystals.

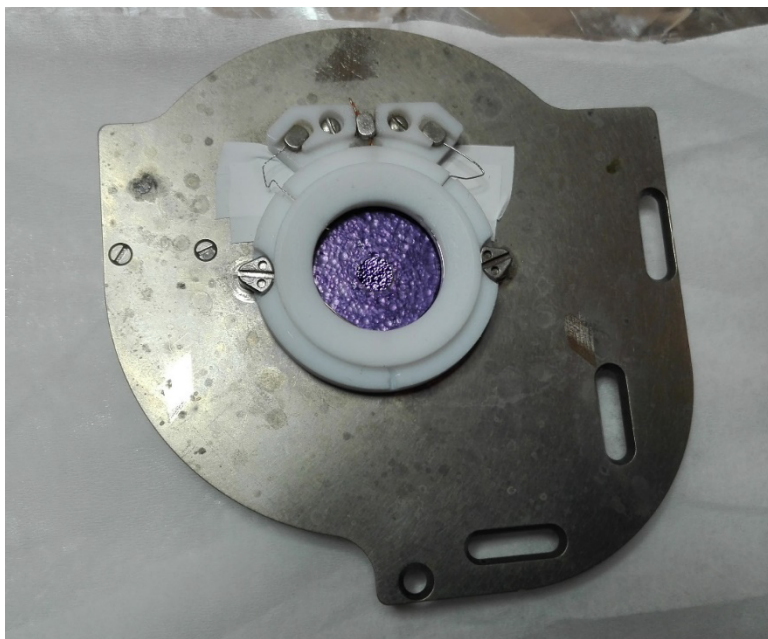


Figure 5.2: Picture of the sample of H2TPP mounted on the sample holder. The film is protected by a layer of PTFE, leaving a hole of 1mm diameter to perform measurements, visible in the center of the purple porphyrin layer.

5.2.3 Raman measurements

Raman spectra were acquired using a Jobin Yvon Labram HR800 Raman spectrometer. A 50x objective mounted on an Olympus BX41 microscope, in backscattering geometry, was used for the measurements. The excitation lines of 457.9 nm and 514 nm (Ar⁺ laser) were selected, setting the laser power at 0.2 mW, to prevent sample degradation. As the noise of the acquired spectra can be reconducted to the low thickness of the film, spectra of the porphyrin powder were collected as well, to facilitate the peaks assignments.

5.3 Results and discussions

AFM images were acquired on H2TPP films as casted (**Figure 5.3, (b)**) and in diluted H₂SO₄ solution with pH=3,2,1,0 (**Figure 5.3 (c), (d), (e) and (f)**), respectively, see **Attachment E¹²⁵**. The H2TPP film

as casted shows well defined crystallites, with many edges of 90°. An interesting parameter that can be calculated from AFM images is the roughness. The roughness of the surface can be estimated using various methods, from the cross-sectional profile of the image (line) or the surface (area)¹²⁶. Resulting from a statistical analysis of the sample, it gives a mean value, 8 nm, in this work. The number of crystallites on the film is approximately 40 ± 10 crystals/ μm^2 , and their lateral size is around 10-100 nm. This crystal distribution allows to monitor the changes on the surface of hundreds of crystallites, providing a good statistic to validate the study. When the porphyrin is in contact with the H_2SO_4 , an oxidation process takes place, proportionally to the pH of the solution. The lower the pH, the more efficient is the dissolution reaction of the porphyrin film. This is particularly evident from the images at different pH in **Figure 5.3**, especially by comparing pH=3 (**c**) and pH=0 (**f**). The latter completely dissolves the crystals, while at higher pH the dissolution happens at a slower rate, allowing the monitoring the kinetics through AFM with time.

A more careful look at the image at pH=0, i.e. when all the crystals are dissolved (**Figure 5.3, (f)**), shows that the morphology is different than mere HOPG (**Figure 5.3, (a)**). In fact, the steps typical of HOPG are not visible, and the sample roughness changes, showing that a layer of porphyrins are still present at the surface. Intermediate pH values allow monitoring the surface with time (cases of pH=3,2,1, **Figure 5.3(c), (d), (e)**). The case of pH=3 shows etch pits forming on the crystallites, as a consequence of molecule oxidation, while the pits become bulges in pH=1. The image acquired at pH=2 represents a mix of pH=1 and 3, as it shows at first the formation of pits, but after a few minutes the pits are abruptly substituted by bulges.

In an effort to monitor and explain the differences in the AFM imaging, giving an insight of the kinetics of the molecule oxidation formation on the molecular level, Raman ex-situ spectra were acquired. 514 and 458 nm excitation wavelengths were chosen to monitor changes in the spectra with the wavelength, but only the spectra at 458 are reported here. I first report a reference spectrum of an isotropic porphyrin sample (powder, **Figure 5.4 (a), (b)**, bottom dark blue spectra). A few differences from the spectra of the isotropic and not-isotropic (film) samples (**Figure 5.4 (a), (b)**, top blue spectra) can be easily detected and are reported as following:

- (i) only the low component of the doublet $196\text{-}211\text{ cm}^{-1}$ is present in the porphyrin film
- (ii) the 330 cm^{-1} Raman line is reduced in intensity in the film
- (iii) a broad feature at 415 cm^{-1} appears in the film
- (iv) the Raman modes 410 , 448 and 494 cm^{-1} disappear in the film
- (v) These differences between the two spectra of the pristine materials can be ascribed to a preferential orientation of the porphyrin films on the HOPG substrate, as confirmed by the AFM images before the treatment in acid (**Figure 5.3 (b)**). The immersion in acid has a first visible effect on the Raman spectra, as the signal to noise ratio is highly reduced after the immersion in H_2SO_4 (**Figure 5.4 (c), (d)**, top light blue spectra). As the spectra were acquired under the same experimental conditions and using the same parameters, this could be an indication that the film is somehow affected by the acid, as less material is present or more defects (pits/ bulges) appear on the surface. Interestingly, no changes regarding the peaks position or their relative intensity is observed after the immersion in acid. An interesting work

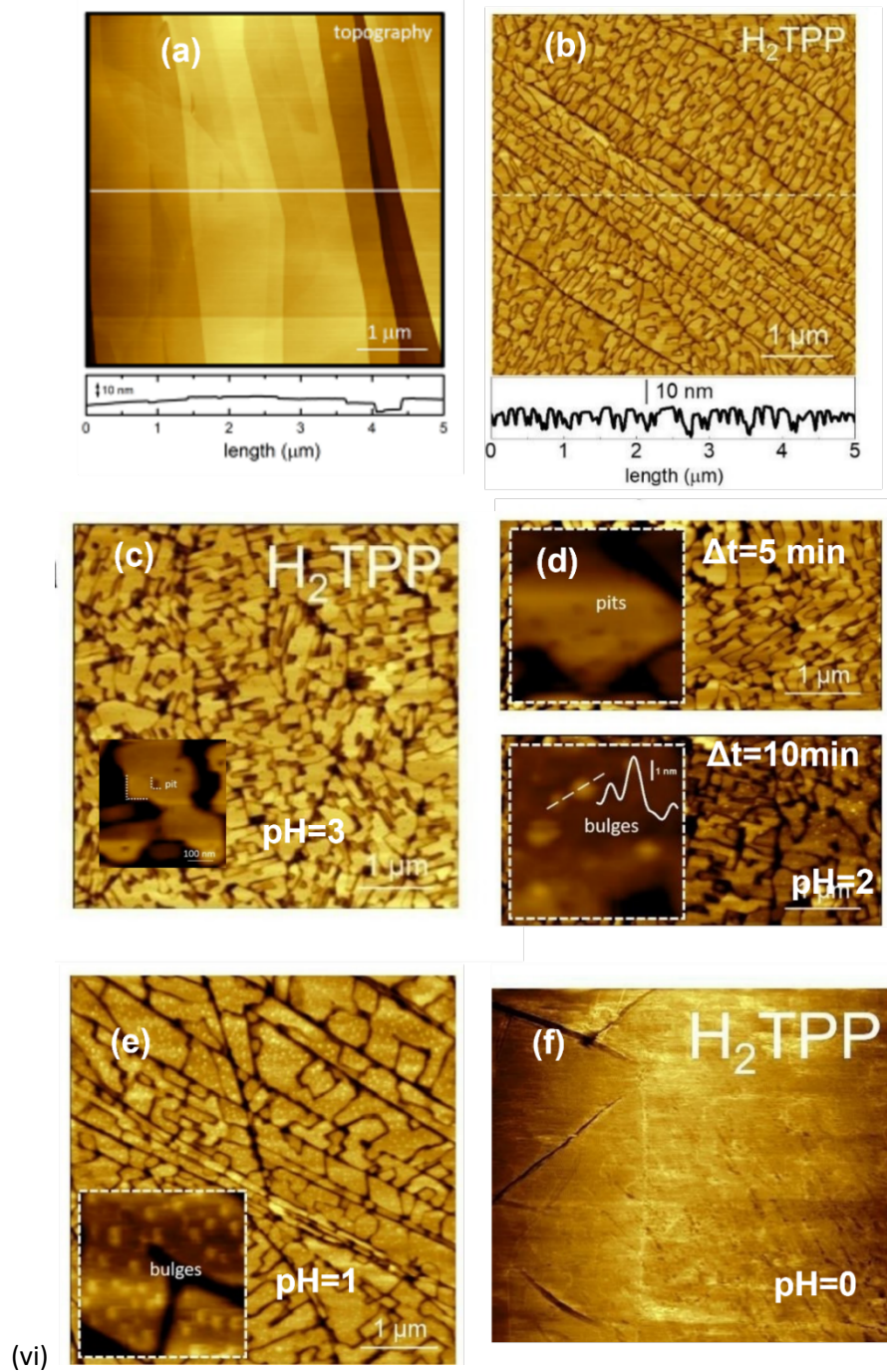


Figure 5.3: In this panel AFM images of (a) HOPG in air¹⁰⁷, H2TPP (b) in air, in H₂SO₄ with (c) pH=3, (d) pH=2, (e) pH=1, (f) pH=0 are shown^{107,125}.

by Gorsky¹²⁷ indicates that the molecule oxidation process deeply affects the Raman bands of the film, which does not happen in this case. As no typical marker band of molecule oxidation are observed, we can conclude that the molecule oxidation process does not affect the bulk of the material, but only the solid-liquid interface. A better understanding of this process could, therefore, be acquired using in-situ experiments while monitoring AFM images.

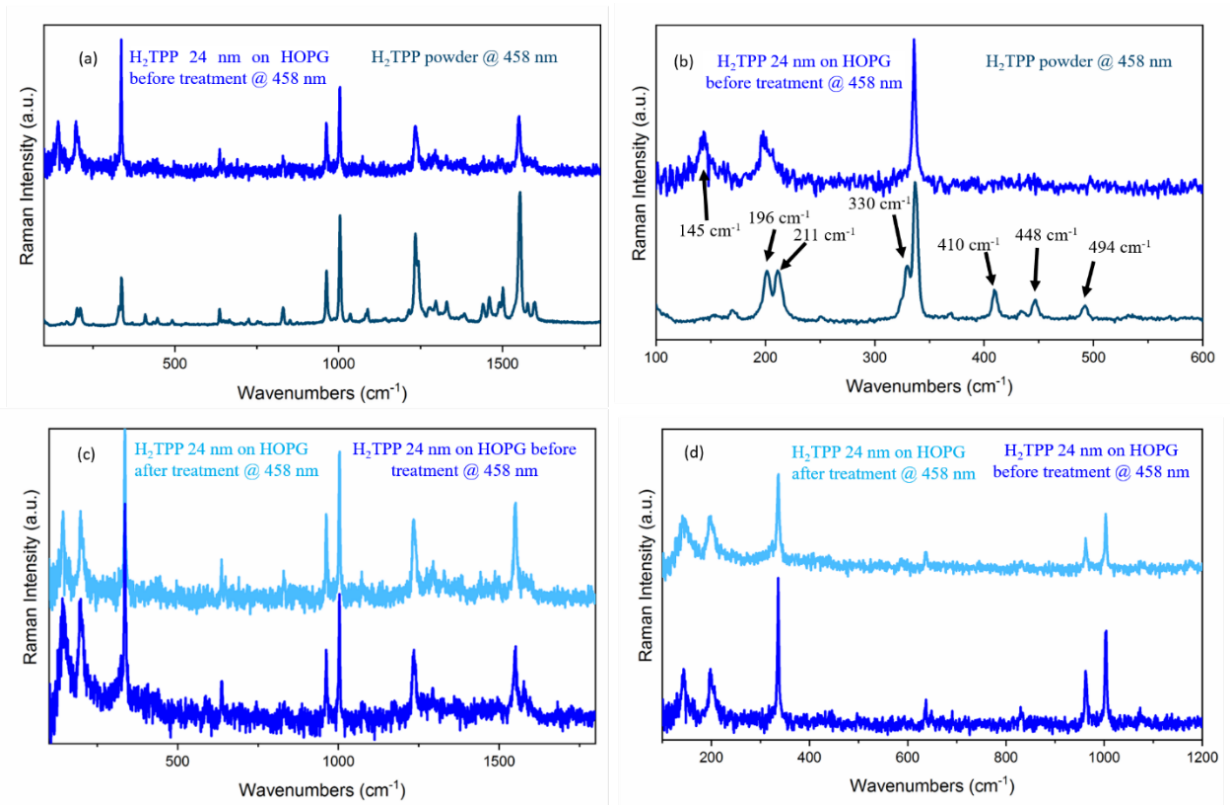


Figure 5.4: Raman spectra of H₂TPP are shown as follows: (a) comparison between powder (bottom dark blue spectrum) and thin film deposited on HOPG (top blue spectrum) and (b) a zoom, (c) comparison between the thin film deposited on HOPG (bottom blue spectrum) and the dried film after the experiments at pH=1 and (d) a zoom

5.4 Conclusions and future developments

The case study of the kinetics of H2TPP crystal dissolution in acidic environment shows how the combination of in-situ Atomic Force Microscopy and Raman techniques can already enhance the understanding the dissolution process. A deeper and better insight on what is happening at the molecular level, can be achieved using in-situ Raman techniques combined with AFM. An interesting combination of Raman spectroscopy and EC-AFM is the Tip-Enhanced Raman Spectroscopy (TERS) being able to give chemical and morphological information with high spatial resolution (nanoscale)^{128,129}. By using a metal tip (typically gold), the Raman signal can be enhanced. The enhancement mechanism is thought to be a chemical (charge transfer) and electromagnetic (plasmonic resonance) phenomenon connected to the geometry and material of the tip. Despite TERS (and generally Raman spectroscopy) is a well-known and spread technique, the combination with Electrochemistry is quite new, as the first measurements were conducted by two separate groups in 2015^{130,131}. By conducting in-situ Raman while scanning the surface of the film, variations in the chemical composition of the porphyrin/HOPG film at different pH could be monitored, in function of time and a more detailed study could be performed at pH=1 when pits become bulges. The combination of Raman spectroscopy and EC-AFM is therefore a powerful tool to explore the liquid-solid interface of various substrates, from biological tissue, to polymers, and more, giving a complete study of the sample from the molecular level to the nanoscale morphological details.

Conclusions

This thesis work is focused on establishing structure-property relationships on doped semiconducting polymers mainly using vibrational spectroscopy techniques. Specifically, the vibrational fingerprints of doping induced charge defects were unveiled and correlated with charge transport properties. This work aims at providing spectroscopically based experimental tools to characterize organic polymers and their properties upon doping, in an effort to better understand the characteristic of the charge carriers in the perspective of realizing more performant materials and devices. Environmental factors, as the exposure to oxygen or the effect of post-processing (e. g. annealing temperature), as well as different dopants and doping methods were taken into consideration. DFT calculations and experimental techniques, from structural (GIWAXS) to electrochemical and surface characterization (AFM) were also presented in support to the interpretation of the data presented in this dissertation.

A first analysis, presented in **Chapter 2**, focused on polaronic features using vibrational spectroscopy on the well know P(NDI2OD-T2) n-type polymer, chemically doped. This study presents an effort to reach the same level of knowledge on polaronic vibrational features as their p-type counterparts. The joint use of infrared spectroscopy and Resonance Raman experiments, with DFT calculations, corroborated the hypothesis that the charge transport mechanism dominating in P(NDI2OD-T2) is the hopping of the charge specie between different chains, and the charge defects are mainly localized on the NDI2OD unit. In this chapter the chemical doping method was adopted, in which dopant and polymeric solution are mixed in the suitable proportion to achieve a given level of doping. This method is widely used in literature, and it involves also annealing the sample for a certain time and at a fixed temperature.

In **Chapter 3** the effect of annealing temperature and time on chemically doped P(NDI2OD-T2) films were studied using different experimental techniques, to which I contributed with infrared in-situ temperature-dependent experiments and GIWAXS experiments. Conductivity measurements, molecular dynamic and Quantum Chemical simulations were performed to have a better understanding of the kinetics of doping. GIWAXS and conductivity measurements show

that doping is already active at room temperature on thin films, and that temperature and annealing time have a further effect on the performances of the material through a refinement of the sample morphology, as also confirmed by the infrared data.

Despite chemical doping is an effective method to increase the conductivity of the polymeric films, electrochemical reduction of the samples has proven to be another effective doping technique. The understanding electrochemical doping is fundamental for many applications fields, in particular in the perspective of application as bio-sensor and, in general, for bio-oriented industries (as wearable interfaces), soft robots and high energy density batteries for energy storage. In fact, water with a salt can be used as electrolyte, making it compatible with many biological processes. Many questions still need to be addressed, as the role of side reactions taking place during the electrochemical processes, the effect of oxygen and environmental factors on doping effectiveness, how changes in the electrolyte characteristics affect charge defect formation, how stable and reversible is the reaction. Some of these questions find an answer in **Chapter 4**, where I illustrate an electrochemical in-situ Raman cell which was custom-designed to conduct electrochemical doping of polymer in-situ. In nitrogen-saturated electrolytes bipolaronic and polaronic features were individuated through Resonant Raman experiments and threshold voltages onsets for the formation of the charge defects were determined, through the observation of their vibrational features. The Raman dataset also confirmed the reversibility of the electrochemical doping. Interestingly, in an oxygen saturated environment the bipolaronic spectral bands did not appear, hindered by the presence of oxygen and by the formation of side-reaction products, such as hydrogen peroxide. Despite lowering the conductivity performances, this finding is particularly important in the field of catalysis reactions, where the production of hydrogen peroxide is a fundamental step. A further theoretical work could be pursued in an attempt to correlate bipolaronic vibrational bands to the structure and properties of the doubly charged defect. This will contribute to a further understanding of the charge transport mechanism, as conductivity lowers when bipolarons are formed.

Finally, **Chapter 5** reports the work I did at SoLINano laboratory, equipped with an EC-AFM apparatus and specialized in in-situ Electrochemical and AFM surface characterization. This

activity exploited the use of Raman spectroscopy as an effective complementary tool in characterizing graphite electrodes surfaces with organic porphyrins deposited on top.

The major achievements of this PhD thesis work concern the use of vibrational spectroscopy for unveiling the nature of charge carriers formed upon doping in n-type semiconducting polymers. The effective combination of Raman, Resonant Raman and infrared with other characterization techniques paves the way to a deeper understanding of the doping mechanism and of its dependence on the processing and environmental factors

Bibliography

1. Rasmussen, S. Low-Bandgap Polymers. in *Encyclopedia of Polymeric Nanomaterials* 1–13 (Springer-Verlag Berlin Heidelberg, 2013). doi:10.1007/978-3-642-36199-9.
2. Kroon, R. *et al.* Thermoelectric plastics: from design to synthesis, processing and structure–property relationships. *Chem. Soc. Rev.* **45**, 6147–6164 (2016).
3. Beverina, L., Pagani, G. A. & Sassi, M. Multichromophoric electrochromic polymers: colour tuning of conjugated polymers through the side chain functionalization approach. *Chem. Commun.* **50**, 5413–5430 (2014).
4. Luzio, A., Criante, L., D’Innocenzo, V. & Caironi, M. Control of charge transport in a semiconducting copolymer by solvent-induced long-range order. *Sci. Rep.* **3**, 3425 (2013).
5. Rivnay, J. *et al.* Drastic Control of Texture in a High Performance n-Type Polymeric Semiconductor and Implications for Charge Transport. *Macromolecules* **44**, 5246–5255 (2011).
6. Li, J. *et al.* The effect of thermal annealing on dopant site choice in conjugated polymers. **33**, 23–31 (2016).
7. Glauddell, A. M., Cochran, J. E., Patel, S. N. & Chabinyk, M. L. Impact of the Doping Method on Conductivity and Thermopower in Semiconducting Polythiophenes. *Adv. Energy Mater.* **5**, 1401072 (2015).
8. Duong, D. T., Wang, C., Antono, E., Toney, M. F. & Salleo, A. The chemical and structural origin of efficient p-type doping in P3HT. *Org. Electron. physics, Mater. Appl.* **14**, 1330–1336 (2013).
9. Chew, A. R. *et al.* Unraveling the Effect of Conformational and Electronic Disorder in the Charge Transport Processes of Semiconducting Polymers. *Adv. Funct. Mater.* **28**, (2018).

10. Kang, K. *et al.* 2D coherent charge transport in highly ordered conducting polymers doped by solid state diffusion. *Nat. Mater.* **15**, (2016).
11. Saglio, B. *et al.* N-Alkyl substituted 1 H-benzimidazoles as improved n-type dopants for a naphthalene-diimide based copolymer. *J. Mater. Chem. A* **6**, 15294–15302 (2018).
12. Liu, J. *et al.* Enhancing Molecular n-Type Doping of Donor–Acceptor Copolymers by Tailoring Side Chains. *Adv. Mater.* **30**, 1–9 (2018).
13. Meng, B., Liu, J. & Wang, L. Recent development of n-type thermoelectric materials based on conjugated polymers. *Nano Mater. Sci.* **3**, 113–123 (2021).
14. Giovannitti, A. *The development of organic semiconductors for p- and n-type accumulation mode OECTs. Imperial College London* (2017).
15. Fazzi, D. & Caironi, M. Multi-length-scale relationships between the polymer molecular structure and charge transport: The case of poly-naphthalene diimide bithiophene. *Phys. Chem. Chem. Phys.* **17**, 8573–8590 (2015).
16. Savva, A. *et al.* Influence of Water on the Performance of Organic Electrochemical Transistors. *Chem. Mater.* **31**, 927–937 (2019).
17. Giovannitti, A. *et al.* The Role of the Side Chain on the Performance of N-type Conjugated Polymers in Aqueous Electrolytes. *Chem. Mater.* **30**, 2945–2953 (2018).
18. Giovannitti, A. *et al.* N-type organic electrochemical transistors with stability in water. *Nat. Commun.* **7**, 13066 (2016).
19. Griggs, S., Marks, A., Bristow, H. & McCulloch, I. n-Type organic semiconducting polymers: stability limitations, design considerations and applications. *J. Mater. Chem. C* **9**, 8099–8128 (2021).
20. Ehrenfreund, E., Vardeny, Z., Brafman, O. & Horovitz, B. *Amplitude and phase modes in trans-polyacetylene: Resonant Raman scattering and induced infrared activity. PHYSICAL REVIEW B* vol. 36 (1987).

21. Z. Vardeny, E. E. & Brafman, and O. Resonant Raman Scattering from Amplitude Modes in trans-(CH)_n and -(CD)_n, *J. Chem. Phys.* **51**, 2336–2329 (1983).
22. Chance, R.; Boudreaux, D. S.; Bredas, J. L.; Silbey, R. Chance, R.; Boudreaux, D. S.; Bredas, J. L.; Silbey, R. In *Handbook of Conducting Polymers*; T. A. Skotheim, Ed.; Dekker: New York, 1986; p 825. in *Handbook of Conducting Polymers* (ed. T. A. Skotheim, E. . D.) 825 (1986).
23. Bredas, J. L. & Street, G. B. Polarons, Bipolarons, and Solitons in Conducting Polymers. *Acc. Chem. Res.* **18**, 309–315 (1985).
24. Chance, R. R., Brédas, J. L. & Silbey, R. Bipolaron transport in doped conjugated polymers. *Phys. Rev. B* **29**, 4491–4495 (1984).
25. Castighoni, C., Navarrete, L., Zerbi, G. & Cnr, M. G. *A simple interpretation of the vibrational spectra of undoped, doped and photoexcited polyacetylene amplitude mode theory in the GF formalism.* vol. 65 (1988).
26. Wilson E B, D. J. C. & C. P. C. No Title. in *Molecular vibrations: the theory of infrared and Raman vibrational spectra.* 388 (McGraw-Hill, 1955).
27. Gussoni, M., Castiglioni, C. & Zerbi, G. Advances in Spectroscopy: Spectroscopy of Advanced Materials. in *Advances in Spectroscopy: Spectroscopy of Advanced Materials* vol. 19 251–251 (Clark, R. J. H., Hester, R. E., Ed.; Wiley & Sons, 1991).
28. Castiglioni, C., Tommasini, M. & Zerbi, G. Raman spectroscopy of polyconjugated molecules and materials: Confinement effect in one and two dimensions. *Philos. Trans. R. Soc. A Math. Phys. Eng. Sci.* **362**, 2425–2459 (2004).
29. Del Zoppo, M., Castiglioni, C., Gerola, V., Zuliani, P. & Zerbi, G. Effect of bond length alternation and of bond length alternation oscillations on the molecular nonlinear optical response of push pull polyenes. *J. Opt. Soc. Am. B* **15**, 308 (1998).
30. Anderson, M. *et al.* Displacement of polarons by vibrational modes in doped conjugated polymers. *Phys. Rev. Mater.* **1**, 1–9 (2017).

31. Chen, Z., Zheng, Y., Yan, H. & Facchetti, A. Naphthalenedicarboximide- vs perylenedicarboximide-based copolymers. synthesis and semiconducting properties in bottom-gate N-channel organic transistors. *J. Am. Chem. Soc.* **131**, 8–9 (2009).
32. Giussani, E., Fazzi, D., Brambilla, L., Caironi, M. & Castiglioni, C. Molecular level investigation of the film structure of a high electron mobility copolymer via vibrational spectroscopy. *Macromolecules* **46**, 2658–2670 (2013).
33. Wang, S. *et al.* Effect of Backbone Regiochemistry on Conductivity, Charge Density, and Polaron Structure of n-Doped Donor-Acceptor Polymers. *Chem. Mater.* **31**, 3395–3406 (2019).
34. Rivnay, J. *et al.* Unconventional face-on texture and exceptional in-plane order of a high mobility n-type polymer. *Adv. Mater.* **22**, 4359–4363 (2010).
35. Furukawa, Y., Sakamoto, A., Ohta, H. & Tasumi, M. Raman characterization of polarons, bipolarons and solitons in conducting polymers. *Synth. Met.* **49**, 335–340 (1992).
36. Francis, C. *et al.* Raman spectroscopy and microscopy of electrochemically and chemically doped high-mobility semiconducting polymers. *J. Mater. Chem. C* **5**, 6176–6184 (2017).
37. Di Pietro, R., Fazzi, D., Kehoe, T. B. & Sirringhaus, H. Spectroscopic investigation of oxygen- and water-induced electron trapping and charge transport instabilities in n-type polymer semiconductors. *J. Am. Chem. Soc.* **134**, 14877–14889 (2012).
38. Yamamoto, J. & Furukawa, Y. Raman characterization and electrical properties of poly(3-hexylthiophene) doped electrochemically in an ionic liquid-gated transistor geometry. *Org. Electron.* **28**, 82–87 (2016).
39. Kiefer, D. *et al.* Enhanced n-Doping Efficiency of a Naphthalenediimide-Based Copolymer through Polar Side Chains for Organic Thermoelectrics. *ACS Energy Lett.* **3**, 278–285 (2018).
40. Naab, B. D. *et al.* Role of Polymer Structure on the Conductivity of N-Doped Polymers. *Adv. Electron. Mater.* **2**, (2016).

41. Wu, R., Matta, M., Paulsen, B. D. & Rivnay, J. Operando Characterization of Organic Mixed Ionic_Electronic Conducting Materials. *Chem. Rev.* **122**, 4493–4551 (2022).
42. Steyrlleuthner, R. *et al.* Aggregation in a high-mobility n-type low-bandgap copolymer with implications on semicrystalline morphology. *J. Am. Chem. Soc.* **134**, 18303–18317 (2012).
43. Wang, S. *et al.* Thermoelectric Properties of Solution-Processed n-Doped Ladder-Type Conducting Polymers. *Adv. Mater.* **28**, 10764–10771 (2016).
44. Moia, D. *et al.* Design and evaluation of conjugated polymers with polar side chains as electrode materials for electrochemical energy storage in aqueous electrolytes. *Energy Environ. Sci.* **12**, 1349–1357 (2019).
45. Szumska, A. A. *et al.* Reversible Electrochemical Charging of n-Type Conjugated Polymer Electrodes in Aqueous Electrolytes. *J. Am. Chem. Soc.* **143**, 14795–14805 (2021).
46. Nielsen, C. B. *et al.* Molecular Design of Semiconducting Polymers for High-Performance Organic Electrochemical Transistors. *J. Am. Chem. Soc.* **138**, 10252–10259 (2016).
47. Chew, A. R. *Polarons, Disorder and Charge Transport in Polymeric Semiconductors.* (2018).
48. Chew, A. R. & Salleo, A. Spectroscopic studies of dopant-induced conformational changes in poly(3-hexylthiophene) thin films. *MRS Commun.* **7**, 728–734 (2017).
49. Ghosh, R. *et al.* Spectral Signatures and Spatial Coherence of Bound and Unbound Polarons in P3HT Films: Theory Versus Experiment. *J. Phys. Chem. C* **122**, 18048–18060 (2018).
50. Pace, G., Bargigia, I., Noh, Y.-Y., Silva, C. & Caironi, M. Intrinsically distinct hole and electron transport in conjugated polymers controlled by intra and intermolecular interactions. *Nat. Commun.* **10**, 5226 (2019).
51. Castiglioni, C., Gussoni, M., Teodomiro Lopez Navarrete, J. & Zerbi, G. *Mikrochimica Acta*

FTIR Spectra (Frequency and Intensity) of Poly-(Para-Phenylenes). vol. I (1988).

52. Kim, N. *et al.* Highly conductive PEDOT:PSS nanofibrils induced by solution-processed crystallization. *Adv. Mater.* **26**, 2268–2272 (2014).
53. Facchetti, A. *et al.* Semiconductor Design for Tuned Charge Transport Characteristics. *Proc. SPIE* **7487**, 748702–2 (2009).
54. Wei, P., Oh, J. H., Dong, G. & Bao, Z. Use of a 1 H -benzimidazole derivative as an n -type dopant and to enable air-stable solution-processed n -channel organic thin-film transistors. *J. Am. Chem. Soc.* **132**, 8852–8853 (2010).
55. Salleo, A., Kline, R. J., DeLongchamp, D. M. & Chabinyc, M. L. Microstructural characterization and charge transport in thin films of conjugated polymers. *Adv. Mater.* **22**, 3812–3838 (2010).
56. Naab, B. D. *et al.* Effective solution- and vacuum-processed n-doping by dimers of benzimidazoline radicals. *Adv. Mater.* **26**, 4268–4272 (2014).
57. Zhang, W. *et al.* Indacenodithiophene semiconducting polymers for high-performance, air-stable transistors. *J. Am. Chem. Soc.* **132**, 11437–11439 (2010).
58. Schlitz, R. A. *et al.* Solubility-Limited Extrinsic n-Type Doping of a High Electron Mobility Polymer for Thermoelectric Applications. *Adv. Mater.* **26**, 2825–2830 (2014).
59. Saglio, B. *Organic Thermoelectrics: Development of New Dopants for n-type Naphtalene Dicarboximide Copolymers*. (2018).
60. Denti, I. *et al.* Polaron Confinement in n-Doped P(NDI2OD-T2) Unveiled by Vibrational Spectroscopy. *Chem. Mater.* **31**, 6726–6739 (2019).
61. M. J. Frisch, G. W. Trucks, H. B. Schlegel, G. E. Scuseria, M., A. Robb, J. R. Cheeseman, G. Scalmani, V. Barone, B. Mennucci, G. A. Petersson, H. & Nakatsuji, M. Caricato, X. Li, H. P. Hratchian, A. F. Izmaylov, J. Bloino, G. Z. Gaussian 09, Revision D.01.
62. Wang, S. *et al.* Sequential Doping of Ladder-Type Conjugated Polymers for Thermally

- Stable n - Type Organic Conductors. *Appl. Mater. Interfaces* **12**, 53003–53011 (2020).
63. Kluge, R. M. *et al.* Doping Dependent In-Plane and Cross-Plane Thermoelectric Performance of Thin n-Type Polymer P(NDI2OD-T2) Films. *Adv. Funct. Mater.* **30**, 2003092 (2020).
 64. Wang, S. *et al.* A Chemically Doped Naphthalenediimide-Bithiazole Polymer for n-Type Organic Thermoelectrics. **30**, 1801898 (2018).
 65. Zhao, K. *et al.* Role of Molecular Weight in Microstructural Transition and Its Correlation to the Mechanical and Electrical Properties of P(NDI2OD-T2) Thin Films. *Macromolecules* **54**, 10203–10215 (2021).
 66. Cochran, J. E. *et al.* Molecular Interactions and Ordering in Electrically Doped Polymers: Blends of PBTTT and F 4 TCNQ. *Macromolecules* **47**, 6836–6846 (2014).
 67. Chiang, C. K. *et al.* Electrical Conductivity in Doped Polyacetylene. *Phys. Rev. Lett.* **39**, 1098–1101 (1977).
 68. Ivory, D. M. *et al.* Highly conducting charge-transfer complexes of poly(p-phenylene). *J. Phys. Chem.* **1506**, 1–3 (2008).
 69. Denti, I. *et al.* Polaron Confinement in n-Doped P(NDI2OD-T2) Unveiled by Vibrational Spectroscopy. *Chem. Mater.* **31**, (2019).
 70. Ilavsky, J. Nika_ software for two-dimensional data reduction. *J. Appl. Crystallogr.* *Crystallogr.* **45**, 324–328 (2012).
 71. Oosterhout, S. D. *et al.* Mixing Behavior in Small Molecule:Fullerene Organic Photovoltaics. *Chem. Mater.* **29**, 3062–3069 (2017).
 72. Jiang, J. *et al.* Polymer Doping for High-Efficiency Perovskite Solar Cells with Improved Moisture Stability. *Adv. Energy Mater.* **8**, 1–9 (2018).
 73. Riera-Galindo, S. *et al.* Impact of Singly Occupied Molecular Orbital Energy on the n-Doping Efficiency of Benzimidazole Derivatives. *ACS Appl. Mater. Interfaces* **11**, 37981–

- 37990 (2019).
74. Pallini, F. *et al.* Unexpected Enhancement of Molecular n - Doping Efficiency in Polymer Thin Films by a Degradation Product. *ACS Appl. Electron. Mater.* **5**, 2421–2429 (2022).
 75. Schwartzkopf, M. & Roth, S. V. Investigating Polymer–Metal Interfaces by Grazing Incidence Small-Angle X-Ray Scattering from Gradients to Real-Time Studies.pdf. *nanomaterials* **6**, 239 (2016).
 76. Kittlesen, G. P., White, H. S. & Wrighton, M. S. Chemical derivatization of microelectrode arrays by oxidation of pyrrole and N-methylpyrrole: fabrication of molecule-based electronic devices. *J. Am. Chem. Soc.* **106**, 7389–7396 (1984).
 77. Parr, Z. S. *et al.* Glycolated Thiophene-Tetrafluorophenylene Copolymers for Bioelectronic Applications: Synthesis by Direct Heteroarylation Polymerisation. *ChemPlusChem* vol. 84 1384–1390 (2019).
 78. Onorato, J. W. & Luscombe, C. K. Morphological effects on polymeric mixed ionic/electronic conductors. *Mol. Syst. Des. Eng.* **4**, 310–324 (2019).
 79. Khodagholy, D. *et al.* High transconductance organic electrochemical transistors. *Nat. Commun.* **4**, 1–6 (2013).
 80. Guo, K. *et al.* Rapid single-molecule detection of COVID-19 and MERS antigens via nanobody-functionalized organic electrochemical transistors. *Nat. Biomed. Eng.* **5**, 666–677 (2021).
 81. Kukhta, N. A., Marks, A. & Luscombe, C. K. Molecular Design Strategies toward Improvement of Charge Injection and Ionic Conduction in Organic Mixed Ionic-Electronic Conductors for Organic Electrochemical Transistors. *Chem. Rev.* **122**, 4325–4355 (2021).
 82. Bargigia, I., Savagian, L. R., Österholm, A. M., Reynolds, J. R. & Silva, C. Charge-Transfer Intermediates in the Electrochemical Doping Mechanism of Conjugated Polymers. *J. Am. Chem. Soc.* **143**, 294–308 (2021).

83. Cendra, C. *et al.* Role of the Anion on the Transport and Structure of Organic Mixed Conductors. **29**, 1807034 (2019).
84. Jones, B. A., Facchetti, A., Wasielewski, M. R. & Marks, T. J. Tuning orbital energetics in arylene diimide semiconductors. Materials design for ambient stability of n-type charge transport. *J. Am. Chem. Soc.* **129**, 15259–15278 (2007).
85. Quinn, J. T. E., Zhu, J., Li, X., Wang, J. & Li, Y. Recent progress in the development of n-type organic semiconductors for organic field effect transistors. *J. Mater. Chem. C* **5**, 8654–8681 (2017).
86. Kerr, R., Pozo-Gonzalo, C., Forsyth, M. & Winther-Jensen, B. Influence of the polymerization method on the oxygen reduction reaction pathway on PEDOT. *ECS Electrochem. Lett.* **2**, 29–32 (2013).
87. Mitraka, E. *et al.* Electrocatalytic Production of Hydrogen Peroxide with Poly(3,4-ethylenedioxythiophene) Electrodes. *Adv. Sustain. Syst.* **3**, 1800110 (2019).
88. Tan, S. T. M. *et al.* High-Gain Chemically Gated Organic Electrochemical Transistor. *Adv. Funct. Mater.* **31**, 1–9 (2021).
89. Weber, A. Z. *et al.* Redox flow batteries : a review. *J. Appl. Electrochem.* **41**, 1137–1164 (2011).
90. Yuan, H., Peng, H., Huang, J. & Zhang, Q. Sulfur Redox Reactions at Working Interfaces in Lithium – Sulfur Batteries : A Perspective. **1802046**, 1–10 (2019).
91. Bartlett, R. J. & Ross, D. S. Chapter 9 Chemistry of Redox Processes in Soils. 461–487 (2005).
92. Ikeda, T. & Kano, K. An electrochemical approach to the studies of biological redox reactions and their applications to biosensors, bioreactors, and biofuel cells. *J. Biosci. Bioeng.* **92**, 9–18 (2001).
93. Hu, A. *et al.* Optimizing Redox Reactions in Aprotic Lithium–Sulfur Batteries. *Adv. Energy*

- Mater.* **10**, 2002180 (2020).
94. Reggente, M., Passeri, D., Rossi, M., Tamburri, E. & Terranova, M. L. Electrochemical atomic force microscopy_ In situ monitoring of electrochemical processes. in *AIP Conference Proceedings 1873* 020009 (2017).
 95. Inaba, M., Jeong, S. K. & Ogumi, Z. In situ scanning probe microscopy of interfacial phenomena in batteries. *Electrochem. Soc. Interface* **20**, 55–59 (2011).
 96. Davoodi, A., Pan, J., C., L. & Norgren, S. In Situ Investigation of Localized Corrosion of Aluminum Alloys in Chloride Solution Using Integrated EC-AFM/SECM Techniques. *Solid-State Lett* **8**, B21–B24 (2005).
 97. Szunerits, S., Pust, S. E. & Wittstock, G. Multidimensional electrochemical imaging in materials science. *Anal. Bioanal. Chem.* **389**, 1103–1120 (2007).
 98. G. Binnig, H. Rohrer, Ch. Gerber, and E. W. Surface Studies by Scanning Tunneling Microscopy. *Phys. Rev. Lett.* **49**, 57–61 (1982).
 99. Bussetti, G. & Duo, L. Anion Intercalation in Graphite Studied by Electrochemical-Scanning Probe Microscopy : State of the Art and Perspectives. *Encycl. Interfacial Chem.* 27–37 (2018) doi:10.1016/B978-0-12-409547-2.14164-2.
 100. Yivlialin, R. Anion intercalation in graphite: a combined Electrochemical Atomic Force and Scanning Tunneling Microscopy investigation. (Politecnico di Milano, 2017).
 101. Alfonta, L. *et al.* Measuring Localized redox Enzyme Electron Transfer in a Live Cell with Conducting Atomic Force Microscopy. *Anal. Chem.* **86**, 7674–7680 (2014).
 102. Doménech-Carbó, A. & Doménech-Carbó, M. T. In situ AFM study of proton-assisted electrochemical oxidation/reduction of microparticles of organic dyes. *Electrochem. commun.* **10**, 1238–1241 (2008).
 103. Bussetti, G. *et al.* Electrochemical scanning probe analysis used as a benchmark for carbon forms. *J. Phys. Condens. Matter* **33**, (2021).

104. Pavoni, E. *et al.* Blisters on graphite surface: A scanning microwave microscopy investigation. *RSC Adv.* **9**, 23156–23160 (2019).
105. Hathcock, K. W., Brumfield, J. C., Goss, C. A., Irene, E. A. & Murray, R. W. Incipient Electrochemical Oxidation of Highly Oriented Pyrolytic Graphite: Correlation between Surface Blistering and Electrolyte Anion Intercalation. *Anal. Chem.* **67**, 2201–2206 (1995).
106. Yivlialin, R., Magagnin, L., Duò, L. & Bussetti, G. Blister evolution time invariance at very low electrolyte pH: H₂SO₄/graphite system investigated by electrochemical atomic force microscopy. *Electrochim. Acta* **276**, 352–361 (2018).
107. Jagadeesh, M. S. *et al.* The effect of cyclic voltammetry speed on anion intercalation in HOPG. *Surf. Sci.* **681**, 111–115 (2019).
108. Moreno Flores, S. & Toca-Herrera, J. L. The new future of scanning probe microscopy: Combining atomic force microscopy with other surface-sensitive techniques{,} optical microscopy and fluorescence techniques. *Nanoscale* **1**, 40–49 (2009).
109. Yivlialin, R. *et al.* Evolution of the graphite surface in phosphoric acid: An AFM and Raman study. *Beilstein J. Nanotechnol.* **7**, 1878–1884 (2016).
110. Jagadeesh, M. S. *et al.* Incipient Anion Intercalation of Highly Oriented Pyrolytic Graphite Close to the Oxygen Evolution Potential: A Combined X-ray Photoemission and Raman Spectroscopy Study. *J. Phys. Chem. C* **123**, 1790–1797 (2019).
111. Yivlialin, R. *et al.* Vacuum-deposited porphyrin protective films on graphite: Electrochemical atomic force microscopy investigation during anion intercalation. *ACS Appl. Mater. Interfaces* **9**, 4100–4105 (2017).
112. Cama, J. *et al.* Fluorite dissolution at acidic pH : In situ AFM and ex situ VSI experiments and Monte Carlo simulations. *Geochim. Cosmochim. Acta* **74**, 4298–4311 (2010).
113. Liu, S. T., Nancollas, G. H. & Gasielki, E. A. SCANNING ELECTRON MICROSCOPIC AND KINETIC STUDIES OF THE CRYSTALLIZATION. *J. Cryst. Growth* **33**, 11–20 (1976).

114. Yu, C. & Lin, K. The atomic-scale studies of the behavior of the crystal dissolution in a molten metal. *Chem. Phys. Lett.* **418**, 433–436 (2006).
115. Thiocyanate, T.-N., Kowalski, M. A. & Harrington, G. W. Solutions of Copper(I) Thiocyanate in Molten Tetra- N-Pentylammonium Thiocyanate. *Anal. Chem.* **44**, 479–483 (1972).
116. You, A., Be, M. A. Y. & In, I. Etching of Dislocations in Sodium Chloride Crystals Dislocation Etch Pit Formation in Lithium Fluoride. *J. Appl. Phys.* **3141**, (2004).
117. BARBER, D. d., FRANK, F. C., MOSS, M., STEEDS, d. W. & TSONG, I. S. T. Prediction of ion-bombarded surface topographies using Frank ' s kinematic theory of crystal dissolution. *J. Mater. Sci.* **8**, 1030–1040 (1973).
118. Tsukamoto, K. & Dold, P. Interferometric Techniques for Investigating Growth and Dissolution of Crystals in Solutions. *AIP Conf. Proc.* **329**, (2013).
119. Fischer, C., Arvidson, R. S. & Lu, A. How predictable are dissolution rates of crystalline material? *Geochim. Cosmochim. Acta* **98**, 177–185 (2012).
120. Fischer, C., Kurganskaya, I., Schäfer, T. & Lüttge, A. Applied Geochemistry Variability of crystal surface reactivity : What do we know ? *Appl. Geochemistry* **43**, 132–157 (2014).
121. Luttge, A., Arvidson, R. S., Fischer, C. & Kurganskaya, I. Kinetic concepts for quantitative prediction of fluid-solid interactions. *Chem. Geol.* **504**, 216–235 (2019).
122. FRANK, F. C. & Ives, M. B. Orientation-Dependent Dissolution of Germanium. *J. Appl. Phys.* **31**, 1996 (1960).
123. Papaioannou, P. C. & Harrington, G. W. Specific Conductance and Density Measurements in Fused Alkali Metal Nitrate Systems. I. Solvent Systems and Binary Solutions. *J. Phys. Chem.* **68**, 2424–2433 (1964).
124. McDougall, D. J. Etch Pits. in *Mineralogy* 150–152 (Springer US, 1983). doi:10.1007/0-387-30720-6_44.

125. Filoni, C., Duò, L., Ciccacci, F., Bassi, L. & Bossi, A. Reactive Dissolution of Organic Nanocrystals at Controlled pH. *ChemNanoMat* **6**, 567–575 (2020).
126. Bhushan, B. Surface roughness analysis and measurement techniques. in *Modern Tribology Handbook, Two Volume Set* 49–119 (2000).
127. Gorski, A., Starukhin, A., Stavrov, S., Gawinkowski, S. & Waluk, J. Resonance Raman spectroscopy study of protonated porphyrin. *Spectrochim. Acta Part A Mol. Biomol. Spectrosc.* **173**, 350–355 (2017).
128. Kolhatkar, G., Plathier, J. & Ruediger, A. Nanoscale investigation of materials{,} chemical reactions{,} and biological systems by tip enhanced Raman spectroscopy – a review. *J. Mater. Chem. C* **6**, 1307–1319 (2018).
129. Britz-Grell, A. B., Saumer, M. & Tarasov, A. Challenges and Opportunities of Tip-Enhanced Raman Spectroscopy in Liquids. *J. Phys. Chem. C* **125**, 21321–21340 (2021).
130. Zeng, Z.-C. *et al.* Electrochemical Tip-Enhanced Raman Spectroscopy. *J. Am. Chem. Soc.* **137**, 11928–11931 (2015).
131. Kurouski, D., Mattei, M. & Van Duyne, R. P. Probing Redox Reactions at the Nanoscale with Electrochemical Tip-Enhanced Raman Spectroscopy. *Nano Lett.* **15**, 7956–7962 (2015).

Attachment A

Denti, I. *et al.* Polaron Confinement in n-Doped P(NDI2OD-T2) Unveiled by Vibrational Spectroscopy. *Chem. Mater.* **31**, 6726–6739 (2019)

Associated Contents (Supporting Information) are enclosed.

Polaron Confinement in n-Doped P(NDI2OD-T2) Unveiled by Vibrational Spectroscopy

Ilaria Denti,[†] Simone Cimò,^{†,‡} Luigi Brambilla,^{†,‡} Alberto Milani,^{†,§} Chiara Bertarelli,^{†,‡} Matteo Tommasini,[†] and Chiara Castiglioni^{*,†,‡}

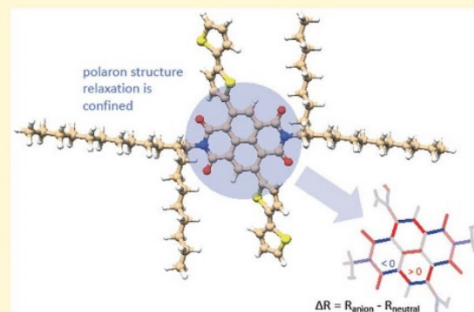
[†]Dipartimento di Chimica, Materiali e Ingegneria Chimica Giulio Natta, Politecnico di Milano, piazza Leonardo da Vinci 32, 20133 Milano, Italy

[‡]Center for Nano Science and Technology@PoliMi, Istituto Italiano di Tecnologia, via Pascoli 70/3, 20133 Milano, Italy

[§]Dipartimento di Energia, Politecnico di Milano, via Ponzio 34, 20133 Milano, Italy

Supporting Information

ABSTRACT: Through specific marker bands, IR and Raman spectra of chemically doped polyconjugated polymers allow investigation of doping and monitoring of its effectiveness. The vibrational modes associated with the doping-induced features provide information about the polymer units affected by the transferred charge and the structure relaxation associated with the formation of the polaron. Here, we doped the P(NDI2OD-T2) copolymer with three differently substituted 1*H*-benzimidazoles, which allow for doping in solution, leading to an increase of conductivity values up to four orders of magnitude. Careful inspection of the IR and Raman spectra of P(NDI2OD-T2) while varying the dopant concentration and the kind of dopant proves that the polaron markers are almost independent from the dopant species. The IR intensity of the polaron markers is a very sensitive probe of charge delocalization upon doping: for n-doped P(NDI2OD-T2), these bands show absorption intensities of the same strength as those of the pristine species. In other words, they are very weak in comparison to the so-called IR_{AV} bands of doped polyacetylene, polythiophenes, and related materials. This experimental observation provides evidence of the strong confinement of the polaron on the NDI2OD unit. Multiwavelength Raman spectra of n-doped P(NDI2OD-T2) further corroborate this point, showing that the T2 moiety is almost unaffected by doping. The analysis of the experimental data is complemented by DFT calculations which fully support the diagnosis of the formation of localized polarons. Hence, vibrational spectroscopy is an effective tool to characterize charge carriers induced by doping P(NDI2OD-T2): it indicates that the observed conductivity enhancement is ascribed to an efficient interchain hopping involving charged NDI2OD units, whereas polaron diffusion along the chain is unlikely.



1. INTRODUCTION

Carrier density in π -conjugated semiconductors can be strongly enhanced by chemical doping with either oxidizing or reducing species.¹ Doped conjugated polymers have recently attracted great interest since they have been successfully applied as interfaces in light emitting diodes, solar cells,² and transistors.³ Moreover, when suitable values of conductivity are reached, they also provide opportunities for development of flexible and wearable thermoelectric generators and coolers.⁴ The p-doping has been extensively investigated since the early studies on intrinsically conducting polymers,^{5,6} and high conductivity values have been reached in the past decade^{7–9} with a remarkable $\sigma = 4380$ S/cm for poly(3,4-ethylene-dioxythiophene):polystyrenesulfonate (PEDOT:PSS) post-treated with H₂SO₄.¹⁰ So far, the study of n-doping is less extensive as air-stable n-type polymers have been reported only recently. In this framework, interest has been gained in the poly(*N,N'*-bis-2-octyldodecyl)naphthalene-1,4,5,8-bis-dicarboximide-2,6-diyl-*alt*-

5,5'-2,2'-bithiophene) P(NDI2OD-T2) and analogous naphthalene or perylene diimide copolymers because they are characterized by relatively high mobility values in the pristine state.^{11–13} Although n-type doping has been performed also using inorganic salts¹⁴ and tetrakis(dimethylamino)ethylene (TDAE),¹⁵ some 1*H*-benzimidazole derivatives are particularly attractive because they are air-stable and allow for an effective doping process in solution.^{16–19}

Dimethyl 1*H*-benzimidazole (DMBI) and diphenyl 1*H*-benzimidazole (DPhBI) were first used to n-dope the P(NDI2OD-T2), achieving a conductivity increase of some order of magnitude.¹⁷ However, phase segregation of the dopants has been demonstrated at relatively high concentration.

Special Issue: Jean-Luc Bredas Festschrift

Received: March 27, 2019

Revised: May 6, 2019

Published: May 15, 2019

N-substitution of the aniline with linear alkyl chains of increasing length or with branched alkyls turned out to further increase the conductivity of P(NDI2OD-T2) due to a better miscibility between dopants and polymer, i.e., an efficient intercalation of the dopant molecules among the polymer chains.¹⁸ It has also been reported that DMBI dimers (DMBI)₂ substituted both with 2-alkyl or 2-metallocenyl groups are effective n-type dopants both in vacuum and solution conditions.

Despite the wide literature, the complex mechanisms involved in the charge transport of doped P(NDI2OD-T2) are not yet fully understood. The relevance of the molecular structure of the charge defect (i.e., polaron), the structure of the polymer chain, and its supramolecular arrangement has been highlighted for the rationalization of the charge transport performances.^{15,19,20} In particular, the size of the charge defect and the associated relaxation of the molecular structure can play a very important role with respect to intermolecular vs. intramolecular electron transfer (e.g., via hopping between polymer sites). In this perspective, the case of P(NDI2OD-T2) is peculiar because of the large torsional angle (about 138°) between NDI2OD and the T2 unit. This partially hinders π -electron conjugation and hence charge delocalization along the whole donor–acceptor backbone.^{21,22} The effect of the distorted backbone has been clearly shown by density functional theory (DFT) calculations on model charged oligomers by Wang et al.,¹⁵ showing that the polaron is mainly localized on one NDI2OD unit. This is different from some copolymers containing NDI2OD units polymerized with comonomers other than bithiophene, which allow for a better planarization of the polymer backbone. In this framework, Naab et al.¹⁹ compared the effect of doping with (2-Cyc-DMBI)₂ several conjugated copolymers based on perylene diimide (PDI) and naphthalene diimide (NDI) acceptors copolymerized with ethynylene, ethylene, and bithiophene. This study provides an experimental probe of the formation of a rather localized defect in P(NDI2OD-T2): the UV–vis–NIR absorption spectra show that the polaron size is modulated by the polymer conformation and by its electronic structure. These experiments also suggest that the ethynylene linker enables a delocalized anion upon n-doping, whereas in n-doped donor–acceptor polymers such as P(NDI2OD-T2), the charge defect is localized on the NDI2OD unit.

Since the earliest studies on doped polymers,^{6,23–26} it was clear that the structure and charge distribution in the doping-induced defects have a remarkable impact on infrared (IR) spectra of conducting polymers. It follows that the detection of features of the doped state and their characteristic IR intensities can provide unique information about possible intrachain vs interchain transport in the doped materials. The pioneering works by Horowitz on the amplitude mode (AM) theory²⁶ and its formulation in the context of molecular spectroscopy, namely the effective conjugation coordinate (ECC) theory,^{23–25,27} demonstrated that strong infrared activated vibrational (IRAV) bands (closely related with the Raman bands of pristine polymers) should be taken as the signature of the charge carriers (solitons, polarons, bipolarons). The prototypical case of polyacetylene was widely investigated through experiments and theoretical models. Worth noting, Brédas et al.²⁸ discussed in a pioneering work the charge distribution and geometry relaxation in charged polyene chains. These studies provided a clear picture of the defect, which involves several polymer units with a relevant modulation of the bond length alternation (BLA) parameter and delocalization of the transferred charge in a large

domain. The mechanisms related to the “activation” of strong Raman active vibrational modes in the IR have been discussed in the past^{23–26} and recently reexamined by means of a detailed molecular modeling based on state-of-the-art DFT calculations.²⁹ The remarkable conclusion is that the absolute IR intensity of IRAV is anomalously higher than the typical IR bands of undoped molecular species. Indeed, even small percentages of dopant give rise to IRAV absorptions as strong as bands associated with pristine neutral species. Moreover, IRAV bands of highly doped materials show IR dipole strengths comparable to those of electronic transitions.²⁹ These huge intensities are ascribed to large electron charge fluxes during vibrational modes coupled with the charged polaron, which suggests a possible phonon assisted intrachain charge transport.^{24,29} In the same framework, the peculiarities of the IRAV modes of doped poly(3-hexylthiophenes) are discussed in ref 30 and show the remarkable contribution of vibrational spectroscopy for a detailed insight on the nature of the charge carriers.

In this work, we prove that IR and Raman spectroscopy are highly informative tools for the description of the charge defects in n-doped P(NDI2OD-T2). The identification of selective markers of the polaron allows for its structural characterization at the molecular level. The present study complements a just published paper which discusses the effects of backbone regiochemistry on the IR features of doped P(NDI2OD-T2).³¹

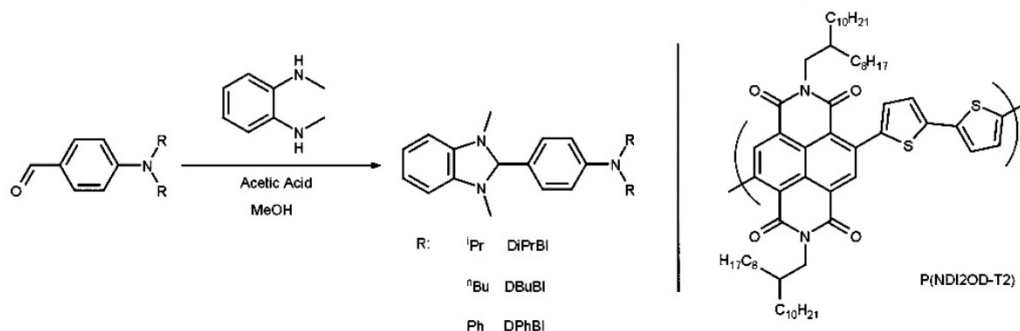
Herein, we investigated with vibrational spectroscopy P(NDI2OD-T2) doped with *N*-alkyl substituted 1*H*-benzimidazoles at different doping ratios, which are known to give an increase in conductivity of more than four orders of magnitude.¹⁸ Our analysis shows the peculiar spectroscopic signatures of the doping-induced defects that are remarkably different from those already described in other doped π -conjugated semiconductors (e.g., *p*-doped polythiophenes, *n/p*-doped polyacetylene). We show that doping-induced features are nicely modeled as vibrational bands of a radical anion localized on the NDI2OD unit, thus proving that the interaction between the NDI2OD and T2 building blocks is limited. To support the interpretation of the experiments and provide absolute IR intensity data, we performed DFT calculations on model molecules and on the polymer chain, characterized by regular conformation and described as a 1-D crystal.

2. METHODS

2.1. Synthesis of the Dopants. All chemicals were purchased from Sigma-Aldrich and used as received. NMR spectra were acquired using a Bruker ARX400 instrument. To synthesize DiPrBI, DPhBI, and DBuBI, the reactants were *p*-aminobenzaldehyde and *N*-disubstituted with isopropyl, phenyl, and butyl, respectively. The first two reactants were synthesized by direct formylation of the *N,N*-disubstituted aniline with POCl₃, and the detailed procedure is reported in the Supporting Information. The *N,N*-diisobutylbenzaldehyde was synthesized according to the literature.^{17,18} In all cases, the final step of synthesis consists in the coupling between the *N*-substituted *p*-aminobenzaldehyde and the *N*,*N*-2-dimethylbenzene-1,2-diamine. Specifically, *N,N*-dibutyl-4-(1,3-dimethyl-2,3-dihydro-1*H*-1,3-benzodiazol-2-yl)aniline (DBuBI) was synthesized as previously reported,¹⁸ whereas modified conditions with respect to the published procedures were tested for *N,N*-diisopropyl-4-(1,3-dimethyl-2,3-dihydro-1*H*-1,3-benzodiazol-2-yl)aniline (DiPrBI) and *N,N*-diphenyl-4-(1,3-dimethyl-2,3-dihydro-1*H*-1,3-benzodiazol-2-yl)aniline (DPhBI) and detailed in the Supporting Information.

2.2. Sample Preparation and Doping Procedure. The samples were prepared starting from a solution of P(NDI2OD-T2) (Polyera ActivInk N2200, Mn = 150 kDa, purchased from Ossila Lim.) in chloroform (CF) that was heated to 60 °C and stirred for 1 h. The

Scheme 1. Synthesis of the Dopants Studied in this Work (Left) and Chemical Structure of P(NDI2OD-T2) (Right)



concentration of the solutions was 10 mg mL⁻¹. The solution was filtered with a 0.45 μ m pore size polytetrafluoroethylene (PTFE) filter. The dopant was dissolved in CF (solution concentration: 20.2 mM). Aliquots of dopant solution (0, 14.3, 42.7, and 100 μ L) were added to four different vials, each containing 200 μ L of the pristine polymer solution and mixed at room temperature. The molar ratio (MR) between the number of dopant molecules and the number of monomeric polymer units was MR = 0, 0.14, 0.43, and 1.00, respectively. The solutions were drop cast on KRSS (thallium bromide) and ZnSe substrates. Films were annealed in a Schlenk tube at 150 °C for 6 h in Ar.

2.3. IR and Raman Spectroscopy. FT-IR spectra of the drop-cast films were acquired in air at room temperature before and after annealing the samples. A Nicolet Nexus spectrometer (resolution 2 cm⁻¹, 256 scans to enhance the signal-to-noise ratio) was used in transmission mode for both the KRSS and the ZnSe substrates. Raman spectra at different exciting wavelengths were acquired on the drop-cast films in the same experimental conditions on each sample. Spectra at $\lambda_{exc} = 457.9$ nm and $\lambda_{exc} = 514$ nm (Ar¹ laser) were performed by means of a Jobin Yvon Labram HR800 Raman spectrometer equipped with an Olympus BX41 microscope and an edge filter system. The experiments were carried out in a backscattering geometry using a 50 \times objective. The laser power was set at 0.200 mWatt to prevent sample degradation. Spectra were recorded in the range 200–3200 cm⁻¹ in the Raman Stokes region. A Si wafer was used for calibration (520.7 cm⁻¹ spectral line). FT-Raman spectra ($\lambda_{exc} = 1064$ nm) were acquired with a Raman Nicolet NXR 9650 spectrometer equipped with a MicroStage (resolution 4 cm⁻¹, 1024 scans, laser power 200 mW).

Both IR and Raman spectra were analyzed with the OMNIC software.

2.4. Computational Details. Periodic DFT calculations on the 1D infinite polymer in the neutral and charged (doped) state were carried out using CRYSTAL14 software.^{32,33} A full geometry optimization of both the atom coordinates and the cell parameters was run before the simulation of the IR and Raman spectra using hybrid B3LYP functional combined with 6-31G(d,p) basis set. This level of theory has been indeed successfully applied in the past for the calculation of vibrational spectra of a variety of molecular crystals, including polyconjugated systems.^{34–37} The prediction of the Raman response has been done by using the Couple-Perturbed Kohn–Sham method, while the calculations for the doped polymer were carried out in the spin polarized (unrestricted) formalism. A shrinking factor of 20, corresponding to 11 k-points in the irreducible Brillouin zone, was used along the periodic direction, while the tolerances on integral screening (TOLINTEG parameters) were fixed to 8, 8, 9, and 30.

We carried out gas-phase DFT calculations on selected molecular fragments of P(NDI2OD-T2) using the Gaussian suite.³⁸ For consistency and for the sake of comparison, we adopted the same functional and basis set of the periodic boundary calculations executed with the CRYSTAL14 code (namely, B3LYP/6-31g(d,p)). A set of postprocessing programs developed at Politecnico di Milano was used to scrutinize the vibrational normal modes and simulate the Raman and IR spectra from the results of DFT calculations. Given the shallowness

of the potential energy surface along the (θ , τ) dihedrals, the calculation of vibrational frequencies corresponding to the structures obtained from constrained optimizations at fixed (θ , τ) did not produce significantly large imaginary frequencies (in any case below 130 cm⁻¹). For this reason, these geometry-constrained calculations of vibrational spectra are deemed reliable in the wavenumber range discussed in this work (1800–800 cm⁻¹).

3. EXPERIMENTAL RESULTS AND DISCUSSION

We chose three dopants with different substitution on the nitrogen of aniline, namely diphenyl (DPhBI), dibutyl (DBuBI), and diisopropyl (DiPrBI) (see Scheme 1, left). The first compound is one of the two species which was first used by Schlitz et al. to dope P(NDI2OD-T2),¹⁷ whereas the last two dopants showed the best conductivity values in ref 18 and differ for the steric hindrance of the substituents. The dopants were synthesized according to the general route already reported in the literature (Scheme 1) with some modifications. Synthesis methods are detailed in the Supporting Information.

Films of both pristine and doped P(NDI2OD-T2) were prepared by drop casting a chloroform solution either on KRSS or ZeSe supports and annealing at 150 °C in inert ambient conditions.¹⁸ Following previous experiments,¹⁸ here we choose relative concentration of the dopant with respect to the polymer at 5, 15, and 35 wt % for DBuBI. This choice of concentrations allowed us to highlight the effect of different doping regimes, namely a relatively small dopant amount, the dopant concentration corresponding to the maximum conductivity,^{17,18} and a very high doping, corresponding to one dopant molecule per polymer chemical unit. In the present work, instead of reporting the weight concentration, we refer to the corresponding molar ratio with respect to the single monomeric unit of the polymer (for DBuBI: MR = 0.14, 0.43, and 1.0, respectively). We kept these MR values fixed for all the dopants we considered. Accordingly, the number of dopant molecules considered for any concentration does not depend on the molar mass of the specific dopant.

3.1. IR Spectra. In this Section, we present and discuss evidence of chemical doping of P(NDI2OD-T2) based on IR spectroscopy. Remarkably, the IR spectra of doped annealed films show several new bands which cannot be ascribed either to the polymer in its pristine state or to unreacted dopant molecules. This is illustrated in Figure 1, which reports the IR spectra of P(NDI2OD-T2) films cast on KRSS substrate from a chloroform solution containing P(NDI2OD-T2) and DPhBI dopant in different molar ratios. The spectra were recorded in transmission mode both before (Figure 1a) and after (Figure 1b) annealing.

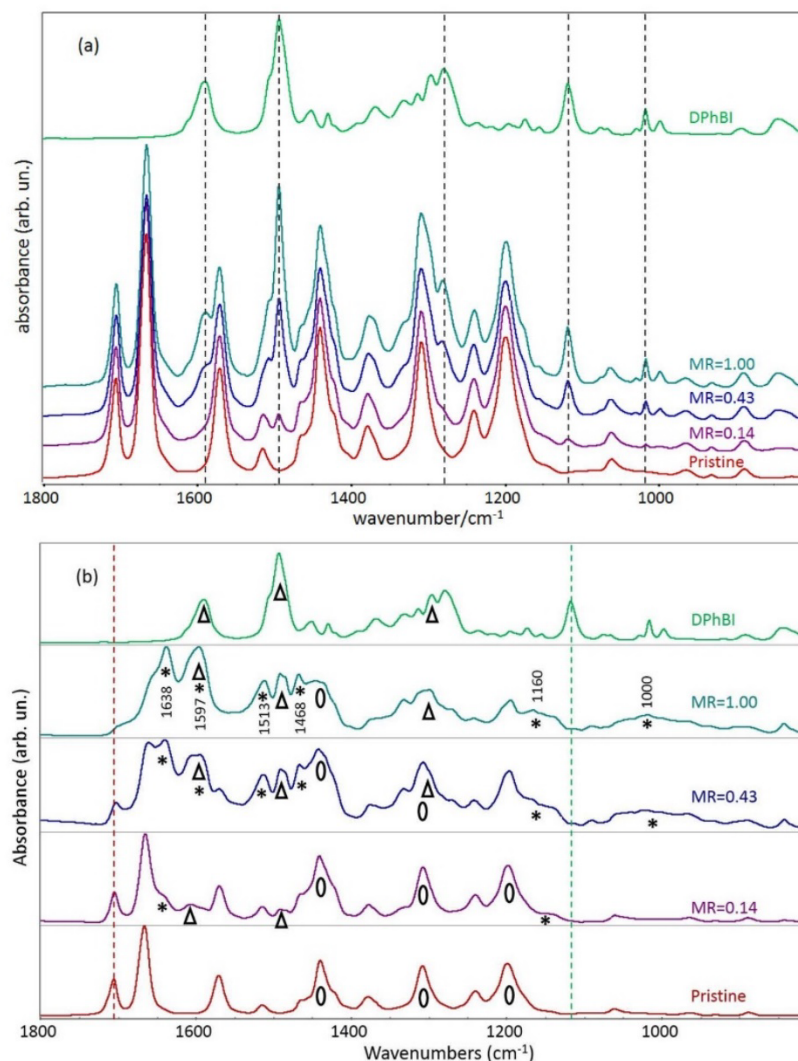


Figure 1. Panel a: IR spectra of P(NDI2OD-T2):DPhBI mixture with increasing molar ratio MR of dopant/polymer (MR = 0.14, 0.43, and 1.0; MR is referred to the polymer chemical unit). Spectra of films were recorded before annealing. The IR spectra of the pristine polymer (bottom) and dopant (top) are reported for comparison. Dotted lines correspond to strong absorption features of pristine DPhBI. Panel b: IR spectra of the same samples reported in panel a after annealing. The red dotted line shows the trend of symmetric CO stretching feature of the pristine polymer. The green dotted line corresponds to a strong marker band of pristine DPhBI. Asterisks label the features assigned to the polaron. Triangles and circles correspond to IR transitions assigned to the dopant molecule and the pristine polymer, respectively.

IR data unveil that the annealing procedure is a mandatory step which promotes the formation of a complex between the polymer and the dopant molecule through the transfer of one electron from the dopant molecule to P(NDI2OD) and the subsequent polaron formation. This is proved by the fact that all the spectra acquired before annealing (Figure 1a) show simultaneous absorption features of the pristine dopant (broken vertical lines) and pristine polymer. Actually, they can be described as a weighted sum of the spectra of the two pristine compounds (i.e., polymer and dopant), as illustrated by spectra processing (Supporting Information, Figure S1), thus suggesting that the as-deposited film is a mixture of the two weakly interacting species.

We observe a completely different situation for the IR spectra of the annealed doped films (Figure 1b), which indeed demonstrates that a remarkable structural relaxation upon doping occurred on the polymer, thus affecting its vibrational dynamics. First, the strong IR band characteristic of the dopant at 1120 cm^{-1} (clearly detectable in the spectra acquired before annealing, Figure 1a) is not observed in all the spectra of the annealed films. This strongly suggests that the dopant reacts almost quantitatively after annealing.

Moreover, two marker bands typical of the pristine polymer weaken while the doping ratio is increased and practically disappear at the highest dopant amount. These are the symmetric C=O stretching band (1706 cm^{-1} , red broken line in Figure 1b) and the band located at 1570 cm^{-1} (CC stretching

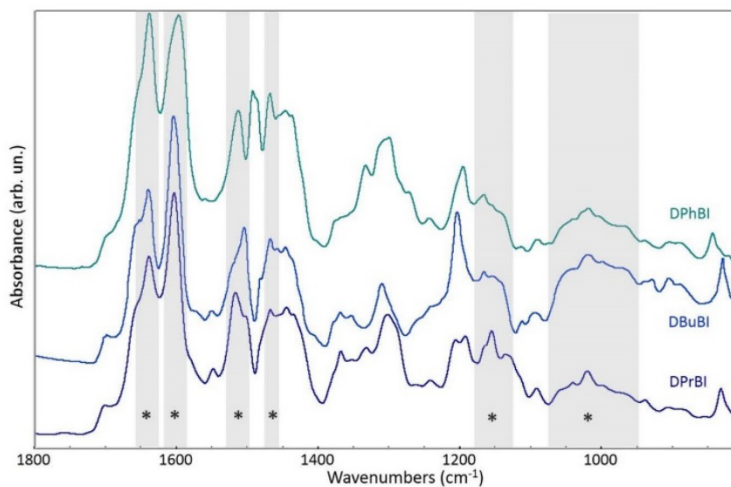


Figure 2. Comparison of the IR spectra of films of P(NDI2OD-T2) doped with DPhBI, DBuBI, or DiPrBI (MR = 1). All spectra were recorded after annealing. Spectral regions corresponding to polaron features are highlighted in gray (see also Figure 1b).

of NDI2OD). Furthermore, when MR = 1, the strong antisymmetric C=O stretching band of the pristine polymer (1666 cm^{-1}) appears as a shoulder of a new absorption feature (starred in Figure 1b).

When the dopant percentage is increased, several additional features emerge. We can group them as follows:

- (i) Bands which are close to IR transitions of the pristine dopant: these could be ascribed to the reacted dopant molecule. These bands (1597 cm^{-1} , 1490 cm^{-1} , and the structured feature at 1300 cm^{-1}) are labeled by triangles in Figure 1b.
- (ii) Features which are close to IR bands of the pristine polymer (labeled by circles in Figure 1b): these can be clearly detected also at high dopant concentration, suggesting that these bands may originate from chemical groups of the polymer that are only weakly affected by doping.
- (iii) New features corresponding to absorption bands neither of the pristine polymer nor of the unreacted dopant: these should be taken as markers of the charge defects formed on the polymer upon doping (i.e., polarons). These bands, namely the 1638 cm^{-1} and the very broad features at 1160 and 1000 cm^{-1} , are marked by asterisks in Figure 1b.
- (iv) Two strong absorptions at 1513 and 1468 cm^{-1} (marked by asterisks in Figure 1b) showing a clear increasing trend in intensity with dopant concentration. The remarkable growth of these bands is certainly ascribed to the doping induced charge defects, while the occurrence of these transitions at frequencies close to those of pristine P(NDI2OD) can be justified according to the vibrational mode. Indeed, normal modes showing a strong coupling between vibrational displacements involving the polaron defect and vibrations of polymer units not affected by the doping are weakly sensitive (in frequency) to the doping. This point will be better clarified considering vibrational nuclear displacements from DFT calculations.

The evidence so far illustrated indicates that the IR spectrum is sensitive to dopant–polymer interactions: several new IR

features (points iii–iv) allow monitoring the progress of the doping, thus providing the signature of the charged polaron.

The experimental findings illustrated in Figure 1 are not exclusive of the DPhBI doped films. Very similar IR features can be observed for annealed P(NDI2OD-T2) films doped with the other two *N*-alkyl 1*H*-benzimidazoles (Figure 2). The whole set of spectroscopic data collected varying the dopant and its concentration is reported in the Supporting Information (Figures S2 and S3). We also ruled out any possible degradation phenomena during the film preparation, as no different IR features arise when comparing the spectrum of a sample cast in air (see Methods) with the spectrum of an analogous sample completely prepared under inert atmosphere (Supporting Information, Figure S4).

Remarkably, the IR spectra of electrochemically doped P(NDI2OD-T2) films³⁹ show the growth of the same bands described at points iii and iv and of the strong feature at 1597 cm^{-1} (point i). On the basis of this evidence, we conclude that the 1597 cm^{-1} band observed in the spectra of the chemically doped samples is another feature characteristic of the doped polymer, possibly superimposed to a band of the dopant molecule (Supporting Information, Figure S5). This conclusion is in agreement with the assignment proposed in ref 31.

Turning to the intensity pattern upon doping, our experiments show that the doping-induced IR bands of P(NDI2OD-T2) behave differently from the so-called IRAV features observed while doping other conductive polymers such as polyacetylene, polythiophenes, and other related materials. IRAV intensities are huge when compared with the IR bands of the pristine polymers. A careful recent experimental determination reported in ref 29 revealed that for doped poly[2,6-(4,4-bis(2-ethylhexyl)-4*H*-cyclopenta[2,1-*b*:3,4-*b'*]dithiophene)-*alt*-4,7-(2,1,3-benzothiadiazole)] (PCPDTBT) and poly(2,6-(4,4-dialkyl)-4*H*-cyclopenta[2,1-*b*:3,4-*b'*]dithiophene) (PCPDT), IRAV dipole strengths are comparable to that of electronic transitions. It is also known that even a small percentage of dopant (see Gussoni et al.²³ and references therein) gives rise to strong IRAV bands in polyacetylene and oligoenes whose intensity exceeds several times that of the pristine material. By contrast, even in highly doped P(NDI2OD-

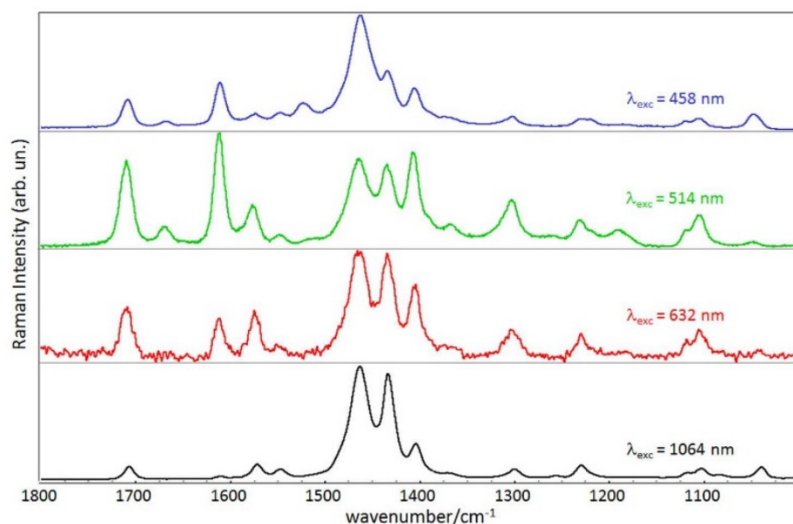


Figure 3. Raman spectra of pristine P(NDI2OD-T2) recorded with different excitation wavelengths ($\lambda_{\text{exc}} = 1064, 632, 514,$ and 458 nm). Standard fluorescence background subtraction was applied to the spectra recorded at 514 and 632 nm.

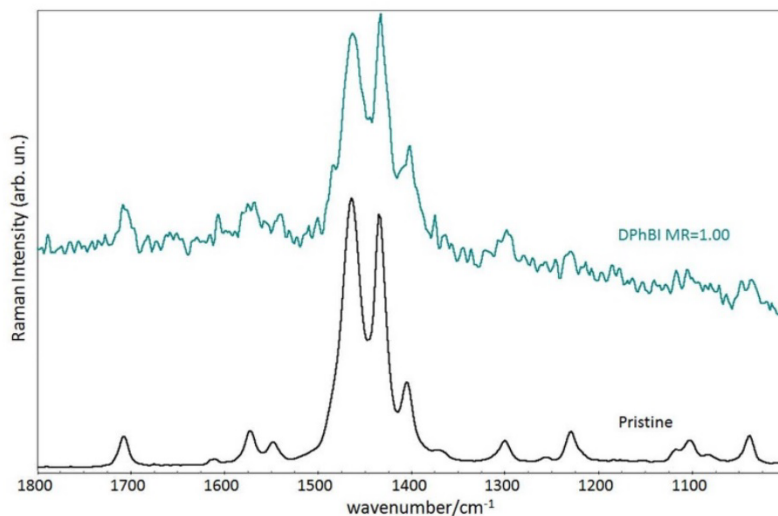


Figure 4. FT-Raman spectra ($\lambda_{\text{exc}} = 1064$ nm) of pristine P(NDI2O2-T2) (bottom) and highly doped P(NDI2O2-T2):DPhBI (MR = 1) (top).

T2), the polaron markers have intensities comparable to those of the pristine polymer (Figure 1b).

In other words, the IR spectral pattern of doped P(NDI2OD-T2) does not indicate the occurrence of peculiar long-range polarization phenomena coupled with the vibrational modes of the polaron such as those active in polyacetylene, polythiophene, and related materials.^{29,23,24,28} Thus, the observed behavior of the IR intensities of doped P(NDI2OD-T2) parallels the conclusions of previous studies,^{19,15,40} suggesting that charge defects in P(NDI2OD-T2) are confined. Quantum chemical molecular modeling, presented in Section 4, corroborates this conclusion.

3.2. Raman Experiments. The discussion of the Raman spectra of doped P(NDI2OD-T2) requires the study of the spectral evolution of the pristine material as a function of the

excitation wavelength. To the best of our knowledge, this analysis has not yet been reported in the literature.

The absorption spectrum of P(NDI2OD-T2) (see Supporting Information, Figure S6), showing strong bands in the visible-NIR region,^{19,15} justifies the occurrence of resonance or preresonance phenomena which affect the Raman response as the excitation wavelength changes along the sequence 458, 514, 632, and 1064 nm (Figure 3). The excitation energy remarkably modulates relative Raman intensities: a pattern of three bands in the region 1500–1380 cm^{-1} dominates the spectrum recorded with 1064 nm excitation, whereas in the spectrum excited at 514 nm, strong Raman transitions appear in the 1720–1520 cm^{-1} region.

The vibrational assignment proposed in ref 21 based on the analysis of computed vibrational eigenvectors indicates that the Raman active bands observed at 1464, 1434, and 1406 cm^{-1} are

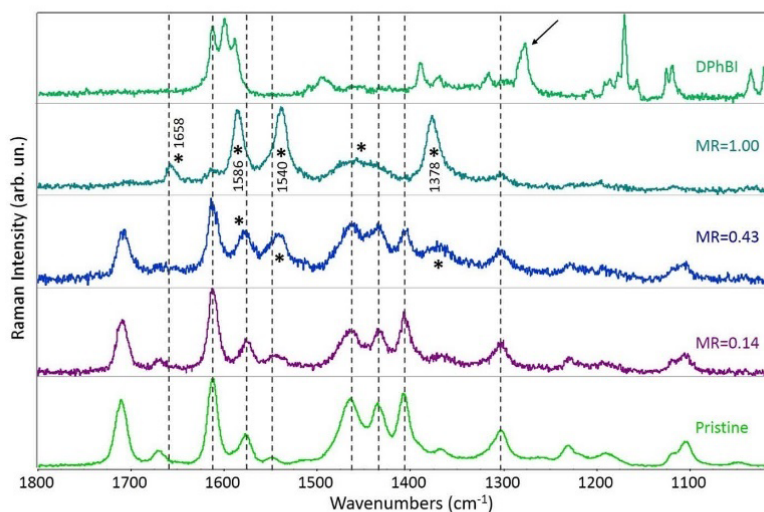


Figure 5. From bottom to top: Raman spectra ($\lambda_{\text{exc}} = 514 \text{ nm}$) of pristine P(NDI2O2-T2), DPhBI doped P(NDI2O2-T2) at increasing dopant/polymer molar ratio (MR = 0.14, 0.43, and 1.00), and pristine DPhBI. Asterisks label doping-induced features. Broken lines correspond to Raman transitions of the pristine polymer.

assigned to normal modes involving the bithiophene unit (T2). The line at 1464 cm^{-1} is assigned to a collective CC stretching of T2, describing the oscillation between aromatic and quinoidal structures. This mode is responsible for the strongest Raman line of oligo- and polythiophenes and is also referred to as the ECC or Я mode.^{23–25} The transition at 1464 cm^{-1} is a marker of the T2 unit and is close in frequency to the main Raman band observed in other thiophene-based materials.⁴¹

According to ref 21, the other two strong bands located at 1434 and 1406 cm^{-1} are assigned to normal modes which involve both CC stretchings of NDI2OD and vibrational displacements of T2, which explains their remarkable intensity in the Raman spectrum excited at 1064 nm . Instead, features assigned to modes localized on the NDI2OD units (CO and CC stretching) are very weak in the spectrum recorded with NIR excitation. This observation suggests the occurrence of selective enhancement of the Raman scattering in preresonance with the low energy $\pi-\pi^*$ transition, which mainly involves electronic excitation from the HOMO level localized on T2.

While increasing the excitation energy, bands associated with normal modes involving T2 become less important in comparison with vibrations of the NDI2OD unit (1708 cm^{-1} symmetric C=O stretching; 1610 and 1572 cm^{-1} CC stretchings), which show a remarkable intensity enhancement. In a parallel way, the change in the relative intensities in the $1500\text{--}1380 \text{ cm}^{-1}$ region is due to the different contributions from the NDI2OD unit in the three normal modes assigned to the 1464 , 1434 , and 1406 cm^{-1} Raman transitions. When exciting at 458 nm , the spectral pattern observed with 1064 nm excitation is partially recovered, thus suggesting the interplay of different electronic excited states contributing to the intensity pattern of the Raman transitions.

In summary, the experimental data analyzed so far indicate that multiwavelength Raman spectroscopy allows focusing selectively on the different building blocks of the pristine polymer. We may expect similar effects also in the case of the doped material. We compare in Figure 4 the FT-Raman spectra (1064 nm excitation) of the highly doped polymer with the

spectrum of the pristine material. The spectrum of the polymer doped with DPhBI is dominated by the normal modes involving T2 units and, except for a moderate broadening, shows the same pattern observed for the pristine polymer. This suggests that T2 moieties are almost unaffected by charge transfer from the dopant. Because the FT-Raman spectra of the doped materials are noisy in the region of the NDI2OD modes, it is hard to infer possible doping induced changes on the NDI2OD units.

Spectra recorded with 514 nm excitation show a completely different situation. Figure 5 shows a clear evolution of the Raman pattern with the dopant percentage: four new strong features show up at 1658 , 1586 , 1540 , and 1378 cm^{-1} , and the triplet at 1464 , 1434 , and 1406 cm^{-1} weakens and broadens. Furthermore, the strong CO stretching (1708 cm^{-1}) vanishes at the highest dopant concentration, as expected based on the evolution of the IR spectrum (Figure 1b). This clearly confirms that electron transfer affects the NDI2OD units. The whole set of spectroscopic Raman data at 514 nm is reported in Supporting Information (Figure S7).

Moreover, we verified that the Raman transitions of the dopant molecules are not observed in the Raman spectra of the doped polymer, as it can be inferred by comparison of the spectra of the doped polymer, reported in Figure 5, with the spectrum of pristine DPhBI (Figure 5, top). This may be expected because the high band gap dopant molecules do not benefit from any near resonance intensification of their Raman transitions, contrary to the low band gap material P(NDI2O2-T2), showing strong Raman features which dominate the Raman spectrum.

The spectra of the doped polymer acquired at 458 nm do not show new features ascribed to the doping until the highest dopant percentage is reached (Supporting Information, Figures S8–S11).

The relevant conclusion from the Raman analysis of the doped polymer is that the Raman signature of the polaron can be clearly detected only by virtue of peculiar resonance enhancement with excitation at 514 nm . Remarkably, the doping induced band observed at 482 nm ¹⁹ in the electronic absorption

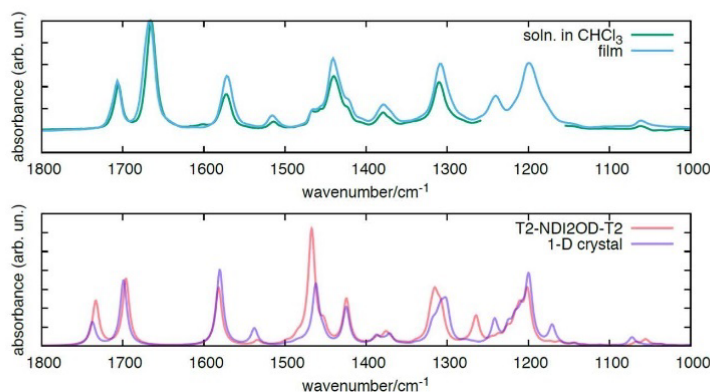


Figure 6. Top panel: experimental IR absorption spectra of P(NDI2OD-T2) in chloroform solution and as a film. Bottom panel: simulated IR spectra of P(NDI2OD-T2) by means of DFT calculations of T2-NDI2OD-T2 and of the polymer chain described as 1-D crystal.

spectrum of doped P(NDI2OD-T2) further supports this finding.

4. DFT MODELING

We present here the results of DFT calculations on models of P(NDI2OD-T2), aiming at the description of the vibrational features of pristine and charged species.

We discuss:

- (i) Possible effects of long-range interactions on the vibrational spectra of the polymer. This is based on the calculation of the IR and Raman spectra of the polymer chain with regular conformation, modeled as a 1-D crystal with the translational unit coincident with the polymer chemical unit (NDI2OD-T2). Calculations using CRYSTAL code (see Methods) are compared with calculations using Gaussian code on a small molecular model of the polymer, namely one central NDI2OD unit linked to two T2 units, hereafter referred as T2-NDI2OD-T2.
- (ii) Modulation of the vibrational spectra through changes of selected conformational degrees of freedom. For the T2-NDI2OD-T2 model, we considered changes of the torsional angle θ around the CC link between NDI2O2 and T2 units and of the torsional angle τ around the CC bond linking the two thiophene rings. The rather flat potential energy surface in a wide range of θ and τ values around the minima motivates this discussion. Gas-phase molecular modeling neglects solid-state effects, which can affect the equilibrium structure of the polymer chain, especially in the presence of such soft degrees of freedom. Thus, intermolecular interactions in solid-state could stabilize conformations different from the one optimized in gas-phase. Calculations carried out on several conformations can also highlight the origin of some observed spectral features, possibly related to structural disorder.
- (iii) We adopted the gas-phase equilibrium structure of neutral T2-NDI2OD-T2 as a guess geometry of the radical anion (negatively charged polaron). After geometry optimization, we computed the IR spectrum of the radical anion. This model provides the theoretical support for the identification and assignment of doping induced IR features. We also compared the results from this molecular model with those obtained for a charged 1-D crystal where each translational unit is a radical anion.

For all the models adopted, we explicitly include octyl-dodecyl side-chains with the only exception of the doped 1-D crystal, where alkyl chains have been replaced by methyl groups for the sake of reducing computational burden (due to the spin-polarized nature of the latter calculation). Following the previous results by Giussani et al.,²¹ we selected a fully *trans* conformation of the side chains without further investigating the effect of conformational defects in the alkyl chains.

4.1. Prediction of the Vibrational Spectra of Pristine P(NDI2OD-T2): 1-D Crystal vs Molecular Model. We compare in Figure 6 the experimental IR spectrum of pristine P(NDI2OD-T2) with that computed for 1-D crystal and for the T2-NDI2OD-T2 molecular model (lower energy conformation). Figure 6 shows a substantial agreement between theory and experiment. Moreover, the computed spectrum of the 1-D crystal and that of T2-NDI2OD-T2 show a similar pattern with a very good coincidence of the position of the main peaks. This suggests that periodic boundary conditions have negligible effects on the vibrational dynamics because of limited electron delocalization effects, which would imply long-range vibrational couplings along the polymer chain and strong dependence of the spectra by the chain length.²⁷ The major discrepancy between the two computed spectra is the higher absorption intensity predicted for T2-NDI2OD-T2 in the region between 1500 and 1400 cm^{-1} , which we assign to vibrational modes involving T2. This discrepancy simply comes from an incorrect T2/NDI2OD ratio in molecular model (i.e., 2 instead of 1). Interestingly, the band observed at 1241 cm^{-1} (assigned to wagging vibrations of CH bonds) is better predicted by the calculation for the infinite chain because of spurious coupling effects with the CH end groups of the T2-NDI2OD-T2 model.

A closer look at Figure 6 shows two more issues:

- (i) compared with the experiment, both calculations predict a too high frequency of the CO stretching bands (by about 30 cm^{-1}), and
- (ii) DFT overestimates the relative intensity of the bands below 1600 cm^{-1} with respect to the CO stretching transitions.

Observation (i) is interesting and related to the degrees of freedom in the choice of the frequency-scaling factor.⁴² For instance, the 0.98 factor we adopt here proves to be the most suitable in the spectral comparison of other polyconjugated systems (see, for instance, ref 43). A lower scaling factor could

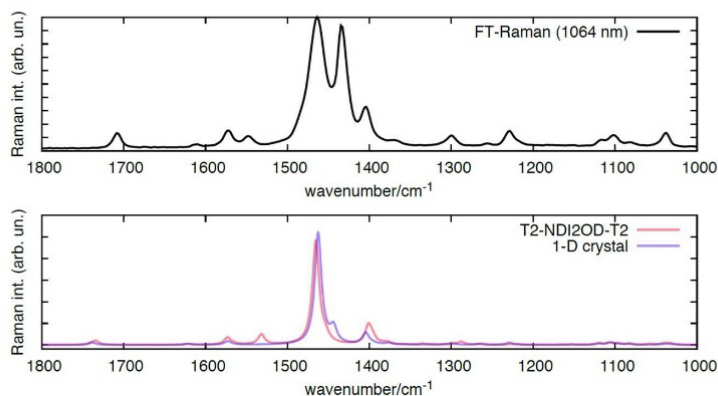


Figure 7. Top panel: experimental FT-Raman spectrum of the pristine polymer film ($\lambda_{\text{exc}} = 1064$ nm). Bottom panel: simulated Raman spectra of P(NDI2OD-T2) by means of DFT calculations of T2-NDI2OD-T2 and of the polymer chain described as 1-D crystal.

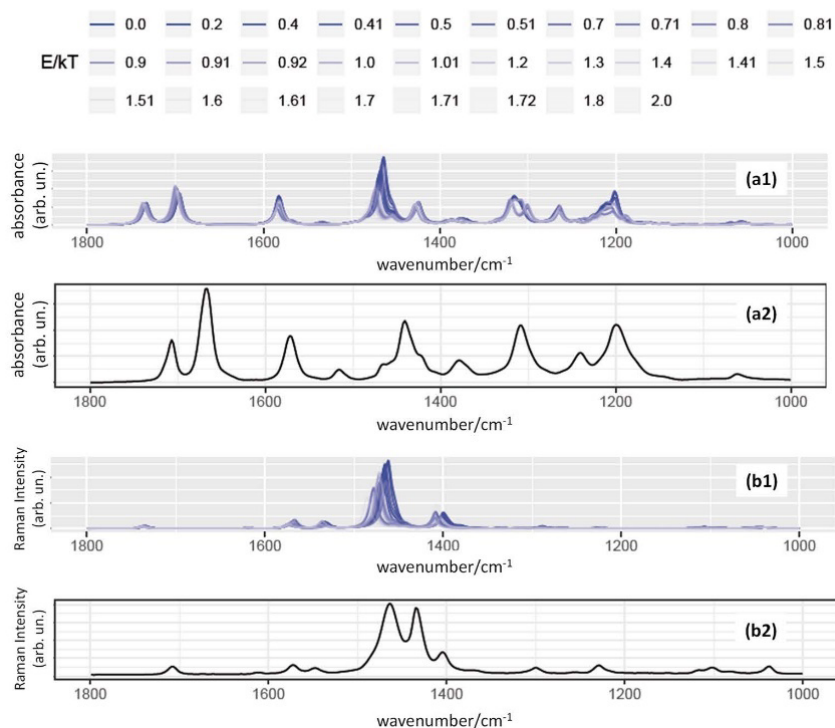


Figure 8. DFT computed IR (a1) and Raman (b1) spectra of the different T2-NDI2OD-T2 conformers with energies in the range $(E - E_0)/kT \leq 2$ (E_0 is the energy of the lower energy conformer; $T = 300$ K). Each conformer corresponds to a pair of selected values (θ, τ) according to the procedure illustrated in the text. The experimental spectra (black lines, a2, b2) are shown for comparison.

guarantee a good fit over the CO stretching region but would systematically underestimate peak frequencies in the range below 1600 cm^{-1} . We believe that this finding unveils the remarkably anharmonic nature of the CO bonds of the NDI2OD unit, as proven experimentally by the presence of a strong combination band at 3359 cm^{-1} (Supporting Information, Figure S12).

Issue (ii), related to the intensity pattern, is discussed in Section 4.2 dealing with conformational effects.

The similarity of the computed Raman spectra of the 1-D crystal and of the oligomer (computed in the limit of static

excitation) is impressive (Figure 7). Because the two calculations give the same predicted frequency of the main Raman transition, this indicates that the interaction of different units along the polymer backbone is weak (this is consistent with the previous discussion on IR).

Due to the rich resonance effects probed by multiwavelength Raman spectra (Section 3.2), we can use the computed Raman spectra for a qualitative discussion of the spectra recorded with NIR excitation (1064 nm). Indeed, both calculations (1-D crystal, T2-NDI2OD-T2) capture the predominance of the Raman features associated with vibrations of the T2 moiety.

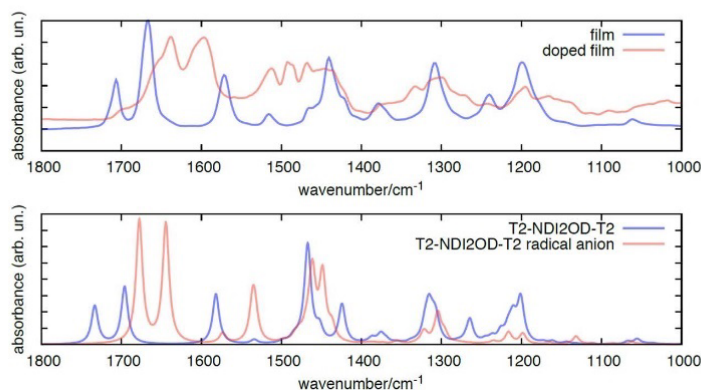


Figure 9. Top panel: experimental IR absorption spectra of pristine P(NDI2OD-T2) and of the polymer doped with DPhBI (MR = 1). Bottom panel: DFT simulated IR spectra of (T2-NDI2OD-T2) and its radical anion.

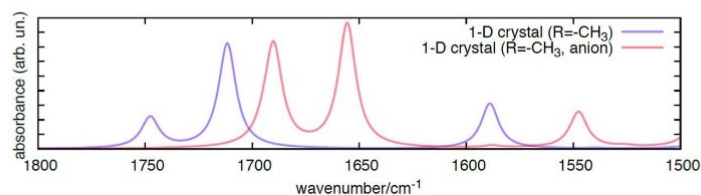


Figure 10. Bottom panel: DFT simulated infrared spectrum of P(NDI2OD-T2) described as a 1-D crystal in the pristine and charged state (1 electron per chemical unit).

However, the two strong bands observed at 1434 and 1406 cm^{-1} have theoretical counterparts showing too weak intensity. In the case of the computed spectrum of T2-NDI2OD-T2, the feature at 1434 cm^{-1} cannot be identified. This disagreement may be due to preresonance effects taking place in the experimental spectrum but not properly described by the calculation and/or may be due to limitations in the adopted basis set (6-31G(d,p)). The better performance in the prediction of the Raman spectrum based on a better basis set (6-311G(d,p))²¹ suggests that the introduction of a split-valence triple- ζ basis set is effective to improve the description of the individual components of the observed triplet (1464, 1434, and 1406 cm^{-1}).

4.2. Conformation Dependent Vibrational Spectra. We computed the vibrational spectra of nonequilibrium conformations of T2-NDI2OD-T2 to investigate the effect of the backbone chain conformation on the spectral pattern. We generated a grid of equally spaced values ($\Delta\theta = \Delta\tau = 10^\circ$) in the range $50^\circ < \theta < 150^\circ$ and $140^\circ < \tau < 180^\circ$. This choice allows exploration of the two minima of the potential energy surface, which correspond to *syn* and *anti* conformations.²¹ For each (θ , τ) value fixed in the grid, we carried out a constrained optimization of the geometry and the calculation of the IR and Raman spectra (Figure 8). The map reported in the Supporting Information (Figure S13) shows potential energy values obtained with this procedure. Among the points of the grid, we selected those corresponding to energies $(E - E_0)/kT \leq 2$ (E_0 is the energy of the lower energy conformer; $T = 300$ K).

Figure 8 shows that changes of the polymer conformation give rise to band shifts and modulation of the intensity pattern. This allows justification of the experimental pattern, characterized by rather broad absorption bands, as the result of contributions coming from chains with different geometries. Notice that the

experimental observation suggests the presence of conformational disorder: remarkably, the IR pattern of the sample in solution and in solid-state are almost superimposed (see Figure 6, top). This is consistent with a distribution of conformations also in solid state, which is known to be characterized by a complex morphology.^{18,22} Among the different conformations examined, several of them provide IR spectra showing a better fit of some experimental features. However, the improvement of the prediction in a given region is often accompanied by a worsening in the prediction of some other details (Supporting Information, Figure S14), which suggests the interpretation of the experimental spectrum in terms of inhomogeneous broadening.

As expected, the frequency position of the main Raman transition is sensitive to the polymer conformation, which modulates the π electron interactions within T2 units and between T2 and NDI2OD. The large width of the strongest band at 1464 cm^{-1} can be thus nicely accounted for by considering the presence of conformational disorder (Figure 8).

4.3. Prediction of the Vibrational Spectra of the Radical anion. Figure 9 shows the IR spectrum of the radical anion of T2-NDI2OD-T2 compared with that of the corresponding neutral species. Doping induced bands computed by DFT show a nice agreement with the experimental findings. The doping-induced bands observed in the spectrum (1638, 1595 cm^{-1}) find their theoretical counterpart in the strong features at 1677 and 1644 cm^{-1} (scaled frequency values⁴⁴). The absorptions observed at 1513 and 1468 cm^{-1} correspond to the doublets predicted at 1533–1536 and 1461–1448 cm^{-1} , respectively. These doping induced IR bands mainly involve CC stretching of the NDI2OD unit dynamically coupled to CC stretching of the thiophenes rings (Supporting Information, Figure S15). The collective character of these modes, involving

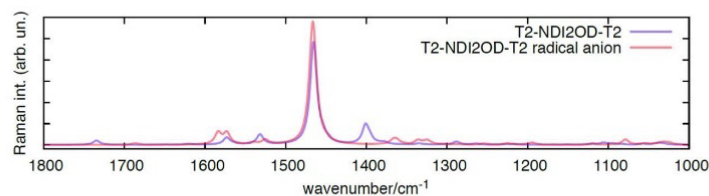


Figure 11. DFT simulated Raman spectrum of (T2-NDI2OD-T2) and of its radical anion.

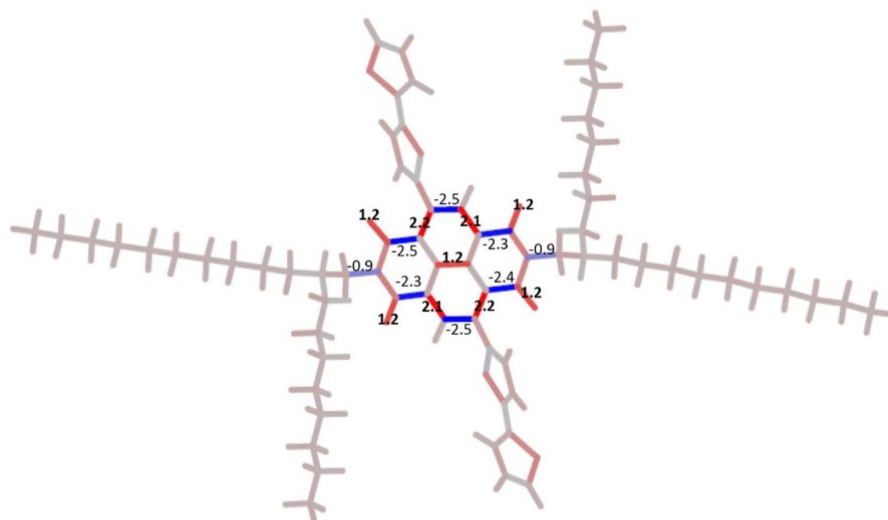


Figure 12. Bond distance changes (ΔR , 10^{-3} nm = pm) occurring upon charging T2-NDI2OD-T2. Gray color indicates that bond lengths are not modified; red and blue color scales are adopted to describe stretching and shrinking of the bonds, respectively. Only values $|\Delta R| \geq 0.9$ pm are reported in the figure.

both T2 and NDI units, nicely explains why these bands find a counterpart very close in frequency but with smaller IR intensity in the spectrum of the undoped species.

DFT calculations show that, overall, the doping induced features have IR absorption intensities comparable with the intensities predicted for the neutral species. Indeed, the total IR intensity (integrated over the whole 1800–1000 cm^{-1} region) amounts to 5014 km mol^{-1} for neutral T2-NDI2OD-T2 and 5788 km mol^{-1} for its radical anion, in agreement with the suggestion from experiments. This confirms that we are not in the presence of anomalously strong IRAV.

The possibility to predict IR features based on a very small molecular model provides further evidence of the localization of the polaron. The prediction of the IR spectrum of a fully doped polymer chain as a 1-D crystal confirms this conclusion. As justified above, we adopted a simplified model of 1-D crystal model, not including alkyl side chains: focusing on the spectral region unaffected by the alkyl chains (1800–1500 cm^{-1}), the doped 1-D crystal shows the same spectra pattern obtained for the small T2-NDI2OD-T2 anion (Figure 10)⁴⁵.

As discussed in Section 4.2, the simulation of the Raman response in the simplified hypothesis of a static field can be used to discuss the case of 1064 nm excitation. The experimental FT-Raman spectrum (1064 nm) of the doped material does not show any strong new doping-induced features because it is dominated by modes of T2 units. It is interesting to notice that DFT predicts small changes of the spectrum, as shown in Figure 11. This supports the conclusion that the T2 unit is practically

unaffected by the doping, in agreement with the previous discussion.

4.4. Structure Relaxation upon Doping. Results from DFT calculations demonstrate that T2-NDI2OD-T2 is an insightful molecular model of the polymer both in its neutral and doped state. Moreover, the spectroscopic experimental data collected, interpreted with the help of theory, suggest that the charging process and subsequent geometry relaxation take place on NDI2OD because the LUMO of the polymer is localized on NDI2OD units. This parallels the conclusions of ref 15 obtained by means of the analysis of spin density maps and geometry relaxation for a charged oligomer.

The data fully reported in the Supporting Information and summarized in Figure 12 show that upon charging, the CO and CC bonds of the naphthalene moiety are greatly affected. The CO bonds stretch and the CC bonds evolve with a pattern which can be described as a collective relaxation toward a quinoidal structure. As expected, the T2 unit undergoes very limited changes.

5. CONCLUSIONS

This paper presents a thorough IR and Raman spectroscopic study of the n-doping process of P(NDI2OD-T2), and shows that vibrational spectra are rich with information on the nature of the charge carriers formed upon doping.

The IR spectra provide a clear signature of the charged species, showing a pattern of marker bands that are independent

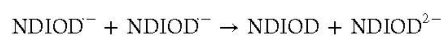
of the specific structure of the N,N-disubstituted 1*H*-benzimidazole. Doping-induced features are nicely modeled as vibrational bands of a radical anion localized on the NDI2OD moiety, thus proving that the interaction between NDI2OD and T2 building blocks is limited. This behavior is ascribed first to the electronic structure of the two comonomeric units, showing a poor energy matching of the frontier orbitals, and to the structure of the polymer backbone, highly distorted from planarity.

FT-Raman spectra are dominated by transitions assigned to T2 units and display very limited changes upon doping, thus confirming that T2 is not involved in the n-doping process. When approaching resonance with the NDI2OD units (514 nm), the evolution of the Raman spectra upon doping is fully consistent with IR findings.

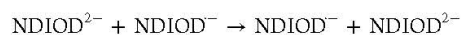
The satisfactory fitting of the experimental spectra of the doped polymer by DFT models of the radical anion of P(NDI2OD-T2) supports the concept that the doping process promoted by 1*H*-benzimidazoles as n-dopant does not involve hydride transfer to the acceptor NDI2OD unit but follows the mechanism of electron transfer between a donor and an electron acceptor.

Because the polaron is localized on NDI2OD units, the observed remarkable increase of the conductivity of n-doped P(NDI2OD-T2) should be ascribed to the strengthening of the intermolecular transport channel rather than to the activation of intrachain polaron diffusion (or hopping) mechanisms.

To reach high conductivity values in P(NDI2OD-T2), one needs high dopant concentrations. This suggests that intermolecular hopping involves new charge carriers and charge transfer processes different from those involved in the pristine case. Indeed, in the presence of a high concentration of charged NDI2OD units, the hopping process should involve both bimolecular reactions of the kind:



and



These processes are unlikely in the pristine state or at very low doping ratio because of the high dilution of charged species. We suggest that such processes have to be considered in models dealing with charge transport.

The presence of new and potentially favorable interchain hopping processes in P(NDI2OD-T2) implies that control of the morphology of the material remains the bottleneck in the search for optimal n-type conductivity. Under this regard, we agree with other authors^{15,19} who stressed the beneficial effect of the introduction of chemical groups which foster effective conjugation along the backbone, enabling the formation of delocalized charge defects, thus opening a new intrachain charge transport channel less affected by the material morphology.

In this framework, IR spectroscopy has an excellent diagnosis capability, as shown by the results presented here. In presence of charged species delocalized along the polymer backbone, very intense IRAV bands are expected. Instead, when localized polarons form upon doping, doping induced IR bands have dipole strengths comparable to those of the IR bands of the pristine material. This is the case of doped P(NDI2OD-T2), for which IR absorption experiments have revealed that polaron diffusion along the chain is unlikely.

■ ASSOCIATED CONTENT

Supporting Information

The Supporting Information is available free of charge on the ACS Publications website at DOI: 10.1021/acs.chemmater.9b01218.

Synthesis of DBuBi, DPhBi, and DPtBi; the whole set of IR and multiwavelength Raman spectra of P(NDI2OD-T2) doped with different molecules (Figures S1–S11); pristine spectra, zoomed on the CO combination bands (Figure S12); energy map for different nonequilibrium conformers of the model molecule T2-NDI2OD-T2 (Figure S13); computed IR spectra for low energy nonequilibrium conformers of T2-NDI2OD-T2 (Figure S14); optimized bond length distances and nuclear Cartesian coordinates for the model molecule T2-NDI2OD-T2 and its radical anion (Figure S15, Table S1, and Sketch S1); optimized Cartesian coordinates of the translational P(NDI2OD-T2) unit (Table S2) (PDF) Cartesian coordinates of the radical anion of T2-NDI2OD-T2 (XYZ)

Cartesian coordinates of T2-NDI2OD-T2 (XYZ)

■ AUTHOR INFORMATION

Corresponding Author

*E-mail: chiara.castiglioni@polimi.it.

ORCID

Luigi Brambilla: 0000-0003-2264-1792

Alberto Milani: 0000-0001-6026-5455

Matteo Tommasini: 0000-0002-7917-426X

Chiara Castiglioni: 0000-0002-6945-9157

Notes

The authors declare no competing financial interest.

■ REFERENCES

- Jacobs, I. E.; Moulé, A. J. Controlling Molecular Doping in Organic Semiconductors. *Adv. Mater.* **2017**, *29* (42), 1703063.
- Walzer, K.; Männig, B.; Pfeiffer, M.; Leo, K. Highly Efficient Organic Devices Based on Electrically Doped Transport Layers. *Chem. Rev.* **2007**, *107* (4), 1233–1271.
- Lüssem, B.; Keum, C. M.; Kasemann, D.; Naab, B.; Bao, Z.; Leo, K. Doped Organic Transistors. *Chem. Rev.* **2016**, *116* (22), 13714–13751.
- Kroon, R.; Mengistie, D. A.; Kiefer, D.; Hynynen, J.; Ryan, J. D.; Yu, L.; Müller, C. Thermoelectric Plastics: From Design to Synthesis, Processing and Structure-Property Relationships. *Chem. Soc. Rev.* **2016**, *45* (22), 6147–6164.
- Pekker, S.; Janossi, A. In *Handbook of Conducting Polymers*, Vol. 1, Chapter 2; Skotheim, T. A., Ed.; Dekker: New York, 1986.
- Brédas, J. L.; Silbey, R. *Conjugated Polymers: The Novel Science and Technology of Highly Conducting and Nonlinear Optically Active Materials*; Springer: Netherlands, 1991.
- Kao, C. Y.; Lee, B.; Wielunski, L. S.; Heeney, M.; McCulloch, I.; Garfunkel, E.; Feldman, L. C.; Podzorov, V. Doping of Conjugated Polythiophenes with Alkyl Silanes. *Adv. Funct. Mater.* **2009**, *19* (12), 1906–1911.
- Arlin, J.-B.; Lazzaroni, R.; Fahlman, M.; Andreasen, J. W.; Wang, H.; Bubnova, O.; Geerts, Y. H.; Murphy, P. J.; Evans, D. R.; Dagnehnd, D.; et al. Semi-Metallic Polymers. *Nat. Mater.* **2014**, *13* (2), 190–194.
- Gemming, S.; Di Pietro, R.; Kiriy, A.; Lappan, U.; Anokhin, D. V.; Erdmann, T.; Binner, M.; Raguzin, L.; Voit, B.; Günther, F.; et al. High Conductivity in Molecularly P-Doped Diketopyrrolopyrrole-Based Polymer: The Impact of a High Dopant Strength and Good Structural Order. *Adv. Mater.* **2016**, *28* (28), 6003–6010.
- Lee, B. H.; Kahng, Y. H.; Lee, K.; Kim, B.-J.; Lee, S. H.; Kim, N.; Jo, Y.-R.; Kee, S. Highly Conductive PEDOT:PSS Nanofibrils Induced

- by Solution-Processed Crystallization. *Adv. Mater.* **2014**, *26* (14), 2268–2272.
- (11) Zhan, X.; Facchetti, A.; Barlow, S.; Marks, T. J.; Ratner, M. A.; Wasielewski, M. R.; Marder, S. R. Rylene and Related Diimides for Organic Electronics. *Adv. Mater.* **2011**, *23* (2), 268–284.
- (12) Zheng, L.; Zhao, Z.; Yin, Z.; Zhu, C.; Chen, H.; Tang, Q.; Tan, S.; Guo, Y.; Liu, Y.; Zhang, L.; et al. High-Performance, Air-Stable Field-Effect Transistors Based on Heteroatom-Substituted Naphthalenediimide-Benzothiadiazole Copolymers Exhibiting Ultrahigh Electron Mobility up to $8.5 \text{ Cm}^{-1} \text{ s}^{-1}$. *Adv. Mater.* **2017**, *29* (4), 1602410.
- (13) Zhang, L.; Wang, Z.; Duan, C.; Wang, Z.; Deng, Y.; Xu, J.; Huang, F.; Cao, Y. Conjugated Polymers Based on Thiazole Flanked Naphthalene Diimide for Unipolar N-Type Organic Field-Effect Transistors. *Chem. Mater.* **2018**, *30* (22), 8343–8351.
- (14) Facchetti, A.; Jing, Y.; Yao, Y.; Rong, Y.; Chen, Z.; Liang, Y. Heavily N-Dopable π -Conjugated Redox Polymers with Ultrafast Energy Storage Capability. *J. Am. Chem. Soc.* **2015**, *137* (15), 4956–4959.
- (15) Wang, S.; Sun, H.; Ail, U.; Vagin, M.; Persson, P. O. Å.; Andreasen, J. W.; Thiel, W.; Berggren, M.; Crispin, X.; Fazzi, D.; et al. Thermoelectric Properties of Solution-Processed n-Doped Ladder-Type Conducting Polymers. *Adv. Mater.* **2016**, *28* (48), 10764–10771.
- (16) Wei, P.; Oh, J. H.; Dong, G.; Bao, Z. Use of a 1 H-Benzimidazole Derivative as an n-Type Dopant and to Enable Air-Stable Solution-Processed n-Channel Organic Thin-Film Transistors. *J. Am. Chem. Soc.* **2010**, *132* (26), 8852–8853.
- (17) Schlitz, R. A.; Brunetti, F. G.; Glaudell, A. M.; Miller, P. L.; Brady, M. A.; Takacs, C. J.; Hawker, C. J.; Chabincyn, M. L. Solubility-Limited Extrinsic n-Type Doping of a High Electron Mobility Polymer for Thermoelectric Applications. *Adv. Mater.* **2014**, *26* (18), 2825–2830.
- (18) Saglio, B.; Mura, M.; Massetti, M.; Scuratti, F.; Beretta, D.; Jiao, X.; McNeill, C. R.; Sommer, M.; Famulari, A.; Lanzani, G.; et al. N-Alkyl Substituted 1 H-Benzimidazoles as Improved n-Type Dopants for a Naphthalene-Diimide Based Copolymer. *J. Mater. Chem. A* **2018**, *6* (31), 15294–15302.
- (19) Naab, B. D.; Gu, X.; Kurosawa, T.; To, J. W. F.; Salleo, A.; Bao, Z. Role of Polymer Structure on the Conductivity of N-Doped Polymers. *Adv. Electron. Mater.* **2016**, *2* (5), 1600004.
- (20) Fazzi, D.; Caironi, M. Multi-Length-Scale Relationships between the Polymer Molecular Structure and Charge Transport: The Case of Poly-Naphthalene Diimide Bithiophene. *Phys. Chem. Chem. Phys.* **2015**, *17* (14), 8573–8590.
- (21) Giussani, E.; Fazzi, D.; Brambilla, L.; Caironi, M.; Castiglioni, C. Molecular Level Investigation of the Film Structure of a High Electron Mobility Copolymer via Vibrational Spectroscopy. *Macromolecules* **2013**, *46* (7), 2658–2670.
- (22) Giussani, E.; Brambilla, L.; Fazzi, D.; Sommer, M.; Kayunkid, N.; Brinkmann, M.; Castiglioni, C. Structural Characterization of Highly Oriented Naphthalene-Diimide-Bithiophene Copolymer Films via Vibrational Spectroscopy. *J. Phys. Chem. B* **2015**, *119* (5), 2062–2073.
- (23) Gussoni, M.; Castiglioni, C.; Zerbi, G. In *Advances in Spectroscopy: Spectroscopy of Advanced Materials*, Vol. 19; Clark, R. J. H., Hester, R. E., Ed.; Wiley & Sons: Chichester, UK, 1991; p 251.
- (24) Del Zoppo, M. E.; Castiglioni, C.; Zuliani, P.; Zerbi, G. In *Handbook of Conducting Polymers*, Vol. 2; Skotheim, T. A., Elsenbaumer, R. L., Reynolds, J. R., Eds.; Dekker: New York, 1998; pp 765–882.
- (25) Castiglioni, C.; Lopez Navarrete, J. T.; Zerbi, G.; Gussoni, M. A Simple Interpretation of the Vibrational Spectra of Undoped, Doped and Photoexcited Polyacetylene: Amplitude Mode Theory in the GF Formalism. *Solid State Commun.* **1988**, *65* (7), 625–630.
- (26) Ehrenfreund, E.; Vardeny, Z.; Brafman, O.; Horovitz, B. Amplitude and Phase Modes in Trans-Polyacetylene: Resonant Raman Scattering and Induced Infrared Activity. *Phys. Rev. B: Condens. Matter Mater. Phys.* **1987**, *36* (3), 1535–1553.
- (27) Castiglioni, C.; Tommasini, M.; Zerbi, G. Raman Spectroscopy of Polyconjugated Molecules and Materials: Confinement Effect in One and Two Dimensions. *Philos. Trans. R. Soc. A Math. Phys. Eng. Sci.* **2004**, *362* (1824), 2425–2459.
- (28) Chance, R.; Boudreaux, D. S.; Bredas, J. L.; Silbey, R. In *Handbook of Conducting Polymers*; Skotheim, T. A., Ed.; Dekker: New York, 1986; p 825.
- (29) Scherf, U.; D'Avino, G.; Allard, S.; Fontanesi, C.; Ramanan, C.; Surana, S.; Frick, A.; Furno, M.; Da Como, E.; Beljonne, D.; et al. Displacement of Polarons by Vibrational Modes in Doped Conjugated. *Polymers. Phys. Rev. Mater.* **2017**, *1* (5), 55604.
- (30) Yin, J.; Wang, Z.; Fazzi, D.; Shen, Z.; Soci, C. First-Principles Study of the Nuclear Dynamics of Doped Conjugated Polymers. *J. Phys. Chem. C* **2016**, *120* (3), 1994–2001.
- (31) Wang, S.; Fazzi, D.; Puttisong, Y.; Jafari, M. J.; Chen, Z.; Ederth, T.; Andreasen, J. W.; Chen, W. M.; Facchetti, A.; Fabiano, S. Effect of Backbone Regiochemistry on Conductivity, Charge Density, and Polaron Structure of n-Doped Donor–Acceptor Polymers. *Chem. Mater.* **2019**, *31*, 3395.
- (32) Rérat, M.; D'Arco, P.; De La Pierre, M.; Maschio, L.; Zicovich-Wilson, C. M.; Civalieri, B.; Kirtman, B.; Orlando, R.; Casassa, S.; Ferrabone, M.; et al. CRYSTAL14: A Program for the Ab Initio Investigation of Crystalline Solids. *Int. J. Quantum Chem.* **2014**, *114* (19), 1287–1317.
- (33) Dovesi, R.; Saunders, V. R.; Roetti, C.; Orlando, R.; Zicovich Wilson, C. M.; Pascale, F.; Civalieri, B.; Doll, K.; Harrison, N. M.; Bush, I. J.; D'Arco, P.; Llunell, M.; Causà, M.; Noël, Y.; *CRYSTAL14 User's Manual*, v 1.0.; University of Torino: Torino, 2014.
- (34) Galimberti, D.; Milani, A.; Maschio, L.; Castiglioni, C. Intermolecular Modulation of IR Intensities in the Solid State: the Role of Weak Interactions in Polyethylene Crystals: A Computational DFT Study. *J. Chem. Phys.* **2016**, *145* (14), 144901.
- (35) Quarti, C.; Milani, A.; Civalieri, B.; Orlando, R.; Castiglioni, C. Ab Initio Calculation of the Crystalline Structure and IR Spectrum of Polymers: Nylon 6 Polymorphs. *J. Phys. Chem. B* **2012**, *116* (28), 8299–8311.
- (36) Milani, A.; Castiglioni, C.; Radice, S. Joint Experimental and Computational Investigation of the Structural and Spectroscopic Properties of Poly(Vinylidene Fluoride) Polymorphs. *J. Phys. Chem. B* **2015**, *119* (14), 4888–4897.
- (37) Maschio, L.; Lorenz, M.; Pullini, D.; Sgroi, M.; Civalieri, B. The Unique Raman Fingerprint of Boron Nitride Substitution Patterns in Graphene. *Phys. Chem. Chem. Phys.* **2016**, *18* (30), 20270–20275.
- (38) Frisch, M. J.; Trucks, G. W.; Schlegel, H. B.; Scuseria, G. E.; Robb, M. A.; Cheeseman, J. R.; Scalmani, G.; Barone, V.; Mennucci, B.; Petersson, G. A.; Nakatsuji, H.; Caricato, M.; Li, X.; Hratchian, H. P.; Izmaylov, A. F.; Bloino, J.; Zheng, G.; Sonnenberg, J. L.; Hada, M.; Ehara, M.; Toyota, K.; Fukuda, R.; Hasegawa, J.; Ishida, M.; Nakajima, T.; Honda, Y.; Kitao, O.; Nakai, H.; Vreven, T.; Montgomery, J. A., Jr.; Peralta, J. E.; Ogliaro, F.; Bearpark, M.; Heyd, J. J.; Brothers, E.; Kudin, K. N.; Staroverov, V. N.; Kobayashi, R.; Normand, J.; Raghavachari, K.; Rendell, A.; Burant, J. C.; Iyengar, S. S.; Tomasi, J.; Cossi, M.; Rega, N.; Millam, J. M.; Klene, M.; Knox, J. E.; Cross, J. B.; Bakken, V.; Adamo, C.; Jaramillo, J.; Gomperts, R.; Stratmann, R. E.; Yazyev, O.; Austin, A. J.; Cammi, R.; Pomelli, C.; Ochterski, J. W.; Martin, R. L.; Morokuma, K.; Zakrzewski, V. G.; Voth, G. A.; Salvador, P.; Dannenberg, J. J.; Dapprich, S.; Daniels, A. D.; Farkas, O.; Foresman, J. B.; Ortiz, J. V.; Cioslowski, J.; Fox, D. J. *Gaussian 09*, revision D.01; Gaussian, Inc.: Wallingford, CT, 2009.
- (39) Giussani, E. Spectroscopic and Electrochemical Investigation of the High Electron Mobility Copolymer P(NDI2OD-T2) and Its Functional Derivates; Ph.D. Thesis, Politecnico di Milano: Milano, Italia, 2014.
- (40) Matsidik, R.; Luzzio, A.; Askin, Ö.; Fazzi, D.; Sepe, A.; Steiner, U.; Komber, H.; Caironi, M.; Sommer, M. Highly Planarized Naphthalene Diimide-Bifuran Copolymers with Unexpected Charge Transport Performance. *Chem. Mater.* **2017**, *29* (13), 5473–5483.
- (41) Brambilla, L.; Capel Ferrón, C.; Tommasini, M.; Hong, K.; López Navarrete, J. T.; Hernández, V.; Zerbi, G. Infrared and Multi-Wavelength Raman Spectroscopy of Regio-Regular P3HT and Its Deutero Derivatives. *J. Raman Spectrosc.* **2018**, *49* (3), 569–580.

(42) Polavarapu, P. L.; Covington, C. L. Comparison of Experimental and Calculated Chiroptical Spectra for Chiral Molecular Structure Determination. *Chirality* **2014**, *26* (9), 539–552.

(43) Daigle, M.; Lucotti, A.; Morin, J.-F.; Miao, D.; Tommasini, M.; Boismenu-Lavoie, J. Toward Thiophene-Annulated Graphene Nanoribbons. *Angew. Chemie Int. Ed.* **2018**, *57* (14), 3588–3592.

(44) As previously observed for the neutral polymer, the large anharmonicity of CO bonds can explain the overestimation of the frequencies of these bands. Indeed, looking to vibrational eigenvectors, the bands at 1677 and 1644 cm^{-1} are assigned to the stretching of C=O bonds heavily affected by doping.

(45) The calculation on 1-D crystal (charged case) corresponds to a model of an ideal case, with $MR = 1$ and quantitative doping. However, some residual neutral ND12OD units are present also at the higher ($MR = 1$) doping percentages. For this reason, the computed spectrum of the doped polymer (and also of the doped model molecule T2-ND12OD-T2, i.e., the radical anion) aims at the rationalization of the new, doping induced features in the spectrum and cannot account for experimental features coming from residual undoped ND12OD units.

Polaron confinement in n-doped P(NDI2OD-T2) unveiled by vibrational spectroscopy

Ilaria Denti[†], Simone Cimò^{†,||}, Luigi Brambilla[†], Alberto Milani^{‡§}, Chiara Bertarelli^{†,||}, Matteo Tommasini[†], Chiara Castiglioni^{†*}

[†] Dipartimento di Chimica, Materiali e Ingegneria Chimica Giulio Natta, Politecnico di Milano, piazza Leonardo da Vinci 32, 20133 Milano, Italy

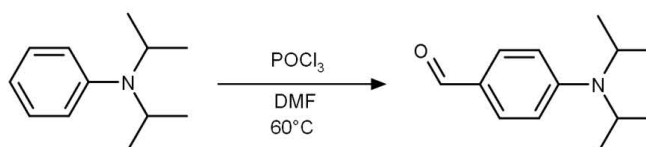
^{||} Center for Nano Science and Technology@PoliMi, Istituto Italiano di tecnologia, via Pascoli 70/3, 20133 Milano, Italy

[§] Dipartimento di Energia, Politecnico di Milano, piazza Leonardo da Vinci 32, 20133 Milano, Italy

SUPPORTING INFORMATION

Synthetic procedures

4-[bis(propan-2-yl)amino]benzaldehyde



N, N-Diisopropylaniline (1.00 g, 5.64 mmol) was dissolved in 2 mL of anhydrous DMF. Then POCl₃ (1.30 g, 8.48 mmol) was added and the solution was heated at 60 °C under stirring in Ar overnight. Then solution was cooled to room temperature, 100 mL of EtOAc were added and the solution was washed with water three times. The organic layer was dried over anhydrous Na₂SO₄ and the solvent was removed under reduced pressure. The crude was purified by flash chromatography using a solution of n-hexane and EtOAc (1:2) as eluent to give 350 mg of the desired product as a white powder in 30% yield.

¹H NMR (CDCl₃, 400 MHz): ppm 9.73 (s, 1H), 7.69 (d, J= 9.0Hz 2H), 6.86 (d, J= 9.0Hz, 2H), 4.01 (m, J= 6.8 Hz, 2H), (d, J= 6.8Hz, 12H).

4-[bis(propan-2-yl)amino]benzaldehyde synthesis is described in the previous procedure. (Reaction yield: 40%).

N,N-dibutyl-4-(1,3-dimethyl-2,3-dihydro-1H-1,3-benzodiazol-2-yl)aniline (DBuBI) was synthesized as previously reported by Saglio, B. et al. N-Alkyl Substituted 1 H-Benzimidazoles as Improved n-Type Dopants for a Naphthalene-Diimide Based Copolymer. *J. Mater. Chem. A* **2018**, *6* (31), 15294–15302.

4-(1,3-dimethyl-2,3-dihydro-1H-1,3-benzodiazol-2-yl)-N,N-bis(propan-2-yl)aniline (DiPrBI):

4-[Bis(propan-2-yl)amino]benzaldehyde (151 mg, 0.736 mmol), N1,N2-dimethylbenzene-1,2-diamine (100 mg, 0.735 mmol) were dissolved in 2mL of MeOH. A drop of glacial acetic acid was added and the solution was sonicated for 10h. The mixture was left at -20° C overnight. The white precipitate was filtered and washed with cold MeOH to yield 80 mg of the desired product as a white powder in 34% yield.

¹H NMR (CDCl₃, 400 MHz): ppm 7.35 (d, J = 8.7 Hz, 2H), 6.87 (d, J = 8.7 Hz, 2H), 6.71-6.68 (m, 2H), 6.42-6.40 (m, 2H), 4.76 (s, 1H), 3.38 (m, J = 6.8 Hz, 2H), 2.56 (s, 6H), 2.52 (d, J = 6.8Hz, 12H).

4-(1,3-dimethyl-2,3-dihydro-1H-1,3-benzodiazol-2-yl)-N,N-diphenylaniline (DPhBI)

The reaction was carried out according to procedure to synthesized DiPrBI. (Reaction yield: 40%).

¹H NMR (CDCl₃, 400 MHz): ppm 7.41 (d, J = 8.5 Hz, 2H), 7.29-7.04 (m, 12H), 6.72-6.70 (m, 2H), 6.45-6.43 (m, 2H), 4.82 (s, 1H), 2.60 (s, 6H)

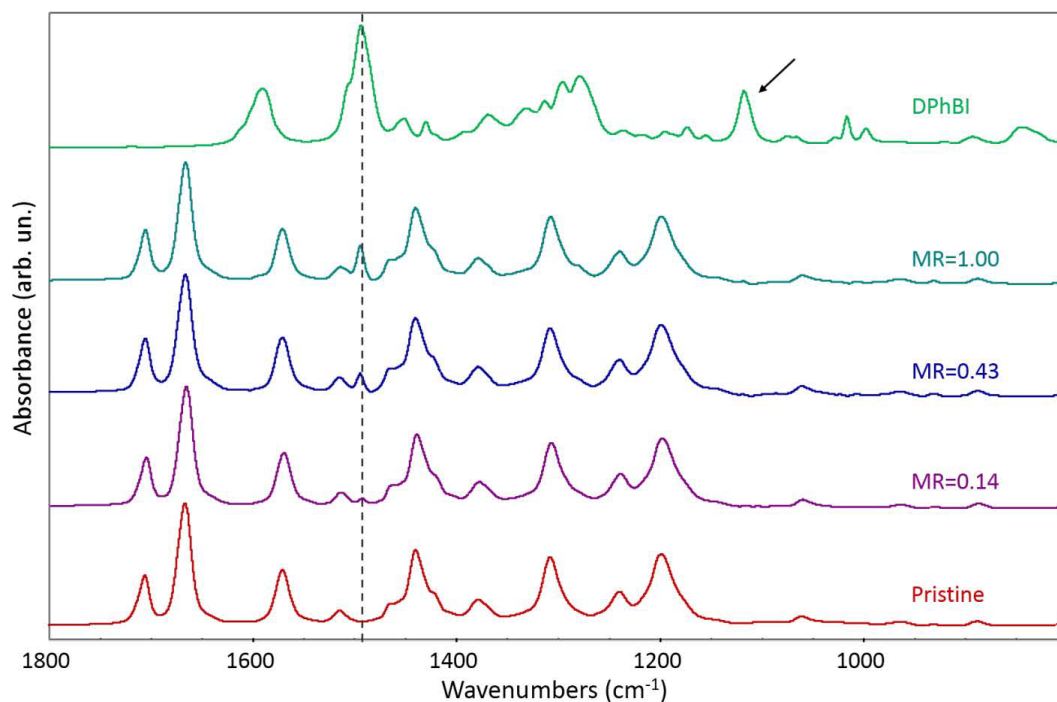


Figure S1. Comparison between the IR spectrum (red, bottom spectrum) of pristine P(NDI2OD-T2) and spectra obtained by post-processing of the spectra of the films at different N-DPhBI/polymer molar ratios (namely MR = 0.14, 0.43, 1.00), before annealing. The spectra are obtained by subtracting the spectrum of the pristine dopant molecule (green, top spectrum) from that of the polymer/dopant film. In order to obtain the suitable weight for the subtraction, we compensated the absorption band of the dopant at 1120 cm^{-1} (black arrow), which lies in a region free from absorption features of the pristine polymer. The spectra after subtraction coincide with that of the pristine polymer, except for a weak residual absorption at 1490 cm^{-1} (vertical broken line). This feature corresponds to the most intense band of the pristine dopant, and grows with MR in the polymer-dopant films. The residue at 1490 cm^{-1} should be ascribed to some lack of spectra compensation or to minor changes of N-DPhBI spectrum, induced by the different intermolecular environment in the film. It cannot be taken as an indication of the formation of charge-transfer complexes (i.e. doping) because of the absence doping induced marker bands (see main text, spectra of the same films after annealing).

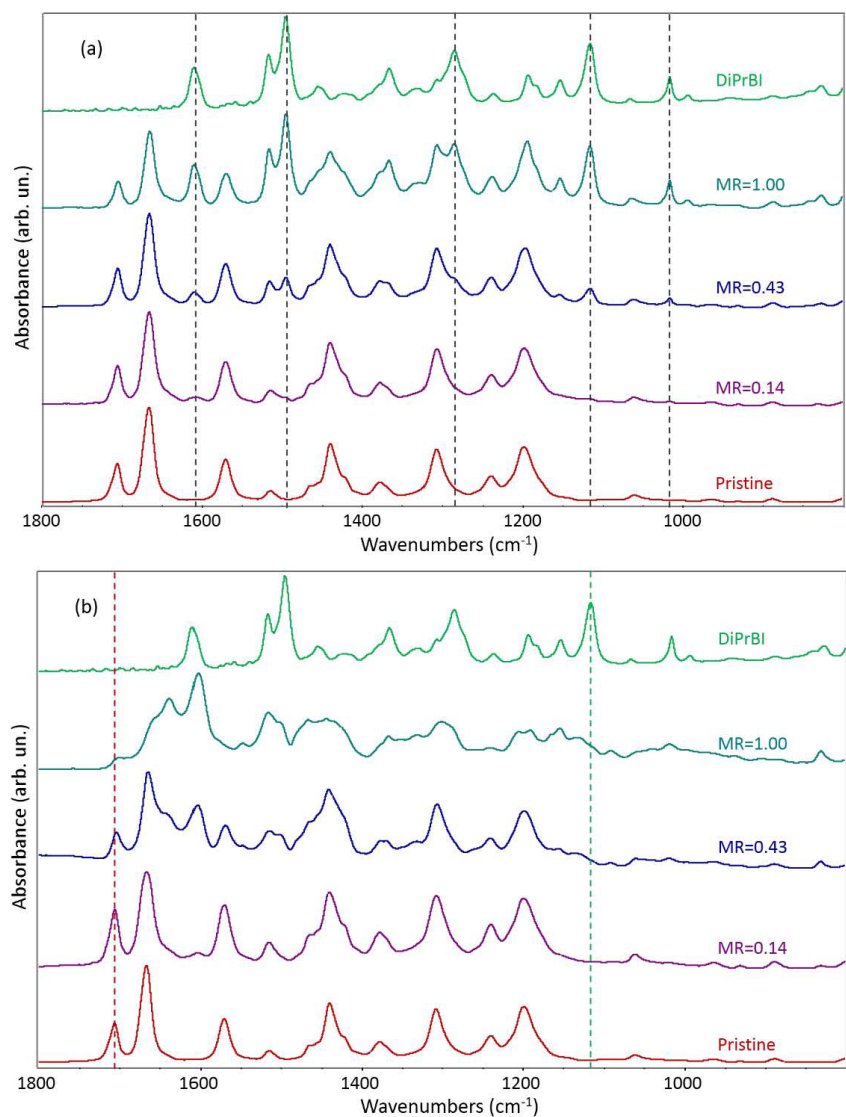


Figure S2. *Panel a:* IR spectra of P(NDI2OD-T2):DiPrBI mixture with increasing molar ratio MR of dopant/polymer (MR=0.14, 0.43 and 1.0, MR is referred to the polymer chemical unit). Spectra of films (cast from CH₃Cl solution) were recorded before annealing. IR spectrum of the pristine polymer (bottom) and of the pure dopant (top) are reported for comparison. Dotted lines correspond to strong absorption features of pristine DiPrBI. *Panel b:* Spectra of samples reported in *panel a*, after annealing. The red dotted line shows the trend of symmetric CO stretching feature of the pristine polymer; the green dotted line corresponds to a strong marker band of pristine DiPrBI.

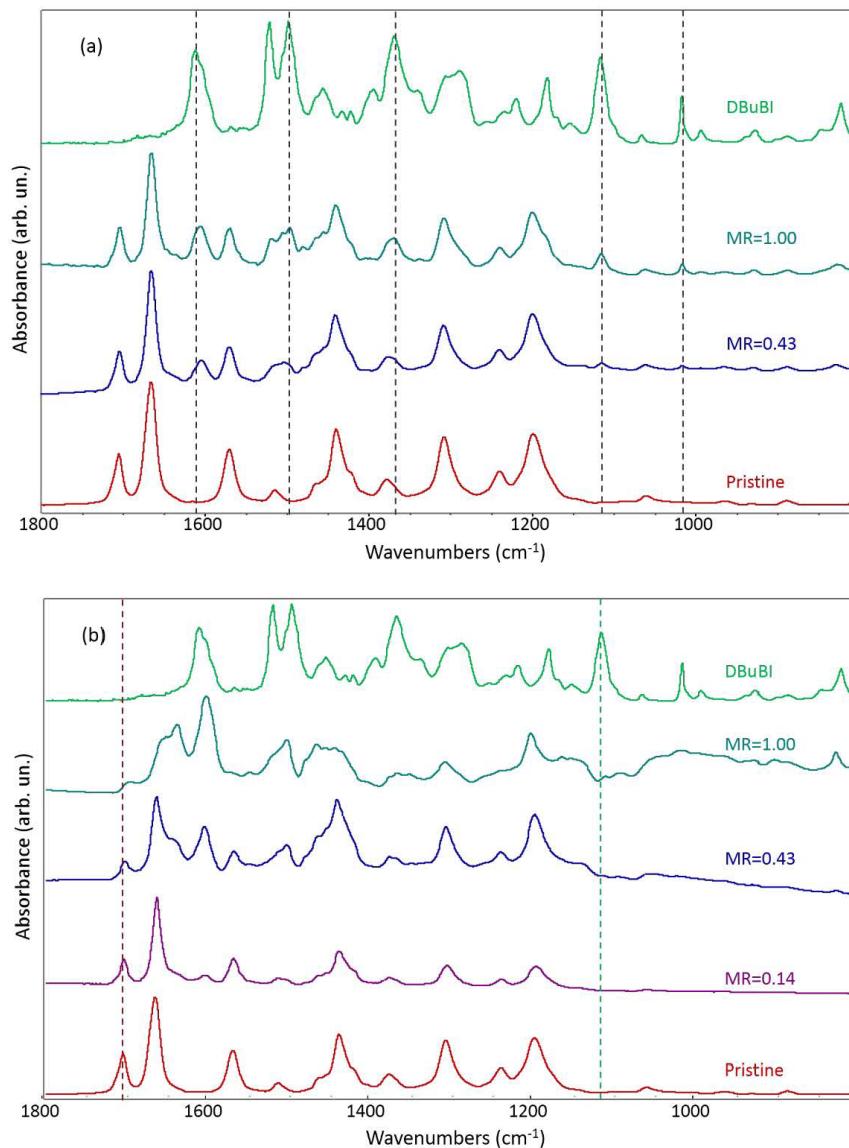


Figure S3. *Panel a:* IR spectra of P(NDI2OD-T2):DBuBI mixture with increasing molar ratio MR of dopant/polymer (MR=0.14, 0.43 and 1.0, MR is referred to the polymer chemical unit). Spectra of films (cast from CH₃Cl solution) were recorded before annealing. IR spectrum of the pristine polymer (bottom) and of the pure dopant (top) are reported for comparison. Dotted lines correspond to strong absorption features of pristine DBuBI. *Panel b:* Spectra of samples reported in *panel a*, after annealing. The red dotted line shows the trend of symmetric CO stretching feature of the pristine polymer; the green dotted line corresponds to a strong marker band of pristine DBuBI.

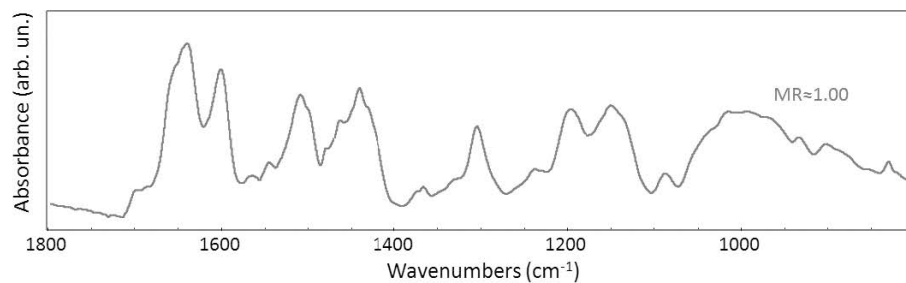


Figure S4. IR Spectrum of P(NDIT2OD-T2):DiPrBI films (MR=1) prepared in glove box under in inert atmosphere (MR≈1.00) and annealed in a Schleck tube.

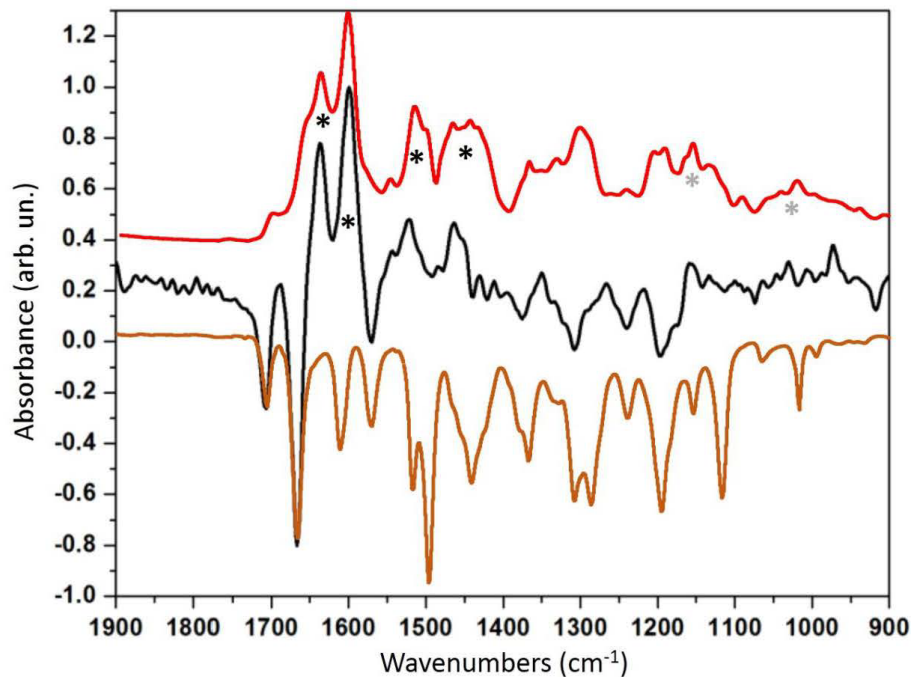


Figure S5. Comparison between pristine (orange line), doped P(NDI2OD-T2):DiPrBI (red line, MR=1.00) IR spectra and the ATR-FTIR spectroelectrochemical spectrum (black line), reported in "Giussani, E. *Spectroscopic and Electrochemical Investigation of the High Electron Mobility Copolymer P(NDI2OD-T2) and Its Functional Derivates*; Ph.D. Thesis, Politecnico di Milano: Milano, Italia, 2014". The spectroelectrochemical spectrum was recorded in situ at the -0.8V cathodic peak. A TBAPF4 0.1 M solution in acetonitrile (ACN) was selected as electrolyte. The spectrum is plotted as difference spectrum between that recorded at the selected voltage value and the reference spectrum: positive features correspond to new products deriving from doping, while negative bands to the molecular species which disappear. The reference spectrum was acquired at 0 V, when the polymer and the electrolyte reached the equilibrium in the spectro-electrochemical cell. Positive bands show a nice correspondence with the polaron marker bands identified for chemically doped P(NDI2OD-T2):DiPrBI (labelled with asterisks). For the sake of comparison, the IR spectra of the pristine and doped P(NDI2OD-T2):DiPrBI have been normalized and adapted to the absorbance scale of the spectroelectrochemical spectrum.

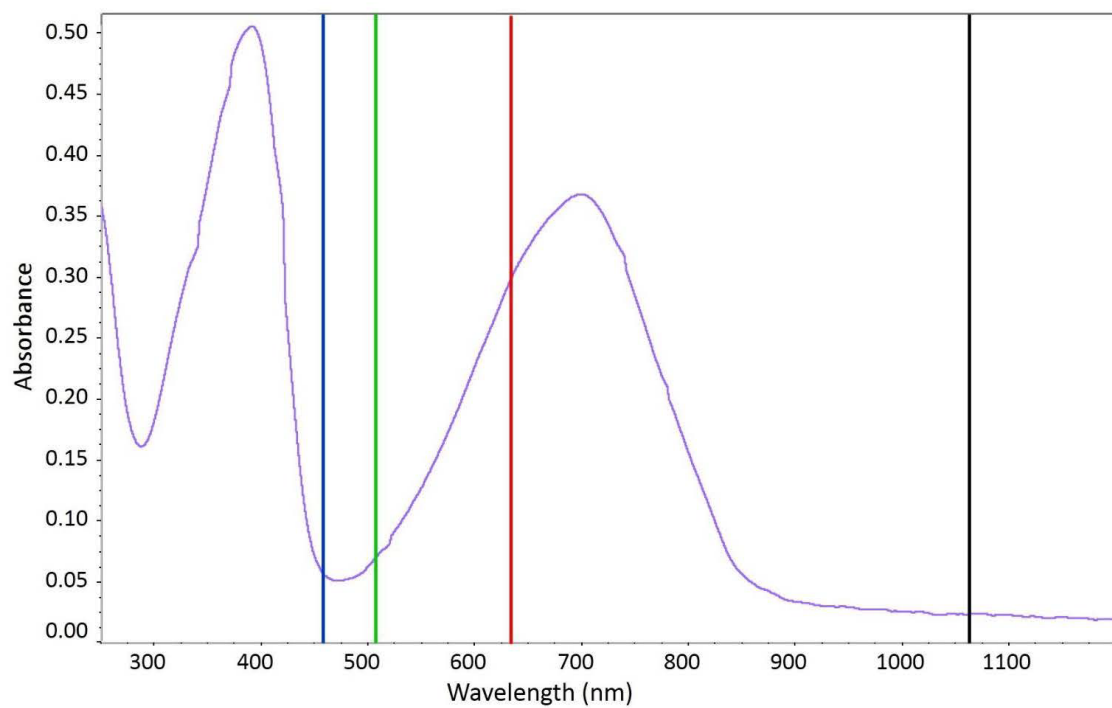


Figure S6. UV-Vis spectrum of P(NDOD2-T2) polymer (film on a quartz slide). Vertical lines indicate the position of the excitation laser wavelengths used for Raman measurements (i.e., 458, 514, 632, 1064 nm).

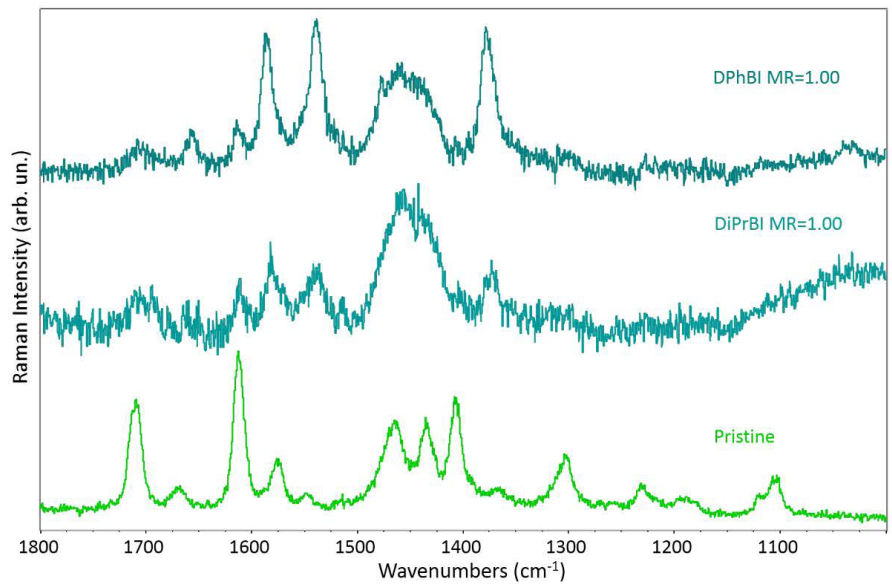


Figure S7.a Comparison between Raman spectra obtained with 514 nm excitation line for – from bottom to top – pristine P(NDI2OD-T2), highly doped (MR =1) P(NDI2OD-T2):DiPrBI and P(NDI2OD-T2):DPhBI

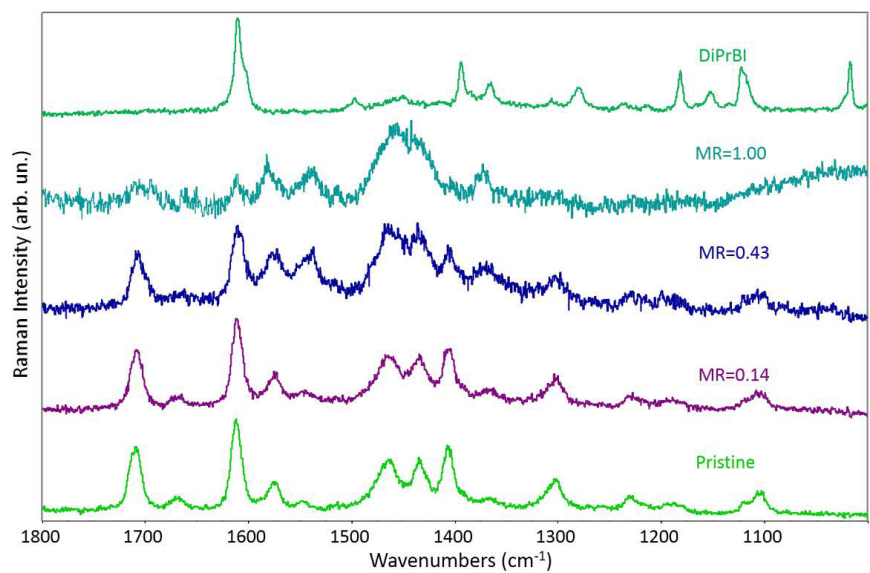


Figure S7.b Raman spectra recorded with 514 nm excitation. From bottom to top: pristine P(NDI2OD-T2), doped P(NDI2OD-T2):DiPrBI at increasing dopant/polymer molar ratio (MR= 0.14, 0.43, 1,0) and pristine DiPrBI.

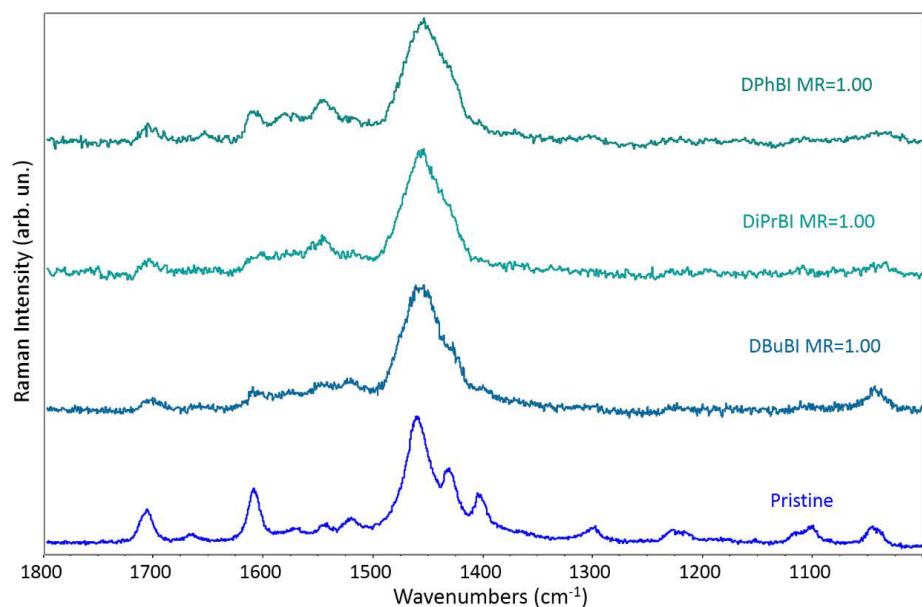


Figure S8. Comparison between Raman spectra obtained with 458 nm excitation line for – from bottom to top – pristine P(NDI2OD-T2), highly doped (MR =1) P(NDI2OD-T2):DBuBI, P(NDI2OD-T2):DiPrBI and P(NDI2OD-T2):DPhBI

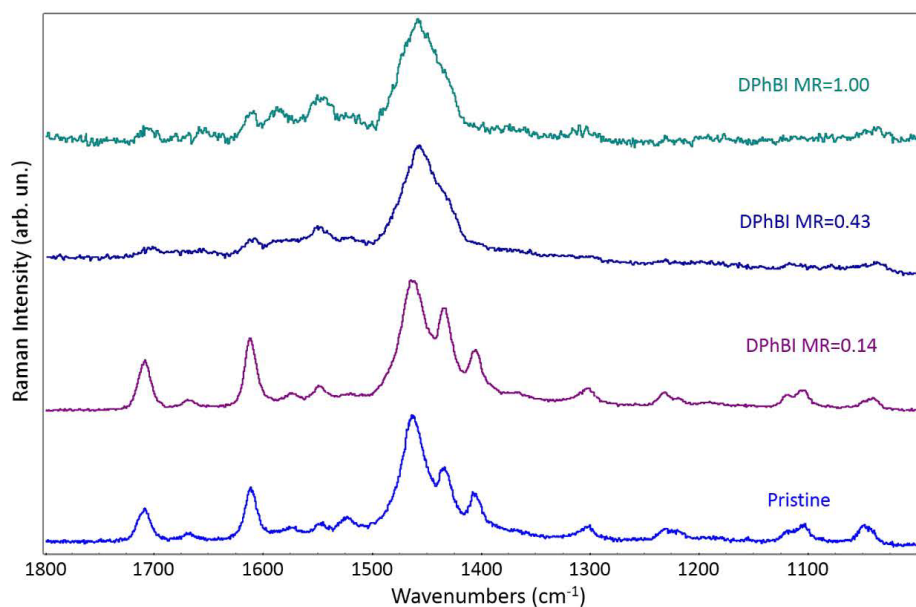


Figure S9. Raman spectra recorded with 458 nm excitation. From bottom to top: pristine P(NDI2OD-T2), doped P(NDI2OD-T2):DPhBI at increasing dopant/polymer molar ratio (MR= 0.14, 0.43, 1,0).

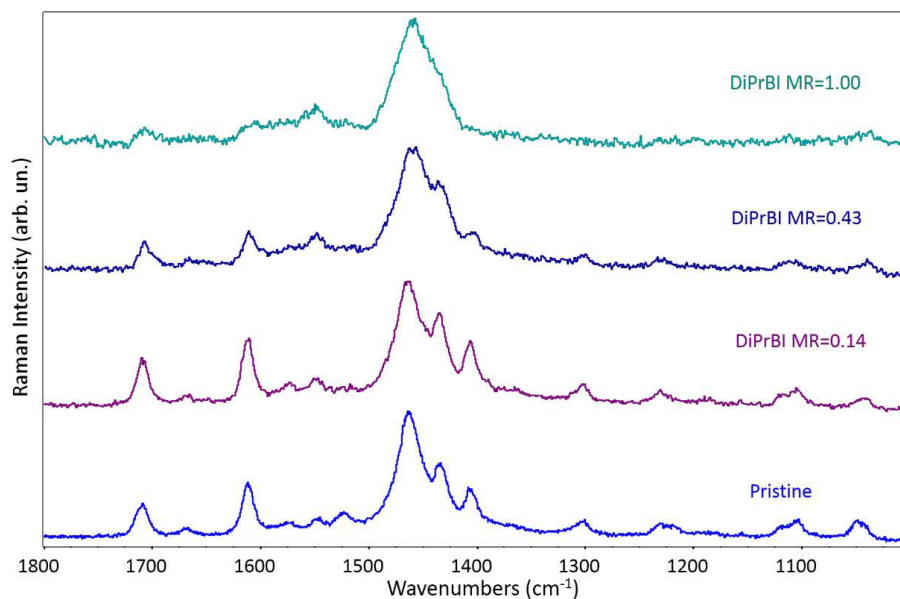


Figure S10. Raman spectra recorded with 458 nm excitation. From bottom to top: pristine P(NDI2OD-T2), doped P(NDI2OD-T2):DiPrBI at increasing dopant/polymer molar ratio (MR= 0.14, 0.42, 1,0).

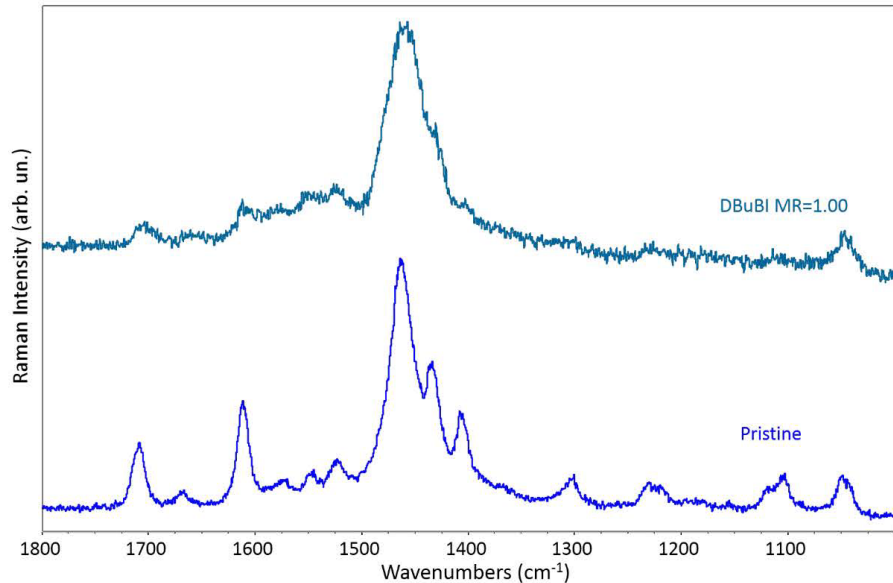


Figure S11. Raman spectra recorded with 458 nm excitation. Pristine P(NDI2OD-T2) and doped P(NDI2OD-T2):DBuBI at molar ratio MR= 1.0.

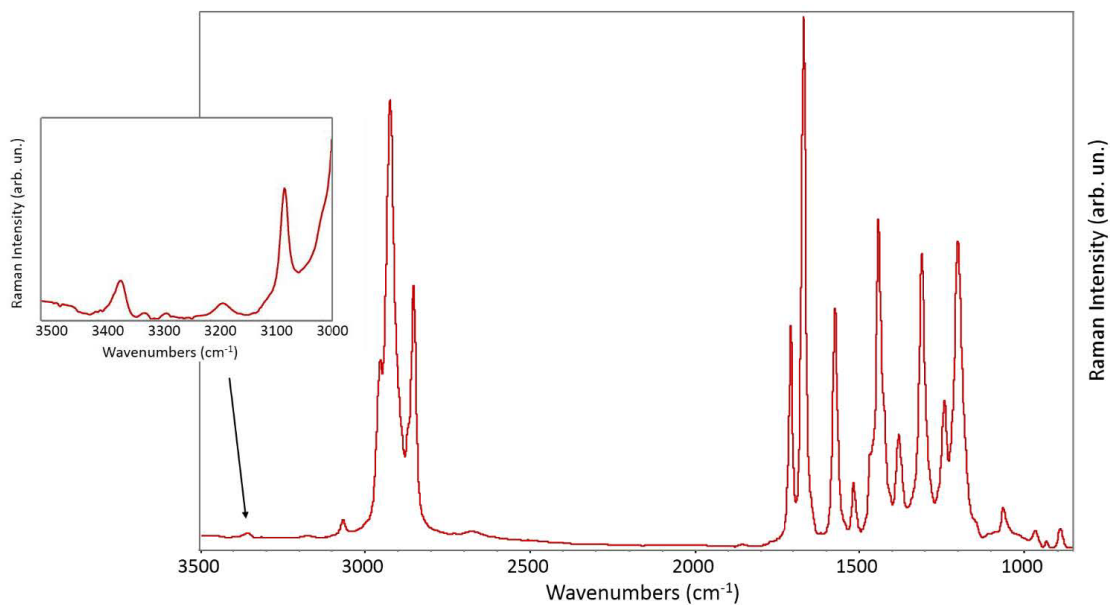


Figure S12. Experimental IR absorption spectrum of a film of P(NDI2OD-T2) from 3500 cm^{-1} to 850 cm^{-1} , showing a CO stretching combination band at 3359 cm^{-1} . The inset shows a zoom on the higher wavenumber region.

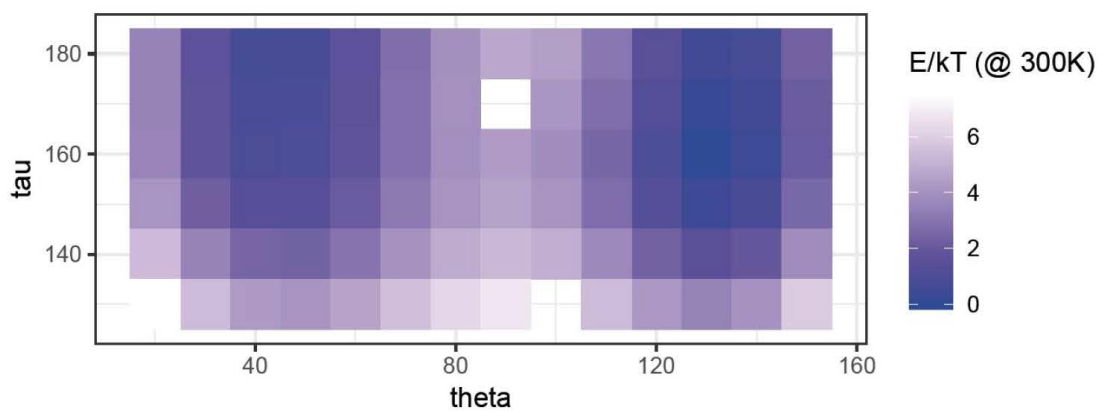


Figure S13. Energy map for different non-equilibrium conformers of the model molecule T2-NDI2OD-T2. Energy are referred to E_0 (energy of the lower energy conformer) and are measured in kT units ($T=300\text{ K}$).

In the following pages:

Figure S14. Computed IR spectra for low energy ($(E-E^*)/kT < 2$) non-equilibrium conformers of the model molecule T2-NDI2OD-T2. The experimental spectrum of P(NDI2OD) is reported (bottom of each panel), for sake of comparison.

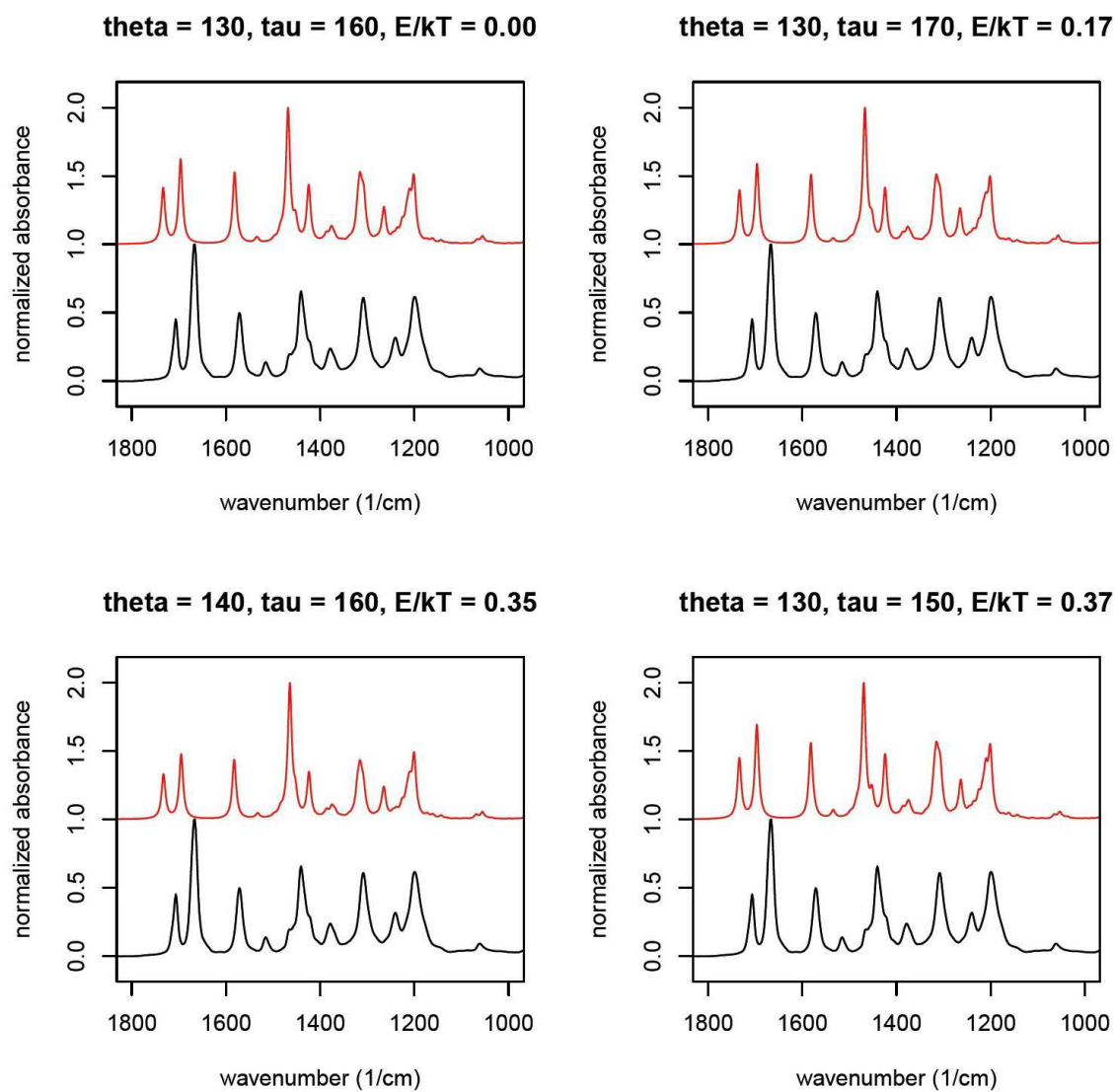
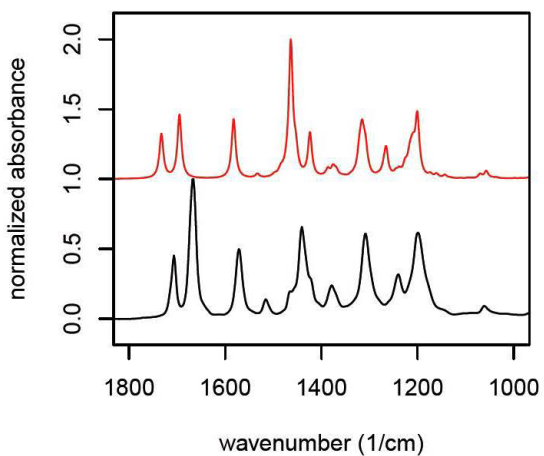
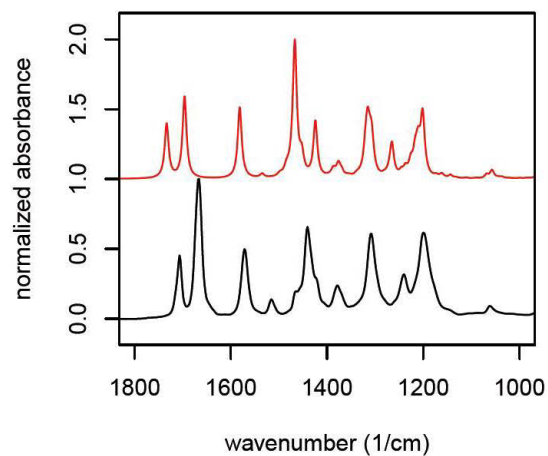


Figure S14 -continued

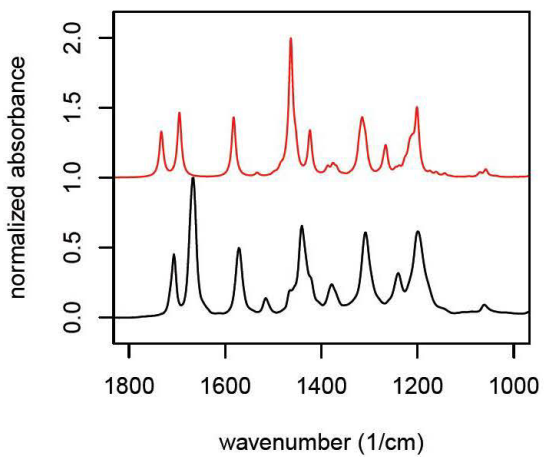
theta = 140, tau = 170, E/kT = 0.46



theta = 130, tau = 180, E/kT = 0.50



theta = 140, tau = 180, E/kT = 0.71



theta = 40, tau = 180, E/kT = 0.73

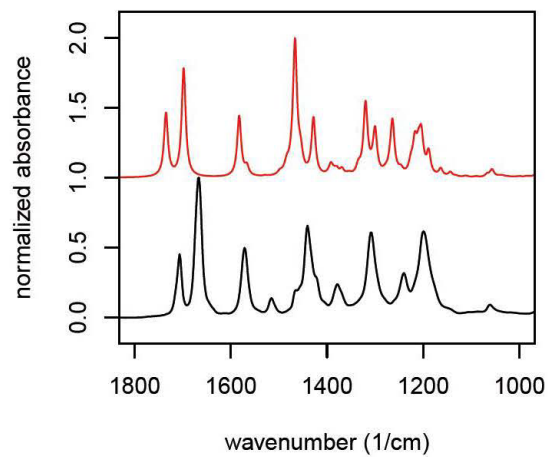
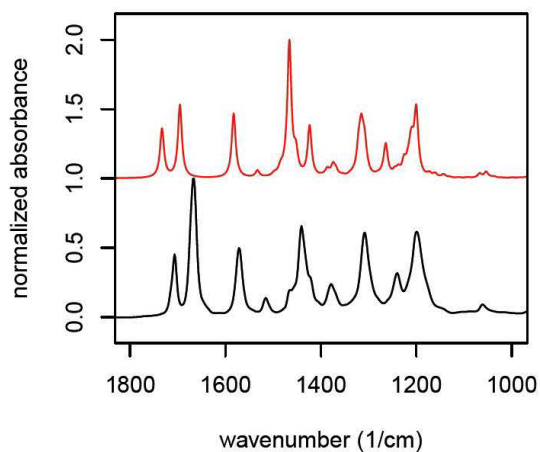
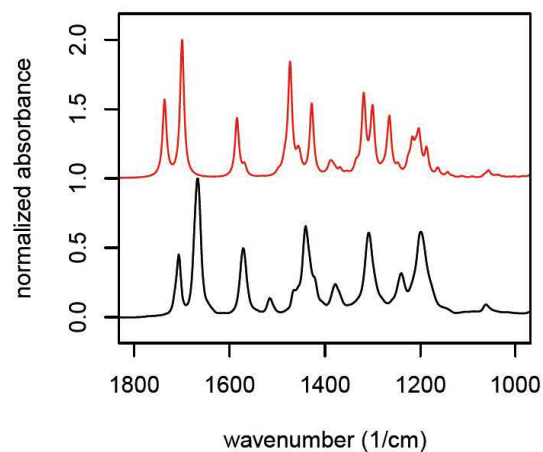


Figure S14 -continued

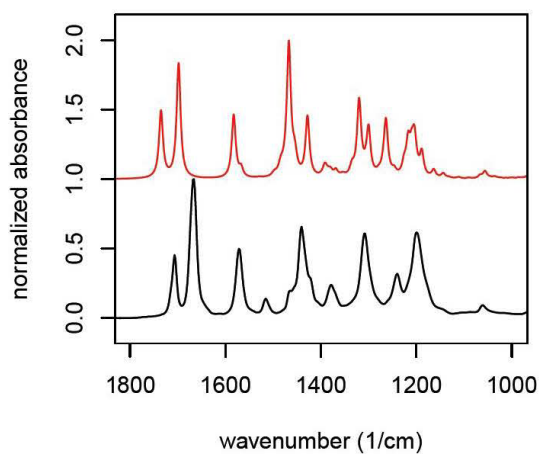
theta = 140, tau = 150, E/kT = 0.77



theta = 50, tau = 180, E/kT = 0.80



theta = 40, tau = 170, E/kT = 0.87



theta = 50, tau = 170, E/kT = 0.89

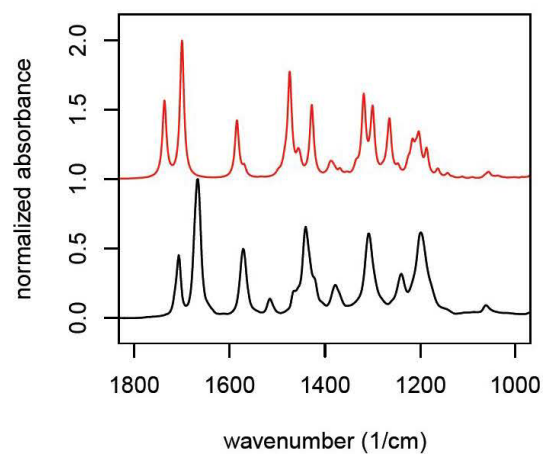
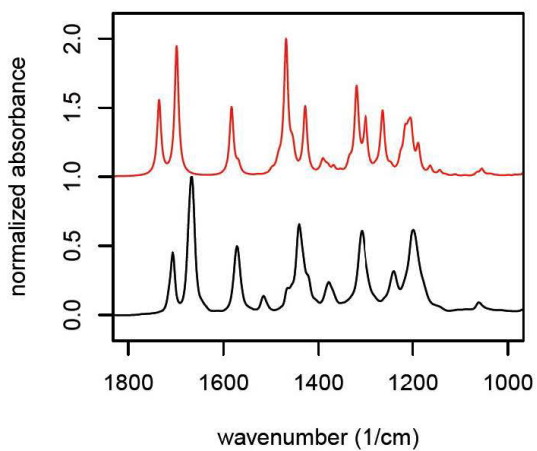
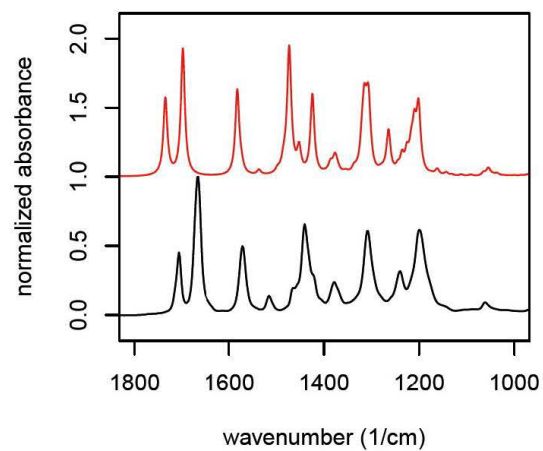


Figure S14 - continued

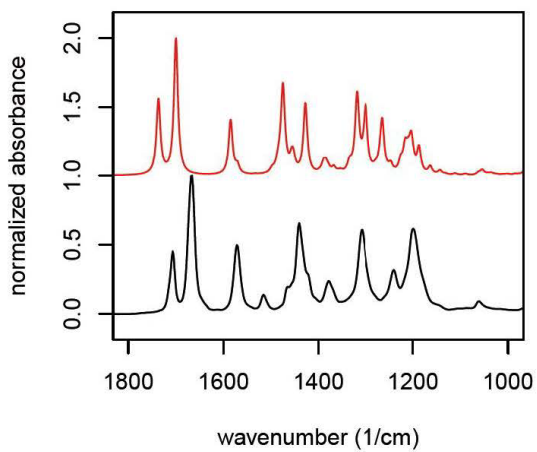
theta = 40, tau = 160, E/kT = 0.92



theta = 120, tau = 160, E/kT = 0.96



theta = 50, tau = 160, E/kT = 0.97



theta = 120, tau = 170, E/kT = 1.19

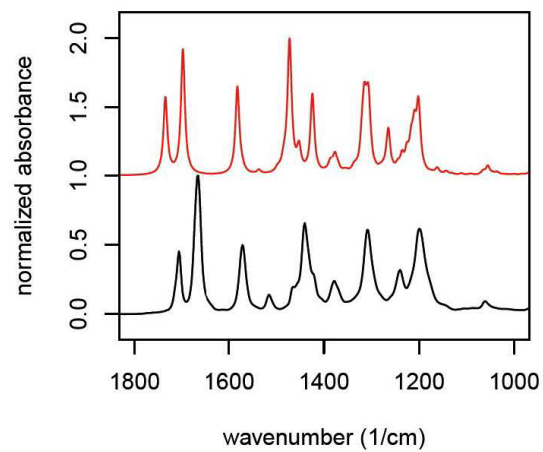
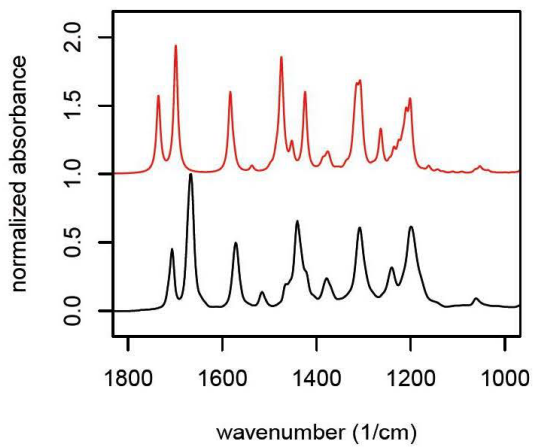
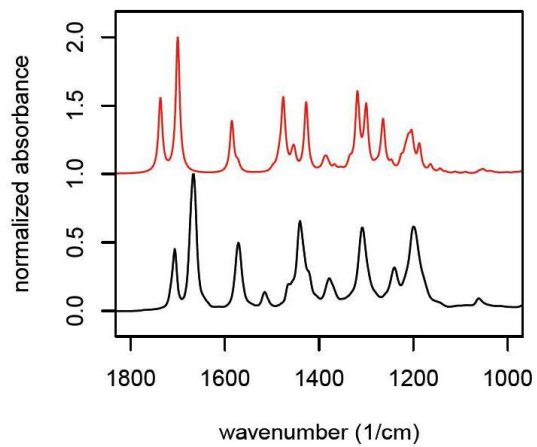


Figure S14 -continued

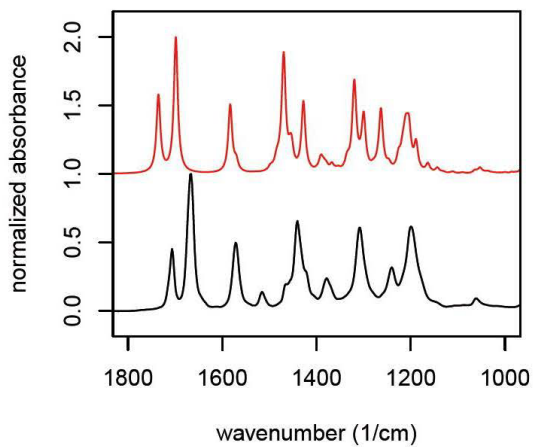
theta = 120, tau = 150, E/kT = 1.28



theta = 50, tau = 150, E/kT = 1.37



theta = 40, tau = 150, E/kT = 1.39



theta = 120, tau = 180, E/kT = 1.49

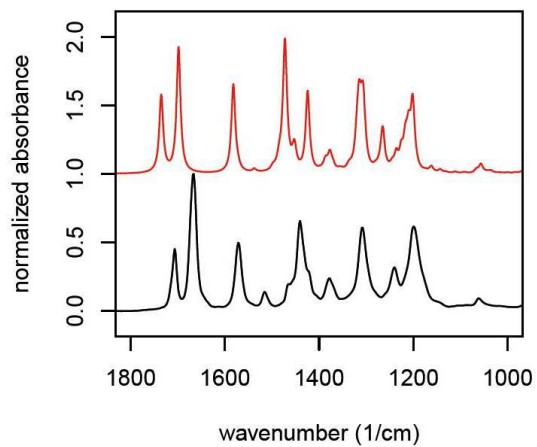


Figure S14 -continued

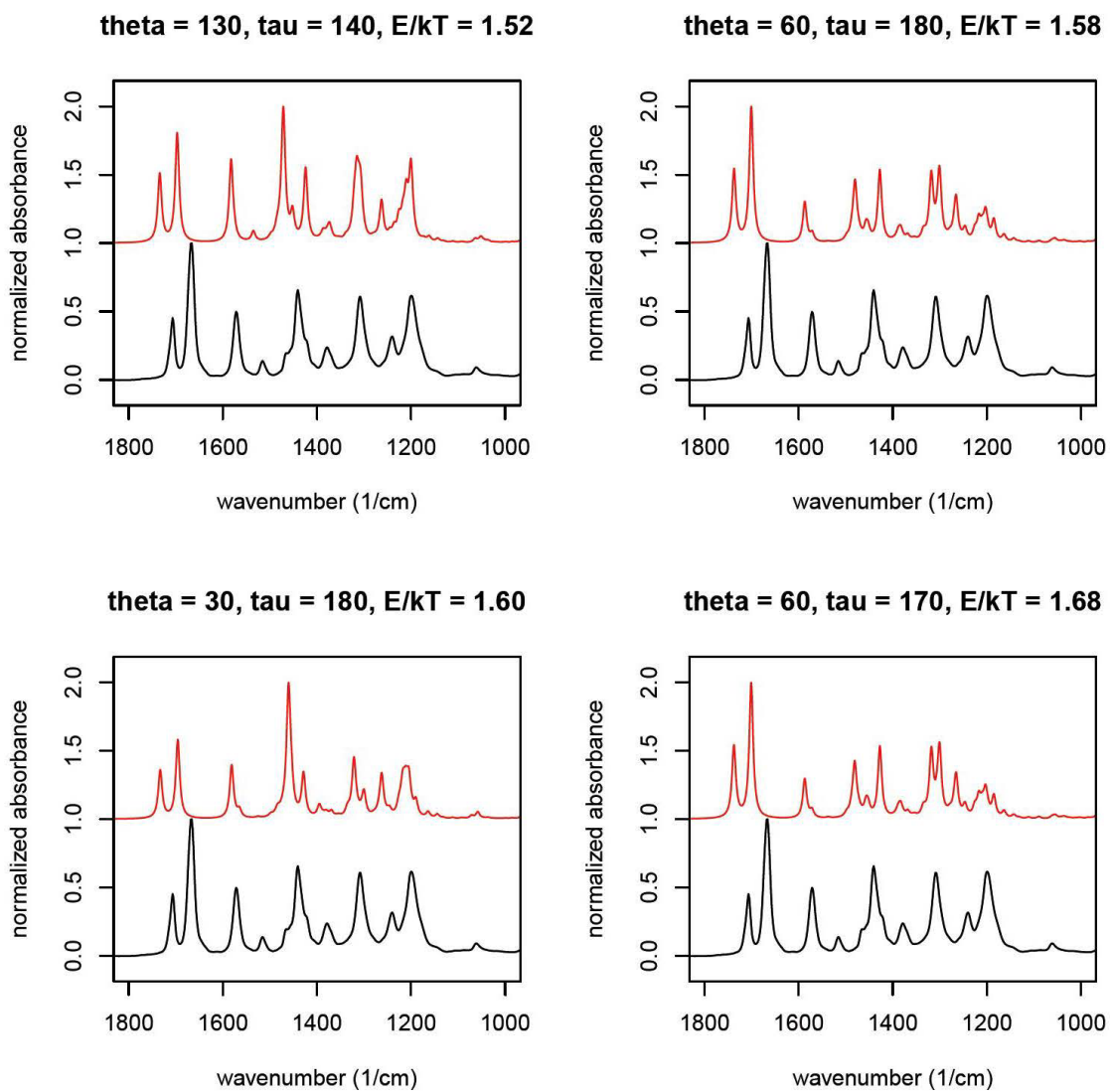
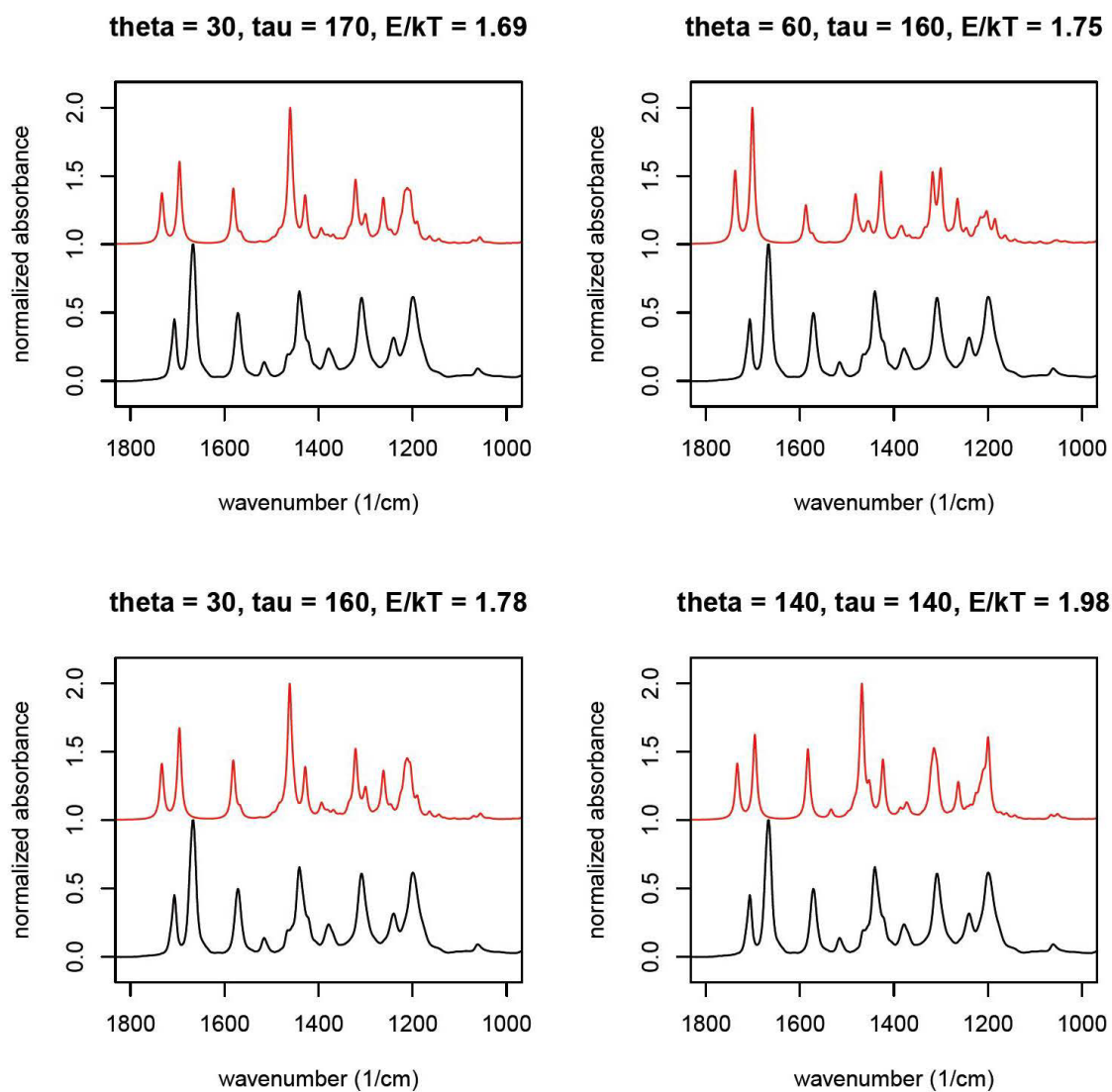
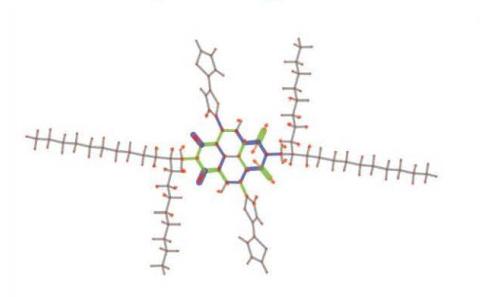


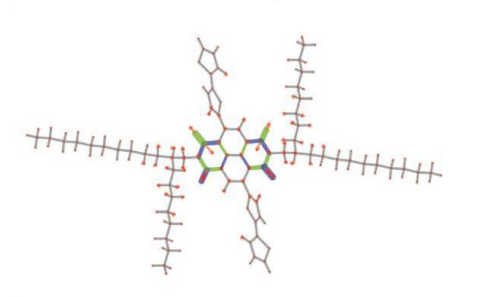
Figure S14 -continued



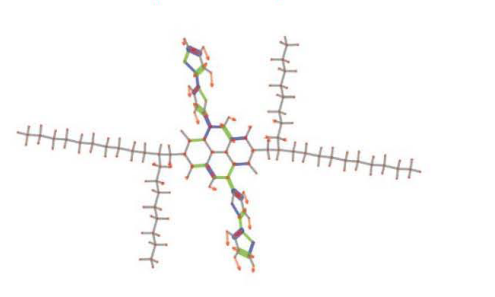
$\nu = 1712 \text{ cm}^{-1}$ (**1677 cm^{-1}**); $I = 1182 \text{ km/mol}$



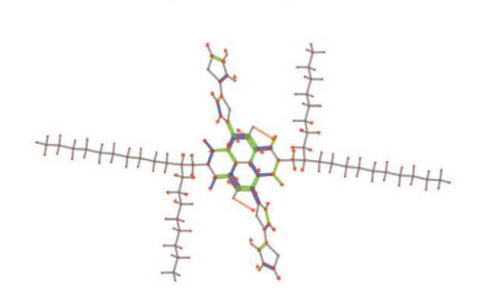
$\nu = 1678 \text{ cm}^{-1}$ (**1644 cm^{-1}**); $I = 1152 \text{ km/mol}$



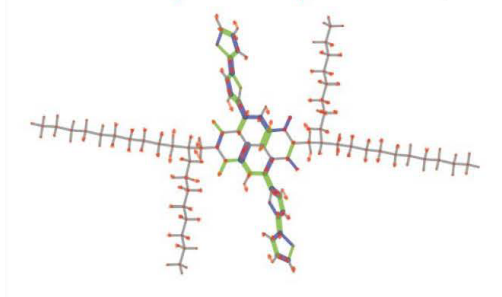
$\nu = 1564 \text{ cm}^{-1}$ (**1533 cm^{-1}**); $I = 229 \text{ km/mol}$



$\nu = 1567 \text{ cm}^{-1}$ (**1536 cm^{-1}**); $I = 375 \text{ km/mol}$



$\nu = 1491 \text{ cm}^{-1}$ (**1461 cm^{-1}**); $I = 644 \text{ km/mol}$



$\nu = 1468 \text{ cm}^{-1}$ (**1448 cm^{-1}**); $I = 640 \text{ km/mol}$

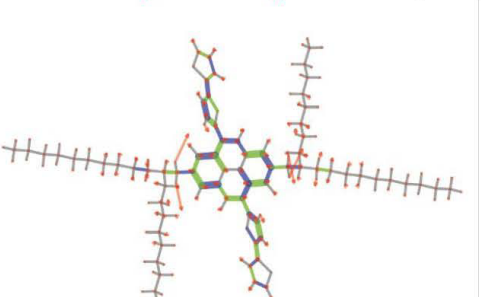


Figure S15. DFT computed vibrational wavenumbers, infrared intensity and sketches of the vibrational eigenvectors of the IR marker bands of the radical anion T2-NDI2OD-T2 (in red, scaled wavenumbers).

NDI2OD				C=O			
CN	Pristine	Charged	ΔR (Å)	Pristine	Charged	ΔR (Å)	
1	1.393	1.399	0.006	1	1.225	1.237	0.012
2	1.393	1.399	0.006	2	1.225	1.237	0.012
3	1.409	1.414	0.005	3	1.223	1.235	0.012
4	1.409	1.414	0.005	4	1.223	1.235	0.012

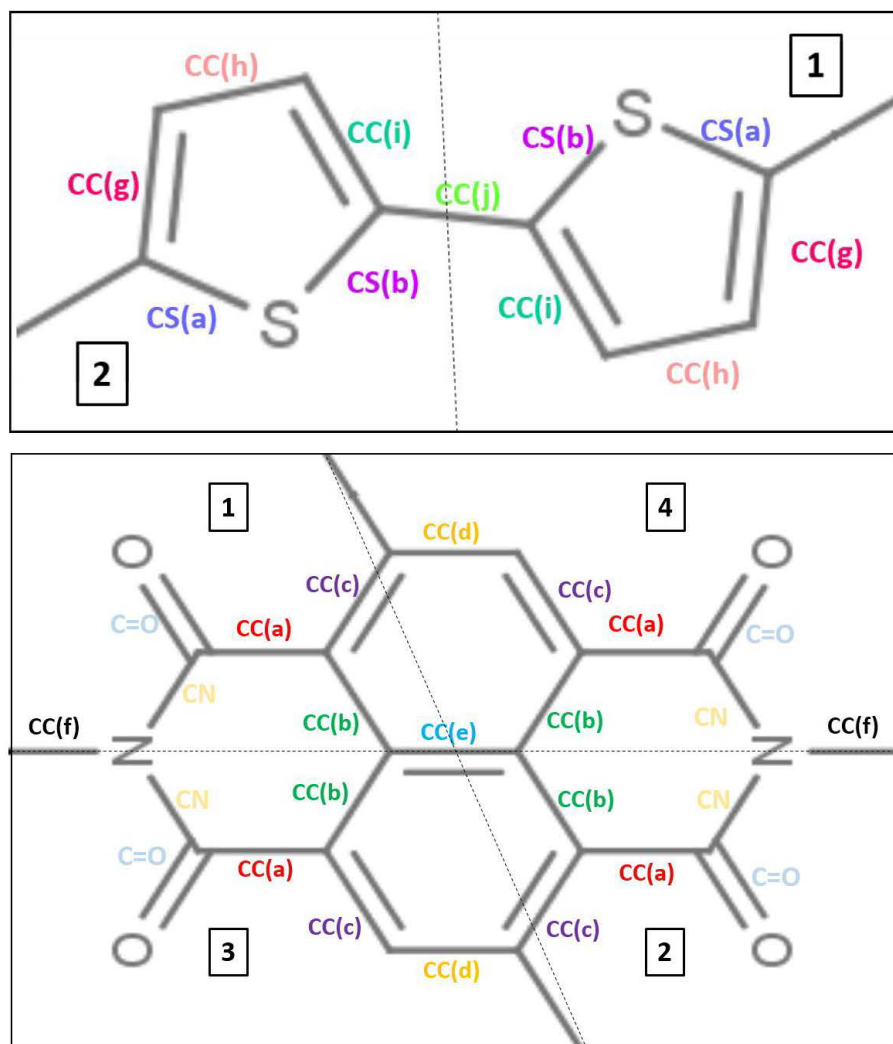
CC(a)	Pristine	Charged	ΔR (Å)	CC(b)	Pristine	Charged	ΔR (Å)	CC(c)	Pristine	Charged	ΔR (Å)
1	1.483	1.46	-0.023	1	1.417	1.418	0.001	1	1.376	1.397	0.02
2	1.483	1.46	-0.023	2	1.417	1.418	0.001	2	1.376	1.397	0.02
3	1.493	1.469	-0.024	3	1.427	1.427	0.000	3	1.415	1.437	0.02
4	1.494	1.469	-0.025	4	1.427	1.427	0.000	4	1.415	1.437	0.02

CC(d)	Pristine	Charged	ΔR (Å)	CC(e)	Pristine	Charged	ΔR (Å)	CC(f)	Pristine	Charged	ΔR (Å)
1	1.421	1.397	-0.024	1	1.426	1.438	0.012	1	1.47	1.474	0.00
2	1.422	1.397	-0.025					2	1.471	1.474	0.00

Thiophene				CC(h)				CC(i)			
CC(g)	Pristine	Charged	ΔR (Å)	Pristine	Charged	ΔR (Å)		Pristine	Charged	ΔR (Å)	
1	1.368	1.367	-0.001	1	1.422	1.424	0.002	1	1.38	1.38	0.00
2	1.379	1.378	-0.001	2	1.412	1.414	0.002	2	1.382	1.381	-0.00

CC(j)	Pristine	Charged	ΔR (Å)	CS(a)	Pristine	Charged	ΔR (Å)	CS(b)	Pristine	Charged	ΔR (Å)
1	1.447	1.446	-0.001	1	1.733	1.739	0.006	1	1.756	1.761	0.00
				2	1.764	1.761	-0.003	2	1.747	1.752	0.00

Table S1. DFT optimized bond lengths (Å) of T2-NDI2OD-T2 in its pristine form (neutral) and of its radical anion (charged). The right column of each sub-table reports the difference of bond length between charged and neutral species. Labels referred to individual bonds are reported in the first column (see Sketch S1).



Sketch S1. Sketches of T2 and NDI2OD units with labels identifying individual bonds (bond lengths reported in table S1)

Table S2. Optimized Cartesian coordinates of the translational P(NDI2OD-T2) unit.

LATTICE PARAMETERS (ANGSTROMS) = 14.39829343

CARTESIAN COORDINATES

```

*****
*          ATOM          X (ANGSTROM)          Y (ANGSTROM)          Z (ANGSTROM)
*****
C          C          6.207288845443E+00      8.206607650170E-01      1.279728457453E-01
C          C          5.536481163363E+00     -1.338452588190E+00      9.917945800864E-01
C          C          4.902110042774E+00      1.187830414440E+00     -1.092020635942E-01
C          C          1.440048388648E+00     -2.283819624782E-01      2.395669373556E-01
C          C          1.810567042581E+00     -1.480714865240E+00      8.022447593319E-01
C          C          5.802079834455E+00     -2.721198102579E+00      1.496703968431E+00
N          N          4.703354252359E+00     -3.577194843908E+00      1.707646974290E+00
C          C          3.365287509094E+00     -3.209310309808E+00      1.575768646754E+00
C          C          4.652497037516E+00      2.549305312797E+00     -6.451792151595E-01
O          O          5.566425564268E+00      3.308301050728E+00     -9.428311868860E-01
C          C          2.481327430921E+00      6.794474426422E-01     -5.895175235686E-02
C          C          2.215406734710E+00      2.063544268699E+00     -5.602304070520E-01
N          N          3.314414658682E+00      2.918791413147E+00     -7.726315718736E-01
C          C          3.009285469897E+00      4.284228746573E+00     -1.255338030711E+00
O          O          1.092772411528E+00      2.494193710489E+00     -7.807958776391E-01
C          C          5.008622295824E+00     -4.940110583247E+00      2.197481779028E+00
C          C          9.946149803040E-01     -7.734449082036E+00     -6.675017947616E-01
C          C          6.689708037278E-02     -7.841861867615E+00     -1.885093012539E+00
C          C          -1.240610526932E+00     -8.592019685768E+00     -1.599553661507E+00
C          C          -2.164363560264E+00     -8.701532054910E+00     -2.820001376144E+00
C          C          -3.472082086768E+00     -9.444760303902E+00     -2.527076549621E+00
H          H          -4.107553460697E+00     -9.507213423465E+00     -3.417132315976E+00
O          O          2.451318168867E+00     -3.969019443893E+00      1.871453624392E+00
H          H          1.044469240403E+00     -2.213559483594E+00      1.028140880274E+00
H          H          6.973341099230E+00      1.553268518951E+00     -9.879427348375E-02
H          H          4.091380700828E+00     -5.309667100042E+00      2.655111882956E+00
H          H          5.775543399353E+00     -4.835480235415E+00      2.967521463040E+00
H          H          2.238443751697E+00      4.184599913009E+00     -2.022098148116E+00
H          H          3.925005685205E+00      4.654186199066E+00     -1.715702922048E+00
C          C          2.504721637684E+00      5.246012331708E+00     -1.562323749673E-01
H          H          2.688550234402E+00     -6.358585962613E+00      1.072181430511E+00
H          H          2.052312166245E+00     -5.965026386245E+00     -1.314778776643E+00
H          H          1.234878703646E+00     -8.744599538985E+00     -3.044747640138E-01
H          H          4.604798357166E-01     -7.236402320701E+00      1.543058179387E-01
H          H          -1.682537673036E-01     -6.831815045463E+00     -2.251363609645E+00
H          H          -1.008045834450E+00     -9.601575535731E+00     -1.229706167455E+00
H          H          -1.777703340645E+00     -8.087710756154E+00     -7.828600129755E-01
H          H          -2.392573749023E+00     -7.692911718957E+00     -3.191804907005E+00
H          H          -1.628983372650E+00     -9.209872790790E+00     -3.634148389686E+00
H          H          -3.278652718325E+00     -1.046835782183E+01     -2.184528678547E+00
H          H          -4.047818860288E+00     -8.938373811093E+00     -1.743033629438E+00
C          C          3.506231693377E+00      5.434436630013E+00      1.006115705355E+00
C          C          2.072979256372E+00      6.564573506857E+00     -8.343505815404E-01
C          C          1.417250857546E+00      7.589284512266E+00      1.019426653716E-01
H          H          2.937376161510E+00      7.028557178730E+00     -1.329979680205E+00
H          H          1.362030423646E+00      6.321685589583E+00     -1.636730727578E+00
C          C          9.215705839934E-01      8.841536034963E+00     -6.347991014059E-01
H          H          5.737262850511E-01      7.116111448227E+00      6.251679922931E-01

```

H	2.127229675144E+00	7.894092220430E+00	8.820257030035E-01
H	3.761615204747E+00	4.444473902138E+00	1.408947408068E+00
C	4.805755124095E+00	6.190209428818E+00	6.873864358065E-01
H	2.987309013446E+00	5.950063087942E+00	1.824703353386E+00
C	5.741172176249E+00	6.282617222982E+00	1.901596901844E+00
H	5.336627230775E+00	5.689184828068E+00	-1.305950200816E-01
H	4.573125229332E+00	7.206081186696E+00	3.398810354632E-01
C	2.818082558570E-01	9.884982069256E+00	2.905135628941E-01
H	1.763989516148E+00	9.302370517714E+00	-1.171225882989E+00
H	1.966449165391E-01	8.546615297715E+00	-1.407357490947E+00
C	-7.353117231221E+00	7.038954614104E+00	1.616297889845E+00
H	5.213530214653E+00	6.769852914268E+00	2.735082866624E+00
H	5.982367507247E+00	5.267122116868E+00	2.248004907388E+00
C	-1.958873066099E-01	1.114480200200E+01	-4.437559453567E-01
H	-5.670597619455E-01	9.429516829383E+00	8.210116958098E-01
H	1.004898849750E+00	1.017161397250E+01	1.068075406643E+00
C	-8.266069658139E-01	1.219301900661E+01	4.824853030529E-01
H	6.533365753247E-01	1.159661655048E+01	-9.770626728541E-01
H	-9.224306293090E-01	1.086049838877E+01	-1.218889774618E+00
H	-1.678888805453E+00	1.174294916409E+01	1.012284100999E+00
H	-1.010834621414E-01	1.247209282774E+01	1.260538473439E+00
H	-2.773804911973E+00	1.406507038551E+01	1.207542702343E+00
H	-1.191809850013E+00	1.478537624385E+01	1.454879842074E+00
C	-6.418444077636E+00	7.125423404770E+00	2.830260310166E+00
H	-6.825885885591E+00	6.549098974258E+00	7.851646575686E-01
H	6.808047068870E+00	8.054980304094E+00	1.267940234848E+00
C	-5.108884579039E+00	7.873330182724E+00	2.548339913897E+00
H	-6.946027251413E+00	7.618195932388E+00	3.660225910319E+00
H	-6.186121888668E+00	6.109321729785E+00	3.181226546055E+00
C	-4.177893802819E+00	7.960520615648E+00	3.765109273464E+00
H	-4.578766787371E+00	7.378399596836E+00	1.721432268142E+00
H	-5.338580846901E+00	8.889260374701E+00	2.194575505448E+00
C	-2.868243880222E+00	8.701890508062E+00	3.476049760603E+00
H	-4.706423365608E+00	8.459221001356E+00	4.589624967121E+00
H	-3.952386919734E+00	6.945474721664E+00	4.120678188589E+00
H	-2.227514282943E+00	8.747819581903E+00	4.363341079537E+00
H	-2.299339503717E+00	8.204663535959E+00	2.681239363192E+00
H	-3.058630941789E+00	9.731452008695E+00	3.150173667436E+00
H	1.601513489366E+00	4.788757553580E+00	2.673422016914E-01
C	6.577882309632E+00	-4.308778693035E-01	6.925328846756E-01
O	6.924358242456E+00	-3.149878456136E+00	1.722997625013E+00
C	5.520441935963E+00	-5.906201136436E+00	1.105639767392E+00
C	4.523042690519E+00	-6.106484977449E+00	-5.827230298667E-02
C	3.225694467520E+00	-6.865371505669E+00	2.618719783341E-01
C	2.296446149767E+00	-6.975377599430E+00	-9.556185459533E-01
C	5.956401450136E+00	-7.218383475915E+00	1.793380550346E+00
C	6.619626020917E+00	-8.246326736697E+00	8.659504595604E-01
C	7.122120780776E+00	-9.489220766195E+00	1.613842257696E+00
C	-6.626104274523E+00	-1.053572469067E+01	6.992715159706E-01
C	-6.138896315400E+00	-1.178416700899E+01	1.446603642038E+00
C	-5.494958467693E+00	-1.283505660211E+01	5.326075584726E-01
C	-5.015734992460E+00	-1.408710620426E+01	1.279094823732E+00
C	-4.376159607701E+00	-1.514094045115E+01	3.656588597162E-01
H	6.422813397363E+00	-5.447622087905E+00	6.817535527144E-01
H	5.046499636153E+00	-6.625579854858E+00	-8.717987390127E-01
H	4.264791118614E+00	-5.120291527342E+00	-4.684374803242E-01
H	3.461476556270E+00	-7.876506625330E+00	6.208951584497E-01
H	5.092947284053E+00	-7.683111250091E+00	2.289935517579E+00

H	6.664118283709E+00	-6.966786217347E+00	2.595925579362E+00
H	5.912739094705E+00	-8.561756918941E+00	8.728578832873E-02
H	-6.937278416192E+00	-7.772087208568E+00	3.402921429240E-01
H	2.830124302914E+00	-7.469730470605E+00	-1.781031684267E+00
H	6.011162425467E-01	-8.343597320158E+00	-2.705389296202E+00
H	-6.555460894402E+00	-9.182788197050E+00	2.385839704466E+00
H	6.281631789997E+00	-9.951665727769E+00	2.151874398610E+00
H	7.053121844975E+00	-1.083586527002E+01	-7.687753244822E-02
H	-5.780102992213E+00	-1.007803369999E+01	1.661526088355E-01
H	-5.417624806357E+00	-1.148561643680E+01	2.221275638497E+00
H	-6.985444776060E+00	-1.223900965241E+01	1.981525184355E+00
H	-6.215331960783E+00	-1.312964438415E+01	-2.444556046957E-01
H	-4.645984308596E+00	-1.238148271106E+01	5.727828721166E-04
H	-4.293845400899E+00	-1.379310733969E+01	2.055014262145E+00
H	-5.865376815084E+00	-1.453770191641E+01	1.812720877282E+00
C	-3.901158165848E+00	-1.639502965828E+01	1.111497844846E+00
H	-5.097127386036E+00	-1.543368911744E+01	-4.117565356503E-01
H	-3.524589624104E+00	-1.469232066718E+01	-1.666743704360E-01
C	-1.294551041832E+00	1.345774101831E+01	-2.496708308725E-01
C	-1.918810539072E+00	1.450929347200E+01	6.769360302433E-01
H	-4.418138173641E-01	1.390425040919E+01	-7.818659226026E-01
H	-2.022504566457E+00	1.317974523227E+01	-1.025862511290E+00
C	-2.381505752534E+00	1.577670964428E+01	-5.399172025565E-02
C	-3.001626819255E+00	1.682193243445E+01	8.795425067750E-01
H	-1.527234485711E+00	1.622023848303E+01	-5.843622296532E-01
H	-3.109032063677E+00	1.550113542806E+01	-8.302104234136E-01
H	-3.321244657747E+00	1.771307057398E+01	3.285947543099E-01
H	-3.879588682107E+00	1.641901475110E+01	1.398236501319E+00
H	-2.286041675744E+00	1.714343386354E+01	1.645582298211E+00
C	-3.264929319538E+00	-1.744237429592E+01	1.912974843870E-01
H	-3.180035332237E+00	-1.610261406411E+01	1.887488229655E+00
H	-4.752059380215E+00	-1.684324665140E+01	1.643259297765E+00
H	-2.936659759441E+00	-1.832377135377E+01	7.526883182118E-01
H	-3.973658007016E+00	-1.778050210115E+01	-5.738944475183E-01
H	-2.389984000445E+00	-1.703429497335E+01	-3.283737429628E-01
C	3.115761725517E+00	-1.847902355884E+00	1.039561356952E+00
C	4.182124513568E+00	-9.639631337568E-01	7.418714508882E-01
C	3.835717221288E+00	3.042779676038E-01	1.894529303565E-01
C	-6.378362918037E+00	-6.185403711622E-01	9.233836049260E-01
C	-5.688939779142E+00	-1.059171198964E+00	2.033708078768E+00
C	-4.286059164346E+00	-9.518073963571E-01	1.917059921927E+00
C	-3.863911877787E+00	-4.353701515761E-01	7.042658844402E-01
S	-5.244061561288E+00	-5.430705066247E-02	-2.988087613585E-01
C	-2.516394547092E+00	-2.217004562096E-01	2.282990352852E-01
S	-1.136351501064E+00	-6.037706088258E-01	1.231213620128E+00
C	-1.966607443790E-03	-3.981733115637E-02	9.195310662089E-03
C	-6.910873452699E-01	4.018272060820E-01	-1.100867950707E+00
C	-2.094043739073E+00	2.950725205728E-01	-9.842889971800E-01
H	-1.958181473174E-01	7.952449767195E-01	-1.977285916702E+00
H	-2.780481878833E+00	5.945178958490E-01	-1.768780073163E+00
H	-3.599511169409E+00	-1.250511259862E+00	2.701731700180E+00
H	-6.183960777242E+00	-1.452551550733E+00	2.910213297558E+00

Attachment B

Cimo' , S. *et al.*, Room temperature activation of n-type doping of naphthalene diimide - bithiophene copolymer by 1H- benzimidazoles, manuscript in preparation, to be submitted to *Advanced Functional Materials*.

Associated Contents (Supporting Information) are enclosed.

Room temperature activation of n-type doping of naphthalene diimide - bithiophene copolymer by 1H- benzimidazoles

*Simone Cimò, Ilaria Denti, Lorenzo Rossi, Marco Cassinelli, Garrett Lecroy, Alberto Salleo, Mario Caironi, Antonino Famulari, Chiara Castiglioni, Chiara Bertarelli**

Simone Cimò, Dr. Marco Cassinelli, Dr. Mario Caironi, Prof. Chiara Bertarelli
Center for Nano Science and Technology @PoliMi, Istituto Italiano di Tecnologia, via Pascoli 70/3, 20133 Milano, Italy.

Simone Cimò, Ilaria Denti, Lorenzo Rossi, Prof. Antonino Famulari, Prof. Chiara Castiglioni, Prof. Chiara Bertarelli
Dipartimento di Chimica, Materiali e Ingegneria Chimica Giulio Natta, Politecnico di Milano, Piazza Leonardo da Vinci 32, 20133 Milano, Italy.

Ilaria Denti, Garrett Lecroy, Alberto Salleo
Department of Materials Science and Engineering, Stanford University, 476 Lomita Mall, Stanford, California 94305, United States

E-mail: chiara.bertarelli@polimi.it

Keywords: doping, annealing, P(NDI2OD-T2), benzimidazoles, conductivity, DFT modelling, GIWAXS

ABSTRACT

N-doped polymer semiconductors are of great interest in the field of organic thermoelectrics, as high conductive materials are still highly desired. In this framework, this paper aims clarifying whether the n-doping of naphthalene diimide - bithiophene copolymer, P(NDI2OD-T2), by 1H- benzimidazoles is a thermally activated process. Annealing with different time and temperature of spin-coated films of the doped polymer is carried out. The study interestingly demonstrates that a dramatic change of conductivity, more than three orders of magnitude higher than that of pristine P(NDI2OD-T2), occurs

before the annealing process takes place, thus revealing that benzimidazole-derived dopants are already active at room temperature. Moreover, despite annealing time and temperature affect the electrical conductivity of the system, their contribution is less relevant, with the increase of electrical conductivity limited to three times. The results from the electrical characterization of the samples are supported by GIWAXS, revealing a dramatic structural change between the undoped and the just-doped P(NDI2OD-T2) films, accompanied by only minor modifications during the annealing process. Finally, based on the results of density functional theory simulations, the conformational modifications of the dopant molecules, induced by the interaction with the NDI2OD-T2 polymer, is proposed as a mechanism explaining the effective doping at room temperature.

1. Introduction

The unique electrical properties, easy processability^[1] and versatile chemical synthesis, have made π -conjugated polymers promising materials to revolutionize many fields of low-cost and flexible electronics.^[2,3] At present, π -conjugated small molecules and polymers find application in transistors^[4-7] thermoelectric devices,^[8-18] solar cells, ^[6, 19-20] light emitting diodes^[21-22] and supercapacitors.^[23] One of the key parameters of these materials is the conductivity of the organic semiconductor active layers. Doping an organic semiconductor either by reducing (*n*-type doping) or by oxidizing (*p*-type doping) can dramatically increase the charge carrier density and therefore the electrical conductivity,^[24] which is a fundamental requirement to develop efficient thermoelectric generators.

Although for the development of thermoelectric devices both *p*-type (hole conducting) and *n*-type (electron conducting) materials are required, in the past the research was particularly focused on the study of the formers.^[25-30] The development of *n*-type organic semiconductors has not been straightforward for their difficult synthesis and because of their intrinsic high LUMO, which often leads to air instability.^[31] In this framework, naphthalene diimide (NDI) - bithiophene (T2) copolymers exhibit relatively high electron mobility and a rather good air stability,^[6,7] which make them attractive for several applications.

Several studies have been conducted on this class of copolymers where both backbone^[28-31] and side chains^[36-39] have been systematically changed. Our work is focused on the widely used P(NDI2OD-T2), characterized by an electrical conductivity in its pristine state of around $4 \times 10^{-7} \text{ S cm}^{-1}$ ^[40-46] It is worth noting that the orientation of the chains changes upon the deposition method of the film. In particular, epitaxially grown films in different forms,^[47] form 1 and form 2, as well as spin coated films were investigated through infrared spectroscopy together with an analytical model to individuate geometrical variables describing the polymer structure. Face-on arrangement of the chains was proposed for form 1, whereas the more thermodynamically stable form 2, characteristic of high molecular weight samples, presents the polymer chain axis pointing out of the substrate. Spin coated films showed a T2 unit mostly parallel to the substrate^[46-50] in a face-on conformation, with a dihedral angle of 38° between the NDI and the T2. Thermal treatment of P(NDI2OD-T2) affects its structure: in particular, melt annealing, followed by slow

cooling, causes the transition to an edge-on structure with the polymer segments running in a direction close to the perpendicular to the substrate. [49]

The *n*-type doping of naphthalene diimide copolymers is hindered by the low stability of *n*-type dopants in air. An electron donor should indeed have a HOMO high enough to enable the transferring of electrons to the polymer LUMO. [50] However, this characteristic makes the dopant rather unstable in air. A common approach to solve this issue is the use of air-stable precursors, which can be converted *in-situ* into reactive reducing agents [51-52]. Recently, 1H-benzimidazoles have attracted great interest since they are air-stable *n*-type dopants. [53-54] P(NDI2OD-T2) doped with the 4-(1,3-dimethyl-2,3-dihydro-1H-benzoimidazol-2-yl)-N,N-dimethylaniline (DMBI) or the 4-(1,3-phenyl-2,3-dihydro-1H-benzoimidazol-2-yl)-N,N-dimethylaniline (DPBI) shows an increase of electrical conductivity of around 3 orders of magnitude with respect to the pristine state. However, at high dopant concentrations, phase segregation occurs, limiting the dopant efficiency. [55] The N-substitution of the aniline with longer linear or branched alkyl chains improves the dopant-polymer miscibility, further increasing the electrical conductivity of the system. P(NDI2OD-T2) doped with 4-(1,3-dimethyl-2,3-dihydro-1H-benzo[d]imidazol-2-yl)-N,N-diisopropylaniline (DiPrBI) exhibits one of the highest electrical conductivities ($7.2 \times 10^{-3} \text{ S cm}^{-1}$) recorded for doped P(NDI2OD-T2). [56] DMBI dimers have also been reported as effective *n*-type dopants. [57]

Recently, x-ray measurements highlighted how the orientation of the P(NDI2OD-T2) crystallites switches from face-on to edge-on upon doping. [58] The remarkably higher

conductivity in the direction parallel to the substrate plane, observed for doped P(NDI2OD-T2), corroborated the idea of a change of morphology upon doping, with the π -stacking direction from out-of-plane to in-plane.^[58] Different doping mechanisms have been considered to explain the interaction and charge transfer between DMBI and P(NDI2OD-T2). As previously reported, an acid-base reaction with a hydride transfer from the dopant to the polymer was ruled out.^[59] Another interesting hypothesis involves the formation of an intermediate radical SOMO followed by a direct electron transfer from such molecular orbital to the LUMO of the polymer. This doping mechanism agrees with the traditional concept that benzimidazole derivatives are thermally activated upon annealing.^[60-61] Despite some specific differences in the procedure to dope P(NDI2OD-T2) with 1-H benzimidazoles found in the literature,^[55, 58-64] this process often shares similar steps: the P(NDI2OD-T2) solution containing the dopant is spin coated, and the deposited films are annealed under inert atmosphere for several hours. Annealing is often carried out at 150°C for 6 hours under N₂ atmosphere,^[55, 56, 59] but there are several examples in the literature with a lower annealing temperature (from 80 to 120°C)^[37, 57-58, 63-64] and from few minutes up to some hours.^[37,63-64]

So far, thermal-annealing was supposed to be mandatory to activate the benzimidazole-derived dopants and to promote a good packing of the polymer chains, as for most of the conjugated polymers in the pristine state. In order to reach the optimal process condition for doping, we systematically changed the annealing temperature and time. Here, we show that a strong change of conductivity is actually achieved before the thermal post-

processing, which allows just for a less significant further increase, demonstrating that the 1H-benzimidazoles do not require a thermal activation above room temperature for the charge transfer to occur. A molecular modelling study, based on density functional theory (DFT), suggests a new model for the doping mechanism providing a rationalisation of the experimental outcomes.

2. Results and Discussion

To study the effect of annealing temperature and time on the *n*-doping process, we selected the well-studied P(NDI2OD-T2) and the 4-(1,3-dimethyl-2,3-dihydro-1H-benzo[d]imidazol-2-yl)-N,N-diisopropylaniline (DiPrBI) as dopant, given the high conductivities reported for this pair.^[56] Films of P(NDI2OD-T2) at two different concentrations of the dopant were prepared, namely 76%_(mol/mol), corresponding to the optimal dopant concentration according to the previous results,^[56] and at 100%_(mol/mol), possibly giving rise to dopant segregation. Dopant concentration is expressed as the ratio between dopant moles and the number of P(NDI2OD-T2) repeating units.

The electrical and morphological properties of both pristine and doped P(NDI2OD-2) were evaluated. Details regarding samples preparation and measurements are reported in the Experimental Section.

2.1 Electrical Properties

To provide a benchmark for doped samples, the conductivity of pristine P(NDI2OD-T2) films annealed at 70°C, 110°C and 150°C were first measured (**Figure 1 A**). Annealing temperatures have been chosen taking into account the range of values reported in the literature, which spans from very mild conditions up to 150°C.^[58-64] For all the samples of the pristine polymer, the electrical conductivity remains stable around $4.0 \times 10^{-7} \text{ S cm}^{-1}$, irrespective of annealing time and temperature. This result is in agreement with literature, reporting significant changes of P(NDI2OD-T2) morphology,^[44, 49] hence of electrical conductivity, only at very high temperature ($>300^\circ\text{C}$) or annealing assisted by rubbing.

Concerning the doping ratio, we analysed samples at the optimal DiPrBI dopant concentration of 76%_(mol/mol), according to the previous results,^[56] and at a higher value (100%_(mol/mol)) where a supposed phase segregation occurs (**Figure 1 B**), leading to a worsening of the electrical conductivity.

The most interesting finding is the conductivity of the as-spun doped films: without any annealing process, the electrical conductivity reaches values of the order of $10^{-3} \text{ S cm}^{-1}$, which is almost four orders of magnitude higher than values of the non-doped polymer. Moreover, all samples demonstrate similar electrical conductivity at around $1.8 \times 10^{-3} \text{ S cm}^{-1}$, independently from the specific dopant concentration. These experimental results clearly demonstrate that the 1H-benzimidazole is already active at room temperature, without annealing, and a thermally-activated doping mechanism is not actually required.

Worth noting that a further change in conductivity is obtained once the DiPrBI:P(NDI2OD-T2) films are annealed, and here different results are obtained depending on both the dopant concentration and the annealing temperature. First, at both annealing temperatures of 70°C and 110°C, a too high concentration of dopant (*i.e.* molar dopant ratio 100%) leads to lower electrical conductivity with respect to the one measured in case of the 76% DiPrBI:P(NDI2OD-T2) molar ratio, regardless of annealing time (**Figure 1 C**). This confirms the conclusions reported by Chabinyč *et al.*^[55] and Bertarelli *et al.*^[56] about the worsening of the doping efficiency at high dopant concentration, ascribed to phase segregation phenomena.

For annealing performed at higher temperatures (*i.e.* 110°C and 150°C), the electrical conductivity σ of the 76% doped P(NDI2OD-T2) samples over annealing time up to 5 hours follows an interesting trend (**Figure 1 D**): an almost constant increase in 15-30 minutes, then reaching plateau for a longer annealing time. Accordingly, we speculate that the doping mechanism consists of different stages. The first occurs at room temperature, and it is responsible for a dramatic increase (>5000 times) of electrical conductivity. The second one is triggered by the annealing process; it occurs within the first 15-30 minutes of annealing and it causes an increase of electrical conductivity of around 50-100%. Finally, the last stage is slower; it requires up to 4-5 hours causing a further increase of electrical conductivity of around 20-30%. Overall, the total contribution of the annealing process to the thin films electrical conductivity amounts to an increase of around 2-3 times only.

Surprisingly, annealing at the lowest temperature (70°C) seems to be detrimental (**Figure 1 C**), showing a decreasing conductivity value as a function of different annealing time. This suggests that competitive mechanisms are responsible for the conductivity changes with thermal post-process, which is ruled by the annealing temperature.

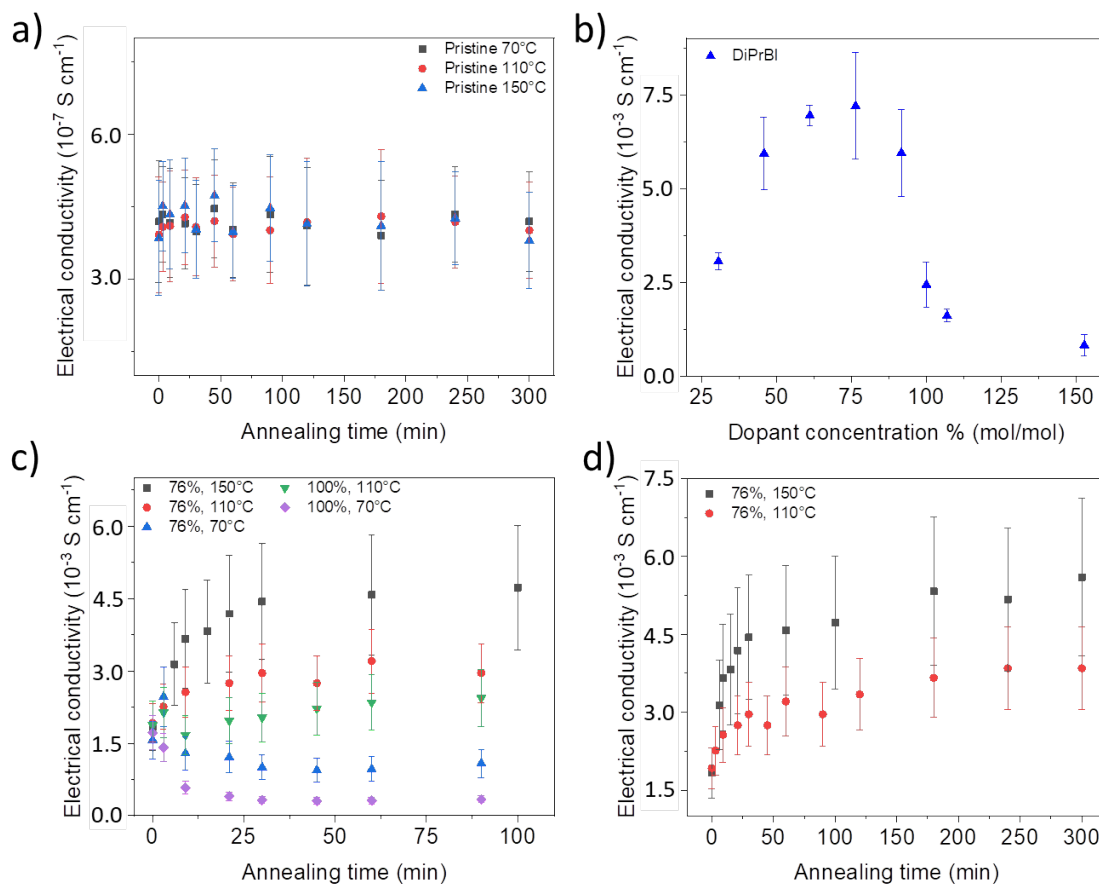


Figure 1: **A:** electrical conductivity of films of pristine P(NDI2OD-T2) annealed at 70°C, 110°C and 150°C over time. **B** electrical conductivity of a P(NDI2OD-T2) film doped at

different concentration with DiPrBI after 5h annealing at 150°C. **C**: electrical conductivity of DiPrBI-doped P(NDI2OD-T2) spin coated films annealed at different temperatures over time. Black, red and blue dots refer to films of P(NDI2OD-T2) 76% doped with DiPrBI annealed at 150°C, 110°C and 70°C, respectively. Green and violet dots refer to films of P(NDI2OD-T2) 100% doped with DiPrBI annealed at 110°C and 70°C, respectively. **D**: electrical conductivity of P(NDI2OD-T2) 76% doped with DiPrBI annealed for a longer period (up to 5h).

2.2 Film Morphology

To study the effects of the different annealing process on the thin films structure and crystallinity, Grazing Incident Wide Angle X-ray Scattering (GIWAXS) measurements were performed on samples subjected to different annealing temperatures and times. Representative GIWAXS patterns for all the samples are shown in **Figure 2**. The reduced 1D line profiles reported in **Figure 3** are taken along the horizontal (in plane, q_{xy}) and approximately vertical (out of plane, $\sim q_z$) scattering directions. The out-of-plane ($\sim q_z$) scattering peak at $q \sim 1.6 \text{ \AA}^{-1}$ is attributed to the (010) planes along the π -stacking direction. There are a number of scattering peaks along the in-plane (q_{xy}) scattering direction attributed to the (001) and (100) planes corresponding to periodicity along the backbone repeat units and in-plane lamellar stacking directions. Figure 3 highlights that up to four orders of lamellar stacking and up to two orders of backbone repeat unit scattering peaks

can be observed in the in-plane direction, agreeing with previous GIWAXS studies that showed P(NDI2OD-T2) has exceptional in-plane ordering.^[49]

To evaluate annealing effects on pristine P(NDI2OD-T2), we performed GIWAXS measurements on an as-spun state and after annealing at 110°C for 90 minutes. Since the annealing temperature is well below the melting point, pristine P(NDI2OD-T2) crystallites exhibit a face-on orientation, already reported in literature.^[44, 49] Annealing P(NDI2OD-T2) had little effect on material structure (figure 2A,B), in agreement with the conductivity data of Figure 1A. However, in the annealed sample, it is possible to notice a slight decrease in the intensity of q_z (010) peak with respect to the q_{xy} (100) and the q_z (100)' peak, which can be ascribed either to a structural relaxation or to an almost negligible face-on to edge-on transition. On the contrary, the unannealed 76% doped sample exhibits a dramatic change in the morphology; particularly, the q_z (010) π -stacking scattering peak ($q \sim 1.6 \text{ \AA}^{-1}$) decreases in intensity and broadens significantly in the doped sample, and the q_{xy} (100) lamellar scattering peak ($q \sim 0.3 \text{ \AA}^{-1}$) shifts to higher q -values. The drop in intensity of the q_z (010) peak is ascribed to a change of the orientation of the crystallites with respect to the substrate, from face-on to edge-on. A transition of this type was reported in literature for P(NDI2OD-T2) doped with DMBI derived molecules. The broadening of the q_z (010) peak indicates that the dopant intercalation alters the π -stacking direction.^[56, 58, 62] A possible explanation of this behaviour is that the dopants intercalate between the NDI units, introducing disorder in the π -stacking distances.

A comparison between the 70°C and 110°C in plane data shows that the (100) lamellar peak (Figure 3a) moves toward higher values of q_{xy} with the increase of annealing temperature and time. In particular, the (100) peak of the 70°C, 90 minutes annealed sample has the same q value of the sample annealed at 110°C for 5 minutes.

The (001) backbone peak does not change in position or in intensity/shape, confirming that the doping process does not influence the intramolecular repeating distance along the polymer chain axis.

Both the 110°C and 70°C samples exhibit a decrease in the coherence length and intensity of the q_z (010) peak with respect to the q_z (100)' peak. In particular, this behaviour is more pronounced in the 110°C series. Furthermore, a shoulder around 1.6 \AA^{-1} arises in the 70°C, 90 minutes annealed sample and in all samples annealed at 110°C. These changes are consistent with a perturbation of the π -stacking direction, characterized by a shorter-range order with respect to the pristine case, as previously discussed.

The q_z (200)' peak gains intensity in the 110°C series. This peak further confirms the edge-on orientation of the polymer crystallites upon doping. Moreover, Saglio *et al.* interpreted this peak as one of the experimental evidences indicating the dopant intercalation between the P(NDI2OD-T2) backbones.^[56] To summarize, our data show a change in the orientation of the crystallites upon doping (from face-on to edge on). Moreover, the broadening of the peak associated to π -stacking (the charge transport direction) upon doping, indicates a higher disorder within the crystallites than in the pristine samples. This demonstrates that the dopant might be intercalated in the crystal domains, causing the chains to rearrange.

From Figure 3, it is interesting to notice that the 70°C series exhibits a more pronounced face-on orientation than both the not annealed and the 110°C data. This behaviour suggests that below 70°C the face-on arrangement is favoured. Moreover, the observed morphology is strongly correlated with the electrical conductivity data, which exhibits a lowering of electrical conductivity for the samples annealed at 70°C.

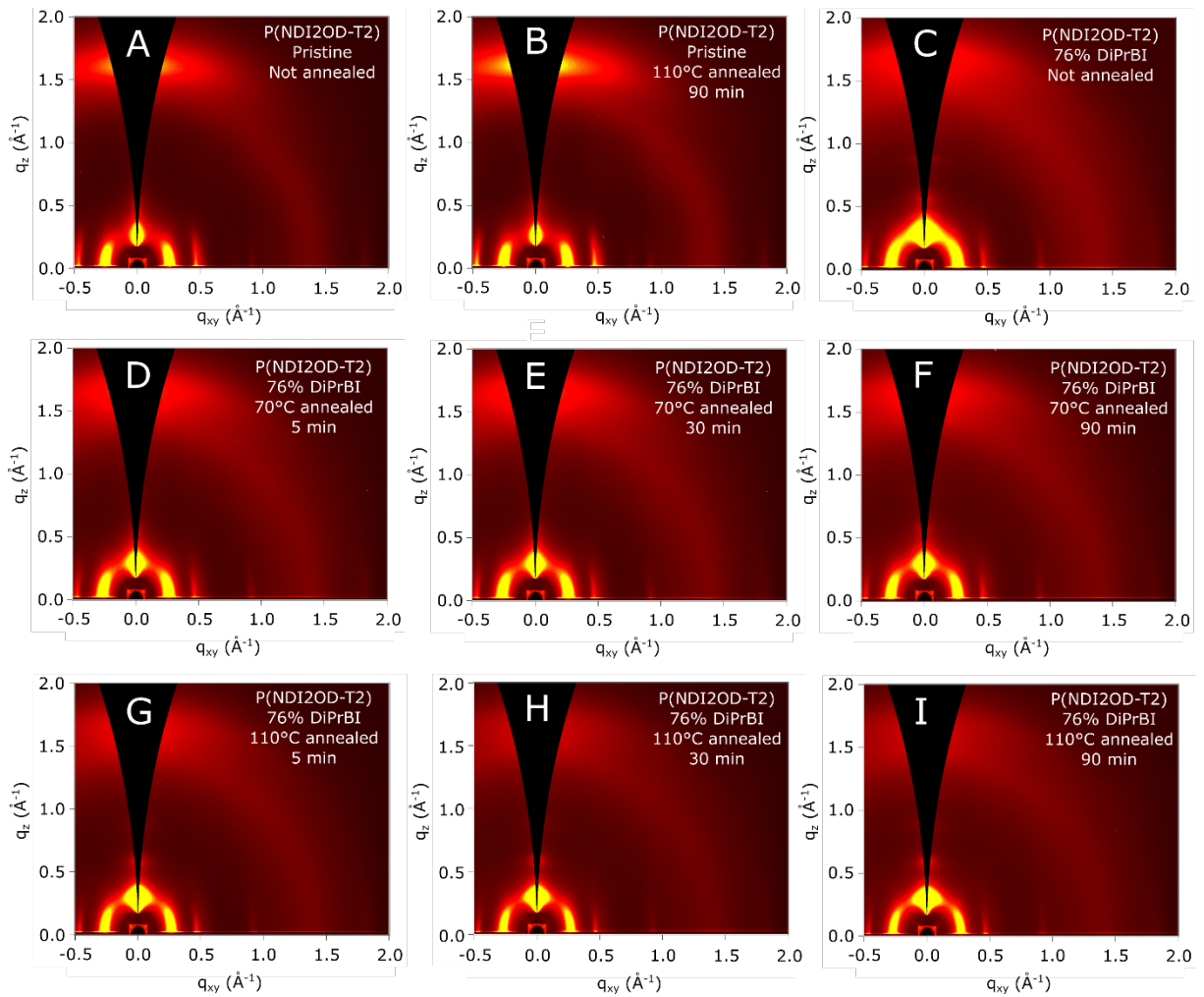


Figure 2: GIWAXS data for A) not annealed pristine P(NDI2OD-T2); B) pristine P(NDI2OD-T2) annealed at 110°C for 90 min; C) not annealed 76% DiPrBI doped

P(NDI2OD-T2); D-F) 76% DiPrBI doped P(NDI2OD-T2) annealed at 70°C for 5, 30 and 90 min, respectively; G-I) 76% DiPrBI doped P(NDI2OD-T2) annealed at 110°C for 5, 30 and 90 min, respectively.

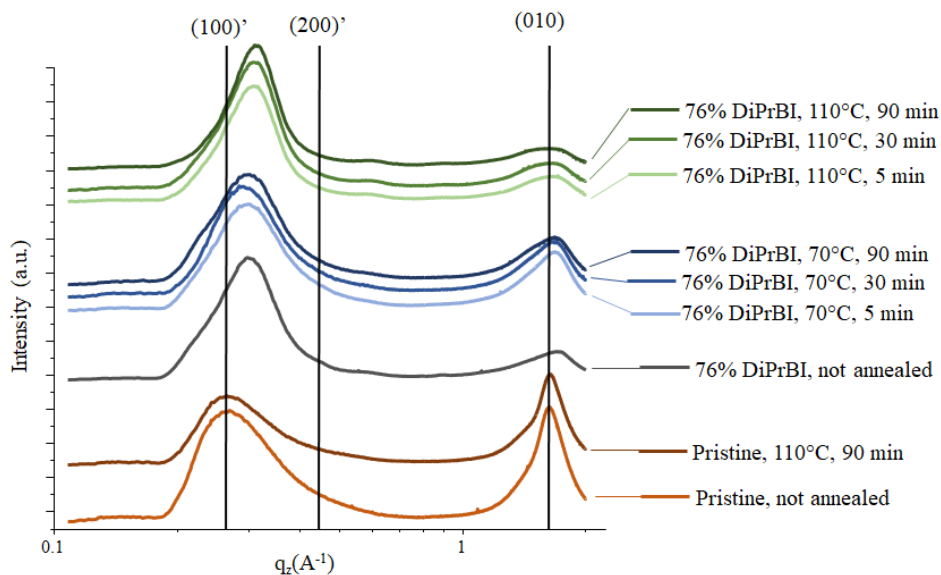
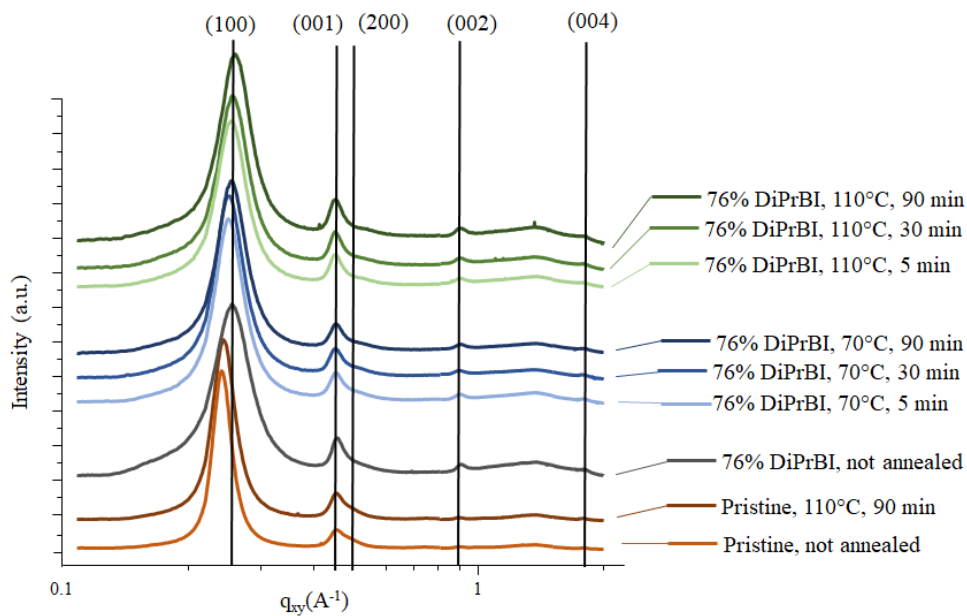


Figure 3 a. Vertical line-cuts (in plane direction) and **b.** horizontal line-cuts (out of plane direction) of the two dimensional GIWAXS spectra for P(NDI2OD-T2) doped with DiPrBi, 76%. In both graphs are shown from bottom to top: pristine samples not annealed and annealed at 110°C for 90 minutes (brown lines); doped not annealed sample (grey line); doped samples annealed at 70°C for 5, 30 and 90 minutes (blue line); doped samples annealed at 110°C for 5, 30 and 90 minutes (green line).

2.3 Molecular Modelling Results

While a hydride transfer reaction has been ruled out,^[59] an electron transfer between the dopants radical SOMO and the polymer LUMO is a valuable hypothesis reported in literature to explain the doping mechanism of benzimidazole derivatives for P(NDI2OD-T2).^[60] The energetical justification for this doping mechanism is based on the radical formation during the annealing process, implying that the dopants are thermally activated. However, this hypothesis is in contrast with our experimental data because we observe a substantial increase of the electrical conductivity before thermal annealing is performed, indicating that the dopant molecules are already active at room temperature. In addition, GIWAXS analysis suggests that the alteration of the q_z (010) peak, associated to the order, *i.e.* coherence length, along the π -stacking direction, might be caused by the presence of dispersed dopant molecules between the polymer units. According to these considerations, we investigated a plausible mechanism in which the dopant electrons could be activated by the intermolecular interactions with the polymer at room temperature. Specifically, we

hypothesize that the dopant could modify its structure (*i.e.* its conformation) while intercalating between the narrow polymer lamellae, and that such structural modification is accompanied by a perturbation of the dopant electronic structure. Therefore, after dopant intercalation, new electronic transitions might be accessible to the dopant electrons, thus allowing for an electron transfer to the polymer. As a first step of our computational study, we performed DFT calculations aiming to evaluate the amount of energy involved in the interaction between the dopant molecules and the polymer. To maintain a good accuracy together with a reasonable computational cost, we performed a geometry optimization on a simplified model system composed of a single DiPrBI molecule interacting with two repeating units of P(NDI2OD-T2). Moreover, to further reduce computational costs, the long branched alkyl chains on the NDI units have been replaced with isobutyl side groups (T-NDI2Bu-T, **figure 4A**). The results of this optimization (**figure 4B**) clearly show a favourable interaction between the NDI units of T-NDI2Bu-T and the benzimidazole part of DiPrBI, whereas the isopropyl chains of DiPrBI orient themselves toward the alkyl chains of the polymer units. The corresponding interaction energy is evaluated as the usual standard supermolecule approaches:

$$E(\text{interaction}) = E_{(\text{SYSTEM})} - E_{(\text{DiPrBI})} - 2E_{(\text{T-NDI2Bu-T})}$$

where $E_{(\text{SYSTEM})}$ is the total energy of the system composed of DiPrBI sandwiched between two T-NDI2Bu-T units; $E_{(\text{DiPrBI})}$ is the total energy of DiPrBI in its absolute conformational minimum and $E_{(\text{T-NDI2Bu-T})}$ is the total energy of a T-NDI2Bu-T unit. The results show a

quite high interaction energy of about -56 kcal/mol. It is clear, by definition, that the negative sign indicates that the interaction between the moieties stabilize the system. Taking this as a starting point, we can make a further simple hypothesis: the stabilisation reached by this interaction can cause conformational changes (*i.e.* distortion from its absolute minimum) into dopant molecules, thus activating and promoting electron transfer to the polymer.

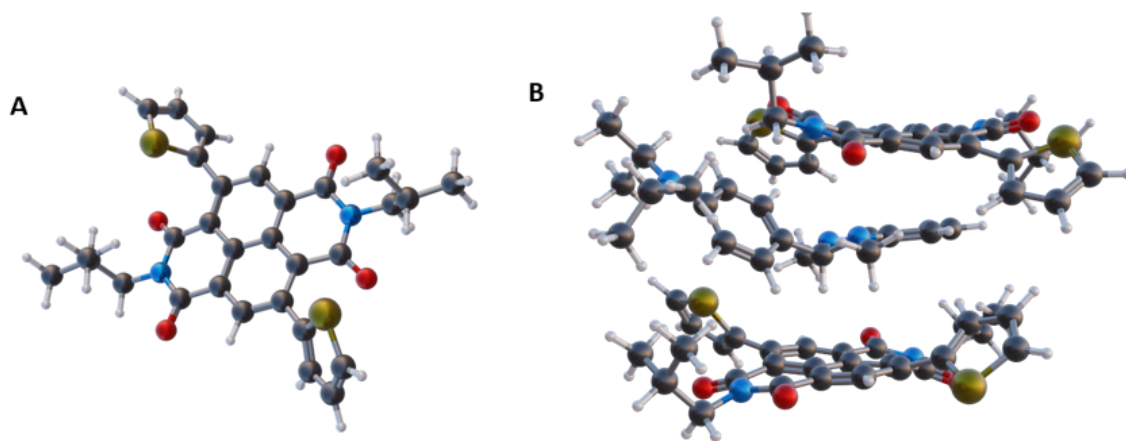


Figure 4: A) A view of T-NDI2Bu-T. B) A view of the model system composed of DiPrBI and two T-NDI2Bu-T units resulting from DFT geometry optimizations.

As previously stated, we hypothesize a doping mechanism involving significant geometrical modifications of the dopant. Specifically, given the marked planar structure of the NDI units of the polymer, we assume a conformational modification, which we can describe as a quasi-planarization of the dopant structure while intercalating within the polymer lamellae. In order to assess the feasibility of this distortion, we performed a systematic study by designing a set of plausibly involved DiPrBI geometries, obviously

assuming that some of these structures can be sampled by the intercalation of the dopants within the polymer lamellae. The DiPrBI molecule in its absolute minimum conformation is reported in **Figure 5A**. In particular, the atoms 5, 6, 13 and 14 define the *xy* plane ($z = 0$ Å) and the origin of the cartesian axis is placed in the middle point of the segment connecting atoms 13 and 14. The dihedral angle between the *xy* plane and the plane passing through atoms 13, 14 and 15 is 29.3° . The dihedral angle between the plane passing through atoms from 7 to 12 and the *xy* plane is 72° . The corresponding calculated HOMO energy level for this conformation is -4.40 eV.

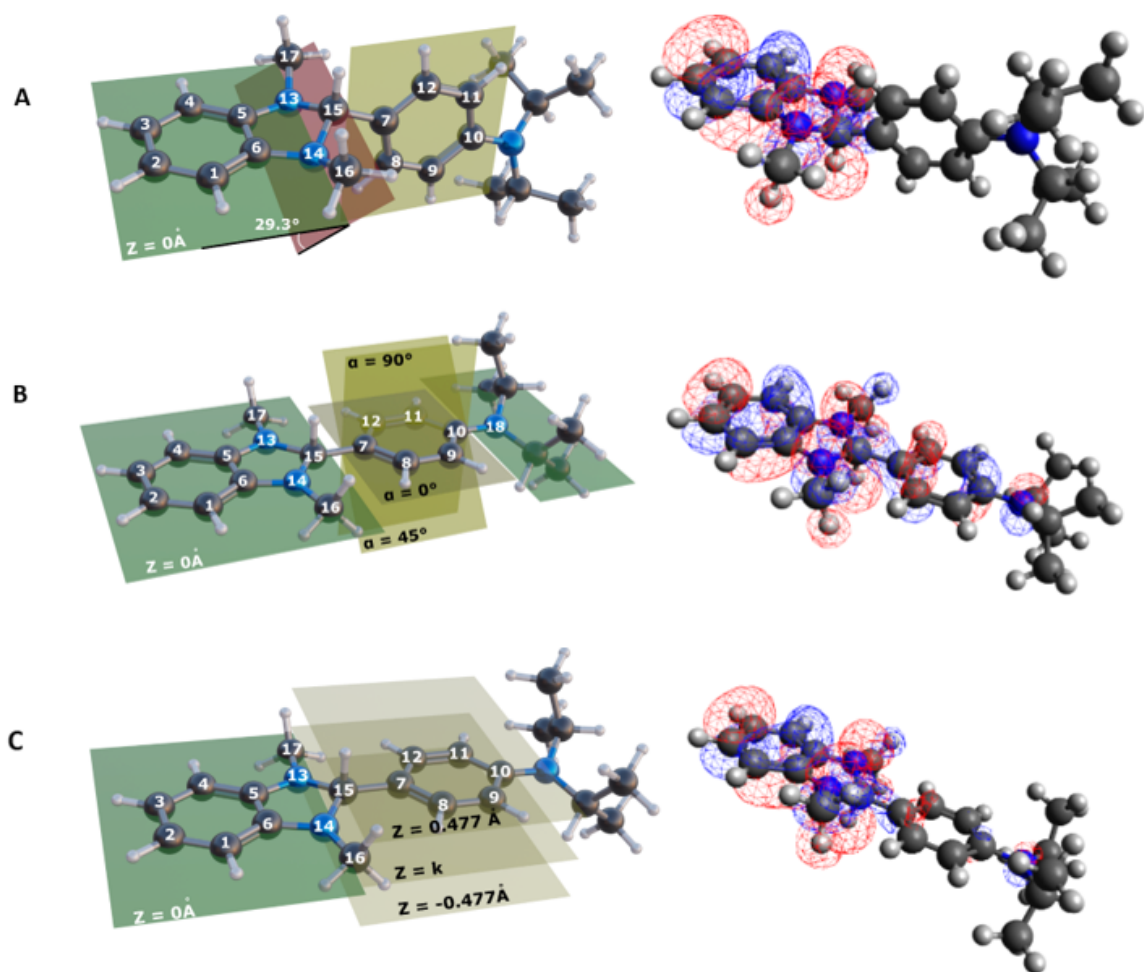


Figure 5: A) Spatial representation of DiPrBI structure in the absolute minimum. B) First set of planar geometries, C) Second set of planar geometries.

We designed two sets of geometries. In the first one, the atoms 15 and 18 are constrained to lay on the xy plane ($z = 0 \text{ \AA}$) and the dihedral angle is systematically scanned between the two phenyl groups (**figure 5B**) while performing geometry optimizations. The

HOMO energy changes upon the molecule distortion have been evaluated together with the energy cost with respect to the DiPrBI absolute minimum conformation, and the results are reported in **Table 1**. To design the second set of geometries we instead forced atoms 7, 8, 9, 10, 11, 12, 15 on the same plane at a parallel to the xy plane ($z = 0 \text{ \AA}$) and placed at different heights ($z = k$). We then systematically varied the distance k between the two planes (**figure 5C**). The calculation results are reported in **Table 2**.

Dihedral Angle ($^{\circ}$)	HOMO (eV)	Cost (kcal/mol)
0	-3.99	47
30	-3.75	44
45	-3.70	44
60	-3.80	48
90	-3.52	41

Table 1. Calculated HOMO energy (eV) upon molecule dihedral angle rotation and energy cost with respect to the DiPrBI absolute minimum conformation.

Z (\AA)	HOMO (eV)	Cost (kcal/mol)
--------------------	-----------	-----------------

- 0.47 7	- 3.32	105
- 0.23 9	- 3.29	84
0.00 0	- 3.59	64
0.23 9	- 3.81	44
0.47 7	- 4.07	30

Table 2. Calculated HOMO energy (eV) upon molecule distortion and energy cost with respect to the DiPrBI absolute minimum conformation. Z is the distance between the plane defined by the phenyl ring composed of carbon atoms 1-6 and the distance between the parallel plane passing through carbon atoms 7-12.

The calculations show that these geometrical distortions cause a substantial rise of the HOMO energies of the dopant, towards matching the LUMO of the polymer, possibly reaching values even higher than the polymer LUMO. Furthermore, the energetic cost for the corresponding geometrical distortion is comparable to the interaction energy involved in the intercalation step of the doping process, meaning that these interactions can compensate for the energy penalty. To summarize, the model here proposed highlights the role of the polymer-dopant interactions in promoting the charge (electron) transfer from the HOMO of the dopants to the LUMO of the polymer. According to our calculations, there exists perturbed conformations - likely originating by the intercalation processes - that would substantially reduce or eliminate the energy barrier for the charge carrier

injection. This charge transfer model suggests a doping mechanism that can explain why benzimidazole derivatives are already active at room temperature.

3. Conclusions

A collection of experimental evidences interestingly demonstrate that n-type doping of P(NDI2OD-T2) by 1H- benzimidazoles is already active at room temperature. We show that before the thermal treatment takes place, the electrical conductivity of P(NDI2OD-T2):DiPrBI thin films already increases more than three orders of magnitude with respect to the pristine polymer. This is a clear indication that DiPrBI is already active at room temperature, whereas annealing has only a minor effect, causing a further doubling of electrical conductivity values. GIWAXS measurements reveal that the morphology of the doped film is remarkably different from that of the non-doped polymer film, namely it shows a mainly edge-on orientation of the polymer, characterized by structural disorder (distribution of π -stacking distances and orientational disorder), which is compatible with dopant intercalation between NDI units. Moreover, the GIWAXS analysis suggests that, while the annealing at 110°C results in increasing the content of the edge-on phase, the annealing at lower temperature (70°C) slightly increases the amount of face-on domains with respect to the doped film as deposited. This plays a role in the conductivity trend observed for films annealed at such a low temperature.

To rationalize the experimental findings, we carried-out a thorough theoretical study based on Quantum Chemical modelling focusing on the relationship between molecular and electronic structure of the dopant. This study shows the importance of specific polymer-

dopants interactions in the doping mechanism. We demonstrate that, due to a quasi-planarization, the HOMO of the dopant rises significantly thus reducing or eliminating the barrier of the electron injection into the polymer LUMO orbital. The planarization of the dopant molecule is expected to occur during intercalation processes, because of the interaction with NDI units: the energy cost is in fact compensated by the large intermolecular energies. According to the calculations, we demonstrated that conformations accessible during intercalation actually exist, which would promote the charge transfer. This simple model likely explains why DiPrBI is already active at room temperature. Overall, the generation of the charge carrier and the edge-on configuration of the doped polymer in the as-deposited films indicates that the doping P(NDI2OD-T2) by *IH*-benzimidazoles basically is a non-thermally activated mechanism. The temperature of the annealing plays a relevant role in decreasing or further increasing the conductivity, with low temperature (*i.e.* 70°C) being detrimental as it induces the formation of face-on domains.

This study highlights the relevance of solid-state intermolecular interactions between dopant and polymer, leading the doping mechanism. This paves the way for the development of strategies to design new stable organic dopants, activated by structural relaxation.

4. Experimental Section

4.1. Dopant Synthesis

All chemicals were purchased from Sigma Aldrich, TCI Chemicals or Fluorochem, and they were used as received. Chemicals, intermediates and products were stored in the fridge, inside a sealed flask containing Argon. P(NDI2OD-T2) (Polyera ActivInk N2200, Mn = 150 kDa) was purchased from Ossila Lim. DiPrBI was synthesized of as previously reported. ^[56]

4.2. Electrical Characterization

4.2.1. Contact deposition

Low-alkali 1737F Corning glass was used as substrate. First, the glasses were cleaned through an ultrasonic bath of Milli-Q water, acetone, and isopropyl alcohol of 10 min for each step, and then exposed to O₂ plasma at 100 W for 10 min. Subsequently, the electrodes were thermally evaporated using a shadow mask, obtaining electrical contact lines made of 1.5 nm thick Cr adhesion layer and 25 nm thick Au film, 2 mm wide, long between 1 and 1.5 cm and distant to each other 8 mm.

4.2.2. Film deposition

Polymer film preparation was carried inside a glovebox in N₂ atmosphere. P(NDI2OD-T2) (Polyera ActivInk N2200, purchased from Ossila Lim, Mn = 150 kDa,) was dissolved in 1,2-dichlorobenzene (DCB, concentration of 10mg/mL). The resulting solution was stirred at 80°C for 1h. The mixture was loaded into a syringe and filtered using a 0.45 µm pore

size polytetrafluoroethylene filter. Aliquots of 50 μL of such solution were added to vials containing 0.124 mg and 0.153 mg of DiPrBI, enough to dope 50 μL of the solution at 76% and 100%, respectively. All concentrations are expressed as dopant moles divided by P(NDI2OD-T2) repeating unit moles. Glass substrates were cleaned with isopropyl alcohol and acetone, then treated with an oxygen plasma for 15 minutes and quickly introduced inside the glovebox. P(NDI2OD-T2) films were spin coated at 1000 rpm for 60 s and then at 3000 rpm for 10 s. For each dopant concentration, one sample was measured without thermal treatment, the remaining were annealed inside a glovebox in N_2 atmosphere on a hot plate.

4.2.3. Electrical Conductivity

The electrical characterizations were carried out at room temperature in N_2 atmosphere using a Wentworth Laboratories probe station with a semiconductor device analyser (Agilent B1550A). Then, the electrical conductivity was calculated through the linear fit of the I-V characteristic curves and the samples geometries. In particular, to measure the thickness of the thin films, an alpha-step IQ profilometer from KLA Tencor was employed. The samples were scratched with a toothpick in multiple regions and the thickness of the films was measured in different points of the sample. This procedure was necessary to assess the uniformity of the conductive layer. The samples were in between 30 and 50 nm thick.

4.3. X-ray Characterization

4.3.1. Film deposition

Native oxide p⁺ silicon substrates 2cm² substrates were cleaned with acetone, isopropyl alcohol, and ethanol. The film preparation was conducted in a N₂ glovebox (<1 ppm of O₂) as previously described, using 890 μL of polymer solution for each sample. One sample was measured without thermal treatment, the others were annealed for 5, 30 and 90 minutes at 110°C and 70°C.

4.3.2. GIWAXS

Grazing incidence wide-angle X-ray scattering (GIWAXS) measurements were conducted at the Stanford Synchrotron Radiation Lightsource (SSRL) on beamline 11-3 equipped with an area detector (Rayonix MAR-225), using an incident energy of 12.73 keV. The measurements were performed in a chamber provided a helium flux, in order to minimize air scattering and beam damage to the sample. The sample and detector distance (321 mm) was calibrated through a LaB₆ polycrystalline standard and the incident angle was chosen at 0.1°. Data analysis was performed with the Igor Pro software packages Nika 1D SAXS29^[65] and WAXStools^[66]. The data were normalized by detector counts and thickness (C1).

4.4 Molecular modelling

All the geometry optimizations were performed using the Orca package ^[67], by employing the B3LYP functional (including explicit Grimme empirical van der Waals contributions) together with the 6-31G** basis set. The geometries were instead drawn and analyzed using Avogadro ^[68].

References

- [1] C. Ruiz, E. M. García-Frutos, G. Hennrich, B. Gómez-Lor, *J. Phys. Chem. Lett.* **2012**, 3, 11, 1428–1436
- [2] S. Savagatrup, A. D. Printz, T. F. O'Connor, A. V. Zaretski, D. J. Lipomi, *Chem. Mater.* **2014**, 26, 10, 3028–3041
- [3] S. E. Root, S. Savagatrup, A. D. Printz, D. Rodriguez, D. J. Lipomi, *Chem. Rev.* **2017**, 117, 9, 6467–6499
- [4] B. Lüssem, C. Keum, D. Kasemann, B. Naab, Z. Bao, K. Leo *Chem. Rev.* **2016**, 116, 22, 13714–13751
- [5] A. Facchetti, *Mater. Today* **2007**, 10, 3, 28-37
- [6] X. Zhan, A. Facchetti, S. Barlow, T. J. Marks, M. A. Ratner, M. R. Wasielewski, S. R. Marder, *Adv. mater.* **2011**, 23, 2, 268-284
- [7] H. Yan, Z. Chen, Y. Zheng, C. Newman, J. R. Quinn, F. Dötz, M. Kastler, A. Facchetti, *Nature*, **2009**, 457, 679-686
- [8] Y. Chen, Y. Zhao, Z. Liang, *Energy Environ. Sci.* **2015**, 8, 401-422

- [9] B. T. McGrail, A. Sehirlioglu, E. Pentzer, *Angew. Chem.* **2015**, 54, 6, 1710-1723
- [10] I. Petsagkourakis, K. Tybrandt, X. Crispin, I. Ohkubo, N. Satoh, T. Mori, *Sci. Technol. Adv. Mater.* **2018**, 19, 1, 836-862
- [11] D. Beretta, N. Neophytou, J. M. Hodges, M. G. Kanatzidis, D. Narducci, M. Martin-Gonzalez, M. Beekman, B. Balke, G. Cerretti, W. Tremel, A. Zevalkink, A. I. Hofmann, C. Müller, B. Dörling, M. Campoy-Quiles, M. Caironi, *Mater. Sci. Eng. R Rep* **2019**, 138, 100501
- [12] H. Yao, Z. Fan, H. Cheng, X. Guan, C. Wang, K. Sun, J. Ouyang, *Macromol. Rapid Commun.* **2018**, 39, 6, 1700727
- [13] R. Kroon, D. A. Mengistie, D. Kiefer, J. Hynynen, J. D. Ryan, L. Yu, C. Müller, *Chem. Soc. Rev.* **2016**, 45, 6147-6164
- [14] O. Bubnova, X. Crispin, *Energy Environ. Sci.* **2012**, 5, 9345-9362
- [15] P. Cataldi, M. Cassinelli, J. A. Heredia-Guerrero, S. Guzman-Puyol, S. Naderizadeh, A. Athanassiou, M. Caironi, *Adv. Func. Mat.* **2020**, 30, 3 1907301
- [16] M. Cassinelli, S. Cimò, T. Biskup, A. Luzio, C. R. McNeill, Y. Noh, Y. Kim, C. Bertarelli, M. Caironi, *Adv. Elec. Mat.* <https://doi.org/10.1002/aelm.202100407>
- [17] M. Massetti, S. Bonfadini, D. Nava, M. Butti, L. Criante, G. Lanzani, L. Qiu, J. C. Hummelen, J. Liu, L. J. A. Koster, M. Caironi, *Nano Energy* **2020**, 75, 104983
- [18] M. Cassinelli, W. Park, Y. Kim, J. Kim, Y. Noh, M. Caironi, *Appl. Phys. Lett.* **2021**, 119, 033301
- [19] A. Facchetti, *Chem. Mater.* **2011**, 23, 3, 733-758

- [20] N. Li, D. Baran, G. D. Spyropoulos, H. Zhang, S. Berny, M. Turbiez, T. Ameri, F. C. Krebs, C. J. Brabec, *Adv. Energy Mater* **2014**, 4, 11, 1400084
- [21] C. Sekine, Y. Tsubata, T. Yamada, M. Kitano, S. Doi, *Sci. Technol. Adv. Mater.* **2014**, 15 034203
- [22] K. Walzer, B. Maennig, M. Pfeiffer, K. Leo, *Chem. Rev.* **2007**, 107, 4, 1233–1271
- [23] Q. Meng, K. Cai, Y. Chen, L. Chen, *Nano Energy* **2017**, 36, 268-285
- [24] I. E. Jacobs, A. J. Moulé, *Adv. Mater.* **2017**, 29, 42 1703063
- [25] C. Yueh, K. Bumsu, L. Leszek, S. Wielunski, M. Heeney, I. McCulloch, E. Garfunkel, L. C. Feldman, V. Podzorov, *Adv. Func. Mat.* **2009**, 19, 12, 1906-1911
- [26] O. Bubnova, Z. U. Khan, H. Wang, S. Braun, D. R. Evans, M. Fabretto, P. Hojati-Talemi, D. Dagnelund, J. Arlin, Y. H. Geerts, S. Desbief, D. W. Breiby, J. W. Andreasen, R. Lazzaroni, W. M. Chen, I. Zozoulenko, M. Fahlman, P. J. Murphy, M. Berggren, X. Crispin, *Nature Materials* **2014**, 13, 190–194
- [27] Y. Karpov, T. Erdmann, I. Raguzin, M. Al-Hussein, M. Binner, U. Lappan, M. Stamm, K. L. Gerasimov, T. Beryozkina, V. Bakulev, D. V. Anokhin, D. A. Ivanov, F. Günther, S. Gemming, G. Seifert, B. Voit, R. Di Pietro, A. Kiriy, *Adv. Mater.* **2016**, 28, 28, 6003-6010
- [28] M. Fabretto, C. Jariego-Moncunill, J. Autere, A. Michelmore, R. D. Short, P. Murphy, *Polymer*, **2011**, 52, 8, 1725-1730
- [29] C. Y. Kao, B. Lee, L. S. Wielunski, M. Heeney, I. McCulloch, E. Garfunkel, L. C. Feldman, V. Podzorov, *Adv. Func. Mat.* **2009**, 19, 12, 1906-1911

- [30] N. Kim, S. Kee, S. H. Lee, B. H. Lee, Y. H. Kahng, Y. Jo, B. Kim, K. Lee, *Adv. Mat.* **2014**, 26, 14, 2268-2272
- [31] B. Russ, A. Glauzell, J. J. Urban, M. L. Chabinye, R. A. Segalman, *Nat. Rev. Mater.* **2016**, 1, 16050
- [32] Z. Zhao, Z. Yin, H. Chen, L. Zheng, C. Zhu, L. Zhang, S. Tan, H. Wang, Y. Guo, Q. Tang, Y. Liu, *Adv. Mater.* **2017**, 29, 4, 1602410
- [33] L. Zhang, Z. Wang, C. Duan, Z. Wang, Y. Deng, J. Xu, F. Huang, Y. Cao, *Chem. Mater.* **2018**, 30, 22, 8343–8351
- [34] S. Wang, H. Sun, T. Erdmann, G. Wang, D. Fazzi, U. Lappan, Y. Puttisong, Z. Chen, M. Berggren, X. Crispin, A. Kiriya, B. Voit, T. J. Marks, S. Fabiano, A. Facchetti, *Adv. Mater.* **2018**, 30, 31, 1801898
- [35] D. Nava, Y. Shin, M. Massetti, X. Jiao, T. Biskup, M. S. Jagadeesh, A. Calloni, L. Duò, G. Lanzani, C. R. McNeill, M. Sommer, M. Caironi, *ACS Appl. Energy Mater.* **2018**, 1, 9, 4626–4634
- [36] A. Sanzone, S. Cimò, S. Mattiello, R. Ruffo, I. Facchinetti, G. E. Bonacchini, M. Caironi, M. Sassi, M. Sommer, L. Beverina, *ChemPlusChem* **2019**, 84, 9, 1346-1352
- [37] J. Liu, L. Qiu, R. Alessandri, X. Qiu, G. Portale, J. Dong, W. Talsma, G. Ye, A. A. Sengrhan, P. C. T. Souza, M. A. Loi, R. C. Chiechi, S. J. Marrink, J. C. Hummelen, L. J. A. Koster, *Adv. Mater.* **2018**, 30, 7, 1704630

- [38] D. Kiefer, A. Giovannitti, H. Sun, T. Biskup, A. Hofmann, M. Koopmans, C. Cendra, S. Weber, L. J. A. Koster, E. Olsson, J. Rivnay, S. Fabiano, I. McCulloch, C. Müller, *ACS Energy Lett.* **2018**, 3, 2, 278–285
- [39] J. Liu, G. Ye, B. van der Zee, J. Dong, X. Qiu, Y. Liu, G. Portale, R. C. Chiechi, L. J. A. Koster, *Adv. Mater* **2018**, 30, 44, 1804290
- [40] J. Rivnay, M. F. Toney, Y. Zheng, I. V. Kauvar, Z. Chen, V. Wagner, A. Facchetti, A. Salleo, *Adv. Mater.* **2010**, 22, 39, 4359-4363
- [41] M. Brinkmann, E. Gonthier, S. Bogen, K. Tremel, S. Ludwigs, M. Hufnagel, M. Sommer, *ACS Nano* **2012**, 6, 11, 10319–10326
- [42] S. J. Brown, R. A. Schlitz, M. L. Chabinyk, J. A. Schuller, *Phys. Rev. B* **2016**, 94, 165105
- [43] A. Luzio, L. Criante, V. D'Innocenzo, M. Caironi, *Sci. Rep.* **2013**, 3, 3425
- [44] K. Tremel, F. S. U. Fischer, N. Kayunkid, R. Di Pietro, R. Tkachov, A. Kiriya, D. Neher, S. Ludwigs, M. Brinkmann, *Adv. Energy Mater.* **2014**, 4, 10, 1301659
- [45] S. Wang, H. Sun, U. Ail, M. Vagin, P. O. Å. Persson, J. W. Andreasen, W. Thiel, M. Berggren, X. Crispin, D. Fazzi, S. Fabiano, *Adv. Mater.* **2016**, 28, 48, 10764-10771
- [46] D. Fazzi, M. Caironi, *Phys. Chem. Chem. Phys.* **2015**, 17, 8573-8590
- [47] E. Giussani; L. Brambilla; D. Fazzi; M. Sommer; N. Kayunkid; M. Brinkmann; C. Castiglioni, *J. Phys. Chem. B*, **2015**, 119 (5), 2062–2073.
- [48] E. Giussani; D. Fazzi; L. Brambilla; M. Caironi; C. Castiglioni, *Macromolecules*, **2013**, 46 (7), 2658–2670.

- [49] J. Rivnay, R. Steyrlleuthner, L. H. Jimison, A. Casadei, Z. Chen, M. F. Toney, A. Facchetti, D. Neher, A. Salleo, *Macromolecules*, **2011**, 44, 13, 5246–5255
- [50] K. P. Goetz, D. Vermeulen, M. E. Payne, C. Kloc, L. E. McNeil, O. D. Jurchescu, *J. Mater. Chem. C*, **2014**, 2, 3065-3076
- [51] T. Menke, P. Wei, D. Ray, H. Kleemann, B. D. Naab, Z. Bao, K. Leo, M. Riede, *Org. Electron.* **2012**, 13, 12, 3319-3325
- [52] P. Wei, T. Menke, B. D. Naab, K. Leo, M. Riede, Z. Bao, *J. Am. Chem. Soc.* **2012**, 134, 9, 3999–4002
- [53] X. Zhu, M. Zhang, A. Yu, C. Wang, J. Cheng, *J. Am. Chem. Soc.* **2008**, 130, 8, 2501–2516
- [54] P. Wei, J. H. Oh, G. Dong, Z. Bao, *J. Am. Chem. Soc.* **2010**, 132, 26, 8852–8853
- [55] R. A. Schlitz, F. G. Brunetti, A. M. Glauddell, P. L. Miller, M. A. Brady, C. J. Takacs, C. J. Hawker, M. L. Chabinyk, *Adv. Mater.* **2014**, 26, 18, 2825-2830
- [56] B. Saglio, M. Mura, M. Massetti, F. Scuratti, D. Beretta, X. Jiao, C. R. McNeill, M. Sommer, A. Famulari, G. Lanzani, M. Caironi, C. Bertarelli, *J. Mater. Chem. A*, **2018**, 6, 15294-15302
- [57] B. D. Naab, X. Gu, T. Kurosawa, J. W. F. To, A. Salleo, Z. Bao, *Adv. Electron. Mater.*, **2016**, 2, 5, 1600004
- [58] R. M. Kluge; N. Saxena, W. Chen, V. Körstgens, M. Schwartzkopf, Q. Zhong, S. V. Roth, P. Müller-Buschbaum, *Adv. Func. Mater.* **2020**, 30, 28, 2003092

- [59] I. Denti, S. Cimò, L. Brambilla, A. Milani, C. Bertarelli, M. Tommasini, C. Castiglioni, *Chem. Mater.* **2019**, 31, 17, 6726–6739
- [60] S. Riera-Galindo, A. O. Biroli, A. Forni, Y. Puttisong, F. Tessore, M. Pizzotti, E. Pavlopoulou, E. Solano, S. Wang, G. Wang, T. Ruoko, W. M. Chen, M. Kemerink, M. Berggren, G. di Carlo, S. Fabiano, *ACS Appl. Mater. Interfaces* **2019**, 11, 41, 37981–37990
- [61] O. Bardagot, C. Aumaitre, A. Monmagnon, J. Pécaut, P. Bayle, R. Demadrille, *Appl. Phys. Lett.* **2021**, 118, 203904
- [62] B. D. Naab, X. Gu, T. Kurosawa, J. W. F. To, A. Salleo, Z. Bao, *Adv. Electron. Mater.* **2016**, 2, 5, 1600004
- [63] B. D. Naab, S. D. Zhang, K. Vandewal, A. Salleo, S. Barlow, S. R. Marder, Z. Bao, *Adv. Mater.* **2014**, 26, 4268-4272
- [64] J. Wang, Y. Liu, H. Li, S. Yan, X. Sun, D. Tu, X. Guo, Z. Ren, *Mater. Chem. Front.*, **2020**, 4, 661-668
- [65] Ilavsky J, *J. Appl. Cryst.*, 2012, 45, 324-328
- [66] Oosterhout, S. D.; Savikhin, V.; Zhang, J.; Zhang, Y.; Burgers, M. A.; Marder, S. R.; Bazan, G. C.; Toney, M. F., *Chem. Mater.*, 2017, 29(7), 3062-3069 [67] F. Neese, *WIREs Comput Mol Sci*, **2018**, 8:e1327
- [68] M. D. Hanwell, D. E. Curtis, D. C. Lonie, T. Vandermeersch, E. Zurek, G. R. Hutchison *Journal of Cheminformatics*, **2012**, 4:17

Supporting Information

Room temperature activation of n-type doping of naphthalene diimide - bithiophene copolymer by 1H- benzimidazoles

Simone Cimò, Ilaria Denti, Lorenzo Rossi, Marco Cassinelli, Garrett Lecroy, Alberto Salleo, Mario Caironi, Antonino Famulari, Chiara Castiglioni, Chiara Bertarelli*

GIWAXS DATA

A summary of peak positions at different annealing temperatures and times is reported in the following tables:

Sample	In plane (Å)		Out Of Plane (Å)	
	(100)	(001)	(100)'	(010)
Pristine @70°C	26.07	13.84	25.44	3.88
Pristine not annealed	24.84	13.78	22.68	3.75
5 min @70°C	25.17	13.75	21.16	3.9
30 min @70°C	25.06	13.78	21.59	3.9
90 min @70°C	24.75	13.78	21.16	3.9

Table S1. Scattering peak position for the GIWAXS experiments at 70 °C and pristine not annealed samples from the reduced 1D line profiles. The peaks are individuated along the horizontal (in plane, qxy) and approximately vertical (out of plane, ~qz) scattering directions.

Sample	In plane (Å)		Out Of Plane (Å)	
	(100)	(001)	(100)'	(010)
Pristine @110°C	26.07	13.84	25.44	3.88
Pristine not annealed	24.84	13.78	22.68	3.75
5 min @110°C	24.74	13.81	22.28	3.86
30 min @110°C	24.54	13.9	21.44	3.95
90 min @110°C	24.35	13.87	21.44	3.96

Table S2. Scattering peak position for the GIWAXS experiments at 110 °C and pristine not annealed samples from the reduced 1D line profiles. the peaks are individuated along the horizontal (in plane, qxy) and approximately vertical (out of plane, ~qz) scattering directions.

Coherence Length

Sample	In plane (Å)		Out Of Plane (Å)	
	(100)	(001)	(100)'	(010)
Pristine @70°C	209.06	210.65	48.33	17.07
Pristine not annealed	107.38	315.35	53.29	7.37
5 min @70°C	132.95	227.90	45.86	10.41
30 min @70°C	133.84	208.80	49.13	10.39
90 min @70°C	131.31	244.38	48.26	9.51

Table S3. Coherence length calculated from the peaks of the GIWAXS experiments at 70 °C and pristine not annealed samples. The coherence length was estimated from the Schererr equation for GIXS: $D = \frac{0.93 \cdot 2\pi}{\Delta q}$

Sample	In plane (Å)		Out Of Plane (Å)	
	(100)	(001)	(100)'	(010)
Pristine @110°C	209.06	210.65	48.33	17.07
Pristine not annealed	107.38	315.35	53.29	7.37
5 min @110°C	128.94	279.85	59.07	8.34
30 min @110°C	125.39	259.99	59.46	8.27
90 min @110°C	120.71	248.49	67.16	7.38

Table S4. Coherence length calculated from the peaks of the GIWAXS experiments at 110 °C and pristine not annealed samples. The coherence length was estimated from the Scherrer equation for GIXS: $D = \frac{0.93 \cdot 2\pi}{\Delta q}$

Attachment C

Bussetti, G. *et al.* Electrochemical scanning probe analysis used as a benchmark for carbon forms.
J. Phys. Condens. Matter **33**, (2021).

PAPER

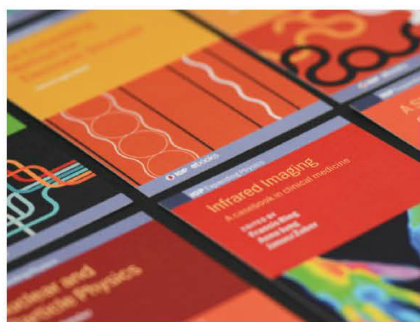
Electrochemical scanning probe analysis used as a benchmark for carbon forms quality test

To cite this article: Gianlorenzo Bussetti *et al* 2021 *J. Phys.: Condens. Matter* **33** 115002

View the [article online](#) for updates and enhancements.

You may also like

- [Focal aberrations of large-aperture HOPG von-Hámos x-ray spectrometers](#)
U Zastrau, C R D Brown, T Döppner *et al.*
- [Electrocatalytic Activity of Metals and Alloys Electrodeposited on Foreign Substrates: I. Some Aspects of Oxygen Reduction on Electrodeposited Silver Films on Pyrolytic Graphite](#)
Ikram Morcos
- [Characterization of strongly-bent HAPG crystals for von-Hámos x-ray spectrographs](#)
U Zastrau, A Woldegeorgis, E Förster *et al.*



IOP | ebooks™

Bringing together innovative digital publishing with leading authors from the global scientific community.

Start exploring the collection—download the first chapter of every title for free.

Electrochemical scanning probe analysis used as a benchmark for carbon forms quality test

Gianlorenzo Bussetti¹, Rossella Yivlialin^{1,5,*}, Franco Ciccacci¹, Lamberto Duò¹, Eugenio Gibertini², Alessandra Accogli², Ilaria Denti², Luca Magagnin², Federico Micciulla³, Antonino Cataldo³, Stefano Bellucci³, Alexander Antonov⁴ and Inna Grigorieva⁴

¹ Department of Physics, Politecnico di Milano, Milano, Italy

² Department of Chemistry, Materials and Chemical Engineering 'Giulio Natta', Politecnico di Milano, Milano, Italy

³ INFN-Laboratori Nazionali di Frascati, Roma, Italy

⁴ Optigraph GmbH, Berlin, Germany

E-mail: rossella.yivlialin@helmholtz-berlin.de

Received 8 August 2020, revised 5 December 2020

Accepted for publication 16 December 2020


Published 6 January 2021



Abstract

Carbon forms (graphite, pyrolytic graphite, highly oriented pyrolytic graphite (HOPG), glassy carbon, carbon foam, graphene, buckypaper, etc) are a wide class of materials largely used in technology and energy storage. The huge request of carbon compounds with reliable and tunable physical and chemical properties is tackled by contriving new production protocols and/or compound functionalizations. To achieve these goals, new samples must be tested in a trial-and-error strategy with techniques that provide information in terms of both specimen quality and properties. In this work, we prove that electrochemical scanning probe techniques allow testing the performances of carbon compounds when are used as an electrode inside an electrochemical cell. Comparing the results with a reference sample (namely, HOPG) gives an insight on defects in the specimen structure, performances, and possible applications of the new samples. In this study, we concentrate on traditional carbon forms already employed in many fields versus new recently-developed specimens, in view of possible applications to the field of energy storage.

Keywords: graphite intercalated compounds, HAPG, pyrolytic graphite, electrochemical SPM

 Supplementary material for this article is available [online](#)

(Some figures may appear in colour only in the online journal)

1. Introduction

Carbon forms (namely, graphite, pyrolytic graphite (PG), highly oriented pyrolytic graphite (HOPG), glassy carbon,

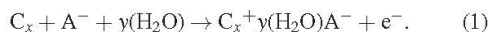
graphene, multi-layered graphene, nanotubes, nano-pellets, buckypaper, carbon foam, etc) are considered of strategical importance in many fields. Graphite and glassy carbon are employed as electrodes in electrochemical cells and/or in new batteries [1–6]; graphene (Gr) and multi-layered Gr sheets are exploited in, e. g., supercapacitors [7] anticorrosive coatings [8] and green energy applications [9]; nanotubes are used for their exceptional transport [10] and mechanical [11] properties and possible application in biomedicine [12]; carbon

* Address for correspondence.

⁵ Current address: Institute for Solar Fuels, Helmholtz-Zentrum Berlin für Materialien und Energie GmbH, Berlin, Germany

nanoplatelets show promising results for natural gas storage [13]; carbon buckypaper is studied for enhancing thermoelectric performances [14] or catalytic processes [15]; finally, carbon foam is also used in military applications being an excellent electromagnetic shield [16]. As a consequence, the technological, strategical and economical interest in producing new carbon forms is continuously expanding in terms of functionalization, tuning their properties and finding new strategies to reduce the time-preparation protocols. In order to achieve these goals, the physical and chemical characterization of the new carbon forms is mandatory. The new specimen properties are generally studied by optical techniques [17], photoelectron spectroscopies [18], diffraction [19], scanning probe microscopy (SPM) [20] and electrochemistry [21] among others.

In this work, we propose a complementary investigation for carbon forms where the specimen undergoes a peculiar electrochemical process. The Faradaic current intensity behavior, together with the sample surface evolution, are monitored. This approach requires two basic preconditions: (i) an experimental set-up, where SPM is coupled with electrochemistry; (ii) a reference for both samples and EC treatments to ensure a clear interpretation of the EC process applied to all the other carbon forms. Issue (i) can be fulfilled by the so-called EC-SPM (namely, EC-atomic force microscopy (EC-AFM) and EC-scanning tunneling microscopy) [22, 23]. These techniques are optimized for acquiring microscopic images with probes directly immersed inside the electrolytes without any contamination or influence in the EC characterization (e. g., by cyclic voltammetry, see below). The second issue is more critical to accomplish: the EC reaction selected for the study has to, on the one hand, produce clear effects on carbon compounds while, on the other hand, present a clear interpretation, in order to get reliable information on the properties of the new carbon specimen. The authors have experience on the HOPG anion intercalation, occurring when graphite is biased in acid electrolytes. HOPG is a high-quality stratified crystal, which allows a control of the electrochemical intercalation of anions. We have acquired data on the role played by the electrolytes [24], the temperature and the time effects [25, 26], the electrolyte pHs [27], the structure [28] and the morphological [29] evolution of the HOPG electrode surface and paved the way to a first investigation of the buried graphite layers [30]. Finally, we succeeded in refining the current interpretation model of the involved chemical reaction [31]. In acid electrolytes, such as diluted sulfuric acid (H_2SO_4 , 1 M), solvated anions are able to intercalate in the stratified HOPG structure as soon as a positive bias is applied to the electrode [26]. HOPG becomes a so-called graphite intercalated compound (GIC) where graphite layers are alternated with solvated anions [32]. When the oxygen evolution reaction (OER) potential is applied to the graphite electrode, the latter undergoes the following chemical reaction:



A reaction of a certain amount of carbon atoms (C_x) with the solvated anions (A) occurs at any buried layer where the intercalation process takes place. The process also develops gases

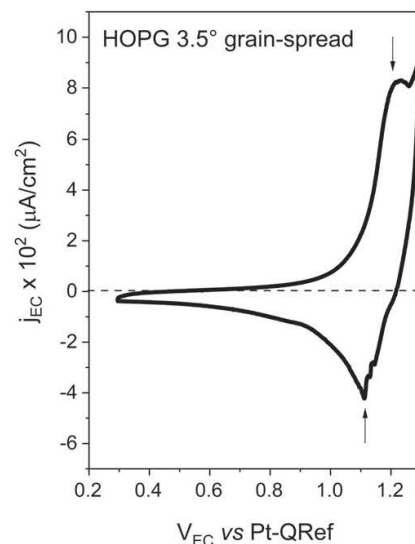


Figure 1. Typical CV of the HOPG 3.5° grain-spread sample. Scan rate = 25 mV s⁻¹.

(namely CO , CO_2 , O_2), which swell the graphite basal plane forming blisters on the electrode surface [33].

The described process was initially studied through EC characterizations. Among various EC techniques, cyclic voltammetry (or CV, consisting in the measurement of the Faradaic current flowing through the electrode as a function of the applied potential) shows a voltammogram with characteristic features (indicated by the arrows in figure 1).

Typically, the shoulder visible in the anodic part of the CV represents the fingerprint of the anion intercalation while the negative (cathodic) peak is traditionally interpreted in terms of a partial de-intercalation process [28, 29]. These ascriptions were furthermore confirmed by EC-AFM investigations, which consist in monitoring the electrode evolution *in situ* and in real time [34]. In particular, the HOPG surface blistering can be detected by the EC-AFM, as showed in figure 2: instead of the well-known graphite morphology, characterized by steps and flat terraces on the overall surface (see panel (a)), rounded 3D structures appear in the topography image (b), which prove that reaction (1) took place.

The interpretative model for blisters described above foresees the two main CV features to be related to specific microscopic processes (intercalation and de-intercalation, respectively), which can only occur in the stratified structure of the graphite crystal. Consequently, the CVs acquired on those carbon forms that are not suitable for a microscopic investigation, due to their high surface roughness (e. g., carbon foam and PG), disclose important information when their cyclic voltammograms are compared to figure 1. However, when it is possible to conduct the microscopic analysis at applied positive EC bias, the evolution of the electrode surface contains details on the quality of the specimen structure and can be directly compared to the one of HOPG. Considering these facts, the anion intercalation mechanism represents the proper chemical reaction for testing different carbon forms.

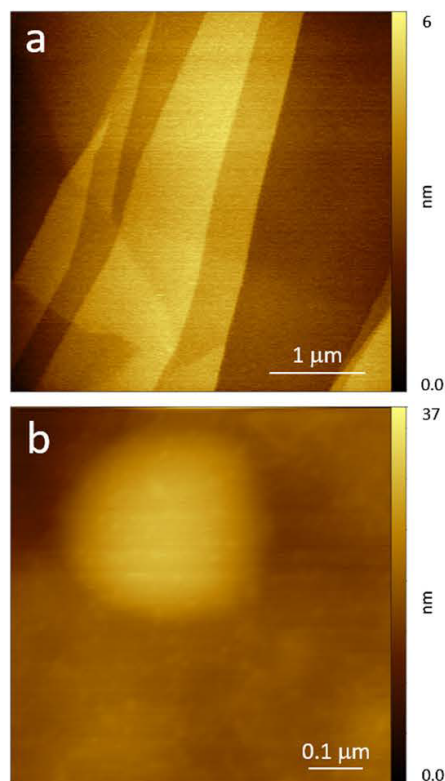
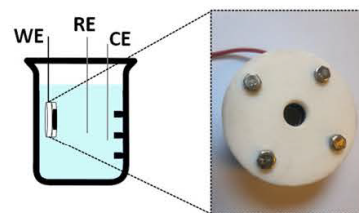


Figure 2. AFM topography images of 3.5° grain-spread HOPG. (a) Pristine sample, (b) post EC acid-treatment.

Our work reports the investigation of the anion intercalation process into three distinct carbon forms classes: (1) samples available from a specialized factory (namely Optigraph GmbH) in the graphite production; (2) a special electrode prepared in lab (buckypaper of graphene nanoplatelets (GNPs)) and (3) other specimens available from the market (graphite, glassy carbon and carbon foam). Regarding the first class, Optigraph provided HOPG samples of different grade, namely both ZYH (mosaic spread 3.5°) and ZYA (mosaic spread 0.4°), as well as new specimens such as HOPG flex, highly aligned pyrolytic graphite (HAPG), pressed thermal conductive pyrolytic graphite (TPG), and special samples suitable for the analysis of the crystal edges (see below for details). Our test strategy is applicable to almost all these cases and we will discuss the different sample behaviors in the following lines.

2. Materials and methods

A commercial EC-AFM (Keysight 5500) was used for the sample analysis. This instrument controls the electrochemical process through a potentiostat that can measure the Faradaic current, with a range from pA to mA. The sample, which represents the working electrode (WE), is placed in a three-electrode cell, where a Pt wire is used as a counter electrode. A



Scheme 1 Configuration of the EC cell adopted for ‘edge graphite samples’. A picture of the custom-made Teflon cell is also reported.

second Pt wire is exploited as a reference. The latter represents a quasi-reference (PtQRef) [35], with a stable (within few mV) shift of +0.74 V with respect to the standard hydrogen electrode, when immersed in acid electrolytes [28]. In some cases (‘edge graphite samples’), the specimens could not be clamped tightly so that a different EC configuration was necessarily adopted, employing a custom-made Teflon sample holder that exposes the sample surface through a circular window (1 cm²); again, Pt wires were used as counter and quasi-reference electrode. A scheme of the configuration adopted for measuring ‘edge graphite samples’ is shown above (scheme 1).

The 5500 EC-AFM allows the immersion of the scanner head inside the electrolyte. Si-tips, mounted on gold or aluminum coated cantilevers, were used in this investigation. Depending on the sample mechanical characteristics and surface roughness, the image acquisition was performed either through contact or tapping mode. We did not observe significant morphological differences after the EC treatment between the samples observed *in situ* and those ones studied *ex situ*. In our research investigation, we collected a set of images by probing different areas of the specimen surfaces. At the end, for each sample analyzed, we chose the more representative images to be shown in this work. An example of our statistical approach is reported in the supplementary information (<https://stacks.iop.org/JPCM/33/115002/mmedia>).


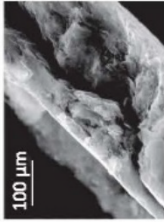
A water-diluted (0.5 or 1 M) H₂SO₄ solution was prepared as an electrolyte and de-aerated by bubbling pure (5.5 grade) Ar for several hours.

The samples (25 × 25 × 1 mm³) were used without any other further cleaning.

Several different types of PG were provided by Optigraph. All types of PG were prepared by high temperature annealing from the same initial material—pyrolytic carbon. The difference in the annealing condition led to a different structure and properties of the PGs under investigation.

In HAPG, HOPG and HOPG-flex the grains are well aligned in the direction of the C–C-plane with mosaic spread below 1°. The samples consisted in plates of 25 × 25 × 1 mm³ size with the main surface parallel to the basal plane (orthogonal to the stacking direction of the graphene layers). The so called ‘edge samples’, similar three PG types of 25 × 3 × 3 mm³ size, are also present. In these samples both the surface, parallel to the basal plane, and the edge surface, consisting of crystallite edges and perpendicular to the basal plane, are of the same size.

Table 1. Schematic overview of all the samples measured in this work. For the GNPs buckypaper sample, scanning electron microscopy (SEM) images for single GNP (top) and lateral section of the final product (bottom) are also shown.

N°	Material	Interlayer spacing, d_{002} (Å)	Production condition	Typical grain size in the basal plane ^a	Samples geometry	State
1	HOPG	3.358 ± 0.001	(2750 °C–2800 °C); uniaxial pressure	(10–20) μm	- Main surface parallel to C–C planes - 'Edge samples' (main surface perpendicular to the C–C planes)	Bulk sample
2	HOPG_flex	3.356 ± 0.001	3000 °C; uniaxial pressure	(30–40) μm	- Main surface parallel to the C–C planes - 'Edge samples' (main surface perpendicular to the C–C planes)	Bulk sample
3	HAPG	3.354 ± 0.001	≥ 3000 °C; volumetric pressure	(100–150) μm	- Main surface parallel to the C–C planes - 'Edge samples' (main surface perpendicular to the C–C planes)	Bulk samples
4	TPG	3.356 ± 0.001	(2750 °C–2800 °C)	(50–100) μm	- Main surface parallel to the C–C planes - 'Edge samples' (main surface perpendicular to the C–C planes)	Pressed powder obtained in activation mill
5	GNPs buckypaper	×	$T = 1000$ °C and ultrasound-bath in isopropyl alcohol to produce GNPs from commercial graphite; uniaxial pressure of 700 N on dried GNPs	 		Pressed 'foamy mat' to obtain the buckypaper
6	Commercial carbon forms				- Glassy carbon - PG - Carbon foam	

^aThe typical grain size was estimated by Sinitayna and Yaminsky in cooperation with Optigraph. The results were obtained by SEM using JSM-6390LA (JEOL) and S-520 (Hitachi) microscopes. The samples were tilted by 30° or 45° relatively to the electron beam direction to get different grain contrasts in the SEM images. The results were presented as a poster [39] and partially published [40]. The results for HOPG also agree with the numbers obtained in [41].

In order to prepare the samples from TPG, the material was grained in an activation mill, and then the powder was pressed in a metal matrix at room temperature without any additional additives. The particles alignment is similar to the initial mosaic spread of this material, which is about 10° . Two types of samples $25 \times 25 \times 2 \text{ mm}^3$ size presented particles aligned along the main surface and particles perpendicular to this surface.

GNPs buckypaper is made by a filtration system of a solution of isopropyl alcohol and GNPs and then pressed by using a constant pressure system [36], loaded with a force of 700 N. GNPs were synthesized starting from commercial intercalated graphite (provided by Asbury®) and they were expanded in a worm-like shape by using a short thermal treatment. The samples were then separated in graphene nanoplatelets by an ultra-sound bath [37, 38].

Schematic overview and description of all the investigated samples are provided in table 1.

3. Results and discussion

3.1. Optigraph samples

The first analysis is focused on understanding the role of the HOPG crystal structure. Traditionally, ZYH-grade (or AGraphH-grade) samples, where the grain misalignment (mosaic spread) is $3.5 \pm 1.5^\circ$, are used to analyze the graphite intercalation. The studied HOPG samples are characterized by a smaller misalignment of $0.4 \pm 0.1^\circ$ (AGraphZ-grade). In figure 3, we show subsequent CVs acquired on these high-quality specimens.

The reported voltammograms show the typical features observed on ZYH-grade HOPG (see figure 1). Their interpretation is thus the same discussed in the introduction.

It is worth mentioning that the ratio between cathodic and anodic currents changes during the consecutive CV scans because of the gradual not-reversible conversion of the material into GIC [29, 31]. The intensity reduction of the anodic features during the subsequent cycles are interpreted in terms of a progressive filling of the inter-layer space inside the crystal. Figure 4 reports the morphological analysis.

Panel a shows different flat terraces with multi-atomic step edges. After the CVs, the graphite basal plane is swollen (blisters), in close comparison with results reported in figure 2. Regardless of the quality grade, HOPG samples undergo the same electrochemical process: anion intercalation (see the CV anodic shoulders and the cathodic peak that ensures a partial de-intercalation of species from the graphite layers) and blister evolution.

Some differences are observed for other PG samples. HOPG-flex was prepared according to the same procedure of standard HOPG, but the annealing conditions, such as time and temperature, and deformation conditions were different. The result is a much softer material that could provide flexible films. The structural investigation showed that the material had fewer defects and a larger grain size compared to HOPG. In HOPG, the grain boundaries are decorated with relatively wide defect regions clearly visible by an acoustic microscope.

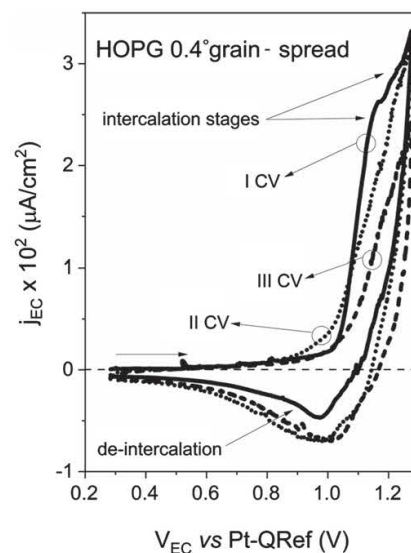


Figure 3. 3 subsequent CVs of the 0.4° grain-spread HOPG samples. Scan rate = 25 mV s^{-1} .

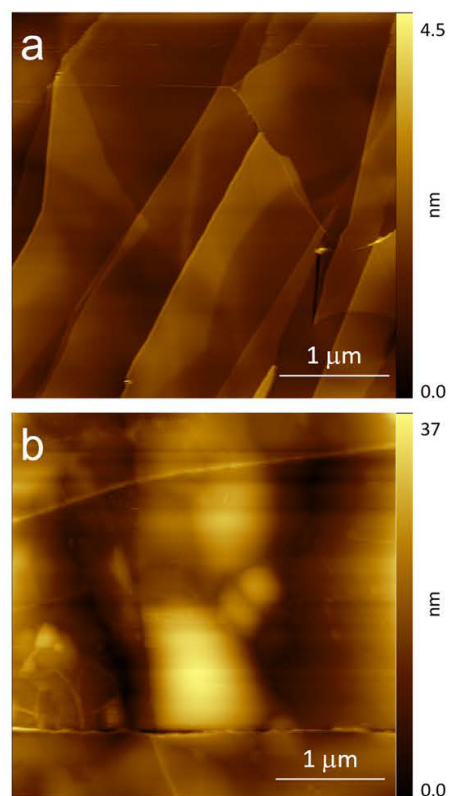


Figure 4. AFM topography images of the 0.4° grain-spread HOPG. (a) Pristine sample, (b) post EC acid-treatment.

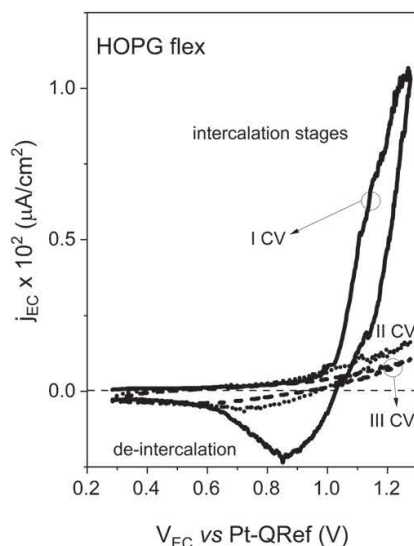


Figure 5. 3 subsequent CVs of the HOPG-flex sample. Scan rate = 25 mV s^{-1} .

In HOPG-flex the grain boundaries are acoustically transparent [42, 43]. Different structure leads to specific material behavior.

Figure 5 shows the collected CVs for the HOPG-flex. In this case, only the first CV recalls those collected in traditional HOPG samples. Starting from the second CV, it is not possible to intercalate any other solvated anion (absence of anodic features) and no de-intercalation cathodic peak is observed. A reduced amount of defects precludes the possibility of intercalation (see the maximum flowing current with respect to the HOPG in figure 3).

This scenario is confirmed by the morphological analysis reported in figure 6.

The pristine specimen shows flat terraces as those observed in the HOPG reference/commercial sample. However, after the CV treatments, the basal plane is not as damaged as the one of the commercial HOPG (see figure 4), where blisters cover all the graphite surface. In the case of the HOPG-flex, blisters are visible only close to steep step edges, i.e., where solvated anions have the possibility to enter inside the graphite crystal. In the other areas, flat terraces are well-visible. In figure 6, small 3D structures are also visible along the step edges, which reasonably consist of some residuals from the original graphite terraces, created as a consequence of carbon dissolution in acid [28] and re-deposition of the surface after the extraction of the sample from the EC cell.

The evolution of the electrode surface completely changes for HAPG. HAPG is also a variant of the well-aligned PG as well as the two HOPGs discussed above. But the annealing technology is completely different, although it is also stress annealing at temperatures near $3000 \text{ }^\circ\text{C}$. A deeper improvement in the structure leads to a material with more flexible films and an even lower level of defects than the HOPG-flex case study [43, 44]. The structure of HAPG is closer to the

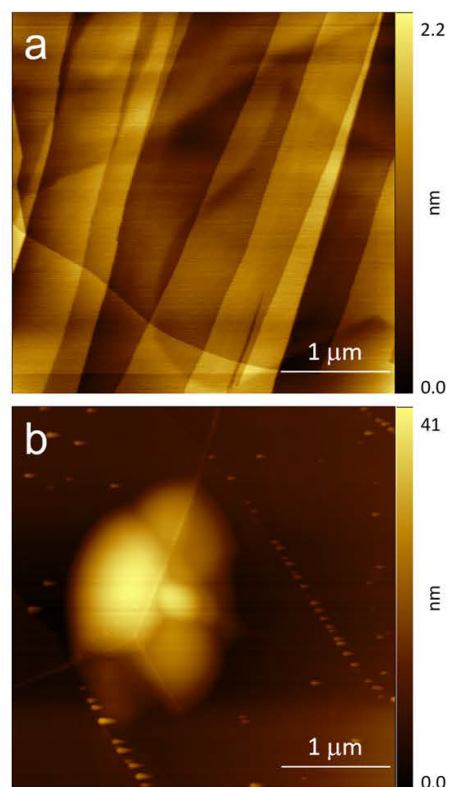


Figure 6. AFM topography images of the HOPG-flex sample. (a) Pristine sample, (b) post EC acid-treatment.

ideal one, which is also confirmed by a smaller interlayer distance of 3.354 \AA compared to 3.356 and 3.358 \AA of HOPG-flex and HOPG, respectively. We report the collected CVs in figure 7.

The electrochemical analysis of HAPG in sulfuric acid does not show any intercalation feature, neither cathodic Faradaic currents. It seems that no solvated anions are able to percolate inside the electrode crystal. The subsequent CVs are superimposed one to the other and the overall behavior mimics the one of an ideal electrode, working close to the OER. The morphological evolution is also significantly changed. In figure 8, we report a representative AFM image. The pristine sample is characterized by very wide flat terraces, with steps almost parallel and well-aligned along the same direction. After the EC treatment, AFM reveals numerous clusters or bubbles showing different behavior with respect to the traditional blisters, both for the lateral and the vertical size. The electrode surface appears as melted as after an intense carbon dissolution caused by the acid electrolyte. In this case, clusters could be ascribed to residuals of the dissolved original terrace.

Furthermore, TPG is a version of PG with a perfect crystalline structure, obtained by annealing without external stress. Due to the absence of stress, the mosaic spread of the material remains quite high—about 10° . At the crystallites level, the material has a perfect structure close to HAPG.

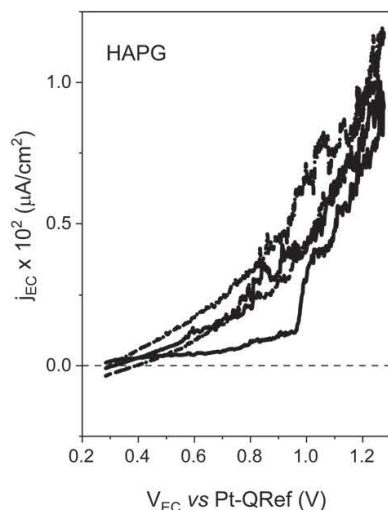


Figure 7. 3 subsequent CVs of the HAPG sample. Scan rate = 25 mV s^{-1} .

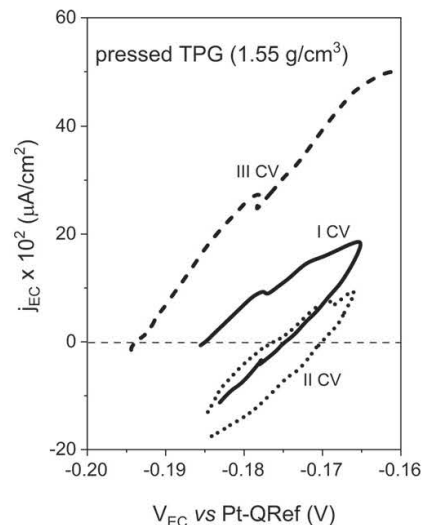


Figure 9. 3 subsequent CVs of the pressed TPG 1.55 g cm^{-3} sample. Scan rate = 25 mV s^{-1} . Only partial voltammograms are reported, not affected by saturation-limited current issues.

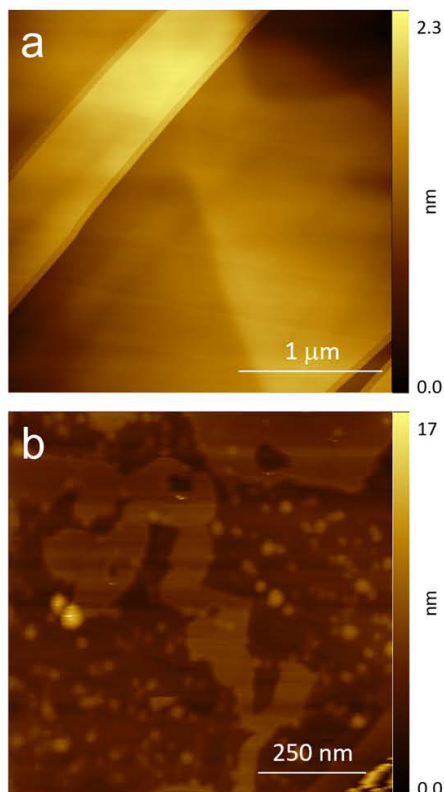


Figure 8. AFM topography images of HAPG. (a) Pristine sample, (b) post EC acid-treatment.

Activation milling induces cleavage steps and dislocation (that is revealed in an increase of rhombohedral phase) which rises the activity of the material in the intercalation

reaction. However, this type of milling process does not make the graphite structure amorphous.

Pressing the powder allows to manufacture samples of any shape, which could be useful for electrochemical research and application. Due to structural features, perfect graphites, such as HOPG and HAPG, are mainly available as plates of 1–2 mm thick with the main surface parallel to the basal plane. For electrochemical experiments, the opposite orientation is required: the extent of the surface parallel to basal plane is less or equal to the edge surface.

Grinded TPG was pressed in metal mold at room temperature. The samples are prepared by applying different pressure loads that change the sample density. In our experiments, the sample density ranges within 1.55 (i) and 2.11 g cm^{-3} (ii). We report and comment only these extreme cases. The CVs of the i-sample are reported in figure 9.

The CVs are completely different with respect to the previous cases. The EC potential (which measures the anodic current) is now slightly negative. The flowing current is order of magnitudes higher with respect to the characteristic values observed for HOPG, and immediately reaches the saturation-limit value of the potentiostat. A significant current intensity shift is also observed when performing subsequent CVs. This behavior suggests that the electrode is not stable and probably affected by a strong detriment that can contaminate the electrolyte and produce a current enhancement. In such conditions, it is not possible to recognize blisters on the electrode surface. The AFM investigation, reported in figure 10, confirms this interpretation.

The pristine sample is rough, and no clear structures are discernible. Reasonably, the electrode surface presents many fractures, defects, holes, etc, where solvated anions can pass through. After the voltammetries, the TPG surface appears

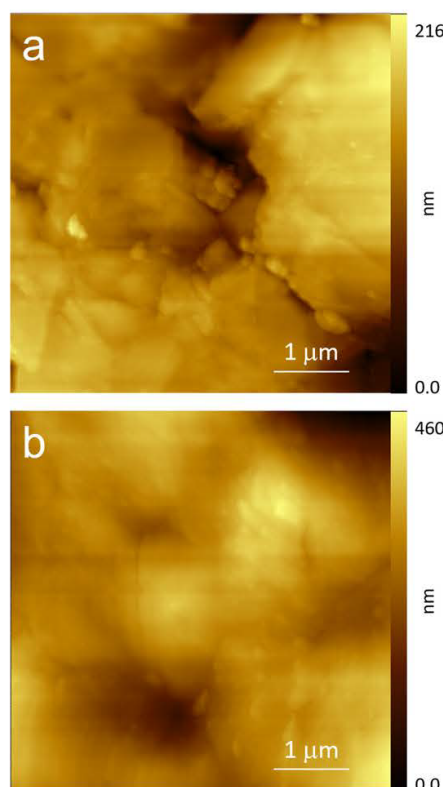


Figure 10. AFM topography images of 1.55 g cm^{-3} -TPG. (a) Pristine sample, (b) post EC acid-treatment.

swollen (see the color gradient values) but no clear features (blisters) are discernible. Moreover, the reduced contrast of the AFM image suggests a strong interaction with the electrolyte.

The results collected for the pressed TPG with a density of 2.11 g cm^{-3} are reported below. The acquired CVs are shown in figure 11. The instability of the voltammeteries is also verified here. The III CV shape is clearly associated to a detriment of the electrode surface. However, we observe that I and II CVs show an anodic current enhancement that recalls the one of the HOPG electrode close to the OER in HOPG. Besides the very different line shapes of the CVs, we report a considerable shifting of the EC potential toward positive values. The higher sample density plays a reasonable role in reducing the number of entrance sites on the electrode surface with respect to the previous case. The crystal quality and the EC behavior of the HOPG electrode in acidic media are not reached, but the qualitative resemblance due to a higher pressure load used to prepare this TPG specimens is indisputable.

The morphological analysis is presented in figure 12.

The pristine sample is characterized by quite wide regions, similar to terraces in the HOPG. Although the surface roughness is higher than in graphite (see the vertical color bar), the morphological investigation highlights the central role of

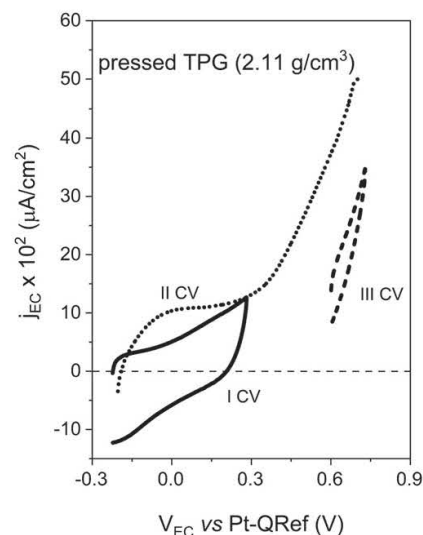


Figure 11. 3 subsequent CVs of the pressed TPG 2.11 g cm^{-3} sample. Scan rate = 25 mV s^{-1} . Only partial voltammograms are reported, not affected by saturation-limited current issues.

the TPG density in the EC and microscopic behavior of the specimen. It is worth noting that, after the CV treatments, terraces are still visible, and clusters appear on the surface. As already observed, the cluster could be composed by some electrolyte residuals after the extraction of the sample from the EC cell.

It is evident from these results that important information on the quality of the specimen can be deduced from the first CV, i.e., before serious damage of the electrode surface occurs, and then confirmed by the AFM investigation.

Finally, we explored the role of crystal edges in the intercalation process. In samples where the treated surface is parallel to the basal plane, the intercalate agent must first diffuse into the sample through atomic steps, grain boundaries and other defects on the sample surface [43]. Thus, diffusion can be a limiting step. To prove this point, ‘edge samples’ of all three well aligned PG, were tested.

It is not possible to perform *in situ* and real time experiments with these specimens. In fact, the sample cannot be clamped below the EC cell used in the Keysight 5500 system otherwise the pressure of the clamp accidentally cleaves the crystal. For this reason, we acquired voltammeteries by inserting the sample into the custom-made Teflon sample described in the materials and methods paragraph. The corresponding cyclic voltammeteries are reported in figure 13.

It is very interesting to compare the results in figure 13 with the results in figures 5–7. For standard samples, the most active material is HOPG, the intercalation in HOPG-flex is not so fast and the maximum current is three times less than for HOPG. When the electrolyte remained in direct contact with edge surface, the ratio is the opposite: HOPG-flex is much more active than HOPG. HAPG also shows typical voltammogram with

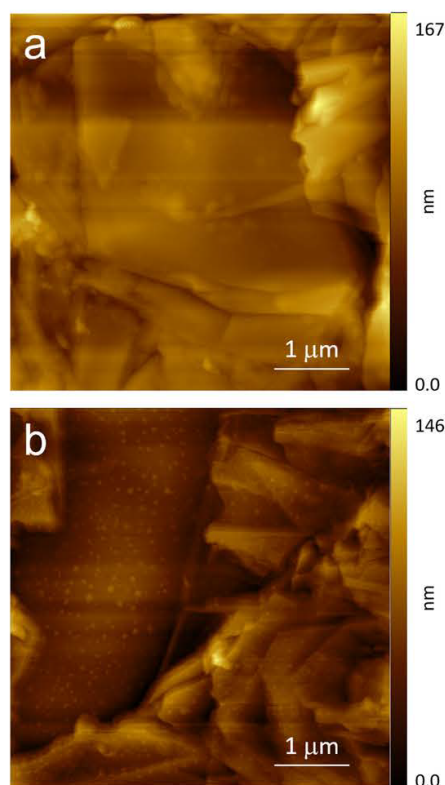


Figure 12. AFM topography images 2.11 g cm^{-3} -TPG. (a) Pristine sample, (b) post EC acid-treatment.

intercalation/de-intercalation features and demonstrates to be more active than HOPG.

3.2. INFN samples

Another interesting study-case consists of GNPs buckypaper (see the materials and methods paragraph for details). In figure 14, we show the voltammogram acquired on such sample.

As reported in the figure, no clear peaks or features along the CV cycle are observed. In this case, the Faradaic current cuts the whole range of the amperemeter within a very small EC potential interval. The preparation procedure for the sample together with a large amount of defects (the sample is obtained after a mechanical pressure load) can explain this result. From this CV, we deduce that no blisters affect the electrode surface as proved in figure 15.

In this case, the flat regions are not as wide as in figure 12. However, considering the morphology and the differences in height between these samples, we believe that the electrode surface is rich in defects and holes, where the electrolyte can easily penetrate inside the sample. By comparing these results to the one obtained for the TPG specimens, we can clearly rule out that, changing the electrode density by tuning the pressure load during the sample

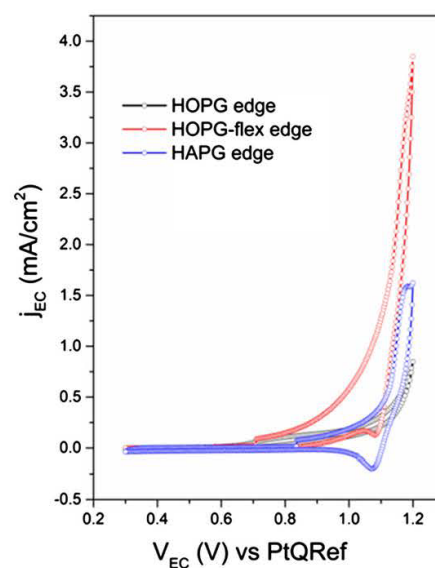


Figure 13. CV of the 'edge-samples' sample. Scan rate = 25 mV s^{-1} .

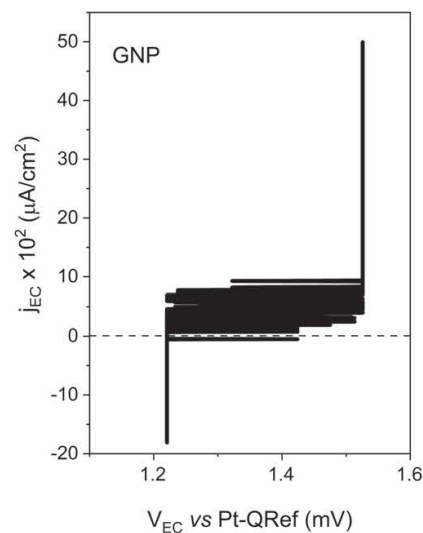


Figure 14. CV of the GNPs buckypaper sample. Scan rate = 25 mV s^{-1} .

preparation, cavities, holes, defects by which the electrolyte intercalates inside the sample significantly influence the current density. The numerous holes represent instead preferential gates for the gas output produced during the anion intercalation. This gives a rationale for the lack of blisters in these samples.

3.3. Other carbon forms

Glassy carbon is widely used in electrochemistry and in industrial application due to its mechanical properties (not exfoliable, good physical and chemical stability, well-finished

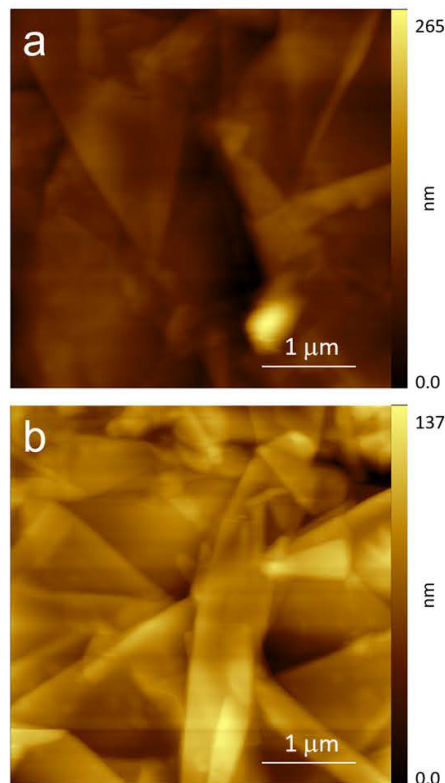


Figure 15. AFM topography images of GNPs buckypaper. (a) Pristine sample, (b) post EC acid-treatment.

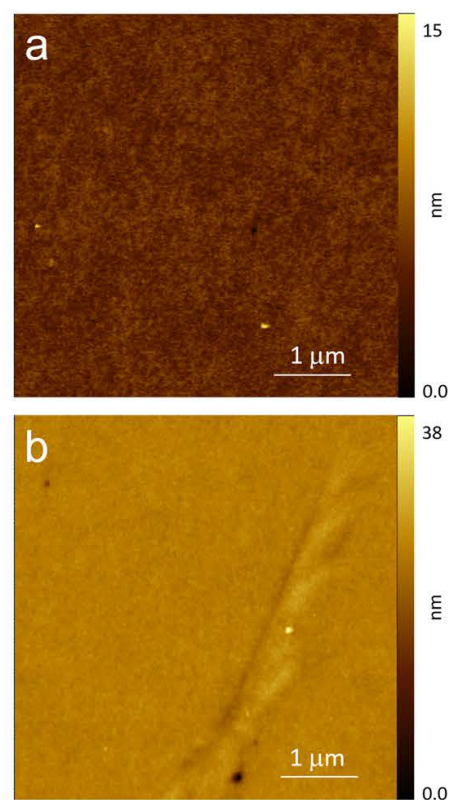


Figure 17. AFM topography images of glassy carbon. (a) Pristine sample, (b) post EC acid-treatment.

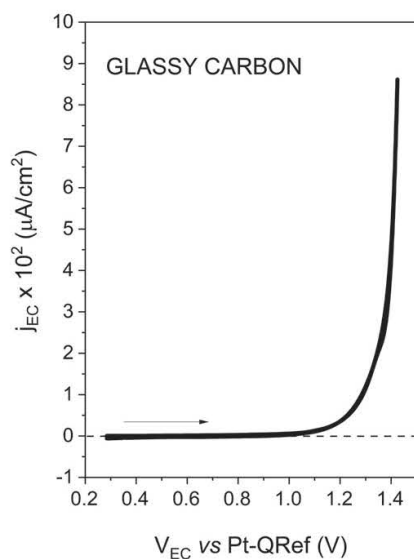


Figure 16. CV of the glassy carbon sample. Scan rate = 25 mV s^{-1} . In figure 17, we report the morphological analysis.

surface). Figure 16 shows a CV acquired with the glassy carbon electrode. The CV presents characteristics of an almost ideal WE: there are no features, the OER is clearly visible and the Faradaic current increases its intensity while the EC potential is changed toward positive values. The electrode stability, the high-quality CV, the absence of any feature related to the solvated anion intercalation suggests that no blisters could affect the glassy carbon surface.

No terraces and steps are visible in panel a. The surface is quite flat (as evident from the color scale). After the EC treatment, no blisters affect the surface morphology, in agreement with our prediction based on the CV analysis. On the AFM length-scale, it is possible to observe some defects on the surface as that one reported in panel b. We speculate that the relative high EC potential used in the experiment, together with the selected electrolyte molarity, can locally affect the sample surface, creating defects. Consequently, it is possible that, if glassy carbon is used for a long time, the surface undergoes a significant detriment, leading to an enhancement of its roughness. However, we do not believe that this progressive surface detriment could cause the basal plane swelling. In fact, blister growth consists in an intercalation inside a stratified bulk structure and GIC formation that is not possible with the glassy carbon structure.

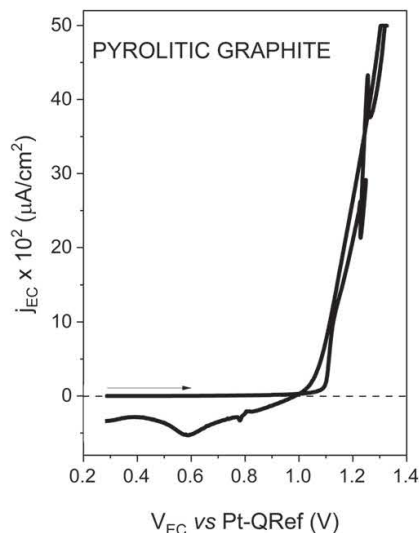


Figure 18. CV of the PG sample. Scan rate = 25 mV s⁻¹.

Since the high surface roughness makes the AFM acquisition very difficult to carry out, PG will be studied only by electrochemistry. In figure 18, we show the acquired CV, which presents some peculiarities.

The first part of the voltammogram seems to mimic the glassy carbon electrode reported in figure 16. However, during the Faradaic current enhancement, some instabilities are observed: the current density maximum reaches the amperemeter saturation and, in the cathodic regime, some features appear. The latter are similar to those observed in the HOPG CV related to the anion de-intercalation process. We speculate that, when high positive potentials are reached during the scan, the electrode undergoes an intense carbon dissolution. On the one hand, this causes the current density to increase; on the other hand, it creates defects and holes for the anion intercalation inside the electrode bulk. The absence of an ordered stratified structure suggests that blisters should not evolve on this electrode. In any case, blisters as those reported in figure 1 could be hidden by the high surface roughness.

Lastly, carbon foam results to be another sample that cannot be investigated by AFM. The collected CV (see figure 19) is interesting compared to the other carbon forms reported above. The maximum current intensity is not very high compared with the CV related to the PG (figure 18). This is probably because carbon foam presents a very low density with respect to the previous samples.

The peak at around 0.9 V is superimposed to the exponential growth due to the oxygen evolution. This feature has a different shape, but the EC potential value is close to the IV HOPG intercalation stage. Probably, the electrode undergoes similar chemical reactions as those related to equation (1). Being a foam (gas cannot be entrapped inside the electrode) we do not observe any de-intercalation feature during the cathodic sweep.

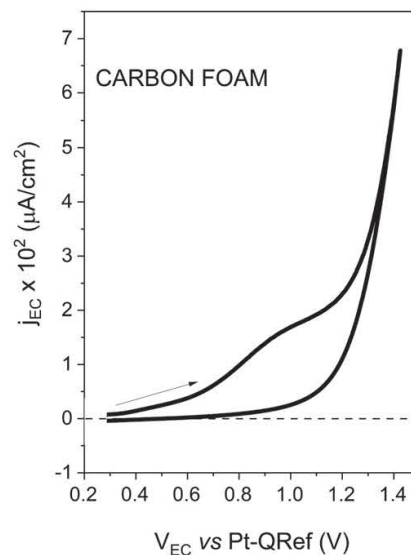


Figure 19. CV of the PG sample. Scan rate = 25 mV s⁻¹.

4. Conclusions

The comparison among various PGs shows that the material structure of graphites plays a key role in redox reaction of the electrochemical cell. Nevertheless, it is rather difficult to give a simple explanation for the role of the defects in such reactions. Indeed, intercalation is a complex process consisting of a several steps, each potentially rate limiting.

Intercalation usually starts at the edge of crystallites. On the contrary, due to peculiarities of PG samples, the intercalate is more often in contact with the basal-plane surface of the sample. Thus, to start the reaction, the anions must first diffuse into the sample, and many researchers noted [40, 44] that the penetration sites are likely grain boundaries, microcracks and atomic steps on the surface.

In HOPG, commonly used for studying the intercalation process, grain boundaries accompanied by wide defect regions observed under the acoustic microscope [42] can be such penetration paths. Thus, in HOPG, intercalation is minimally limited by diffusion of the intercalate from the basal plane into the sample.

In HOPG-flex and HAPG, the grain boundary is quite perfect [40], and the intercalation is severely limited by the need to diffuse the agent (e. g., anions, solvated ions) into the sample and reach the intercalation points. It seems that, for these two materials under the conditions in our experiments, intercalation occurs mainly in the atomic steps on the basal-surface. This is confirmed by the observed blister formation predominantly near the edge of steep steps. Furthermore, blisters can appear at the most defective areas of the grain boundary, for example, at a triple junction of the grain boundaries, as can be seen in figure 6. We assume that this explains why only the very first intercalation/deintercalation run is observed in HOPG-flex

According to [40, 45], the number and the height of atomic steps on the basal surface in HAPG is even much smaller than in HOPG-flex, the grains are several times larger, and the grain boundary is ideal. Therefore, in HAPG, under given experimental conditions, the intercalation reaction is missed compared to the simple carbon oxidation reaction.

For edge samples, the intercalate is in direct contact with the edges of crystallites, and only the defects within the crystallites affect the reaction.

A direct measurement of defects in various PG [40] reveals a greater number of interlayer defects in HOPG compared to HOPG-flex, which may explain the lower intercalation activity of HOPG sample compared to HOPG-flex and HAPG, providing that diffusion of the intercalate into the sample does not limit the reaction. An interlayer defect binds adjacent carbon layers, and this bond must be broken for the intercalate inserting into interlayer space. Thus, more perfect structures are more easily intercalated by anions, as was mentioned by many researchers [32, 46]

According to [40], HAPG has a minimum of defects, and should present an even easier intercalation than the one expected for HOPG-flex. However, this is not the case. A possible explanation might be the presence of much larger grains in HAPG compared to other materials. Those grains lead to slower diffusion of the intercalate into the grains themselves, which are additionally suppressed by the stress caused by deformation of the carbon layers between the intercalated and clean areas.


The results show that the intercalation reaction is very sensitive to the structure of graphite material. The structural features, as well as the alignment of the structural element within the sample, can change the rate of the number of steps and the behavior of graphite material as an electrode in an electrochemical cell.

Acknowledgments

The wide research activity reported in this work was possible thanks to the help of and interaction with many people. The authors are grateful to A Li Bassi, C S Casari, C Castiglioni, M Tommasini, L Brambilla (Politecnico di Milano), S Bistarelli (INFN – Laboratori Nazionali di Frascati) for useful discussion.

ORCID iDs

Rossella Yivlialin  <https://orcid.org/0000-0002-6824-1519>

Luca Magagnin  <https://orcid.org/0000-0001-5553-6441>

References

- [1] Fan L, Liu Q, Chen S, Lin K, Xu Z and Lu B 2017 *Small* **13** 1701011
- [2] Yao K P C, Okasinski J S, Kalaga K, Shkrob I A and Abraham D P 2019 *Energy Environ. Sci.* **12** 656
- [3] Yivlialin R, Bussetti G, Penconi M, Bossi A, Ciccacci F, Finazzi M and Duò L 2017 *ACS Appl. Mater. Interfaces* **9** 4100
- [4] Yi Y, Weinberg G, Prenzel M, Greiner M, Heumann S, Becker S and Schlögl R 2017 *Catal. Today* **295** 32
- [5] Wang J, Yang B, Zhong J, Yan B, Zhang K, Zhai C, Shiraishi Y, Du Y and Yang P 2017 *J. Colloid Interface Sci.* **497** 172
- [6] Wu Y, Deng P, Tian Y, Ding Z, Li G, Liu J, Zuberi Z and He Q 2020 *Bioelectrochemistry* **131** 107393
- [7] Bai M, Wu W, Meng Y and Liu L 2020 *Chem. Eng. Process.* **149** 107839
- [8] Lin Y, Chen R, Zhang Y, Lin Z, Liu Q, Liu J, Wang Y, Gao L and Wang J 2020 *Mater. Des.* **186** 108304
- [9] Tsang C H A, Huang H, Xuan J, Wang H and Leung D Y C 2020 *Renewable Sustainable Energy Rev.* **120** 109656
- [10] Ismail A F, Goh P S, Sanip S M and Aziz M 2009 *Sep. Purif. Technol.* **70** 12
- [11] Qian D, Wagner G J, Liu W K, Yu M-F and Ruoff R S 2002 *Appl. Mech. Rev.* **55** 495
- [12] Sinha N and Yeow J T-W 2005 *IEEE Trans. NanoBioscience* **4** 180
- [13] Inomata K, Kanazawa K, Urabe Y, Hosono H and Araki T 2002 *Carbon* **40** 87
- [14] Kim J, Kwon O H, Kang Y H, Jang K-S, Cho S Y and Yoo Y 2017 *Compos. Sci. Technol.* **153** 32
- [15] Huang S-Y, Li Q, Zhu Y and Fedkiw P S 2017 *J. Appl. Electrochem.* **47** 105
- [16] Farhan S, Wang R and Li K 2016 *J. Mater. Sci.* **51** 7991
- [17] Wang Y, Serrano S and Santiago-Avilés J J 2003 *Synth. Met.* **138** 423
- [18] Estrade-Szwarckopf H 2004 *Carbon* **42** 1713
- [19] Cao A, Xu C, Liang J, Wu D and Wei B 2001 *Chem. Phys. Lett.* **344** 13
- [20] Gallagher M J et al 1993 *Surf. Sci.* **281** L335
- [21] Bleda-Martínez M J, Lozano-Castelló D, Morallón E, Cazorla-Amorós D and Linares-Solano A 2006 *Carbon* **44** 2642
- [22] Vidu R, Quinlan F T and Stroeve P 2002 *Ind. Eng. Chem. Res.* **41** 6546
- [23] Sugita S, Abe T and Itaya K 1993 *J. Phys. Chem.* **97** 8780
- [24] De Rosa S, Branchini P, Yivlialin R, Duò L, Bussetti G and Tortora L 2020 *ACS Appl. Nano Mater.* **3** 691
- [25] Bussetti G, Yivlialin R, Goletti C, Zani M and Duò L 2019 *Condens. Matter* **4** 23
- [26] Yivlialin R, Bussetti G, Magagnin L, Ciccacci F and Duò L 2017 *Phys. Chem. Chem. Phys.* **19** 13855
- [27] Yivlialin R, Magagnin L, Duò L and Bussetti G 2018 *Electrochim. Acta* **276** 352
- [28] Bussetti G et al 2016 *J. Phys. Chem. C* **120** 6088
- [29] Yivlialin R et al 2017 *J. Phys. Chem. C* **121** 14246
- [30] Pavoni E, Yivlialin R, Hardly Joseph C, Fabi G, Mencarelli D, Pierantoni L, Bussetti G and Farina M 2019 *RSC Adv.* **9** 23156
- [31] Yivlialin R et al 2020 *Appl. Surf. Sci.* **504** 144440
- [32] Dresselhaus M S and Dresselhaus G 2002 *Adv. Phys.* **51** 1
- [33] Goss C A, Brumfield J C, Irene E A and Murray R W 1993 *Anal. Chem.* **65** 1378
- [34] Allia D, Häring P, Haas O, Kötz R and Siegenthaler H 1999 *Electrochem. Commun.* **1** 5
- [35] Inzelt G 2013 Pseudo-reference electrodes *Handbook of Reference Electrodes* ed G Inzelt, A Lewenstam and F Scholz (Berlin: Springer)
- [36] Bellucci S, Bovesecchi G, Cataldo A, Coppa P, Corasaniti S and Potenza M 2019 *Materials* **12** 696
- [37] Maffucci A, Micciulla F, Cataldo A, Miano G and Bellucci S 2016 *Nanotechnology* **27** 095204
- [38] Dabrowska A, Bellucci S, Cataldo A, Micciulla F and Huczko A 2014 *Phys. Status Solidi B* **251** 1–4
- [39] Sinititsyna O, Khestanova E A, Antonov A, Grigorieva I and Yaminsky I 2012 New promising pyrolytic graphite for micro-mechanical exfoliation of graphene 2012 *Graphene Int. Conf.* (Brussel, Belgium April 10–13)

- [40] Sinitsyna O V, Meshkov G B, Grigorieva A V, Antonov A A, Grigorieva I G and Yaminsky I V 2018 *Beilstein J. Nanotechnol.* **9** 407–14
- [41] Katrakova D 2002 Anwendungen der Orientierungsabbildenden Mikroskopie zur Gefügecharakterisierung kristalliner Werkstoffe *PhD Thesis* Universität des Saarlandes, Saarbrücken
- [42] Grigorieva I G and Antonov A A 2003 *X-Ray Spectrom.* **32** 64–8
- [43] Grigorieva I, Antonov A and Gudi G 2019 *Condens. Matter* **4** 18
- [44] Eklund P C, Olk C H, Holler F J, Spolar J G and Arakawa E T 1986 *J. Mater. Res.* **1** 361–7
- [45] Sinitsyna O, Ahmetova A, Meshkov G, Goncharova T, Pylev I, Smirnova M, Belov Y and Yaminsky I 2018 *Nano Industry* **2** 170–2
- [46] Anderson Axdal S H and Chung D D L 1987 *Carbon* **25** 377–89

Attachment D

Jagadeesh, M. S. *et al.* The effect of cyclic voltammetry speed on anion intercalation in HOPG., *Surf. Sci.* **681**, 111-115 (2019).



The effect of cyclic voltammetry speed on anion intercalation in HOPG

M.S. Jagadeesh^a, A. Calloni^{a,*}, I. Denti^b, C. Goletti^c, F. Ciccacci^a, L. Duò^a, G. Bussetti^a

^a Department of Physics, Politecnico di Milano, Piazza Leonardo da Vinci 32, 20133 Milano, Italy

^b Department of Chemistry, Materials and Chemical Engineering "G. Natta", Politecnico di Milano, Piazza Leonardo da Vinci 32, 20133 Milano, Italy

^c Department of Physics, Università di Roma Tor Vergata, Via della Ricerca Scientifica 1, 00133 Roma, Italy

ARTICLE INFO

Keywords:

HOPG
Blister
Cyclic voltammetry
Photoemission spectroscopy

ABSTRACT

It is generally accepted that anion intercalation occurs when HOPG is kept at high electrochemical potentials in oxidant electrolytes, such as perchloric and sulfuric acids. The graphite surface undergoes a detriment, made also evident by the swelling of the uppermost layers (blisters formation) caused by gas evolution in standard electrochemical conditions (namely, by cycling the HOPG voltage at speeds up to 25 mV/s). Surface swelling is therefore considered as being indicative of anion intercalation. Recently, suppression of blister formation when the potential is swept at larger speeds (such as 600 mV/s) has been observed, raising the question as to whether this phenomenon might be able to suppress anion intercalation. In this work, by combining atomic force microscopy and X-ray photoemission spectroscopy, we unequivocally show that the HOPG electrode undergoes similar chemical modifications, regardless of the chosen electrochemical conditions and consequently of the morphological evolution at the surface.

1. Introduction

Graphite electrodes are widely used in conventional acid-lead batteries [1], where graphite is immersed in a diluted sulfuric acid (H₂SO₄) electrolyte [2]. Both applied researches and technological efforts are devoted to the enhancement of the performances of acid-lead batteries in terms of efficiency and stability [3,4]. In these respects, the mechanical and electrochemical stability of the graphite electrode play a key role. For instance, it has been largely proved that, when graphite is immersed in diluted oxidants, such as sulfuric and perchloric electrolytes, it undergoes carbon dissolution and blister formation at relatively high potentials (few volts) [5–12]. These phenomena are usually prevented by protecting the electrode surface with a polymeric coating [13–17] that, however, might alter the graphite transport properties. Nonetheless, in view of using unprotected graphite electrodes, an in-depth analysis of the blister formation mechanism can potentially suggest new strategies to prevent and, eventually, to suppress this process [11,18–20].

The detriment of the graphite electrode can be reproduced through cyclic voltammetry (CV) on highly oriented pyrolytic graphite (HOPG), as shown in Refs. [11,12,21]. Indeed, an enhancement in the electrochemical (EC) current at specific potentials marks ion intercalation inside HOPG, leading to blister formation in standard CV conditions [9,10]. In addition, it was proved that this strong EC treatment deeply modifies the HOPG crystal and clear spectroscopic signatures of

intercalated ionic species are observed with X-ray photoemission spectroscopy (XPS), performed *ex-situ* after CV [8].

Recently [20], we showed with atomic force microscopy (AFM) that blisters do not form when the EC potential sweep exceeds the critical value of 600 mV/s, even if the characteristic CV features of intercalation are still observed in the voltammograms. In order to highlight possible differences in the chemical composition of the HOPG electrode after this treatment, we combined AFM and XPS on samples submitted to fast CV both with perchloric and sulfuric acid electrolytes. Standard CV (scan speed up to 25 mV/s [9]) is added as a reference. Interestingly, the XPS intercalation fingerprints are observed in both cases, while AFM confirms that blisters appear on the electrode surface only if the CV scan is slow.

2. Experimental methods

After exfoliation, 1 × 1 cm² HOPG samples (Optigraph GmbH, Z-grade) were immersed in diluted acid solutions (namely, 2 M HClO₄ and 1 M H₂SO₄ from Sigma Aldrich Ltd.), purified by Ar bubbling for some hours [9,10]. A three-electrode cell was used (see Fig. 1a), where HOPG represents the working electrode (WE) and Pt wires are selected for both the counter electrode (CE) and the reference electrode (RE) [22,23]. In this experimental condition, the latter shows a stable energy shift of +0.743 V with respect to the standard hydrogen electrode. The EC cell, sealed by a Viton O-ring, is filled with a few milliliters of electrolyte.

* Corresponding author.

E-mail address: alberto.calloni@polimi.it (A. Calloni).

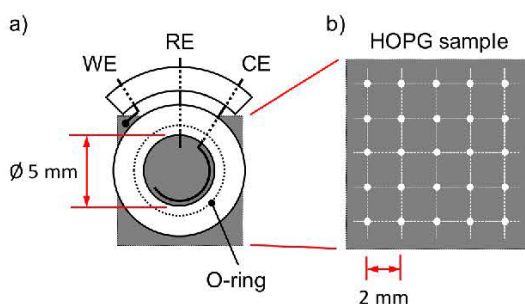


Fig. 1. a) Sketch of the three-electrode EC cell. HOPG, *i.e.* the working electrode (WE), is drawn as a grey square. Above the WE, a Teflon ring (with a central hole of 5 mm diameter) is filled with the electrolyte. The EC cell sealing is ensured by a Viton O-ring (dotted line). Two other electrodes enter the EC cell through the Teflon ring: the reference electrode (RE) and the counter electrode (CE). b) HOPG surface with overlaid the 2 mm mesh virtual grid described in the text. XPS data were acquired for each point of the grid.

A commercial AFM instrument (Keysight 5500) was used in non-contact mode for an *ex-situ* morphological characterization before (not shown) and after the EC treatment.

The XPS analysis was performed *ex-situ* by first removing the electrolyte solution, flushing the HOPG surface gently with dry N_2 in order to eliminate remaining droplets and then inserting the samples in the photoemission spectrometer, operating at a base pressure of about 1×10^{-10} mbar. The spectrometer houses a 150 mm hemispherical analyzer from SPECS GmbH working in magnification mode at a pass energy of 20 eV, and an Al $K\alpha$ ($h\nu = 1486.6$ eV) source, yielding an overall Full Width at Half Maximum spatial and energetic resolution of about 2 mm and 1 eV, respectively [24]. The information depth of the XPS technique is taken as three times the inelastic mean free path of the detected photoelectrons and corresponds in the present case to about 7 nm, *i.e.* 20 HOPG planes [25,26].

In order to determine the location of the points with the highest and most uniform concentration of intercalated species, a series of XPS profiles was acquired on each sample along a virtual grid of coordinates devised to cover the entire HOPG area (Fig. 1b). For each (i,j) point of the grid, the spectra were analyzed and deconvolved as explained in the next section, and the intensity I_{ij} of the characteristic intercalation features was evaluated. The resulting matrices were graphically represented as two dimensional contour plots, such as those shown in Figs. 3c and 4c, and used for the accurate positioning of the samples

before acquiring high statistics photoemission spectra, each one being an average over tens of fast scans over the energy regions of interest.

3. Results and discussion

Fig. 2a shows an AFM image acquired onto a not-intercalated HOPG sample, where the typical graphite steps are visible. Low-voltage CVs, *i.e.* acquired by applying anode voltages well below the onset of anion intercalation in either 2 M $HClO_4$ or 1 M H_2SO_4 solutions, do not show any significant feature (data not reported). In contrast with CV and AFM, XPS detects clear photoemission signals after low voltage CVs. This is highlighted in Fig. 2b, where photoemission spectra acquired on HOPG samples either clean (*i.e.* untreated) or submitted to low voltage CV are compared in the binding energy (BE) range of Cl 2p and S 2p orbitals. The observed features can be assigned to Cl- and S-containing species (more specifically perchlorate and sulfate ions) weakly adsorbed, or physisorbed, on the HOPG surface [8,27,28].

Fig. 3a reports the characteristic CV of HOPG in 2 M $HClO_4$ when anion intercalation and de-intercalation occur. During the anodic (positive) current enhancement, the voltammogram shows two shoulders (marked by red arrows) that represent consecutive graphite intercalation stages. An exponentially increasing background (according to the Butler-Volmer equation) was subtracted to the experimental data (bottom of Fig. 3a) in order to accentuate such intercalation-induced features [29]. In the cathodic (negative) regime other features (blue arrows) appear, which are traditionally interpreted in terms of anion de-intercalation [5,6,8]. The exchanged charge (anodic, cathodic) is different, suggesting an overall irreversible process, *i.e.* part of the solvated anions are retained inside the stratified HOPG crystal [5,6].

The Cl 2p XPS analysis performed on the intercalated sample is shown in Fig. 3b. Two points, labeled (A) and (B) are representative of two different regions of the XPS matrix, one well inside and the other outside the treated area, respectively (Fig. 3c). Outside the area of the EC cell (dashed circle in the XPS matrix), the XPS signal from Cl species is negligible, as expected.

The same experimental approach was exploited for the analysis of the spectroscopic data from samples treated with sulfuric acid. Fig. 4a shows the CV measured on HOPG immersed in 1 M H_2SO_4 . The features observed in the voltammogram (see also the background-subtracted anodic portion of the CV in the bottom panel) are related to characteristic intercalation (red arrow) and de-intercalation (blue arrow) stages [5,6,27]. Fig. 4b reports the S 2p XPS spectra and Fig. 4c the XPS matrix acquired *ex-situ* on the same sample. As above, spectra (A) and (B) refer to regions being subject to anion intercalation or left

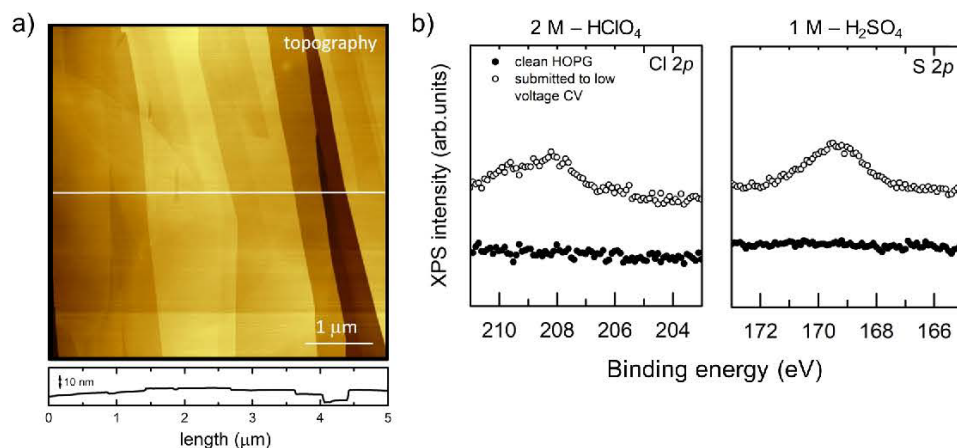


Fig. 2. a) AFM image of not-intercalated HOPG surface. b) XPS spectra related to clean (*i.e.* untreated) HOPG (filled symbols) and to HOPG samples submitted to low voltage CV (open symbols) in 2 M $HClO_4$ (left panel, $0_{MAX} = 0.55$ V) and 1 M H_2SO_4 (right panel, $V_{MAX} = 0.7$ V) electrolytes.

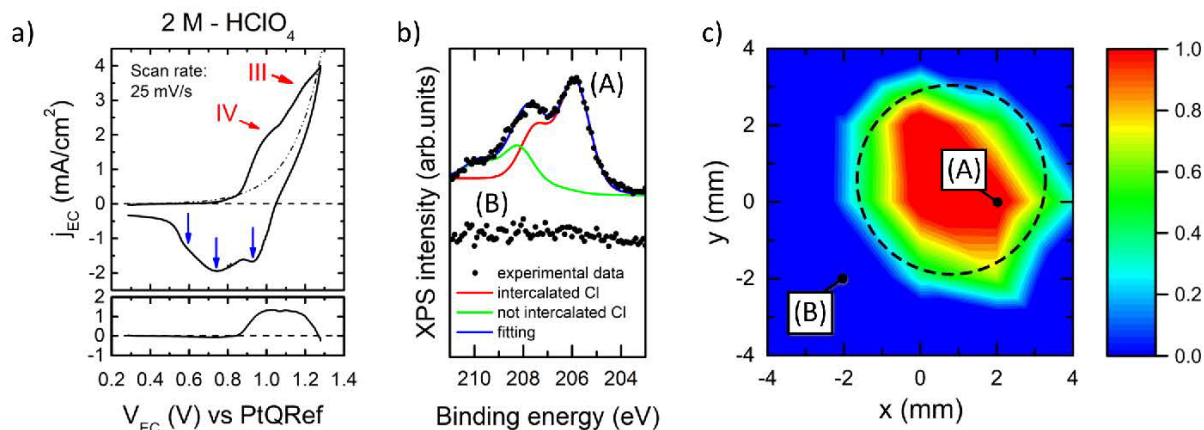


Fig. 3. a) Voltammogram acquired at a scan speed of 25 mV/s on HOPG in contact with the 2 M perchloric acid solution as the electrolyte. Red arrows identify successive intercalation stages, numbered according to Ref. [9], while cathodic features are marked with blue arrows. In order to highlight anodic features, a Butler-Volmer background (dash-dotted line) has been subtracted to the experimental data (bottom of panel a). b) XPS spectra related to positions (A) and (B) in the XPS matrix (panel c). Red and green lines highlight the contribution of intercalated and not-intercalated Cl-containing species, respectively. In the XPS matrix, the color scale is proportional to the intensity of photoemission from intercalated species (Cl $2p_{3/2}$ binding energy 205.9 eV). For interpretation of the references to colour in this figure caption, the reader is referred to the web version of this article.

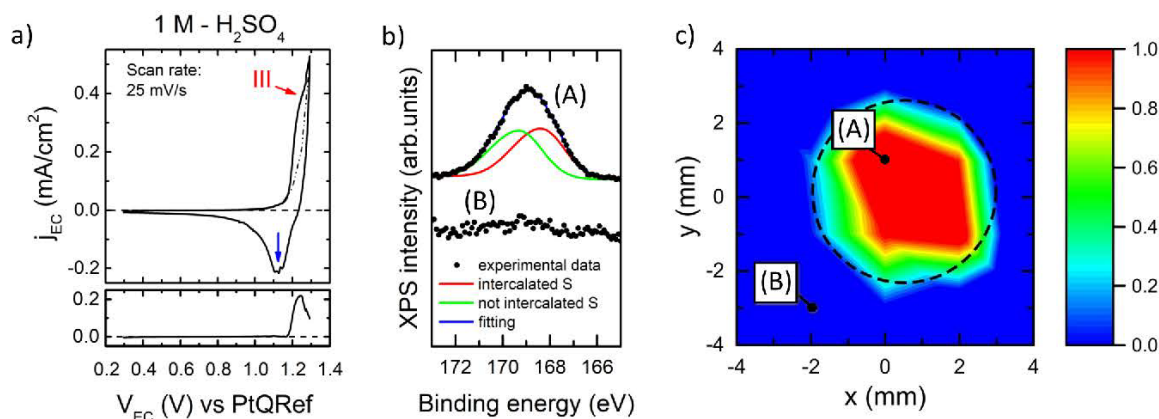


Fig. 4. a) Voltammogram acquired at a scan speed of 25 mV/s on HOPG in contact with the 1 M sulfuric acid solution as the electrolyte. Intercalation stage III [9] is marked with a red arrow, while the blue arrow identifies the negative peak visible in the cathodic region. In order to highlight anodic features, a Butler-Volmer background (dash-dotted line) has been subtracted to the experimental data (bottom of panel a). b) XPS spectra related to positions (A) and (B) in the XPS matrix (panel c). Red and green lines highlight the contribution of intercalated and not-intercalated S-containing species, respectively. In the XPS matrix, the color scale is proportional to the intensity of photoemission from intercalated species (S $2p_{3/2}$ binding energy 168.1 eV). For interpretation of the references to colour in this figure caption, the reader is referred to the web version of this article.

untreated, respectively.

The Cl $2p$ and S $2p$ spectra (Figs. 3b and 4b) were analyzed as follows. After the subtraction of an integral (Shirley) background, a numerical routine (implemented in the Casa XPS software [30]) was used to fit the overall lineshape of spectrum (A) with two doublets. Each doublet is composed by two symmetrical Voigt-like peaks with a BE difference of 1.6 (1.2) eV, representative of photoemission from the spin-orbit split Cl (S) $2p_{3/2}$ and $2p_{1/2}$ orbitals [31,32]. The high BE doublet (green line) is located at the same BE position of the feature shown in Fig. 2b and is therefore related to photoemission from not-intercalated perchlorate (sulfate) ions, while the low BE doublet (red line) is related to Cl (S)-containing species intercalated during the CV scan. The BE shift between the two doublets is about 2.4 eV and 1.1 eV for Cl $2p$ and S $2p$, respectively. We remark that, in order to avoid possible uncertainties coming from electrolyte spills occurring during EC cell dismounting, the results presented in the XPS matrices of Figs. 3 and 4 consider only the photoemission intensity coming from

intercalated species. This signal is seen to slightly exceed the physical dimension of the EC cell (dashed lines) due to the limited spatial resolution of our XPS analysis.

Once the methodology for the XPS data analysis was clarified, new samples were prepared by CV using a high scan speed (600 mV/s), thus precluding blister formation, in agreement with Ref. [20]. Figs. 5a and 5b show the CV voltammograms for perchloric and sulfuric acids, respectively. Both of them are characterized by cathodic (negative) currents, thus ensuring HOPG intercalation. The related topography images are shown in Fig. 5c and d. Despite the significant detriment of the surface quality due to carbon dissolution [18], flat terraces are still recognizable in both cases, and no blisters affect the HOPG morphology, as expected from our previous investigations [18,20].

The photoemission spectra acquired at the center of the intercalated region are shown in Fig. 6a and b for perchloric and sulfuric acid, respectively, and compared with the results previously obtained with low CV speeds. In order to highlight differences in the relative weight of

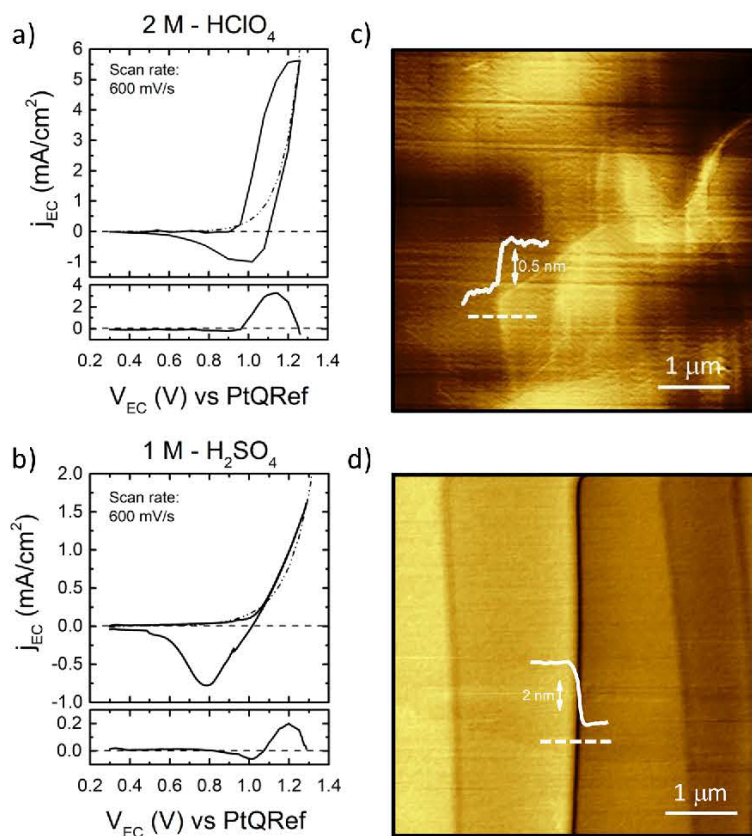


Fig. 5. a,b) Voltammograms acquired at a high scan rate on HOPG by using perchloric and sulfuric acid solutions, respectively. In order to highlight anodic features, a Butler-Volmer background (dash-dotted line) has been subtracted to the experimental data (bottom of each panel) c,d) non-contact AFM images of the HOPG surface after the treatment in the electrolytes of a) and b), respectively. The profiles reported in the images are related to mono (panel c) and multi (panel d) atomic steps.

photoemission from intercalated species, the spectra related to the same BE range have been normalized to their overall intensity. We note that slightly lower (by about 15%) absolute XPS intensities are detected in the case of fast CV. This, on the one hand, confirms that massive anion intercalation still occurs inside HOPG and, on the other, is consistent with our previous observations reported in Ref. [18]. There, when the electrode is kept at high potentials for longer time (as in the case of low CV speeds), HOPG undergoes carbon dissolution, which results in an

enhancement of surface roughness and defectivity, possibly reflected in a slight increase of adsorbed and intercalated species.

We observe a slight variability (close to the experimental uncertainty) in the BE position of the photoemission features from Cl and S species, which is at present difficult to link to a specific physical origin. Notwithstanding this variability, the spectra from the two sets of samples do not reveal significant differences concerning the relative weight of photoemission signals from the intercalated species. A first

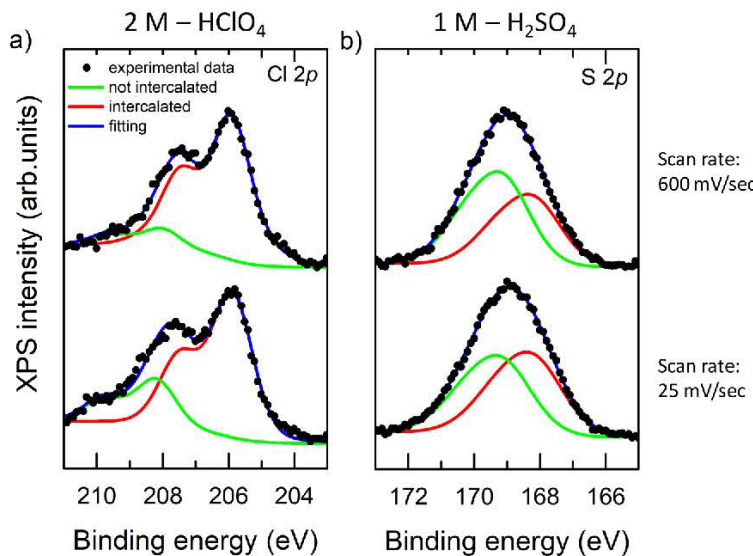


Fig. 6. Top (bottom) spectra: Cl 2p (a) and S 2p (b) detailed scans acquired after fast (slow) CV at a scan speed of 600 (25) mV/s. Red and green lines highlight the contribution of intercalated and non-intercalated species, respectively. Spectra related to the same BE range have been normalized to their overall intensity. For interpretation of the references to colour in this figure caption, the reader is referred to the web version of this article.

consequence of these results is that the scan speed, which is, on the one hand, known for influencing both ion diffusion inside the electrolyte and the thickness of the double layer at the liquid/solid interface, on the other hand does not affect the chemical composition of the uppermost HOPG layers after CV. Moreover, our results show that XPS is not sensitive to the presence of blisters on the HOPG surface. It is reasonable to link the formation of blisters during CV to at least two processes with different kinetics: (i) the adsorption/incorporation (in-depth diffusion) of ionic species into HOPG (independent of scan speed within the depth resolution of XPS) and (ii) the assembly or lateral diffusion of evolved gaseous species during the sweep (finally leading to blistering). The uniform incorporation of ionic species (process i) is supported by the detection, together with blisters (process ii), of a measurable increase of HOPG interplanar spacing as a result of anion intercalation [9]. Although fully disentangling these two processes is outside the scope of the present study, our results unequivocally prove that anion intercalation by itself does not imply a swelling of the electrode surface by evolution of gaseous species.

4. Conclusions

We investigated the effect of CV scan speed on HOPG electrodes reacting with oxidant electrolytes (perchloric and sulfuric acids). Low speed CV (up to 25 mV/s) is traditionally used to intercalate graphite and to produce blisters on the surface, and XPS has been previously used to characterize the chemical composition of the HOPG surface after CV in perchloric acid solutions. In this work, we observe that the XPS results are not altered by changing the CV speed (600 mV/s vs 25 mV/s), proving that intercalation occurs under a wide range of EC parameters, without being directly related to the sample morphology. This result is particularly important in view of a clarification of the processes leading to the detriment of the surface under oxidizing conditions, currently limiting the use of unprotected graphite electrodes in technological applications.

Acknowledgements

Part of the results presented in this work were collected at the Solid–Liquid Interface and Nanomicroscopy (SoLiNano) laboratory, an inter-departmental laboratory of Politecnico di Milano. We are grateful to Rossella Yivlialin (Department of Materials Science, Università degli studi di Milano Bicocca) for the help provided during CV data acquisition and to Luca Magagnin and Alessandra Accogli (Department of Chemistry, Materials and Chemical Engineering, Politecnico di Milano) for useful discussion.

References

- [1] G.J. May, A. Davidson, B. Monahov, *J. Energy Storage* 15 (2018) 145.
- [2] L. Wang, H. Zhang, W. Zhang, G. Cao, H. Zhao, Y. Yang, *Mater. Lett.* 206 (2017) 113.
- [3] J. Settelein, H. Lormann, G. Sextl, *Electrochim. Acta* 233 (2017) 173.
- [4] J. Valenciano, A. Sánchez, F. Trinidad, A.F. Hollenkamp, *J. Power Sources* 158 (2006) 851.
- [5] K. Kinoshita, *Carbon: Electrochemical and Physicochemical Properties*, Wiley, 1988.
- [6] K.W. Hathcock, J.C. Brumfield, C.A. Goss, E.A. Irene, R.W. Murray, *Anal. Chem.* 67 (1995) 2201.
- [7] C.A. Goss, J.C. Brumfield, E.A. Irene, R.W. Murray, *Anal. Chem.* 65 (1993) 1378.
- [8] B. Schnyder, D. Alllata, R. Kötz, H. Siegenthaler, *Appl. Surf. Sci.* 173 (2001) 221.
- [9] D. Alllata, R. Kötz, O. Haas, H. Siegenthaler, *Langmuir* 15 (1999) 8483.
- [10] G. Bussetti, R. Yivlialin, D. Alllata, A. Li Bassi, C. Castiglioni, M. Tommasini, C.S. Casari, M. Passoni, P. Biagioni, F. Ciccacci, L. Duò, *J. Phys. Chem. C* 120 (2016) 6088.
- [11] Z.Y. Xia, S. Pezzini, E. Treossi, G. Giambastiani, F. Corticelli, V. Morandi, A. Zanelli, V. Bellani, V. Palermo, *Adv. Funct. Mater.* 23 (2013) 4684.
- [12] R. Yivlialin, G. Bussetti, L. Brambilla, C. Castiglioni, M. Tommasini, L. Duò, M. Passoni, M. Ghidelli, C.S. Casari, A. Li Bassi, *J. Phys. Chem. C* 121 (2017) 14246.
- [13] R.M.N.M. Rathnayake, M.M.M.G.P.G. Mantilaka, M. Hara, H.-H. Huang, H.W.M.A.C. Wijayasinghe, M. Yoshimura, H.M.T.G.A. Pitawala, *Appl. Surf. Sci.* 410 (2017) 445.
- [14] Y. Deng, *Int. J. Electrochem. Sci.* 13 (2018) 5923.
- [15] M. Ates, *J. Adhes. Sci. Technol.* 30 (2016) 1510.
- [16] R. Yivlialin, G. Bussetti, M. Penconi, A. Bossi, F. Ciccacci, M. Finazzi, L. Duò, *ACS Appl. Mater. Interfaces* 9 (2017) 4100.
- [17] R. Yivlialin, M. Penconi, G. Bussetti, A.O. Biroli, M. Finazzi, L. Duò, A. Bossi, *Appl. Surf. Sci.* 442 (2018) 501.
- [18] R. Yivlialin, G. Bussetti, L. Magagnin, F. Ciccacci, L. Duò, *Phys. Chem. Chem. Phys.* 19 (2017) 13855.
- [19] R. Yivlialin, L. Brambilla, G. Bussetti, M. Tommasini, A. Li Bassi, C.S. Casari, M. Passoni, F. Ciccacci, L. Duò, C. Castiglioni, *Beilstein J. Nanotechnol.* 7 (2016) 1878.
- [20] R. Yivlialin, L. Magagnin, L. Duò, G. Bussetti, *Electrochim. Acta* 276 (2018) 352.
- [21] A.A. Gewirth, A.J. Bard, *J. Phys. Chem.* 92 (1988) 5563.
- [22] Inzelt, A. Lewenstam, F. Scholz (Eds.), *Handbook of Reference Electrodes*, Springer, Berlin, Heidelberg, 2013.
- [23] K.K. Kasem, S. Jones, *Platin. Met. Rev.* 52 (2008) 100.
- [24] G. Berti, A. Calloni, A. Brambilla, G. Bussetti, L. Duò, F. Ciccacci, *Rev. Sci. Instrum.* 85 (2014) 073901.
- [25] S. Tanuma, C.J. Powell, D.R. Penn, *Surf. Interface Anal.* 21 (1994) 165.
- [26] T. Susi, T. Pichler, P. Ayala, *Beilstein J. Nanotechnol.* 6 (2015) 177.
- [27] D. Alllata, *Investigation of Nanoscale Intercalation Into Graphite and Carbon Materials By in Situ Scanning Probe Microscopy*, University of Bern, 2000.
- [28] S.H. Goh, S.Y. Lee, J. Dai, K.L. Tan, *Polymer (Guildf)* 37 (1996) 5305.
- [29] A.J. Bard, L.R. Faulkner, *Electrochemical Methods: Fundamentals and Applications*, Wiley, 2001.
- [30] N. Fairley, <http://www.Casaxps.com>, (2005).
- [31] G. Morea, C. Malitesta, L. Sabbatini, P.G. Zambonin, *J. Chem. Soc. Faraday Trans.* 86 (1990) 3769.
- [32] A. Calloni, A. Brambilla, G. Berti, G. Bussetti, E.V. Ganesi, M. Binda, A. Petrozza, M. Finazzi, F. Ciccacci, L. Duò, *Langmuir* 29 (2013) 8302.

Attachment E

Filoni, C., *et al.* Reactive Dissolution of Organic Nanocrystals at Controlled pH. *ChemNanoMat* **6**, 567–575 (2020).

Associated Contents (Supporting Information) are enclosed.

Reactive Dissolution of Organic Nanocrystals at Controlled pH

Claudia Filoni,^[a] Lamberto Duò,^[a] Franco Ciccacci,^[a] Andrea Li Bassi,^[b] Alberto Bossi,^[c, d] Marcello Campione,^[e] Giancarlo Capitani,^[e] Ilaria Denti,^[f] Matteo Tommasini,^[f] Chiara Castiglioni,^[f] Stefania De Rosa,^[g, h] Luca Tortora,^[g, i] and Gianlorenzo Bussetti*^[a]

Abstract: The development of novel protocols and techniques for waste treatment represents the state of the art in the so-called “green conversion”. Chemical wastes deriving from industrial and power-station processes, which involve organic crystals, can be very hazardous for the environment. Studying their dissolution mechanism, both theoretically and experimentally, represents a mandatory step in the critical task of their disposal. Surprisingly, most of the studies are focused on millimeter scale length, from which one could estimate the crystal dissolution rate. In these studies, where no information about the dissolution mechanism on a molecular scale is provided, etch-pit formation is recognized as the ultimate mechanism of crystal dissolution.

In this work, we show the morphological evolution of organic nanocrystals on the sub-micrometer scale range in a reactive dissolution process controlled by pH. This approach allows us to explore ranges of high undersaturation, whereby crystal dissolution occurs even though etch-pit formation is suppressed. Adopting different surface and bulk-sensitive techniques (atomic force microscopy, time-of-flight secondary ion mass spectroscopy and X-ray/electron diffraction, Raman spectroscopy, respectively), we investigate the dissolution process of porphyrin thin films deposited on the basal plane of highly oriented pyrolytic graphite, proving that such films constitute a model system to unveil the dissolution mechanism of organic nanocrystals.

1. Introduction

Among many organic materials, porphyrin molecules represent relevant building-blocks for functional material^[1] whose optical/electronic properties can be modulated electrochemically^[2] or by the proper control of pH and solvent.^[3] Nowadays, controlling the morphology of advanced organic materials is a key task for their applications in different fields, ranging from the fabrication of organic electronic devices,^[4] sensors,^[5–7] as well as applications to the biomedical field.^[8–11] In this framework, studying the formation of porphyrin thin films, their phase stability and dissolution mechanisms is beneficial.

By controlling the dissolution time scale with pH and solvent, one can monitor changes of the film structure with selected techniques. From a thermodynamic point of view,

dissolution is the reverse process of the crystal growth. The latter has focused a wide experimental and theoretical effort being the key field in Material Science in view of fabricating materials with controlled properties. Different techniques (*e.g.*: molecular beam epitaxy, spin-coating, chemical casting, *etc.*) were exploited to study the crystal growth step-by-step starting from a clean substrate. This experimental approach avoids using neat crystals, which could present high surface roughness, as well as many defects and dislocations. Conversely, it allows making a better comparison with theoretical results and/or models of ideal crystals. A first fruitful tentative of studying dissolution as an independent process was made by F. C. Frank in the 50s focusing on germanium crystals.^[11,12] Later on, his conclusions were verified by Ives,^[13] Harrington,^[14,15] and Barber.^[16,17] The characterization of crystals after the immersion

[a] C. Filoni, Prof. L. Duò, Prof. F. Ciccacci, Prof. G. Bussetti
Department of Physics
Politecnico di Milano
p.zza Leonardo da Vinci 32, I-20133 Milano (Italy)
E-mail: gianlorenzo.bussetti@polimi.it

[b] Prof. A. Li Bassi
Department of Energy
Politecnico di Milano
Via Ponzio 34/3, I-20133 Milano (Italy)

[c] Dr. A. Bossi
Istituto di Scienze e Tecnologie Chimiche “G. Natta”
Consiglio Nazionale delle Ricerche (CNR-SCITEC)
PST via G. Fantoli 16/15, I-20138 Milano, Italy

[d] Dr. A. Bossi
SmartMatLab Center
Via Golgi 19, I-20133 Milano (Italy)

[e] Prof. M. Campione, Prof. G. Capitani
Department of Earth and Environmental Sciences
Università degli Studi di Milano – Bicocca
Piazza della Scienza 4, I-20126 Milano (Italy)

[f] I. Denti, Prof. M. Tommasini, Prof. C. Castiglioni
Department of Chemistry
Materials and Chemical Engineering
Politecnico di Milano
p.zza Leonardo da Vinci 32, I-20133 Milano (Italy)

[g] S. De Rosa, Prof. L. Tortora
Surface Analysis Laboratory INFN
Roma Tre University
Via della Vasca Navale 84, 00146, Rome (Italy)

[h] S. De Rosa
Department of Mathematics and Physics
Roma Tre University
Via della Vasca Navale 84, 00146, Rome (Italy)

[i] Prof. L. Tortora
Department of Science
Roma Tre University
Via della Vasca Navale 84, 00146, Rome (Italy)

Supporting information for this article is available on the WWW under <https://doi.org/10.1002/cnma.202000024>

in solvents, made by optical interferometry,^[18] electronic microscopy^[19] and diffraction,^[20] showed that dissolution can be rapid or slow depending on driving effects on the surface. More recently, scanning probe microscopies (SPM), such as atomic force microscopy (AFM),^[21–27] have been exploited to study the local morphology of crystals and their dissolution kinetics. Moreover, SPM offers the possibility to immerse the tip inside the solution, to observe in real time the *in-situ* evolution of the surface. By using an AFM, Cama and co-workers clarified the evolution of surface etch-pitting during the fluorite crystal dissolution.^[28] Etch-pits observed on the surface are deep holes crystallographically oriented with respect to the main axis of the crystal. According to the Frank's model,^[12] the etch-pit forms when undersaturation overcomes a critical value. This phenomenon takes place when the dissolution of a terrace (defined as the removal of an atom or molecule from the uppermost surface) happens near dislocations or a crystal defects. These, interpreted as regions confined within high Miller-indexes surfaces, change the kinetic rates between nucleation and dissolution of kinks, thus enhancing surface erosion close to the crystal defects (etch-pit growth). As recently pointed out by Lüttge,^[29] the state of art in etch-pit-controlled crystal dissolution is focused on millimetric-scale crystals, while theoretical calculations (in view of having computable data) require nano-sized crystals on surfaces with different roughness.^[29]

In this context, we propose a model system based on porphyrin nanocrystals immersed in a diluted sulfuric acid solution. By combining surface [AFM, time of flight secondary ion mass spectrometry (ToF-SIMS)] and bulk-sensitive [transmission electron microscopy (TEM), X-ray diffraction (XRD) and Raman spectroscopy] techniques, we disclose that etch-pit formation only affects organic nanocrystals at specific pH. The change of the pH offers the possibility to explore unprecedented ranges of undersaturation revealing the strong non-linear character of the dissolution process (different phases) especially in relation to the crystal morphological evolution.

2. Results

The deposition of both H₂TPP and ZnTPP molecules under high vacuum on HOPG substrates follows a layer-plus-island growth mode (see Figure S1 in the SI).^[30,31] The film surface morphology (Figure 1) is characterized by an ensemble of many crystals (approximately 30–50 crystals/μm²), showing many edges at 90° and is organized in domains with different orientations. The porphyrin crystal lateral size ranges from tens to hundreds of nanometers. Thus, such films perfectly suit the current study, since they offer the possibility of studying the effect of the electrolyte solution, *i.e.* the acid interactions, by monitoring hundreds of nanocrystals within the same scanned area.

The film roughness, defined as the arithmetic mean value (Ra) between the peaks and the minima of different image cross-sections, is approximately 8 nm for both H₂TPP and ZnTPP samples. Other morphological differences between the free-base porphyrin molecules and those with the Zn metal ion

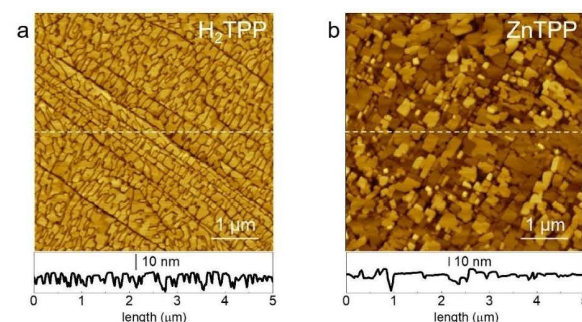


Figure 1. AFM image of the pristine (a) H₂TPP and (b) ZnTPP film. At the bottom, a representative cross section of the image is reported.

(the latter are qualitatively wider and less regular than the former) are irrelevant for the present investigation.

The XRD patterns (see Figure 2a), acquired on wet-transferred pristine H₂TPP films, display only one reflection at $2\theta = 19.21^\circ$, corresponding to an interlayer spacing of 4.61 Å. This spacing is consistent with the stacking distance among free-base porphyrins, indicating that the detected crystal phase is entirely constituted of molecules that lay flat on the substrate surface. In wet-transferred ZnTPP films, two diffraction peaks were detected, one at $2\theta = 18.26^\circ$, corresponding to a spacing of 4.85 Å, and one at $2\theta = 20.21^\circ$, corresponding to a spacing of 4.39 Å. These spacings are indicative of two polymorphs, with a common structural motif characterized by metalated molecules lying flat on the substrate surface. Electron diffraction measurements performed by TEM were acquired on selected islands with the electron beam impinging normal to the film surface (Figure 2b). The diffraction pattern of all the films is consistent with that of a square lattice projection on the substrate surface, with unit cell parameters $a = b = 13.4$ Å (See SI), *i.e.* compatible with the diameter of a porphyrin molecule (about 14 Å). It is worth noting the systematic extinction of $h0l$ reflection with odd h , indicating translational symmetry elements along the a direction. Bright-field TEM images show a single intermediate grey level for islands of H₂TPP (see Figure S2 in the SI), and two intermediate grey levels for islands of ZnTPP (see Figure S6 in the SI), in accordance to the single H₂TPP polymorph and the presence of two polymorphs of ZnTPP detected by XRD. Due to the complementarity of XRD and TEM data, we propose a tentative structural model of our films, which show close affinity with the known tetragonal ($I4/m$) polymorph of Cu-TPP.^[32] In Ref. 36, the porphyrin unit cell parameters are $a = b = 13.37$ Å, and $c/2$ ($d002$) = 4.86 Å (see Figure S8 in the SI) while, in our films, $a = b = 13.4$ Å and $d002$ is within 4.39 Å and 4.85 Å.

When immersed in acidic media, free-base porphyrins undergo the following protonation:



This reaction triggers the dissolution of the porphyrin crystals (reactive dissolution) with a kinetics dependent on the

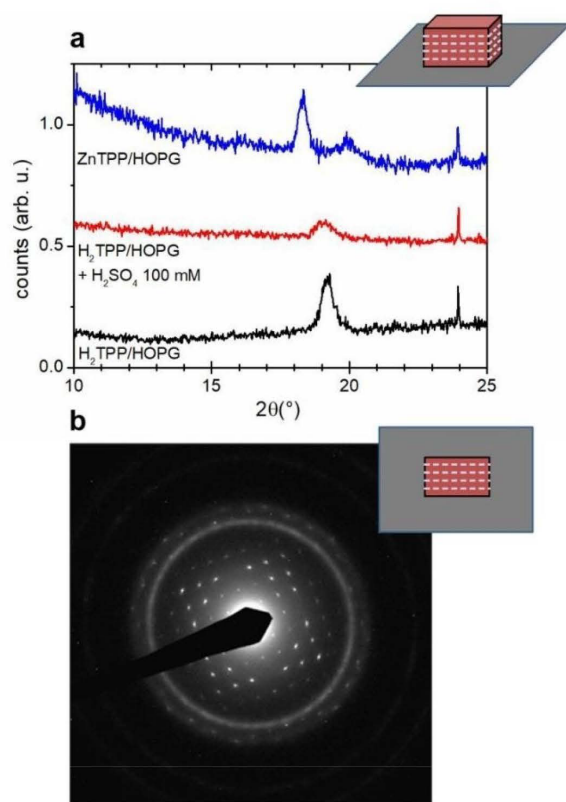


Figure 2. a) XRD patterns acquired on porphyrin films wet-transferred on Si plates. The sharp peak at 24° is the 002 reflection of HOPG due to residual Cu K β radiation ($\lambda = 1.3922 \text{ \AA}$) and is taken as internal reference for the comparison of the patterns. In this configuration diffraction peaks identify crystallographic planes parallel to the substrate surface (see inset). b) Representative electron diffraction pattern acquired on a single H_2TPP nanocrystal of a thin film wet-transferred on a copper grid. Continuous diffused rings are due to the thin Au film used for calibration. Diffraction spots identify planes orthogonal to the substrate surface (see inset).

acid concentration (pH). On the contrary, ZnTPP is insensitive to the presence of Brønsted acids, giving rise to no reaction with H_2SO_4 . From a morphological point of view, etch-pit formation is thus expected on the H_2TPP nanocrystals surface, while no changes are expected for ZnTPP films.

In agreement with this scenario, once placed in the diluted sulfuric acid, H_2TPP films undergo a significant morphological change with a clear trend as a function of the pH. At $\text{pH}=3$, nanocrystals show characteristic etch-pits well aligned with the crystal edges (see Figure 3a and b). No changes are observed in the number ($\sim 15 \text{ pits}/\mu\text{m}^2$) and shape of pits until the acidic solution is replaced with a fresh one (data not reported). The presence of etch-pits clearly indicates that molecules are progressively removed from the crystal and that, even at $\text{pH}=3$, the undersaturation value is beyond the critical point for effective dissolution (i.e. the absolute value of the Gibbs free energy of dissolution is higher than the critical one: $|\Delta G| > |\Delta G_{\text{crit}}|$). Instead, at $\text{pH}=0$, crystals undergo to an abrupt

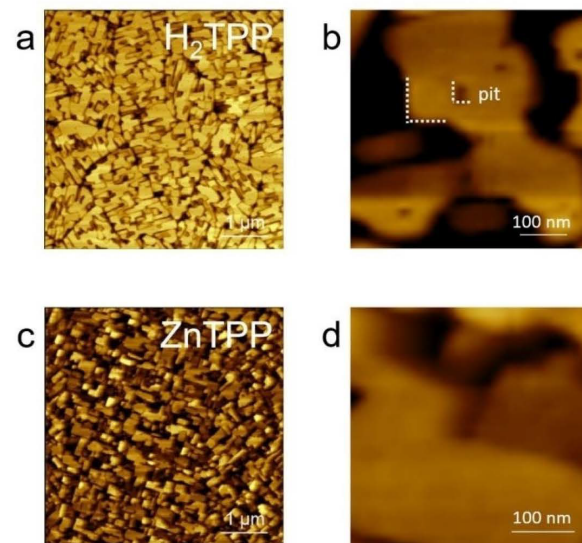


Figure 3. Comparison of AFM images of H_2TPP (panels a and b) and ZnTPP crystals (panels c and d) when immersed in diluted sulfuric acid solution of $\text{pH}=3$. Panels b and d represent blow-ups of porphyrin crystals.

dissolution (Figure 4a). However, the surface morphology is significantly different from the pristine HOPG (i.e., no detectable mono-atomic steps, enhanced terrace roughness, etc.), indicating that a residual layer of porphyrins is still present on the surface, in agreement with previous results.^[33] Conversely, being not sensitive to the acidic media, ZnTPP crystals do not show any significant difference with respect to the as-prepared sample, as reported in Figure 3c ($\text{pH}=3$) and Figure 4b ($\text{pH}=0$). Different measurements acquired over several hours always show the same crystal assembly and surface roughness.

For a better understanding of the H_2TPP film evolution, in-situ AFM images were acquired at intermediate pH values, at which wider etch-pits are expected. In Figure 5, we report results obtained with $\text{pH}=2$ and 1 (panel a and c, respectively). Surprisingly, we note that nanocrystals do not show wider etch-pits after the immersion in the solution at $\text{pH}=2$. Indeed, after waiting few minutes, etch-pits abruptly disappear and nanocrystal surfaces are observed to be decorated by bulges (shown

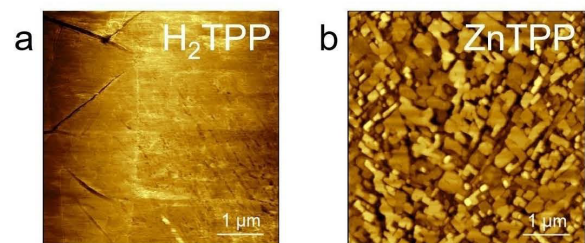


Figure 4. Comparison of AFM images of H_2TPP (panel a) and ZnTPP crystals (panel b) when immersed in diluted sulfuric acid solution of $\text{pH}=0$.

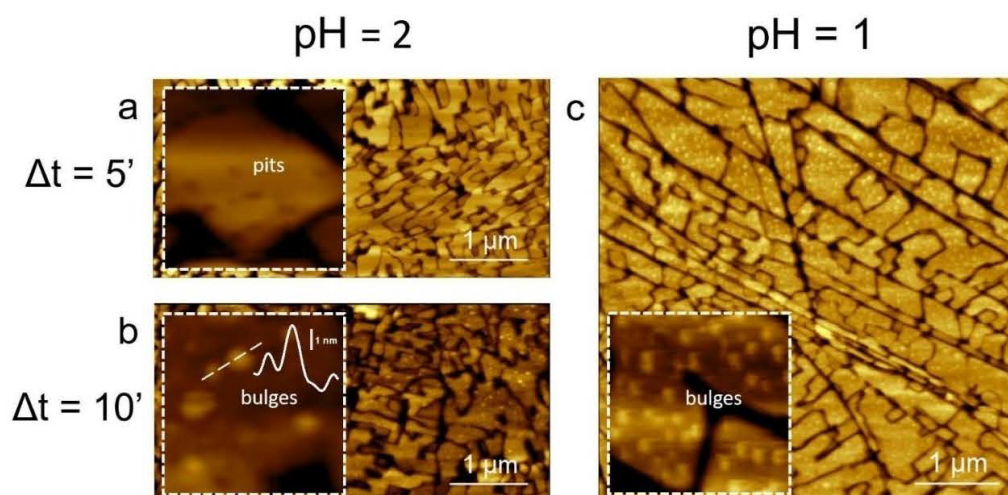


Figure 5. AFM images comparison of H₂TPP when immersed in diluted sulfuric acid solution of pH=2 (panels a and b, which represent two consecutive acquisitions) and pH=1 (panel c). In the latter case, no further evolution as a function of time is observed. The reported Δt indicates how many minutes after the sample immersion in the sulfuric acid solution the image scan started. *Insets:* blow-ups of the sample surface characterized by etch-pits (panel a) or bulges (panels b and c) are reported.

in Figure 5 panel b), whose density is comparable to that of the etch-pits (see above).

The bulges reported in Figure 5b are similar to those observed immediately after the sample immersion in the pH=1 solution (panel c). However, in the latter case, the bulges density (45 bulges/ μm^2) is three times higher than in panel b. The morphological change from etch-pit to bulge structures is probably due to a dissolution kinetics enhancement. In fact, the level of undersaturation of the system increases as the pH decreases, shifting the dissolution plateau. Our results reveal that etch-pit dissolution is not an exhaustive mechanism for dissolution under far-from-equilibrium conditions ($|\Delta G| > |\Delta G_{\text{crit}}|$). Additional non-linearities appear as the undersaturation is further lowered giving rise to more complex morphological changes (namely, bulges) of the dissolving interface.

In Table 1, we report a summary of the relation occurring among pH, undersaturation level, and dissolution mechanism of H₂TPP nanocrystals. Due to the logarithmic relationship between undersaturation ratio (proportional to $[\text{H}^+]$) and Gibbs free energy, ΔG spans one order of magnitude, while $[\text{H}^+]$ spans 3 orders of magnitude. ΔG_{crit} is the critical variation of Gibbs free energy for the onset of etch-pit dissolution.

pH	$[\text{H}^+]$	ΔG (Gibbs free energy of dissolution)	Dominant dissolution mechanism
3	10^{-3}	$> \Delta G_{\text{crit}} $	Etch-pit dissolution
2	10^{-2}	$> 2 \Delta G_{\text{crit}} $	Etch-pit dissolution + incipient Bulges formation
1	10^{-1}	$> 5 \Delta G_{\text{crit}} $	Bulges formation
0	1	$> 10 \Delta G_{\text{crit}} $	Flattening

In the light of these results, two main problems arise. On the one hand, it is important to understand if the dissolution process affects the uppermost part of the nanocrystals or, conversely, if all the crystal volume is rapidly affected by the diluted sulfuric acid. On the other hand, the chemistry of dissolution requires an in-depth investigation. To solve the first problem, some hints can be obtained from both a diffraction analysis and a Raman spectroscopy investigation.

XRD data acquired on acid-treated films of H₂TPP show only slight variations with respect to those acquired on pristine ones (Figure 2a). The single detected peak slightly broadens and decreases in intensity, while an increment of 1% is observed in the corresponding interlayer spacing. Such small variations prove that neither phase transitions nor amorphization the porphyrin films. Since diffraction volumes are different for each measurement reported in Figure 2, intensities and integrated areas of the same peak of different samples cannot be compared with the aim of defining different level of crystallinity. On the contrary, we can compare the FWHM of the same peak of different samples. We estimated for the pristine sample $\text{FWHM} = 0.5^\circ$, whereas for the acid-treated one $\text{FWHM} = 0.7^\circ$. This evaluation partially quantifies the loss of coherence thickness of crystal domains after the acid treatment.

Raman spectra recorded with 514 and 458 nm excitations and display matching peaks relative intensities are slightly modulated by resonance effects. Resonance conditions are reached with 514 nm excitations,^[33,34] which results in a Raman spectrum where overtones/combinations display a sizeable intensity, together with a fluorescence background. The 458 nm excitation lies in between two electronic transitions of H₂TPP,^[33] which justifies the observed decrease of the relative intensity of overtones/combinations compared to the previous case. In any case, the piece of information contained in the spectra is rather

independent the excitation. We focus here on the Raman spectra recorded with 458 nm excitation (Figure 6, panel a), which is also free from fluorescence background. The interested reader may find in Figures S9 and S10 of the SI the complete set of data.

To interpret the Raman spectra of the H₂TPP film deposited on HOPG, we compared the results with those acquired from a porphyrin powder used as a reference spectrum (isotropic sample). This comparison (Figure 6b) highlights the following changes in the spectrum of the film: i) absence of the Raman modes at 494, 448, 410 cm⁻¹; ii) remarkable weakening of the 330 cm⁻¹ line; iii) appearance of a broad feature at 145 cm⁻¹; iv) presence of just the low wavenumber component of the doublet at 196–211 cm⁻¹. Similar studies on H₂TPP show the same spectral features for both 514 and 458 excitation wavelength.^[34–36] These effects on the band intensities can be justified by an overall preferential orientation of the H₂TPP crystals grown on the HOPG surface, in agreement with AFM, XRD, and TEM measurements. After immersion in acid environment (H₂SO₄, 100 mM), the spectra are noisier (see panels c and d) presumably due to a lower quality of the film (i.e., less crystalline order and/or presence of more defects), but the spectral features do not significantly change (no evident effects can be detected neither in peak position nor in relative intensities, as reported in the Supporting Information). Evidence of how reactive dissolution through protonation affects the Raman spectra of porphyrins can be found in the literature.^[37] Both density functional theory (DFT) calculations and Raman

experiments show that protonation remarkably modifies the Raman spectrum of H₂TPP. In our experiments we do not observe marker bands of protonation, suggesting that the molecules in the bulk of the 3-D structures are not protonated. We thus infer that protonated porphyrins are confined on the uppermost layers of the nano-crystals and/or have left the film dissolving in the acidic solution.

The rationale of the chemical process that justifies the surface morphological changes was studied by a high-sensitive surface technique such as ToF-SIMS.

Low-energy ion bombardment experiments were conducted on the pristine H₂TPP sample and H₂TPP samples immersed in 1 mM and 100 mM solution. Secondary ions coming from the H₂TPP characteristic fragmentation process were detected. In Figure 7, the results for the as grown sample (gray solid line), the sample where stable etch pits have been found (pH=3, blue dotted line), and the sample characterized by bulges (red dashed line) are presented. In order to interpret the changes in the surface chemistry of the sample, we monitored the intensity evolution of two of the most abundant ion peaks at high masses (C₄₄H₃₀N₄⁻ at 614.24 *m/z* and C₉H₅N₂⁻ at 141.04 *m/z*) and two ion peaks at lower masses (C₅N⁻ at *m/z* 74.00 and NH⁻ at *m/z* 15.01). These ion peaks were selected as representatives of the porphyrin macrocycle. In particular, variations in signal intensity of the two ion peaks at high masses could indicate a degradation of the macrocycle, while changes in signal intensity of the low-mass peaks could give information about the degradation of the pyrrole unit. The

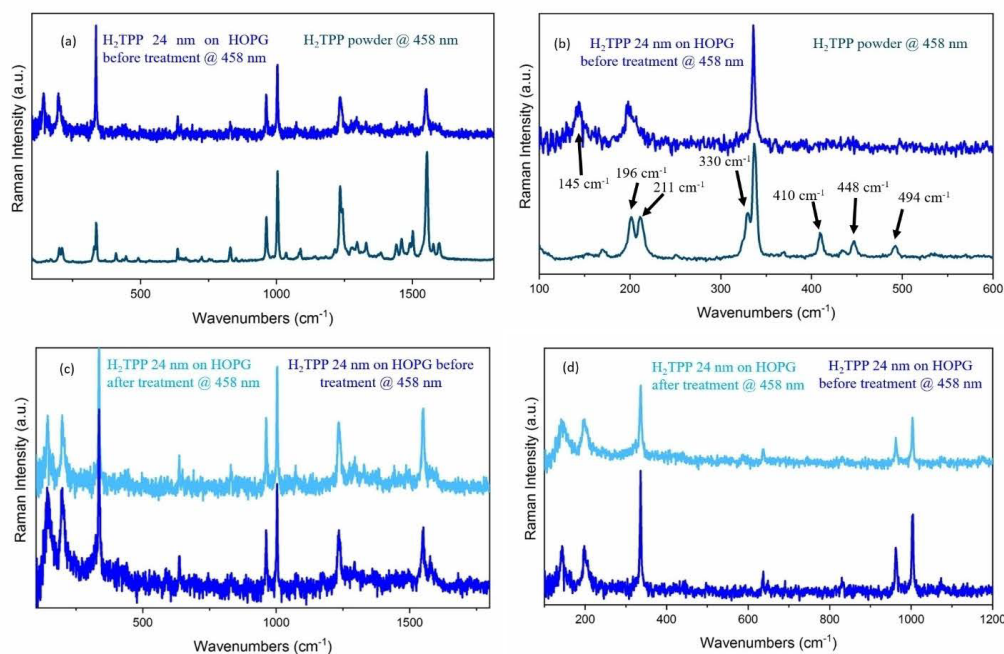


Figure 6. Raman spectra acquired at 458 nm excitation wavelength: (a) comparison between spectra of a powder H₂TPP sample and the film sample (before the immersion in H₂SO₄, 1 M) and (b) zoom over the (600–1200 cm⁻¹) spectral region; (c) comparison between spectra of the H₂TPP nano-crystals deposited on the HOPG sample before and after the immersion in pH = 1 H₂SO₄ and (d) zoom over the (1200–1200 cm⁻¹) spectral region.

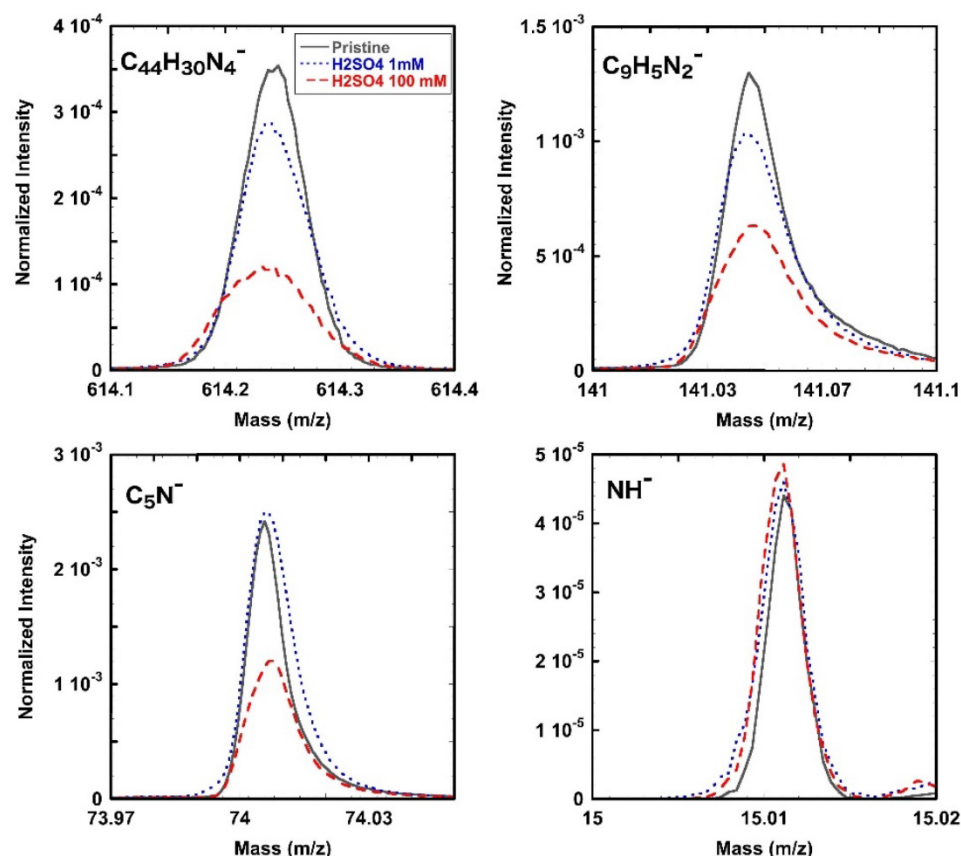


Figure 7. Comparison of normalized ToF-SIMS negative ion peaks from pristine H₂TPP sample (gray solid line), H₂TPP sample immersed in 1 mM (blue dotted line) and 100 mM (red dashed line) sulfuric acid solution. Changes in ion peak intensity for C₄₄H₃₀N₄⁻ (*m/z* 614.24), C₉H₅N₂⁻ (*m/z* 141.04), C₅N⁻ (*m/z* 74.00), and NH⁻ (*m/z* 15.01) are represented, respectively.

plots in Figure 7 show the changes in signal intensity of the C₄₄H₃₀N₄⁻, H₂TPP molecular ion peak, and C₉H₅N₂⁻ fragment ion (top panels, left and right, respectively), the latter probably coming from the fragmentation of two pyrrole units of the tetrapyrrolic macrocycle. For both ions, the signal intensity drops progressively with increasing concentrations of sulfuric acid.

On the other hand, this trend seems to change exploring the lower mass range. The peak intensity of the C₅N⁻ signal acquired on the 1 mM-sample is quite similar to the pristine H₂TPP (panel at the bottom left). The signal intensity of NH⁻ is substantially equivalent for all the samples (panel at the bottom left). If we consider the ratio between NH⁻ ion signal and the H₂TPP molecular ion peak (C₄₄H₃₀N₄⁻), it becomes evident that the availability of NH⁻ fragment ions in the volume of analysis is greater for H₂TPP film immersed in sulfuric acid solution than for pristine H₂TPP sample.

This result, together with the gradual decrease in intensity of the abovementioned high mass molecular ion peaks, can be attributable to the fact that the porphyrin ring is destroyed by the interaction with the acid. The picture of the dissolution

mechanism is further corroborated by the chemical maps collected from the H₂TPP sample treated with 100 mM sulfuric acid solution (see Figure S11). The effects of the diluted sulfuric acid can be appreciated on the micrometer scale by observing the total ion image (panel at the top left), the chemical maps of OH⁻ (panel at the top right) and the H₃S₂O₈⁻ map (panel at the bottom left). In particular, the distribution of the strong H₃S₂O₈⁻ ion signal clearly highlights the areas where the acid has reacted with the porphyrin film surface. At the same time, in the same areas, the C₄₄H₃₀N₄⁻ ion image shows significantly lower signal intensity. In other words, the chemical map of the H₂TPP molecular ion peak seems to be complementary to the sulfuric acid map; this effect is more evident comparing the chemical map of the H₂SO₄-related peak (OH⁻) to the C₄₄H₃₀N₄⁻ map. These circular regions have different sizes ranging from tens of microns, as shown in the line-scan of H₃S₂O₈⁻ ion distribution (panel at the bottom center), up to hundreds of microns.

3. Discussion

The porphyrin nanocrystal network of H₂TPP and ZnTPP films on HOPG allows studying the effect of acid solutions as a function of the pH on a great number of crystal domains. When the films are immersed in acidic environment, the system reaches an equilibrium state studied with *in-situ* techniques (e.g. AFM). On the graphite substrate, TPP molecules retain an arrangement characterized by molecules lying parallel to the buried substrate. The chemical reactivity in acidic (non oxidizing) environment^[38] is mostly driven by the non-coordinated pyrrolic N-atoms that, if present, are directly exposed to the liquid environment at the liquid solid interface. In our case, free-base porphyrins and Zn-porphyrins behave differently in terms of the reactions that can be induced by the acidic solution. ZnTPP crystals are stable in diluted H₂SO₄ solution. Conversely, H₂TPP can store charges (protons) on two of the four N-atoms placed in the inner cavity of the molecule. In fact, when protonated (eq. 1), the molecule becomes sufficiently soluble in the aqueous media to be removed from the crystal (reactive dissolution). The molecular fragmentation, observed at the ToF-SIMS analysis, confirms that this picture is at least reliable for the uppermost layers of the 3-D structures. At higher pH (namely, pH=3), the presence of etch-pits on the crystal surface suggests that the Frank dissolution process is active also for nanocrystals.^[28] Conversely, if the pH is further reduced, etch-pit evolution does not represent the ultimate dissolution process. Rather, bulges start to decorate the film surface as observed by the ToF-SIMS analysis. The chemical maps acquired from the free-base porphyrin sample clearly show the presence of residual acid within circular areas with different sizes ranging from tens up to hundreds of microns. At the same time, the porphyrin molecular ion peak signal appears not homogeneously distributed over the film surface; it seems to be attenuated where the acid is more concentrated. These evidences underline the degradation of the tetrapyrrolic macrocycle confirming the formation of bulges as an intermediate step in the crystal dissolution.

TEM and Raman analysis clarify that the H₂TPP crystal dissolution process occurs on the uppermost layers of the 3-D structures while the crystal bulk is preserved. The dissolution process stops when 3-D crystals disappear leaving a flat layer of free-base porphyrins on graphite (see Figure 4a) that are no longer altered by the presence of the acid solution, as reported in Ref. 31.

Finally, it is interesting to compare our results with similar studies, which – e.g. – explore the role of the pH, on inorganic crystals and where AFM is exploited to observe nano-defects on macroscopic crystals. We note that etch-pits^[39–42] are observed together with 3-D structures, sometimes called hillocks (e.g., in Refs. 43 and 44) or bulges.^[45] Different interpretation are given for these structures: a precipitation of solutes^[43] or swelling of the substrates,^[44,45] even if their formation mechanism is still unclear.^[45] In Ref. 45, in particular, the authors describe a diagram that summarizes different dissolution processes: in that work, etch-pits and bulges characterize different diagram regions at low pH. Conversely, our results show an unusual

dissolution behavior in organic nanocrystals: bulges evolve as a function of time when the sample is immersed at room temperature in a solution of pH=2. Generally, bulges are interpreted in terms of hydration of a layer caused by local variation of the surface charge.^[46] This explanation is unfulfilling for our data that show an increase of bulges density when the solution pH is reduced. On the other hand, the possibility of solute precipitation on the top of the organic nanocrystal surface, according to the interpretation reported in Ref. 43, is not fully convincing because our AFM analysis does not reveal significant differences in sulphate-compounds between samples immersed in pH=3 (etch-pits) and pH=1 (bulges). According to Ref. 45, we speculate that bulges could be related to swelling fronts or cracks, but organic nanocrystals show a peculiarity: they have roundish profile even in low pH solutions.

4. Conclusions

We discussed the reactive dissolution of a model system of organic nanocrystals in a dilute acidic solution. While many investigations were performed on millimetric-size crystals, our knowledge on the evolution of nanocrystals is still scarce. To this end, we proposed a model system of nanocrystals obtained by thermal evaporation of porphyrins on HOPG. We compared two structurally congruent systems, namely, free-base porphyrins (H₂TPP) and its Zn(II) complex (ZnTPP). The two systems show totally different behavior in diluted sulfuric acid. In particular, while the nanocrystals and 3-D structures of H₂TPP undergo significantly surface alteration as a function of the solvent pH, ZnTPP crystals are completely stable under the same conditions. Our results demonstrate that etch-pitting is not the ultimate mechanism of crystal dissolution under far-from-equilibrium conditions. Rather, thanks to the possibility offered by our system to exploit pH reduction for shifting the saturation plateau, we showed that different morphological features can appear, spanning from bulges and flattening, affecting the crystal surface for level of undersaturation overpassing the critical one for etch-pit formation.

Experimental methods

Porphyrin nanocrystal film preparation

Z-grade highly oriented pyrolytic graphite (HOPG) was acquired from Optigraph and used as substrate for porphyrin deposition. The substrate surface (0.2 cm²) was mechanically exfoliated before each experiment by mean of an adhesive tape. A solution of 1 M sulfuric acid (H₂SO₄) was prepared diluting a concentrated H₂SO₄ solution (95–97% w/w, Merck) and de-aerated by bubbling pure Ar in a Squibb separator funnel for some hours. 1 mM solutions were obtained diluting the original 1 M solution with MilliQ type 1 water without further purifications.^[47]

Meso-tetra-phenyl porphyrin (H₂TPP, C₄₄H₃₀N₄) and zinc(II) tetra-phenyl porphyrin (ZnTPP, C₄₄H₃₀N₄Zn) were outgassed in high vacuum before their use (base pressure in the low 10⁻⁶ Torr range) by varying the temperature up to the sublimation temperature (300 °C).

H₂TPP and ZnTPP films are grown by physical vapor deposition (PVD) at a pressure of low 10^{-5} Torr. A Kenosistec KE-500 deposition setup, comprehensive of four effusive (Knudsen) sources and two thermal (Joule) sources, was used. The sample holder, with a pneumatic actuated shutter, is positioned 300 mm away from the Knudsen cells (K-cell) and kept at room temperature. The K-cells are thermally controlled by mean of a thermocouple inserted into the crucible. Typically, 30–40 mg of the porphyrin powder are loaded into the K-cell crucible and used for multiple depositions. A quartz-crystal microbalance, placed in proximity of the sample, monitors the material flux. In this work, the reported sample thickness is the time-integrated molecular flux. A good compromise between a great number of crystals (for statistical analysis) and a thin molecular film is represented by 20 nominal layers. The growth rate was set at 0.4–0.5 Å/s and the source temperature at approximately 350 °C and 370 °C for H₂TPP and ZnTPP, respectively.

A Teflon cell was positioned on the deposited sample (for further information on the experimental set-up, please, see Ref. 48) and filled with the solvent (about 1 ml in volume). Under these experimental conditions, the number of available protons in solution is at least 3 orders of magnitude greater than the one of the porphyrin molecules deposited on the substrate. A Viton ring avoids leaks in the cell. The minimum time interval between the filling of the chemical bath and the start of the first AFM scansion is 5 minutes.

Diffraction characterization of porphyrin nanocrystals

Porphyrin thin films were delaminated from the HOPG substrate via a wet-transfer method before acquiring XRD and TEM data.^[49,50] A 0.5 cm-diameter drop of 25% (w/w) water solution of poly(acrylic) acid was deposited on the film surface and let dry (solidify) overnight. The solid polymer layer embedding the porphyrin film was then removed from the HOPG substrate with a glaucoma knife and placed upside-down on a chamber for carbon sputtering. An amorphous carbon layer was deposited on the porphyrin film side after checking that no macroscopic HOPG residues were present. The sample was then placed on the surface of distilled water contained in a glass vessel. The polymer was left to dissolve overnight by leaving the porphyrin film coated with carbon floating on the water surface. Millimeter-sized fragments of the film were transferred on 200-mesh Cu-grids for TEM analysis (vide infra). The rest of the film was transferred on a silicon plate (100 surface with native oxide) and placed on the sample holder of a X'Pert Pro powder diffractometer (PANalytical) equipped with a Cu X-ray tube. Nickel foil is used to reduce the intensity of K β radiation ($\lambda = 1.3922$ Å) while maintaining intense K α radiation ($\lambda = 1.5406$ Å). X-ray reflections in the adopted geometry come from crystallographic planes parallel to the film (and substrate) surface.

Microscopic (TEM, AFM) analysis of the porphyrin nanocrystal system

TEM analysis was performed with a Jeol JEM 2010 electron microscope equipped with an Olympus Tengra CCD camera for image acquisition. Selected Area Electron Diffraction (SAED) patterns were acquired along the [001] direction after internal calibration of the camera length through deposition of gold nanoparticles on the sample. Any distortion was corrected according to Mitchell and Van den Berg.^[51]

AFM images were collected by a Keysight 5500 model in non-contact mode, with specific tips for tapping measurements (Nano-andMore, Poinprobe plus, silicon tip coated with Al on detector side). Resonance frequency was around 130 kHz and images were

collected in attractive regime. The tip force to the sample was estimated of about few nN. This evaluation is deduced from the geometrical and mechanical (elastic constant measured by the thermal noise method) properties of the cantilever and minimizing the normal force by reducing the set point to the disengagement limit, after a proper calibration onto a fresh graphite sample. Images with a maximum scan area of $(6 \times 6) \mu\text{m}^2$ were collected at a frequency of about 1 MHz. The very low scan rate was required to avoid damages of the crystals during the tip scan.

Chemical characterization (Raman, ToF-SIMS) of the organic film

Raman spectra were acquired with a Jobin Yvon Labram HR800 Raman spectrometer, equipped with an Olympus BX41 microscope in backscattering geometry. We used a $50\times$ objective and two excitation lines (457.9 nm and 514 nm Ar⁺ laser). The laser power was set at 0.2 mW, to prevent sample degradation. Due to the low thickness of the film, the spectra are inevitably noisy. Therefore, to validate the assignment to H₂TPP in the thin sample spectra, we compared these measurements with those recorded on porphyrin powder under the same experimental conditions (see the Supporting Information).

ToF-SIMS experiments were performed using a customized ToF-SIMS V instrument (ION-TOF GmbH, Münster, Germany). A 30 keV bismuth liquid metal ion gun (LMIG) was used as primary ion beam providing Bi, Bi₃²⁺, Bi₅²⁺. Positive and negative ion mass spectra were acquired with the high-current bunched mode using Bi₃²⁺ (target current 0.3 pA). Ion beam dose rates were maintained below the static limit ($< 5 \times 10^{12}$ ions/cm²) per analysis. The sample was held at room temperature during the ion bombardment. Secondary ions were collected into a two-stage reflectron ToF analyzer by applying an extraction pulse of 2 kV, and then post-accelerated to 10 keV. The cycle time of the ToF analyzer was set to 100 μs , allowing the acquisition of the spectra in the mass range $1 \leq m/z \leq 850$. Negative mass spectra were calibrated using C⁻, CH⁻, C₂⁻, C₂H⁻, C₄⁻, C₆⁻ peaks, respectively. The resolution achieved ($m/\Delta m$) was equal to 12000 at mass 72 (C₂).

Five measurements, in different areas of the samples, were collected in both polarities, in order to perform reliable statistical analysis on the datasets. All ToF-SIMS data were acquired, calibrated, pre-processed and exported for further analysis by SurfaceLab v6.5. For the statistical analysis, peaks were manually selected from mass spectra. Three different scaling options were tested for scaling mass spectra: normalization to the total ion dose, total counts, and sum of selected peaks. Here, ToF-SIMS spectra were normalized to the sum of selected peaks characteristic of the porphyrin fragmentation. ToF-SIMS images were acquired using 30 keV Bi₃²⁺ primary ions rastered over 256×256 pixels with a field of view of the image of $(500 \times 500) \mu\text{m}^2$. 2D maps were thus acquired with a lateral resolution of 1.9 μm , approximately. Ion images were normalized to the total ion image.

Acknowledgements

The authors are grateful to the Department of Physical Sciences, Earth and Environment, University of Siena (Italy) for the TEM data. M.C. acknowledges the financial support of the University of Milano – Bicocca with FAQC Grant No. 2018-ATESP-0010.

Conflict of Interest

The authors declare no conflict of interest.

Keywords: Porphyrin · porphyrin protonation · etch-pit formation · dissolution rate · dissolution plateau · reactive dissolution · nanocrystals · liquid-phase atomic force microscopy · TEM · ToF-SIMS · Raman spectroscopy

- [1] W. Auwärter, D. Écija, F. Klappenberger, J. V. Barth, *Nat. Chem.* **2015**, *105*, 7.
- [2] Y. Fang, X. Jiang, K. M. Kadish, S. E. Nefedov, G. A. Kirakosyan, Y. Y. Enakieva, Y. G. Gorbunova, A. Y. Tsivadze, C. Stern, A. Bessmertnykh-Lemeune, R. Guillard, *Inorg. Chem.* **2019**, *58*, 7, 4665.
- [3] B. Şahin, M. Z. Ongun, S. Z. Topal, A. G. Gürek, D. Atilla, *J. Porphyrins Phthalocyanines* **2019**, *23*, 469.
- [4] Y. Watanabe, D. Yokoyama, T. Koganezawa, H. Katagiri, T. Ito, S. Ohisa, T. Chiba, H. Sasabe, J. Kido, *Adv. Mater.* **2019**, *31*, 1808300.
- [5] M. Biesaga, K. P. Ska, M. Trojanowicz, *Talanta* **2000**, *51*, 209.
- [6] R. Purrello, S. Gurrieri, R. Lauceri, *Coord. Chem. Rev.* **1999**, *683*, 190.
- [7] M. Kielmann, M. O. Senge, *Angew. Chem. Int. Ed.* **2019**, *58*, 418.
- [8] W. Yang, B. Zhang, *MRS Bull.* **2019**, *3*, 44.
- [9] P. G. Mahajan, N. C. Dige, B. D. Vanjare, S. H. Eo, S. Y. Seo, S. J. Kim, S. K. Hong, C. S. Choi, K. H. Lee, *J. Photochem. Photobiol. A* **2019**, *377*, 26.
- [10] A. García-Sampedro, A. Tabero, I. Mahamed, P. Acedo, *J. Porphyrins Phthalocyanines* **2019**, *23*, 11.
- [11] F. C. Frank, "Growth and Perfection of Crystals", J. Wiley and Sons, New York, **1958**.
- [12] F. C. Frank, M. B. Ives, *J. Appl. Phys.* **1960**, *31*, 1996.
- [13] M. B. Ives, *PhD thesis*, university of Bristol, **1959**.
- [14] P. C. Papaioannou, G. W. Harrington, *J. Phys. Chem.* **1964**, *68*, 2424.
- [15] M. A. Kowalski, G. W. Harrington, *Anal. Chem.* **1972**, *44*, 479.
- [16] D. J. Barber, *J. Appl. Phys.* **1962**, *33*, 3141.
- [17] D. J. Barber, F. C. Frank, M. Moss, J. W. Steeds, I. S. T. Tsong, *J. Mater. Sci.* **1973**, *8*, 1030.
- [18] K. Tsukamoto, P. Dold, *AIP Conf. Proc.* **2007**, *916*, 329.
- [19] S. T. Liu, G. H. Nancollas, E. A. Gasiecki, *J. Cryst. Growth* **1976**, *33*, 11.
- [20] C.-H. Yu, K.-L. Lin, *Chem. Phys. Lett.* **2006**, *418*, 433.
- [21] A. C. Lasaga, A. Lüttge, *Science* **2001**, *291*, 2400.
- [22] A. C. Lasaga, A. Lüttge, *Eur. J. Mineral.* **2003**, *15*, 603.
- [23] C. Fisher, R. S. Arvidson, A. Lüttge, *Geochim. Cosmochim. Acta* **2012**, *98*, 177.
- [24] A. Lüttge, R. S. Arvidson, C. Fisher, *Elements* **2013**, *9*, 183.
- [25] C. Fisher, I. Kurganskaya, T. Schäfer, A. Lüttge, *Appl. Geochem.* **2014**, *43*, 132.
- [26] I. Bibi, R. S. Arvidson, C. Fisher, A. Lüttge, *Minerals* **2018**, *8*, 256.
- [27] A. Lüttge, R. S. Arvidson, C. Fischer, I. Kurganskaya, *Chem. Geol.* **2019**, *504*, 216.
- [28] J. Cama, L. Zhang, J. M. Soler, G. De Giudici, R. S. Arvidson, A. Lüttge, *Geochim. Cosmochim. Acta* **2010**, *74*, 4298.
- [29] L. Briese, R. S. Arvidson, A. Lüttge, *Geochim. Cosmochim. Acta* **2017**, *212*, 167.
- [30] G. Bussetti, M. Campione, M. Riva, A. Picone, L. Raimondo, L. Ferraro, C. Hogan, M. Palumbo, A. Brambilla, M. Finazzi, L. Duò, A. Sassella, F. Ciccacci, *Adv. Funct. Mater.* **2014**, *24*, 958.
- [31] R. Yivlialin, G. Bussetti, M. Penconi, A. Bossi, F. Ciccacci, M. Finazzi, L. Duò, *ACS Appl. Mater. Interfaces* **2017**, *9*, 4100.
- [32] H.-S. He, *Acta Crystallogr. Sect. E* **2007**, *63*, m976.
- [33] V. M. Albers, H. V. Knorr, *J. Chem. Phys.* **1936**, *4*, 422.
- [34] P. Stein, A. Ulman, T. G. Spiro, *J. Phys. Chem.* **1984**, *374*, 883369.
- [35] G. S. S. Saini, *Spectrochim. Acta Part A* **2006**, *64*, 981.
- [36] R. E. Oakes, S. E. J. Bell, *J. Phys. Chem. A* **2003**, *10959*, 10750.
- [37] A. Gorski, A. Starukhin, S. Stavrov, S. Gawinkowski, J. Waluk, *Spectrochim. Acta Part A* **2017**, *173*, 350–355.
- [38] R. Yivlialin, M. Penconi, G. Bussetti, A. Orbelli-Birolì, M. Finazzi, L. Duò, A. Bossi, *Appl. Surf. Sci.* **2018**, *442*, 501.
- [39] K. Sangwal, J. N. Sutaria, *J. Mater. Sci.* **1976**, *11*, 2271.
- [40] Q. Hong, M. F. Suárez, B. A. Coles, R. G. Compton, *J. Phys. Chem. B* **1997**, *101*, 5557.
- [41] K. Aldushin, G. Jordan, W. W. Schmahl, *Geochim. Cosmochim. Acta* **2006**, *70*, 4380.
- [42] C. Cappelli, A. E. S. Van Driessche, J. Cama, F. J. Huertas, *Cryst. Growth Des.* **2013**, *13*, 2880.
- [43] M. F. Suárez, R. G. Compton, *J. Phys. Chem. B* **1998**, *102*, 7156.
- [44] M. Li, L. Wang, W. Zhang, C. V. Putnis, A. Putnis, *Cryst. Growth Des.* **2016**, *16*, 4509.
- [45] D. Lamarca-Irisarri, A. E. S. Van Driessche, G. Jordan, C. Cappelli, F. J. Huertas, *ACS Earth Space Chem.* **2019**, *3*, 2613.
- [46] C. Cappelli, D. Lamarca-Irisarri, J. Camas, F. J. Huertas, A. E. S. Van Driessche, *Beilstein J. Nanotechnol.* **2015**, *6*, 665.
- [47] S. De Rosa, P. Branchini, R. Yivlialin, L. Duò, G. Bussetti, L. Tortora, *ACS Appl. Nano Mater.* **2020**, *3*, 691.
- [48] M. S. Jagadeesh, A. Calloni, I. Denti, C. Goletti, F. Ciccacci, L. Duò, G. Bussetti, *Surf. Sci.* **2019**, *681*, 111.
- [49] A. Thierry, J. C. Wittmann, B. Lotz, V. da Costa, J. Le Moigne, M. Campione, A. Borghesi, A. Sassella, H. Plank, R. Resel, *Org. Electron.* **2004**, *5*, 7.
- [50] M. Campione, A. Borghesi, M. Moret, A. Sassella, B. Lotz, A. Thierry, *Org. Electron.* **2004**, *5*, 141.
- [51] D. R. G. Mitchell, J. A. van den Berg, *Ultramicroscopy* **2016**, *160*, 140.

Manuscript received: January 7, 2020
Accepted manuscript online: January 30, 2020
Version of record online: March 6, 2020

Supporting Information

Reactive dissolution of organic nanocrystals at controlled pH

C. Filoni¹, L. Duò¹, F. Ciccacci¹, A. Li Bassi², A. Bossi³, M. Campione⁴, G. Capitani⁵, I. Denti⁶, M. Tommasini⁶, C. Castiglioni⁶, S. De Rosa⁷, L. Tortora⁷, G. Bussetti^{1*}

- 1) Department of Physics, Politecnico di Milano, p.za Leonardo da Vinci 32, I-20133 Milano, Italy
- 2) Department of Energy, Politecnico di Milano, via Ponzio 34/3, I-20133 Milano, Italy
- 3) Istituto di Scienze e Tecnologie Chimiche “G. Natta”, Consiglio Nazionale delle Ricerche (CNR-SCITEC), PST via G. Fantoli 16/15, I-20138 Milano, Italy and via Golgi 19, I-20133 Milano, Italy; SmartMatLab Center, via Golgi 19, I-20133 Milano, Italy.
- 4) Department of Earth and Environmental Sciences, Università degli Studi di Milano – Bicocca, Piazza della Scienza 4, I-20126 Milano, Italy.
- 5) Department of Earth and Environmental Sciences, Università degli Studi di Milano Bicocca, Piazza della Scienza 4, I-20126 Milano, Italy.
- 6) Department of Chemistry, Materials and Chemical Engineering, Politecnico di Milano, p.za Leonardo da Vinci 32, I-20133 Milano, Italy.
- 7) Department of Mathematics and Physics, Roma Tre University, via della Vasca Navale 84, 00146, Rome, Italy

AFM characterization.

Deposition of the H₂TPP molecules under high vacuum on HOPG substrates follows a layer-plus-island growth mode^[1]. The nominal 20 nm thick deposited film presents, on a preliminary microscopic investigation performed by AFM, the typical 2D wetting-layer on top of which wide 3-D structures grow, as evident in **Figure S1**.

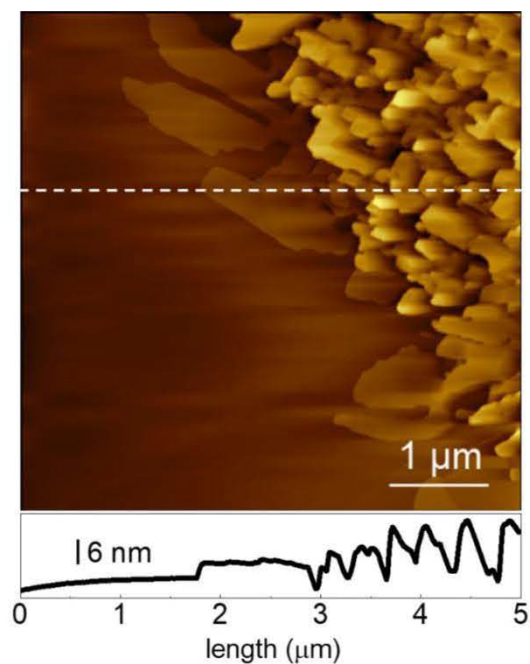


Figure S1. AFM image of a ZnTPP film where the left side of the organic film is removed. The image is acquired on the border of a sample, where half of the surface was exfoliated by adhesive tape. The buried porphyrin structures are wider with respect to the uppermost ones, showing a shrinkage of the crystals that produces an organic film composed by many nanocrystals.

TEM and diffraction characterization.

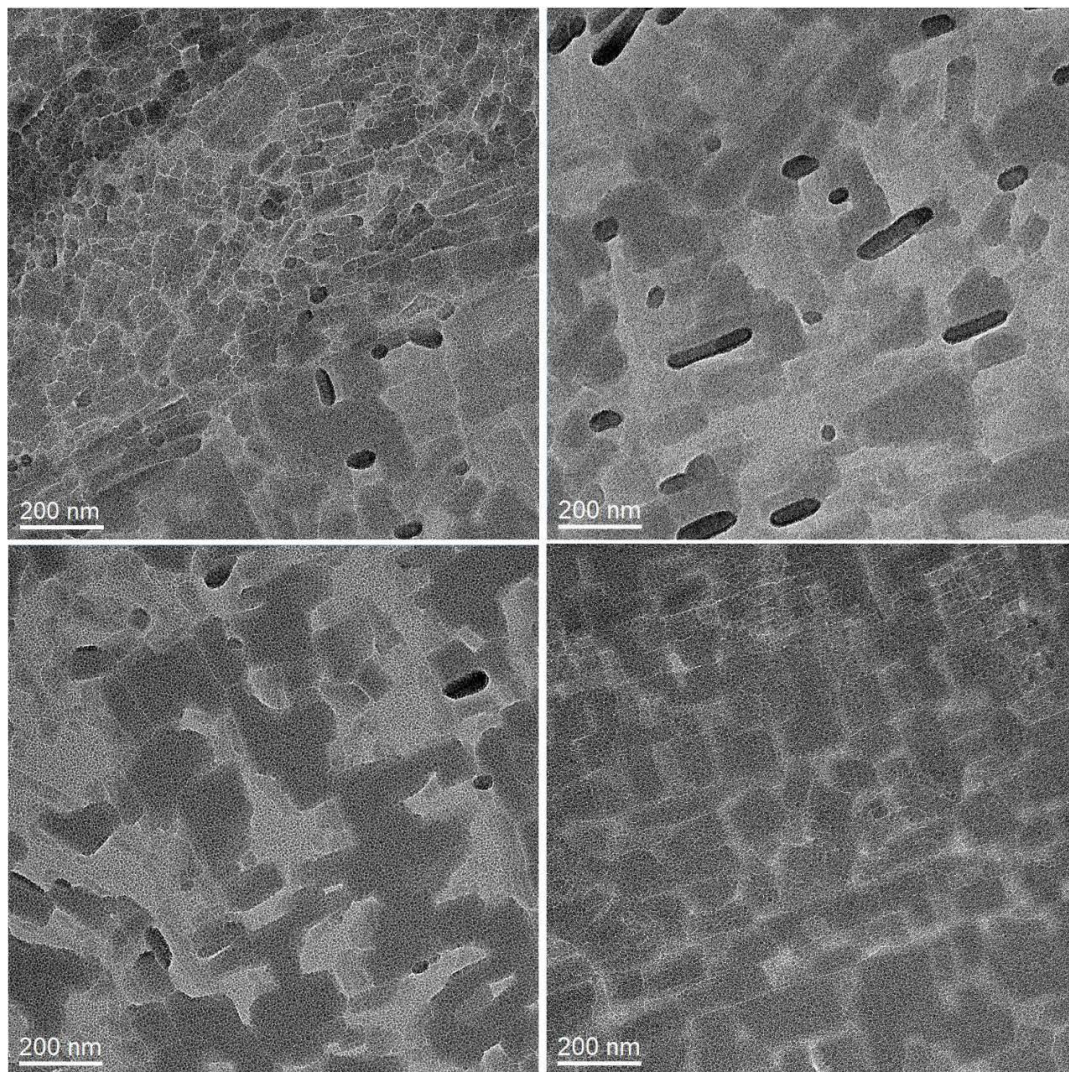


Figure S2. Bright-field TEM images of pristine 24 nm-thick H₂TPP films on HOPG after wet-transfer on Cu-grids. Tabular crystalline domains separated by grain-boundaries are clearly visible (intermediate gray level), together with some rare oriented needle-like crystallites (dark contrast).

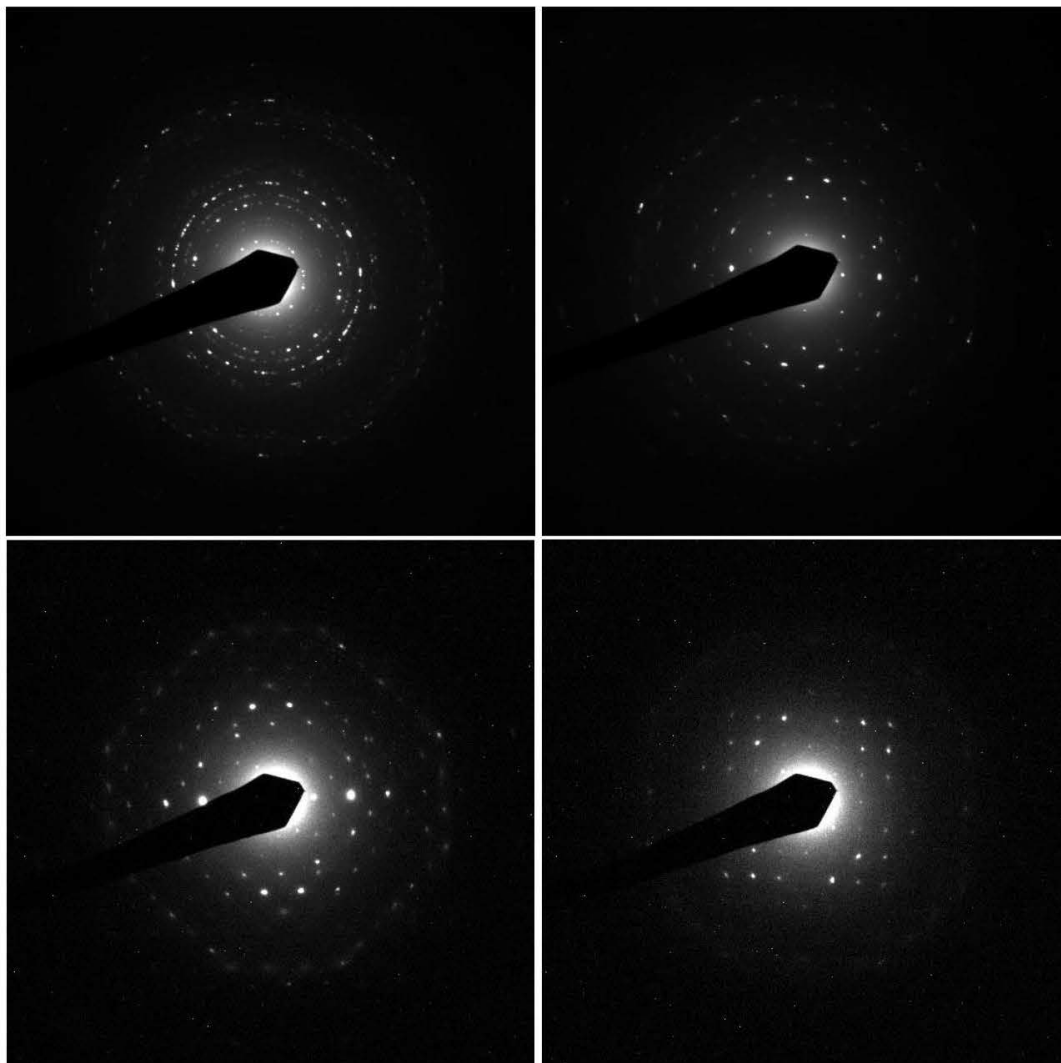


Figure S3. Electron diffraction patterns of polycrystal (top-left) and single crystal (other panels) domains of pristine 24 nm-thick H₂TPP films on HOPG after wet-transfer on Cu-grids.

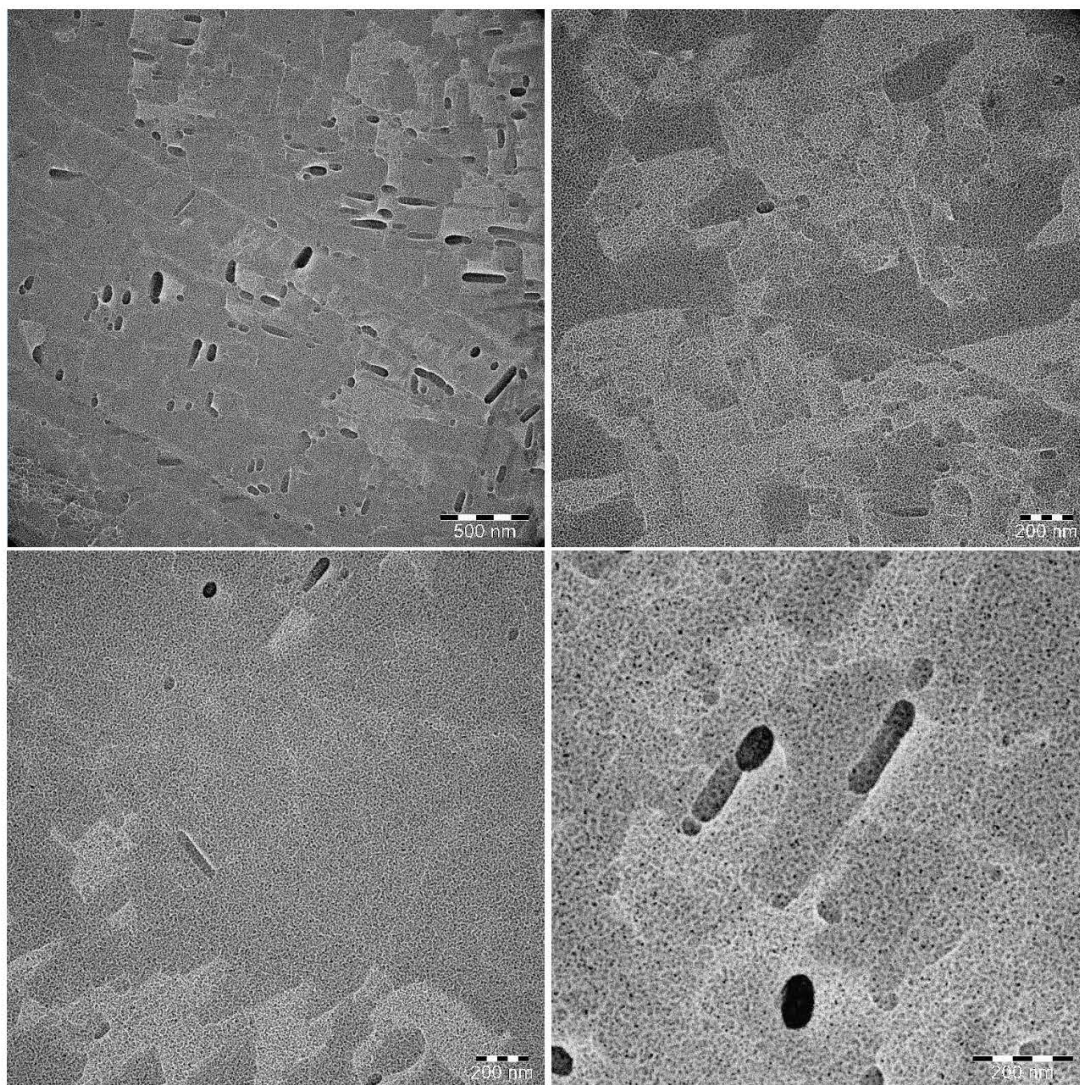


Figure S4. Bright-field TEM images of H_2SO_4 100mM-treated 24 nm-thick H_2TPP films on HOPG after wet-transfer on Cu-grids and Au coating for diffraction calibration (see Figure S5). Tabular crystalline domains separated by grain-boundaries are clearly visible (intermediate gray level), together with some rare oriented needle-like crystallites (dark contrast). The spotty contrast observable at high magnification is due to the Au coating.

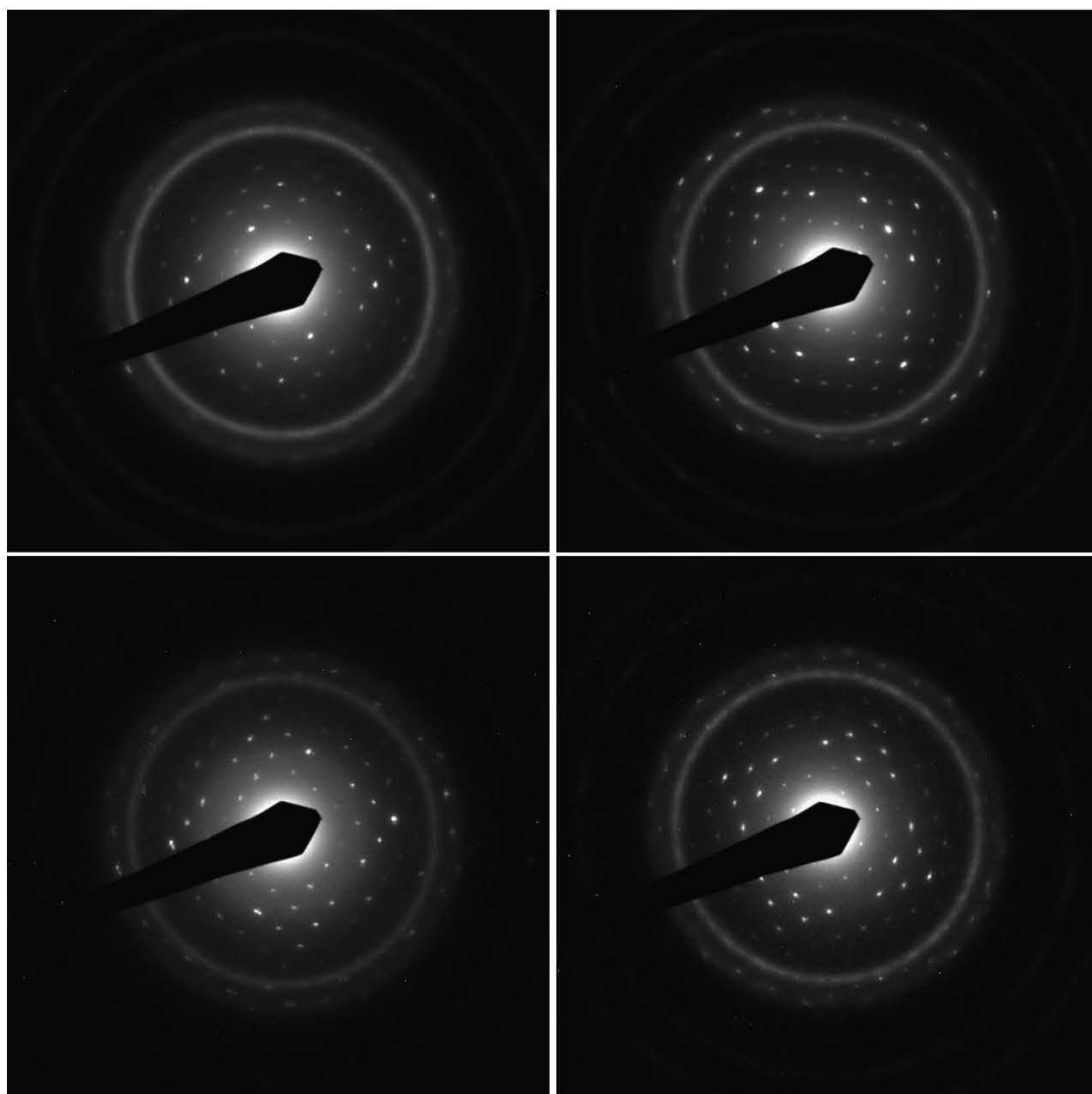


Figure S5. Electron diffraction patterns of crystal domains of H_2SO_4 100mM-treated 24 nm-thick H_2TPP films on HOPG after wet-transfer on Cu-grids and Au coating. Diffused rings are due to the Au nanocrystalline layer used for calibration.

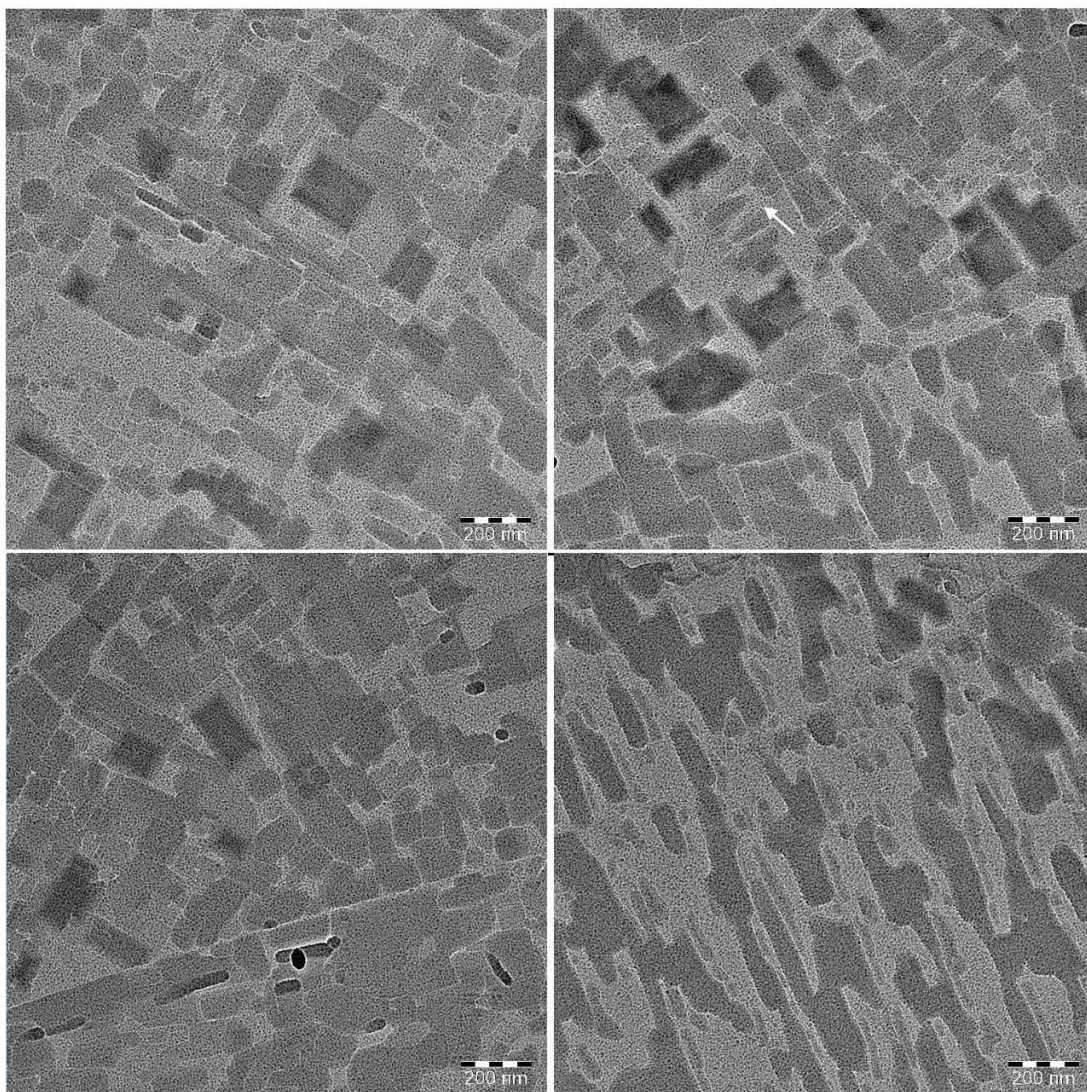


Figure S6. Bright-field TEM images of 24 nm-thick ZnTPP films on HOPG after wet-transfer on Cu-grids. Tabular crystalline domains separated by grain-boundaries are clearly visible with two intermediate gray levels, together with some rare oriented needle-like crystallites (dark contrast).

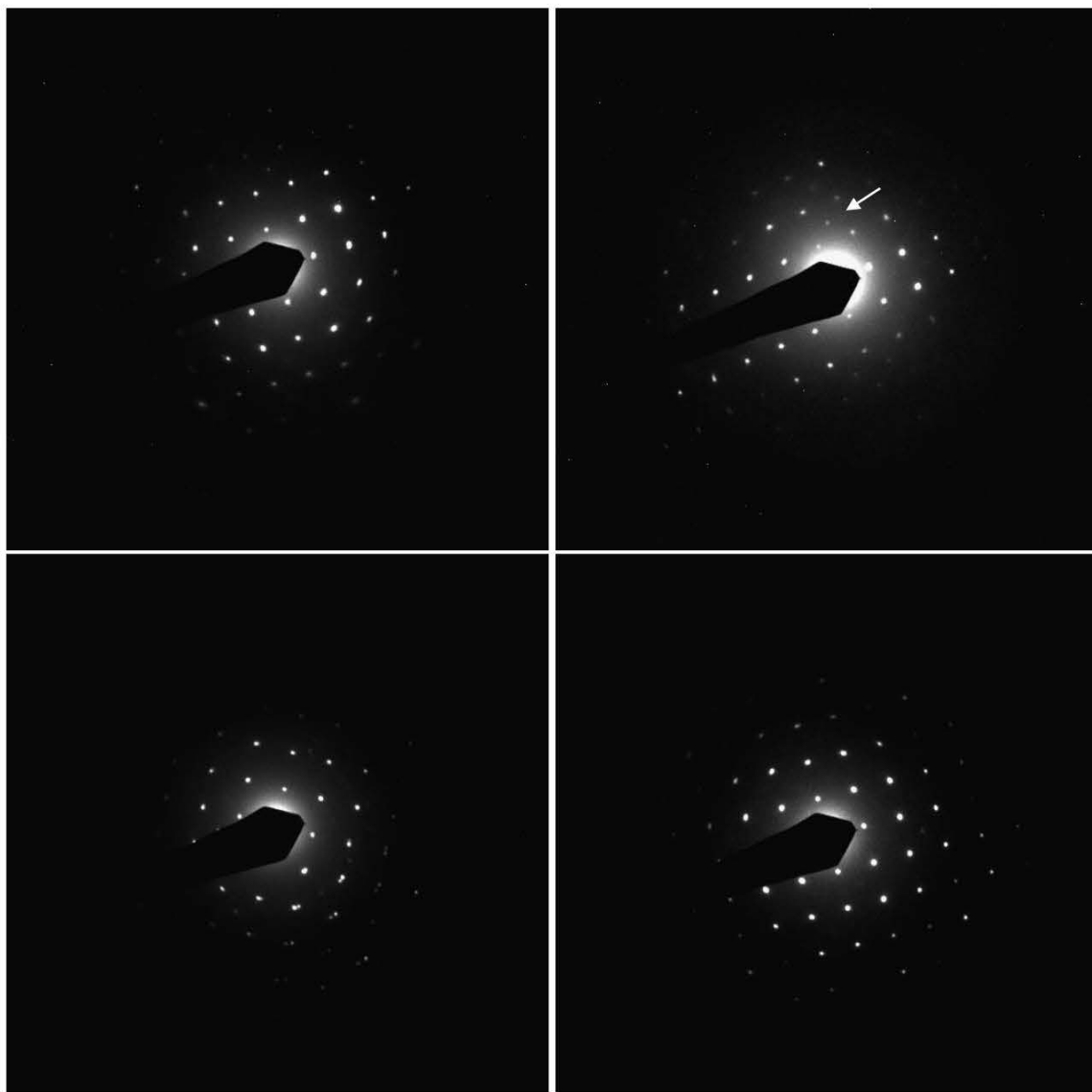


Figure S7. Electron diffraction patterns of crystal domains of 24 nm-thick ZnTPP films on HOPG after wet-transfer on Cu-grids. The white arrow indicates h0l reflections with odd h which in other patterns are systematically extinguished.

Table S1. In-plane unit-cell parameters (base vectors a and b and angle γ) of TPP films as deduced from electron diffraction analysis. Standard deviations are reported in brackets.

	H ₂ TPP			H ₂ TPP + H ₂ SO ₄		ZnTPP	
a	13.52 (7)	12.96 (6)	13.61 (7)	13.44 (3)	13.41 (6)		
b	13.69 (7)	13.38 (7)	13.60 (7)	13.34 (4)	13.32 (6)		
γ	90.2 (5)	93.3 (5)	90.4 (5)	90.2 (2)	90.1 (2)		

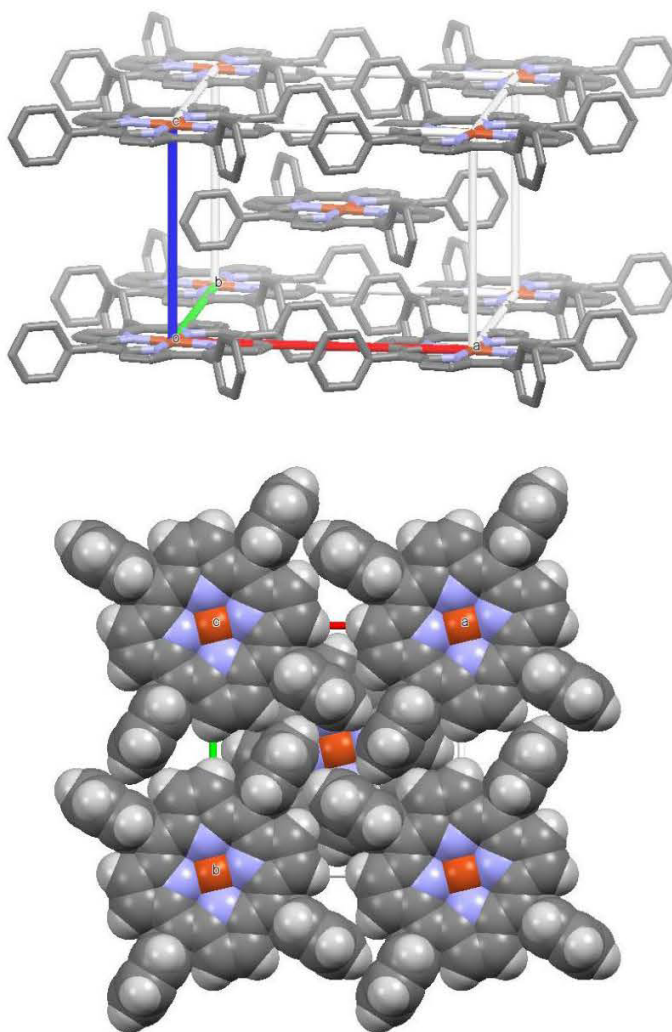


Figure S8. Structural model of the tetragonal polymorph of CuTPP^[2], with unit cell parameters $a = b = 13.37 \text{ \AA}$ and $c = 9.73 \text{ \AA}$.

Raman characterization.

We compare in **Figure S9** the Raman spectra of the same H₂TPP powders excited at 514 nm and 458 nm. Both spectra show a manifold of first- and second-order Raman transitions with corresponding wavenumber, but different relative intensities. This behavior is due to resonance effects that are stronger with the 514 nm excitation, as proved by the presence of intense overtones and a fluorescence background.

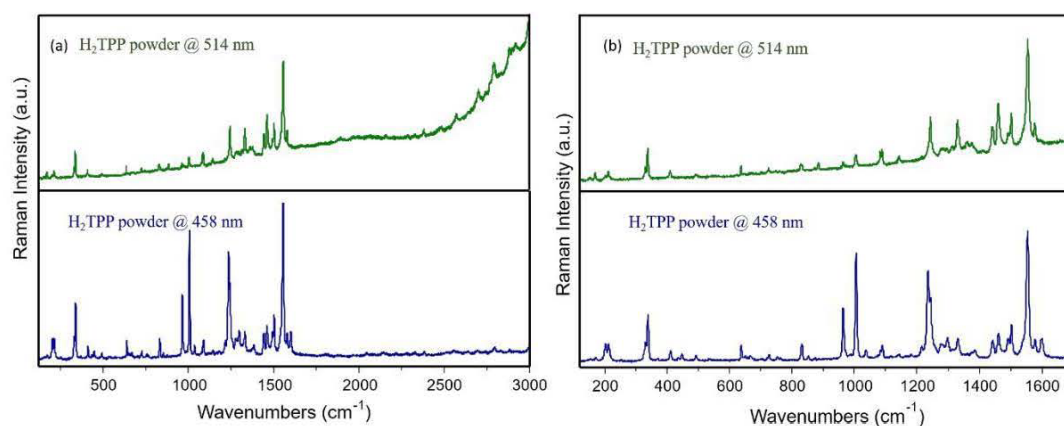


Figure S9: (a) Comparison between the Raman spectra of H₂TPP powders recorded with 514 nm and 458 nm excitation wavelengths, (b) zoom over the 150-1800 cm⁻¹ region.

We report in **Figure S10** the full set of spectra acquired with the 514 nm excitation. To ease comparison, the panels of Figure S9 match those of Figure 6 of the main text (458 nm excitation; notice that the sample preparation and acquisition parameters do not change along the two series of experiments with different excitation). Figure S9a directly compares the 24 nm thick H₂TPP sample on HOPG with the reference isotropic H₂TPP sample (powder).

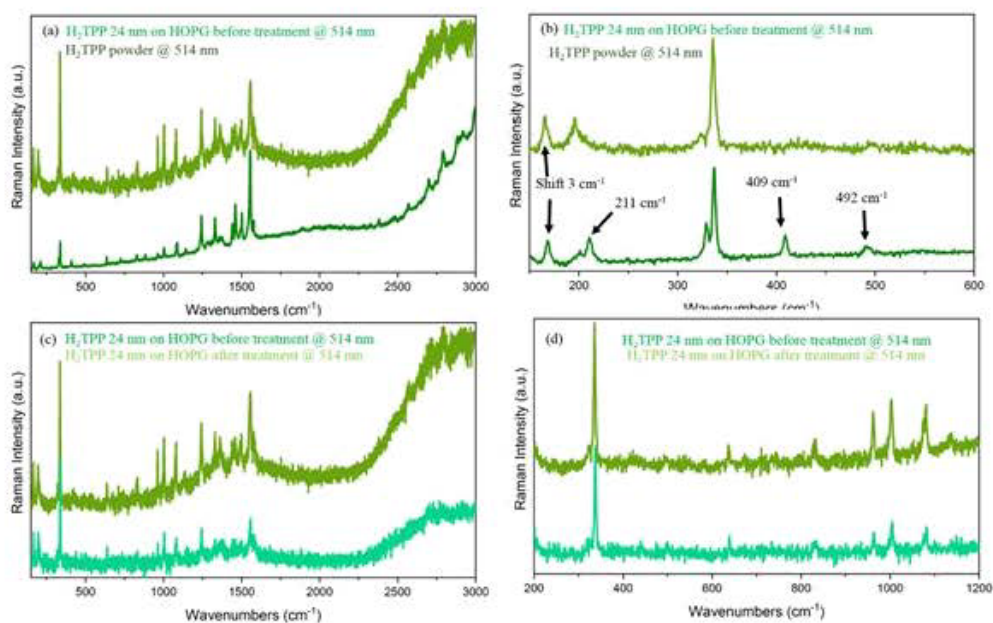


Figure S10. Raman spectra acquired at 514 nm excitation wavelength: (a) comparison between spectra of a powder H_2TPP sample and 24 nm deposited H_2TPP on HOPG sample (before the immersion in H_2SO_4 , 1 M) and (b) zoom over the (600-120 cm^{-1}) spectral region; (c) comparison between spectra of a 24 nm deposited H_2TPP on HOPG sample before and after the immersion H_2SO_4 , 1M and (d) zoom over the (1200-1200 cm^{-1}) spectral region.

Figure S9b emphasizes the differences observed between the spectrum of the film and the reference spectrum of the powders, namely:

- the lines at 492 and 409 cm^{-1} disappear in the Raman spectrum of the film;
- the doublet at 196 - 211 cm^{-1} in the Raman spectrum of the powders shows only the component at 196 cm^{-1} in the spectrum of the film; the peak at 211 cm^{-1} , evident in the powders spectrum, disappears in the film spectrum.

Raman measurement with 458 nm excitation, these differences between the spectrum of the powders and the spectrum of the film are due to the preferential orientation of H_2TPP molecules within the film grown on the HOPG surface. The Raman intensity of isotropic samples (with no preferential orientation) depends on the orientational average of the Raman tensor^[9] whereas the Raman intensity of oriented samples (e.g., crystals) depends on the spatial relation between the

Raman tensor and the polarization vectors of the excitation and collection^[4]. For this reason, relative intensities in the Raman spectra of isotropic vs. oriented samples of the same substance may differ.

The panels c and d of Figure S3 compare the spectra before and after the immersion of the H₂TPP film in the acidic environment (H₂SO₄, 100 mM). Even though, as expected, the overall quality of the film decreases (leading to noisier spectra), both the peak positions and the relative intensities remain the same after such film treatment. This behavior matches the observations made with 458 nm excitation (see main text). The similarity among the data acquired at 514 nm and 458 nm, as well as the absence of marker bands for protonation, confirms that the 3D structure of the porphyrin crystal is not affected during the tested acidic treatment.

ToF-SIMS characterization.

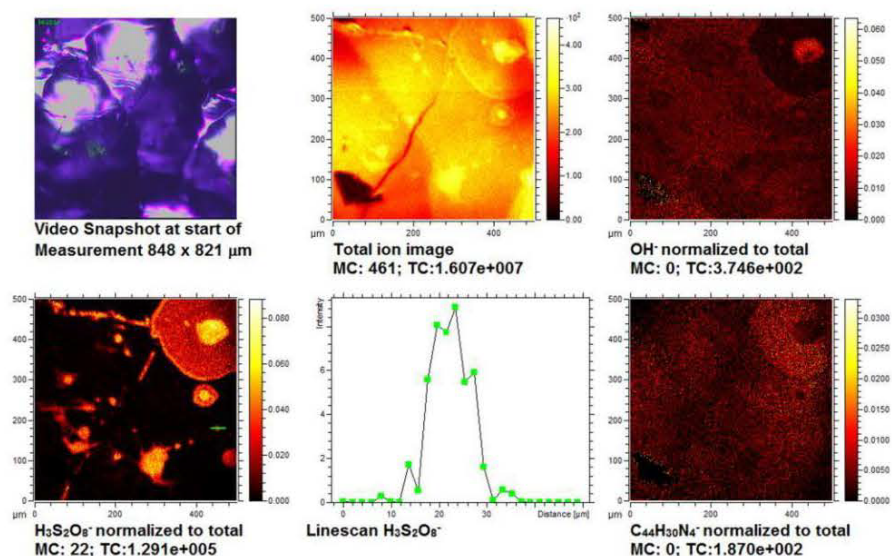


Figure S11 Negative ion images from H₂TPP sample immersed in 100mM sulfuric acid solution. (Top left) Video snapshot from the built-in microcamera of the ToF-SIMS apparatus showing the sample surface (848 × 821 μm). (Top center) Total negative ion image. Negative ion images of: (Top right) OH⁻, *m/z* 17.00, (Bottom left) H₃S₂O₈⁻, *m/z* 194.93, (Bottom center) Linescan of H₃S₂O₈⁻ ion distribution; the x-axis is highlighted in green in the related chemical map. (Bottom right) C₄₄H₃₀N₄⁻, *m/z* 614.24.

References.

[1] G. Bussetti, M. Campione, M. Riva, A. Picone, L. Raimondo, L. Ferraro, C. Hogan, M. Palumbo, A. Brambilla, M. Finazzi, L. Duò, A. Sassella, F. Ciccacci, *Adv. Funct. Mater.* **2014**, *24*, 958.

[2] Hong-Shan He, *Acta Crystallogr.E* **2007**, *63*, m976.

[3] D. A. Long, *The Raman Effect: A Unified Treatment of the Theory of Raman Scattering by Molecules*, chapter 5, 2002 John Wiley & Sons Ltd.

[4] R. Loudon (1964): The Raman effect in crystals, *Advances in Physics*, *13*:52, 423-482.

